AN ABSTRACT OF THE DISSERTATION OF

Justyna Sikorska for the degree of Doctor of Philosophy in Pharmacy presented on August 29, 2012.

Title: Application of Modern NMR Techniques to Structure Elucidation of Bioactive Natural Products from Tunicates

Abstract approved:

Kerry L. McPhail

Recent developments in NMR hardware have extended the reach of natural products chemists to structure elucidation of compounds isolated on a nanomolar scale. In parallel with advances in hardware new NMR techniques for structure elucidation have evolved, e.g. quantitative NOEs, residual dipolar couplings (RDCs) and diffusion-ordered spectroscopy (DOSY). The application of recent NMR techniques was utilized in the screening and structural assignment of natural products isolated from a 2004 collection of South African tunicates. Assignment of the planar structures of mandelalides A-D from a new *Lissoclinum* sp. was feasible only after data acquisition on a 700 MHz magnet equipped with 5 mm ^{13}C cryogenic probe. While relative configuration of the polyketide mandelalides was established after extensive *J*-coupling and NOE analysis, quantitative ROESY and RDC measurements were also explored before the absolute configuration was accomplished by chemical degradation and comparison with standards. The application of DOSY, a greatly under-appreciated technique in natural products research, led to the identification of new rubrolide analogues, compounds with moderate antibacterial properties from the new species *Synoicum globosum*. Finally, relative and absolute configuration of new and known unstable amino alcohols from two *Pseudodistoma* species was based on *J*-coupling analysis and application of the Mosher method.

© Copyright by Justyna Sikorska

August 29, 2012

All Rights Reserved

Application of Modern NMR Techniques to Structure Elucidation of Bioactive Natural Products from Tunicates

by

Justyna Sikorska

A DISSERTATION

submitted to

Oregon State University

in partial fulfillment of

the requirements for the

degree of

Doctor of Philosophy

Presented August 29, 2012

Commencement June 2013

Doctor of Philosophy dissertation of Justyna Sikorska presented on August 29, 2012.

APPROVED:

Major Professor, representing Pharmacy

Dean of the College of Pharmacy

Dean of the Graduate School

I understand that my dissertation will become part of the permanent collection of Oregon State University libraries. My signature below authorizes release of my dissertation to any reader upon request.

Justyna Sikorska, Author

ACKNOWLEDGEMENTS

First and foremost I would like to thank my family members who have been there when I have needed them the most.

I would like to thank my advisor, Dr. Kerry L. McPhail, for guiding me along the path to being a better scientist and allowing me the freedom to learn from my own mistakes and direct my own projects.

I also wish to acknowledge Dr. Philip J. Proteau and Dr. Mark Zabriskie for their guidance and support; Rodger Kohnert for patience and time in introducing me to the field of NMR spectroscopy; members, past and present, of the McPhail, Zabriskie, Ishmael, Mahmud and Proteau labs for technical assistance; my committee members for providing valuable insights.

CONTRIBUTION OF AUTHORS

The collection of sixty extracts from tunicates collected in Algoa Bay, South Africa (2004) was kindly provided by Dr. Michael T. Davies-Coleman from Rhodes University, South Africa, while taxonomic assignment was performed by Dr. Shirley Parker-Nance of the Nelson Mandela Metropolitan University, South Africa. Dr. Kerry L. McPhail contributed to research design, data analysis, writing and editing. Acquisition of NMR data for mandelalides A-D (700 MHz, inverse cryogenic probe) was performed by Dr. Clemens Anklin (Bruker Biospin). Establishment of assays and further support in biological testing was given by Andrew M. Hau, Oliver B. Vining, Dr. Jane E. Ishmael and Dr. Aleksandra E. Sikora.

TABLE OF CONTENTS

Page

CHAPTER ONE: GENERAL INTRODUCTION 1

Progress and new approaches in NMR techniques applicable to natural products 4

Application of NMR techniques to the assignment of relative configuration 12

Application of NMR techniques to the assignment of absolute configuration 22

CHAPTER TWO: BIOLOGICAL AND CHEMICAL SCREENING OF TUNICATE EXTRACTS 33

Abstract 34

Introduction 35

Results and Discussion 37

Experimental 64

CHAPTER THREE: MANDELALIDES A-D, CYTOTOXIC MACROLIDES FROM A NEW *LISSOCLINUM* SPECIES OF SOUTH AFRICAN TUNICATE. 72

Abstract 73

Introduction 74

Results and Discussion 76

Experimental 111

CHAPTER FOUR: AMINO ALCOHOLS FROM SOUTH AFRICAN SPECIES OF *PSEUDODISTOMA* TUNICATES 120

Abstract 121

Introduction 122

Results and Discussion 124

Experimental 151

CHAPTER FIVE: GENERAL CONCLUSIONS 157

LIST OF FIGURES

Figure Page

Figure 1.1 Structures of ciguatoxin (top) and glycinoeclepin A (bottom). 5

Figure 1.2 Structure of sperm activating and attracting factor..... 5

Figure 1.3 Structures of phorbazide A, muironolide A and hemi-phorboxazole A (from left to right, respectively). 6

Figure 1.4 Chemical structures of myrmicarin 430A and sulfated guanosine derivatives respectively. 7

Figure 1.5 a) ^{1}H NMR spectrum of unmodified *T. agrestis* venom in D_2O at 500 MHz. 8

Figure 1.6 Partial DOSY spectrum for an extract fraction from the sponge *Agelas* sp 10

Figure 1.7 Chemical structures of flavone (1), fisetin (2) and (+)-catechin (3), upper line. DOSY spectrum before and after addition of SDS to mixture of flavone, fisetin and (+)-catechin. 11

Figure 1.8 Fit of DFT-calculated interproton distances to experimental values from 1D-ROESY experiments for both diastereoisomers of conicaterol F. 13

Figure 1.9 Relationships between dihedral angles and coupling constant values for $^{3}J_{HH}$, $^{2}J_{CH}$ and $^{3}J_{CH}$. 14

Figure 1.10 a) Partial HETLOC spectrum with correlations responsible for peak splitting in the *F1* and *F2* dimensions indicated on the spectrum together with partial structure. b) The partial α/β-selHSQMBC-TOCSY spectrum for progesterone showing correlations (indicated on the partial structure) that are responsible for peak splitting in the *F2* dimension. 15

Figure 1.11 Partial (0 to 60 ppm) ^{13}C NMR gated decoupled spectra (175 MHz) for strychnine: isotropic solution of strychnine in $CDCl_3$ (top); anisotropic solution of strychnine in poly benzyl-L-glutamate (PBLG) /$CDCl_3$ (bottom)..... 17

LIST OF FIGURES (Continued)

Figure | Page

Figure 1.12 a) Chemical structure of sagittamide A as proposed by Lievens and confirmed by analysis of RDCs, b) Configuration of C4/C10 fragment proposed by Seike, c –e) Configurations proposed for sagittamide A by Schuetz. 18

Figure 1.13 Chemical structure of prorocentrol with measured and standard $^{3}J_{HH}$ values indicated. 20

Figure 1.14 Schematic representation of changes in chemical shift values for *syn*- and *anti*- acetonides (top and bottom respectively). 21

Figure 1.15 Chemical structure of the acetonide derivative of marinisporolide A. 21

Figure 1.16 a) A schematic representation of the application of the Mosher method for (*R*)-2-pentanol; b) Structure of (*R*)-2-pentanol with $\Delta\delta_{RS}$ values indicated. 23

Figure 1.17 The derivatizing reagents used for assignment of absolute configuration of a) alcohols, b) amines, c) acids. 25

Figure 2.1 ^{1}H NMR spectra at 300 MHz for extracts SAF04-54, -16, -59 and -57 (left from top to bottom), and for SAF04-60, -44, -71 and -65 (right from top to bottom). 41

Figure 2.2 ^{1}H (700 MHz) and ^{13}C (175 MHz) NMR spectra for homarine (1). 42

Figure 2.3 ^{1}H NMR spectrum at 300 MHz for SAF04-56 (upper) and SAF04-68 (lower). 43

Figure 2.4 2D DOSY spectra at 300 MHz for SAF04-65 and SAF04-54 (left upper and lower, respectively), and SAF04-57 and SAF04-44 (right upper and lower, respectively). 44

Figure 2.5 Chemical structures of new rubrolides 2-5 and known rubrolides E (6) and F (7). 45

Figure 2.6 ^{1}H NMR spectrum for 3″-bromorubrolide F (2; 700 MHz, CD_3OD)..... 48

LIST OF FIGURES (Continued)

Figure Page

Figure 2.7 HSQC spectrum for 3″-bromorubrolide F (2; 700 MHz, CD_3OD) 48

Figure 2.8 HMBC spectrum for 3″-bromorubrolide F (2; 700 MHz, CD_3OD) 49

Figure 2.9 NOESY spectrum for 3″-bromorubrolide F (2; 700 MHz, CD_3OD)..... 49

Figure 2.10 ^1H NMR spectrum for 3′-bromorubrolide E (3; 700 MHz, CD_3OD) 50

Figure 2.11 COSY spectrum for 3′-bromorubrolide E (3; 700 MHz, CD_3OD)..... 50

Figure 2.12 HMBC spectrum for 3′-bromorubrolide E (3; 700 MHz, CD_3OD)..... 51

Figure 2.13 ^1H NMR spectrum for 3′-bromo-rubrolide F (4; 700 MHz, CD_3OD) 54

Figure 2.14 ^1H NMR spectrum for 3′, 3″-dibromorubrolide E (5; 700 MHz, CD_3OD) 54

Figure 2.15 COSY spectrum for 3′, 3″-dibromorubrolide E (5; 700 MHz, CD_3OD).. 55

Figure 2.16 HMBC spectrum for 3′, 3″-dibromorubrolide E (5; 700 MHz, CD_3OD). 55

Figure 2.17 ^1H NMR spectrum for rubrolide E (6; 300 MHz, CD_3OD)..... 57

Figure 2.18 HMBC NMR spectrum for rubrolide E (6; 300 MHz, CD_3OD) 57

Figure 2.19 ^1H NMR spectrum for rubrolide F (7; 300 MHz, CD_3OD) 58

Figure 2.20 ^1H NMR spectrum for rubrolide F (7; 700 MHz, CD_3OD) 58

Figure 2.21 ^1H NMR spectrum for rubrolide F + NaOH (7; 300 MHz, CD_3OD) 59

Figure 2.22 ^1H NMR spectrum for rubrolide F + NaOH + HCOOH (7; 300 MHz, CD_3OD)..... 59

LIST OF FIGURES (Continued)

Figure Page

Figure 2.23 Chemical structures of tetillapurone, opuntioside III, thymidine (8), uracil (9), uridine (10), inosine (11). 61

Figure 2.24 ^{1}H and ^{13}C NMR spectra for thymidine (8; 700 MHz, CD_3OD) 63

Figure 3.1 ^{1}H NMR spectrum for mandelalide A (1; 700 MHz, $CDCl_3$)..... 79

Figure 3.2 ^{13}C NMR spectrum for mandelalide A (1; 175 MHz, $CDCl_3$) 79

Figure 3.3 HSQC spectrum for mandelalide A (1; 700 MHz, $CDCl_3$) 80

Figure 3.4. Planar structure of 1 showing TOCSY correlations from H-2, H-6, H-8, H-10b, H-13, H-17, H-21, H-1′, H-2′ 80

Figure 3.5 COSY spectrum for mandelalide A (1; 700 MHz, $CDCl_3$) 81

Figure 3.6 TOCSY spectrum for mandelalide A (1), TOCSY mixing time = 100 ms (700 MHz, $CDCl_3$) 81

Figure 3.7 HMBC spectrum for mandelalide A (1; 700 MHz, $CDCl_3$) 82

Figure 3.8 ROESY spectrum for mandelalide A (1; 700 MHz, $CDCl_3$). 82

Figure 3.9 ^{1}H NMR spectrum for mandelalide B (2; 700 MHz, $CDCl_3$)..... 84

Figure 3.10 ^{13}C NMR spectrum for mandelalide B (2; 175 MHz, $CDCl_3$)..... 84

Figure 3.11 . HSQC spectrum for mandelalide B, (2; 700 MHz, $CDCl_3$) 85

Figure 3.12 HMBC spectrum for mandelalide B, (2; 700 MHz, $CDCl_3$) 85

Figure 3.13 ^{1}H NMR spectrum for mandelalide C (3; 700 MHz, $CDCl_3$)..... 89

Figure 3.14 ^{13}C NMR spectrum for mandelalide C (3; 175 MHz, $CDCl_3$)..... 89

LIST OF FIGURES (Continued)

Figure | Page

Figure 3.15 ^{1}H NMR spectrum for mandelalide D (4; 700 MHz, $CDCl_3$) 90

Figure 3.16 HMBC spectrum for mandelalide D (4; 700 MHz, $CDCl_3$) 90

Figure 3.17 a) Key ROESY correlations indicated on the C-5/C-15 fragment of 1; b) Two possible rotamers around the C-9/C-10 bond; c) Most feasible rotamers around the C-10/C-11 bond of 1, with anticipated large/small heteronuclear coupling constant indicated on each. 93

Figure 3.18 ROESY NMR spectrum for mandelalide A (1; 700 MHz, py-d_5) 94

Figure 3.19 HETLOC spectrum for mandelalide A (1; 700 MHz, $CDCl_3$) 94

Figure 3.20. a) Newman projections along the C-16/C-17 and C-20/C-21 bonds in 1; b) The most feasible *cis* orientation of the THF ring with double-headed arrows indicating ROESY correlations; c) Newman projection along the C-21/C-22 bond with applicable J_{HH} and J_{HC} values ($CDCl_3$) indicated on the right. d) Newman projection along the C-22/C-23 bond and relevant coupling constants. 96

Figure 3.21. a) Partial TOCSY spectrum for mandelalide A (1) showing the α-2-O-methylrhamnose region, TOCSY mixing time = 100 ms (700 MHz, $CDCl_3$), b) The magnetization transfer pattern of TOCSY signals for the mandelalide A monosaccharide and α- and β-L-rhamnose. 97

Figure 3.22. *F2* slice of HETLOC spectrum for mandelalide A (1) anomeric C-1′ (700 MHz, $CDCl_3$) 98

Figure 3.23. a) Key ROESY correlations for the C-3/C-5 fragment of 2 are indicated by double-headed arrows on the partial structure. b) The most probable rotamer along the C-3/C-4 bond highlighted by the dashed outline and alternative equilibrium of two rotamers explaining medium size coupling constants. 99

Figure 3.24 Gated decoupled ^{13}C NMR spectra of 20 and 2.9 mg strychnine in PBLG and $CHCl_3$, extended region from 0 - 60 ppm (700 MHz with ^{13}C cryoprobe) 100

Figure 3.25 ^{1}H NMR spectrum for mandelalide B (2; 700 MHz, py-*d5*) 102

LIST OF FIGURES (Continued)

Figure Page

Figure 3.26 COSY NMR spectrum for mandelalide B (2; 700 MHz, py-*d5*)..... 102

Figure 3.27 a) Assigned rotamers along the C-21/C-22 and C-22/C-23 bonds in 2. b) ROESY correlations around the γ-butyrolactone of 2 103

Figure 3.28 a) Key ROE correlations ($CDCl_3$) between the monosaccharide and the macrolide THP moiety in mandelalide A; b) Key ROE correlations between the monosaccharide and the macrolide, as well as through ring correlations for mandelalide B..... 104

Figure 3.29 GC-MS chromatograms..... 105

Figure 3.30. Computational model of the lowest energy conformer for mandelalide B (2). 106

Figure 3.31. The dose response curves for mandelalides A (1) and B (2) in mouse Neuro2A neuroblastoma and human NCI-H460 cell lines, following 48 h incubation. 109

Figure 3.32 Chemical structures for madeirolides A and B. 110

Figure 4.1 ^{1}H NMR spectrum for Boc-pseudodistaminol A (1a; 400 MHz, CD_3OD) 128

Figure 4.2 ^{13}C NMR spectrum for Boc-pseudodistaminol A (1a; 100 MHz, CD_3OD) 128

Figure 4.3 HSQC spectrum for Boc-pseudodistaminol A (1a; 400 MHz, CD_3OD). 129

Figure 4.4 HMBC spectrum for Boc-pseudodistaminol A (1a; 400 MHz, CD_3OD). 129

Figure 4.5 COSY spectrum for Boc-pseudodistaminol A (1a; 400 MHz, CD_3OD). 130

Figure 4.6 ROESY spectrum for Boc-pseudodistaminol A (1a; 400 MHz, CD_3OD) 130

LIST OF FIGURES (Continued)

Figure Page

Figure 4.7 1D NOESY spectrum for Boc-pseudodistaminol A confirming a cis THP ring, as indicated on partial structure (1; 400 MHz, CD_3OD) 131

Figure 4.8 1H NMR spectrum for Boc-pseudodistaminol B (2a; 400 MHz, CD_3OD) 131

Figure 4.9 ^{13}C NMR spectrum for Boc-pseudodistaminol B (2a; 100 MHz, CD_3OD) 132

Figure 4.10 HSQC spectrum for Boc-pseudodistaminol B (2a; 400 MHz, CD_3OD) 132

Figure 4.11 COSY spectrum for Boc-pseudodistaminol B (2a; 400 MHz, CD_3OD) 133

Figure 4.12 ROESY spectrum for Boc-pseudodistaminol B (2a; 400 MHz, CD_3OD) 133

Figure 4.13 ^{1}H NMR spectrum for Boc-pseudodistaminol C (3a; 400 MHz, CD_3OD) 134

Figure 4.14 ^{13}C NMR spectrum for Boc-pseudodistaminol C (3a; 100 MHz, CD_3OD 134

Figure 4.15 HSQC spectrum for Boc-pseudodistaminol C (3a; 400 MHz, CD_3OD) 135

Figure 4.16 COSY spectrum for Boc-pseudodistaminol C (3a; 400 MHz, CD_3OD) 135

Figure 4.17 HMBC spectrum for Boc-pseudodistaminol C (3a; 400 MHz, CD_3OD) 136

Figure 4.18 ^{1}H NMR spectrum for *S*-BPG amide of 4 (4a; 700 MHz, $CDCl_3$) 143

Figure 4.19 ^{13}C NMR spectrum for *S*-BPG amide of 4 (4a; 175 MHz, $CDCl_3$) 143

Figure 4.20 COSY spectrum for *S*-BPG amide of 4 (4a; 700 MHz, $CDCl_3$) 144

LIST OF FIGURES (Continued)

Figure Page

Figure 4.21 NOESY spectrum for *S*-BPG amide of 4 (4a; 700 MHz, $CDCl_3$) 144

Figure 4.22 ^{1}H NMR spectrum for *R*-BPG amide of 4 (4b; 700 MHz, $CDCl_3$) 145

Figure 4.23 The absolute configuration of 4 (2*S*, 3*S*) with $\Delta\delta = \delta_R - \delta_S$ values indicated on the structure. 145

Figure 4.24 ^{1}H NMR spectrum for *S*-BPG amide of 5 (5a; 700 MHz, $CDCl_3$) 146

Figure 4.25 ^{13}C NMR spectrum for *S*-BPG amide of 5 (5a; 700 MHz, $CDCl_3$) 146

Figure 4.26 HSQC spectrum for *S*-BPG amide of 5 (5a; 700 MHz, $CDCl_3$) 147

Figure 4.27 ^{1}H NMR spectrum for *R*-BPG amide of 5 (5b; 700 MHz, $CDCl_3$) 147

Figure 4.28 ^{1}H NMR spectrum for *S*-BPG amide of 6 (6a; 700 MHz, $CDCl_3$) 148

Figure 4.29 ^{13}C NMR spectrum for *S*-BPG amide of 6 (6a; 175 MHz, $CDCl_3$) 148

Figure 4.30 HSQC spectrum for *S*-BPG amide of 6 (6a; 700 MHz, $CDCl_3$) 149

Figure 4.31 COSY spectrum for *S*-BPG amide of 6 (6a; 700 MHz, $CDCl_3$) 149

Figure 4.32 ^{1}H NMR spectrum for *R*-BPG amide of 6 (6b; 700 MHz, $CDCl_3$) 150

LIST OF TABLES

Table | Page

Table 2.1 Biological activity of organic extracts from South African tunicates..... 38

Table 2.2. ^{1}H (700 MHz) and ^{13}C (175 MHz) NMR Data (CD_3OD) for Rubrolides 2 and 3. 47

Table 2.3. ^{1}H (700 MHz) and ^{13}C (175 MHz) NMR Data (CD_3OD) for Rubrolides 4 and 5. 53

Table 2.4 Antibacterial Properties of Rubrolides 2-5, 6 and 7. 60

Table 3.1 NMR data at 700 MHz for mandelalide A (1) in $CDCl_3$ 78

Table 3.2 ^{1}H and ^{13}C NMR data for mandelalides B-C (2-3) in $CDCl_3$ 86

Table 3.3. ^{1}H and ^{13}C NMR data for mandelalides D (4 in $CDCl_3$ and 4b in CD_3OD). 91

Table 3.4. The values of interproton distances obtained for mandelalide B (2) from ROESY acquired at mixing time = 400ms..... 107

Table 3.5 Cytotoxicity of *Lissoclinum* sp. organic extract and mandelalides A (1) and B (2) to mouse Neuro-2A neuroblastoma and human NCI-H460 lung and MDA-MB-231 breast cancer cells. 108

Table 4.1. ^{1}H and ^{13}C NMR data for Boc-derivatized pseudodistaminols A and B (1a and 2a) in CD_3OD. 127

Table 4.2. ^{1}H and ^{13}C NMR data for derivatized amino alcohols 4a and 4b in $CDCl_3$ 140

Table 4.3. ^{1}H and ^{13}C NMR data for derivatized amino alcohols 5a and 5b in $CDCl_3$ 141

Table 4.4 Cytotoxicity of derivatized amino alcohols 4-6 to mouse Neuro-2A neuroblastoma and human NCI-H460 lung cancer cell lines..... 142

CHAPTER ONE

GENERAL INTRODUCTION

Justyna Sikorska

The rich diversity of natural product chemical skeletons isolated from marine organisms, in parallel with their pronounced biological activity, clearly highlights the importance of natural products drug discovery. Marine organisms such as tunicates, sponges and mollusks have been a focus of work in many laboratories and have led to the discovery of compounds already approved as anticancer drugs or in clinical trials, e.g. ecteinascidin 743 (Yondelis®) (Fayette et al., 2006), dehydrodidemnin B (Aplidin®) (Le Tourneau et al., 2007), KRN7000 (Alpha-GalCer®) (Schneiders et al., 2011). Therefore, extracts of a 2004 collection of sixty tunicates from Algoa Bay, South Africa were subjected to biological and chemical screening to identify potential new drug leads. To facilitate the process of isolation and identification of new and biologically active pure compounds, the prioritized extracts were further subjected to activity-guided fractionation supported by a dereplication approach. Dereplication of known and/or "nuisance" compounds was based on comparison of taxonomic, MS and NMR data for each active fraction or pure compound with information gathered in MarinLit, a database of the marine natural products literature. This screening process led to identification of three groups of biologically active natural products that are presented in chapters 2 – 4. Due to the limited amounts of tunicate extracts in hand, most of the pure compounds were isolated in sub-milligram quantities. Therefore, the application of some less routine and more recent NMR techniques in structure assignment was necessary, and demonstrates the extended scope of natural products isolation and elucidation to very limited quantities of pure metabolites.

The following chapters present details of the approach undertaken to identify bioactive natural products from tunicates through application of activity-guided fractionation and modern NMR techniques, which are reviewed in the remainder of this chapter (Chapter One). Chapter Two describes screening of the sixty South African tunicate extracts for cytotoxicity to brine shrimp and Neuro-2A mouse neuroblastoma cells and antibacterial activity against *Staphylococcus aureus* and *Vibro cholerae*. Also described in this chapter is the applicability of ^{1}H NMR and diffusion-ordered spectroscopy (DOSY) to chemical screening, as well as the

compounds identified in this process (homarine, rubrolides and previously miss-assigned nucleosides).

Chapter Three lays out the structural assignment and preliminary biological evaluation of mandelalides A-D, isolated from a new *Lissoclinum* species. The relative configuration was established after interpretation of homo- and hetero-nuclear coupling constants in parallel with ROESY analysis. The applicability of qROESY was explored to assign mandelalide B conformation. Assignment of absolute configuration was accomplished after hydrolysis of the monosaccharide unit of mandelalide A, its chiral GC-MS analysis and consideration of ROESY correlations between monosaccharide and aglycone. Evaluation of the cytotoxic properties of mandelalides A and B revealed nanomolar activity against NCI-H460 human lung and Neuro-2A mouse neuroblastoma cell lines.

Chapter Four presents the isolation and structure elucidation of three new pseudodistaminols A-C and three known amino alcohols isolated from *Pseudodistoma* sp. and *Pseudodistoma digitum*, respectively. The assignment of planar structure was accomplished after analysis of 1D and 2D NMR experiments, while determination of absolute configuration resulted from ^{1}H NMR chemical shift comparisons of *S*- and *R*-Boc-phenylglycine (BPG) derivatives of the amino alcohols. Testing of *S*- and *R*-BPG amino alcohol derivatives against NCI-H460 and Neuro-2A cell lines indicated only mild cytotoxic properties, in contrast to the potent cytotoxicity observed for the underivatized parent extract.

The final conclusion chapter (Chapter Five) summarizes the outcomes of the projects described in chapters 2 - 4 and briefly discusses future work that could be based on these results.

Progress and new approaches in NMR techniques applicable to natural products

Since the time when the first nuclear magnetic resonance (NMR) spectra were acquired, nuclear magnetic resonance (NMR) spectroscopy has become a central technique for molecular structure determination. This method not only allows establishing number and type of nuclei in an organic molecule, but also characterizes their proximal environment and connectivity. Nowadays acquisition of a "standard" set of 1D and 2D NMR experiments: ^{1}H, ^{13}C, COSY, HSQC, HMBC, NOESY, on 400-500 MHz spectrometers, in conjugation with high resolution mass spectrometric (HR-MS) data, is a routine approach to "small molecule" structure assignment on milligram and even microgram sample quantities.

Advances in NMR techniques have enabled structure assignment on sub-milligram quantities of natural products, and also dereplication and isolation of unstable compounds. In the early days of natural products isolation and structure elucidation, gram quantities of compounds were necessary to assign chemical structures by chemical degradation and/or derivatization (Murata et al., 2006). However, since the 1970's and 1980's when 1D and 2D NMR techniques became more accessible and allowed for assignment of homo- and hetero-nuclear correlation, molecular structure assignment has become strongly rooted in NMR techniques (Bax & Summers, 1986; Murata, et al., 2006). Biologically active compounds are often minor constituents of organisms, and limited sample availability from many terrestrial and marine sources puts an even greater demand on methodologies that facilitate structure determination. Even though the application of NMR enabled the assignment of very close to the correct structure for glycinoeclepin A at 2.2 μM in 1987, and ciguatoxin at 0.3 μM in 1990 (Figure 1.1), the unambiguous structure assignment of samples at low nanomolar concentrations became feasible only more recently (Masamune et al., 1987; Molinski, 2010). The requisite improvement in NMR sensitivity has been achieved by the use of smaller probe volumes (microprobe diameters ranging from 1.0 to 1.7 mm), as well as the development of cryoprobes

(probes with a built in signal preamplifier cooled to 20 K to decrease the level of thermal noise), increasing the signal to noise ratio even 10- to 20-fold and overall facilitating structure elucidation of samples in extremely limited quantities.

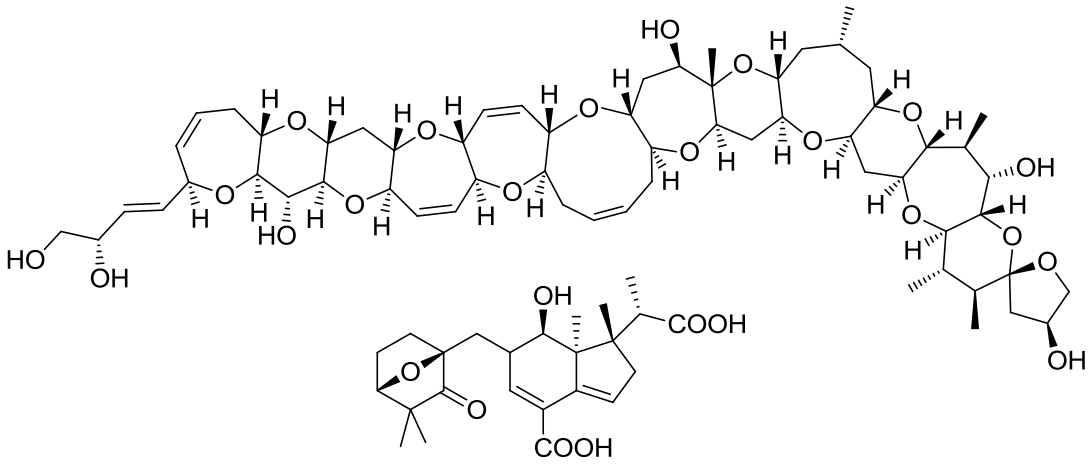

Figure 1.1 Structures of ciguatoxin (top) and glycinoeclepin A (bottom).

One of the first nanomole-scale structure assignments was described for sperm-activating and attracting factor (4 μg, 6 nmol) isolated from eggs of the ascidian *Ciona intestinalis* (Figure 1.2), (Oishi et al., 2004). The ^{1}H NMR and TOCSY data acquired at 500 MHz using a 1.7 mm probe, in tandem with MS-MS data, revealed a sulfated sterol structure, which was subsequently confirmed by total synthesis of the compound.

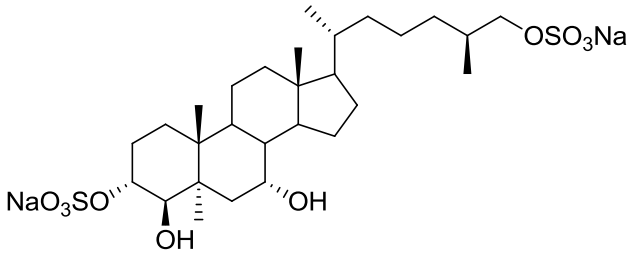

Figure 1.2 Structure of sperm activating and attracting factor.

Several cases of nanomolar structure elucidation have been accomplished in Molinski's laboratory, where major and minor components of the extract from the sponge *Phorbas sp.* were identified (Dalisay & Molinski, 2009; Dalisay et al., 2009). While in 1995 phorboxazoles A and B were isolated in hundreds of milligrams, in 2003 phorbazides A-E were identified from the same extract and their structures were assigned on 0.1-2.7 mg quantities using a 600 MHz spectrometer equipped with an inverse 5 mm cryoprobe (Figure 1.3), (Molinski, 2010). Subsequently, state-of-the-art structure elucidation was performed on a 600 MHz spectrometer equipped with a 1.7 mm micro-cryoprobe for muironolide A (90 μg, 152 nmol) and hemi-phorboxazole A (16.5 μg, 28 nmol) (Figure 1.3), (Dalisay & Molinski, 2009; Dalisay, et al., 2009). In the case of hemi-phorboxazole A, a combination of nano-LC HR-MS data with the standard suite of 1D and 2D NMR experiments, measurement of *J* couplings, and circular dichroism (CD) measurements permitted the final structure assignment. For muironolide A additional microscale degradation was necessary to determine the stereochemistry of the trans-2-chlorocyclopropylketide element. Overall the examples of hemi-phorboxazole A and muironolide A illustrate the extended limits of structure assignment possible in natural products research.

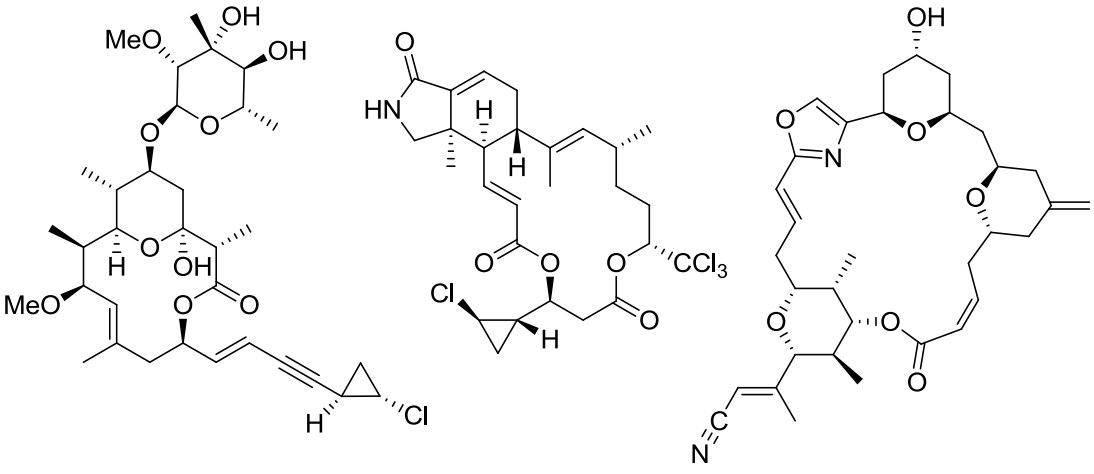

Figure 1.3 Structures of phorbazide A, muironolide A and hemi-phorboxazole A (from left to right, respectively).

Another challenge in natural products identification is the isolation and structure assignment of compounds prone to degradation. The application of 2D NMR experiments to complex mixtures has been shown to be a way to directly determine structures in complex organic extracts. The very interesting case of unstable myrmicarin 430A was described by Schroeder et al, who assigned the structure of the active component in a mixture collected from the poison glands of African ants based on DQFCOSY data (Figure 1.4), (Schroeder et al., 1996).

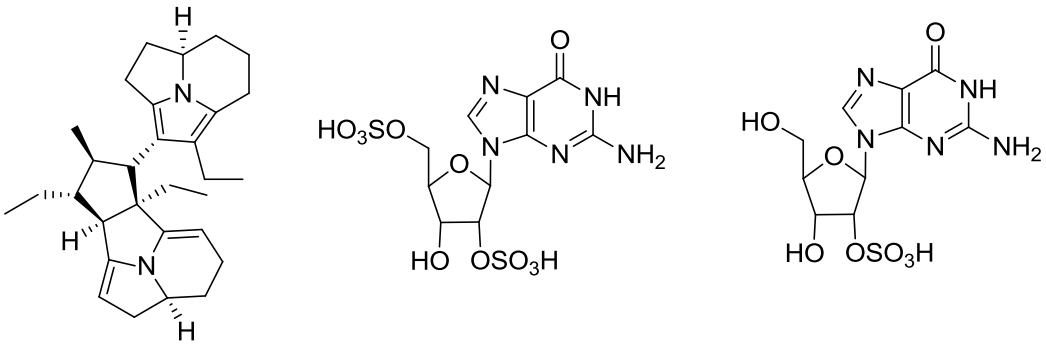

Figure 1.4 Chemical structures of myrmicarin 430A and sulfated guanosine derivatives respectively.

The DQFCOSY delineated three spin systems for myrmicarin 430A that were in turn connected based on HSQC and HMBC correlations, giving enough resolution to distinguish it from myrmicarins 215A, 215B and 217, also present in mixture.

Structure elucidation of the active components (neurotoxic sulfated nucleosides) of spider venom directly from the complex mixture has also been described (Taggi et al., 2004). The unmodified venom sample was analyzed by DQFCOSY due to the much greater resolution of this experiment than for magnitude mode COSY, and the resultant ease of measuring coupling constants values. ^{1}H NMR confirmed the presence of ribose anomeric protons, while DQFCOSY led to identification of bis-sulfated sugar fragments (Figure 1.5). Due to significant overlap of resonances, separation of the mixture was needed, however only mono-sulfated compounds were isolated in pure form. Knowing that the bis-sulfated form degrades under

chromatographic separation conditions, the authors increased the pH of collected fractions and isolated the toxins as pyr-d_5 salts. The example of sulfated guanosine derivatives illustrates the need for screening of natural product extracts not only for biological properties but also by NMR, to help with identification of labile components. Moreover, this methodology can facilitate rapid identification or dereplication of secondary metabolites (Schroeder et al., 2008).

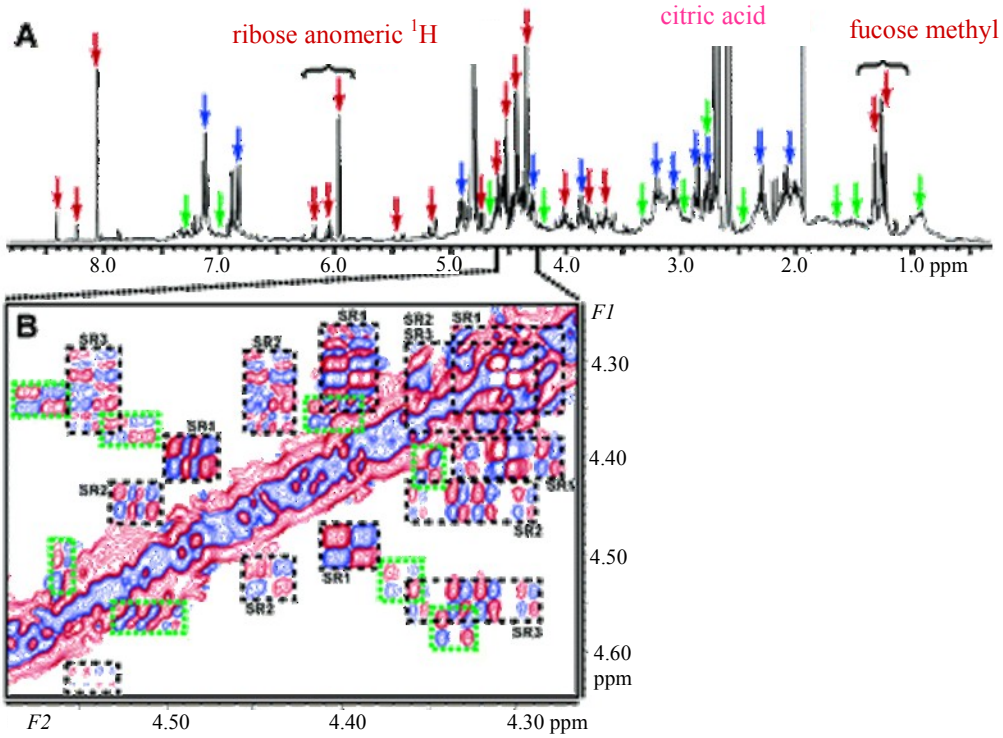

Figure 1.5 a) ^{1}H NMR spectrum of unmodified *T. agrestis* venom in D_2O at 500 MHz. Arrows indicate: nucleoside derivatives in red, proteins in green, and polyamines in blue; b) Partial DQFCOSY spectrum: dashed line black boxes indicate cross-peaks of three sulfated ribonucleosides (SR1−SR3); green boxes are cross-peaks for polyamines and peptides. Reproduced with permission from Andrew E. Taggi et al., *JACS*, 2004, 126, 10364-10369. Copyright 2012 American Chemical Society.

The continual development of new NMR pulse programs and processing methods has broadened NMR applications to the identification of single or multiple

components in complex mixtures. The simplest approach involves acquisition of ^{1}H NMR spectra for many crude extracts and comparison of data through principle component analysis (PCA), for example, to identify similarities and differences between analyzed samples, without the need for individual assignment of peaks (Ward et al., 2007). Food chemistry, drug authenticity and quality control are the main areas of utilization of this technique. However it can be also employed to monitor changes in secondary metabolite production of living organisms, or as a solution to the main problem of natural product chemists: dereplication of known metabolites. Despite the fact that ^{1}H NMR provides a very useful tool to screen for the presence or absence of desired secondary metabolites in extracts, its main disadvantage is overlap of component signals in mixtures. The answer to this problem is the application of 2D experiments in which the presence of a second dimension increases the resolution in acquired spectra, such as *J*-resolved, COSY, HSQC or DOSY experiments. Recently the application of diffusion ordered spectroscopy (DOSY), "in tube chromatography", has become an important tool, especially for metabolomic fingerprinting and unraveling complex mixtures (Cassani et al., 2012; Politi et al., 2009). DOSY potentially allows extraction of important information directly from mixtures, without prior time consuming separations, and can facilitate the dereplication of known compounds. This method enables separation of components based on molecular weight/shape, similar to size exclusion chromatography, and results in 2D spectra with chemical shift in the *F1* and diffusion coefficient in the *F2* dimension (Figure 1.6), (Huo et al., 2003). Compounds with higher molecular weights diffuse slower than low molecular weight molecules, therefore one can differentiate between mixture components which have sufficiently different molecular weights (Novoa-Carballal et al., 2011). The resulting spectrum is very useful because it "correlates" all protons within one molecule, without being dependent on spin system correlations (e.g. TOCSY), so allowing one to identify all protons for the compound of interest. However, despite its applicability DOSY is greatly under-appreciated in the natural products field, with only a few examples in the literature: monitoring of lovastatin

production by *Aspergillus terreus* (Macías et al., 2010), identification of agesamides A and B (Rodrigues et al., 2009), and flavonoid glycosides derived from quercetin in *Bidens sulfurea* and saponins in *Agave brittoniana* leaves (Macías et al., 2010; Rodrigues et al., 2009; Tsuda et al., 2006).

Recently the application of matrix-assisted DOSY was described, where sample was dissolved in a mixture of solvent and deuterated sodium dodecyl sulfate (matrix).

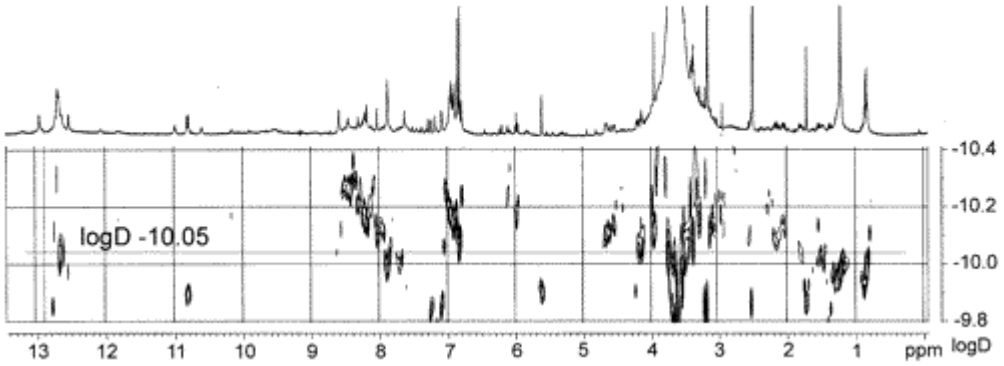

Figure 1.6 Partial DOSY spectrum for an extract fraction from the sponge *Agelas* sp. containing agesamides A and B. Reproduced with permission from Masashi Tsuda et al, *Org. Lett.*, 2006, 8, 4235-4238. Copyright 2012 American Chemical Society.

This modification of DOSY technique permits even more effective differentiation between compounds as closely related as flavone, fistein and (+)-catechin (Figure 1.7), (Cassani, et al., 2012).

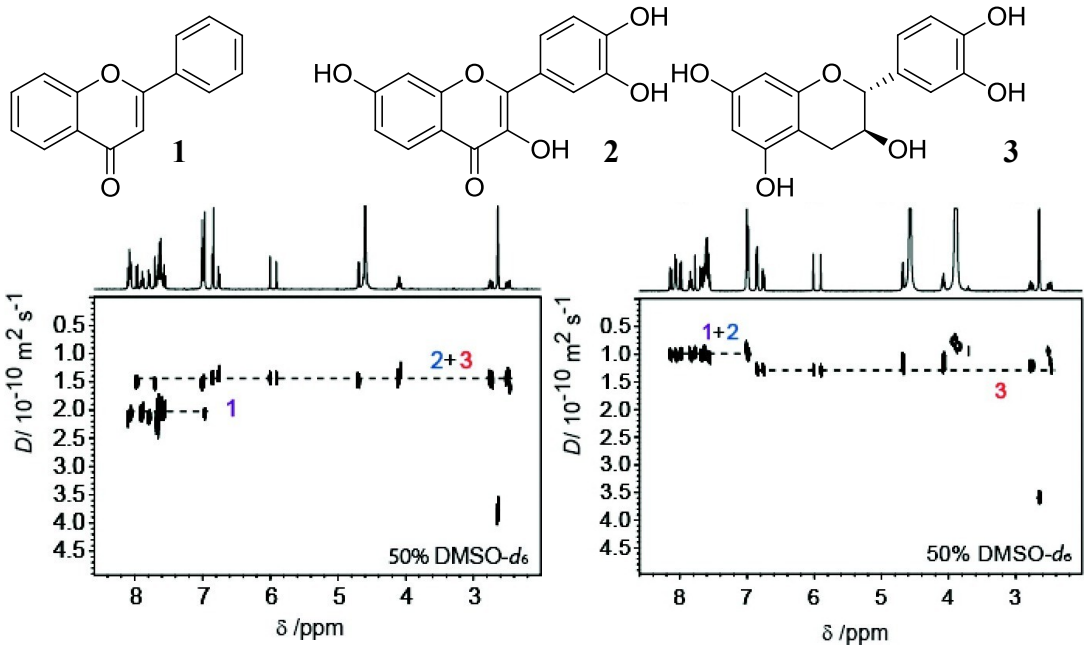

Figure 1.7 Chemical structures of flavone (**1**), fisetin (**2**) and (+)-catechin (**3**), upper line. DOSY spectrum before and after addition of SDS to mixture of flavone, fisetin and (+)-catechin. Modified with permission from Julia Cassani et al., *JNP*, 2012, 75, 131-134. Copyright 2012 American Chemical Society.

Application of NMR techniques to the assignment of relative configuration

The spatial arrangement of functional groups in small molecules is very often correlated with the presence or absence of biological activity and toxicity, emphasizing the importance of the correct assignment of relative and absolute configuration to unambiguously determine mechanism of action of biologically active new compounds. NMR-based experiments are the most informative when it comes to the assignment of relative configuration of organic molecules, with Murata's *J*-based method, NOEs, Kishi's chemical shift database, acetonides and residual dipolar couplings (RDS) being the complementary methods most commonly used.

The nuclear Overhauser effect (NOE) based methods, in combination with computational molecular modeling, are common tools for relative configuration assignment of macrocyclic compounds because the presence of NOE correlations is indicative of close proximity (up to 5-6 Å) of two nuclei in space (Neuhaus & Williamson, 2000). The most recent applications of NOE for rigid molecules demonstrated that, in combination with molecular modeling, this technique is capable of very accurate conformational assignment and differentiation between otherwise indistinguishable structural candidates (Butts, Jones, Towers, et al., 2011; Chini et al., 2011). In particular, when quantitative measurement of NOE distances is performed one can distinguish between as challenging stereochemical problems as identification of the correct diastereoisomer of conicaterol F (Figure 1.8), (Chini, et al., 2011). Nevertheless, when interpretation of NOEs for a flexible molecule is attempted, very often the assignment of relative configuration is much more challenging due to the fact that the resulting NOEs are usually the average of the signals from several lowest energy conformers present in solution (Butts, Jones, & Harvey, 2011).

Murata's method (*J*-based configuration analysis, JBCA) can be used to confirm stereochemistry assigned based on NOE correlations. The analysis of homo- and hetero-nuclear coupling constants can provide information about relative orientation of

two nuclei separated by 1, 2 or 3 bonds, due to coupling constant dependence on dihedral angle values (Figure 1.9), (Matsumori et al., 1999). The most frequently used coupling constants are $^{3}J_{HH}$, easily measured from ^{1}H NMR, or DQFCOSY if close overlap is observed in the ^{1}H spectrum (Hoye et al., 1994; Hoye & Zhao, 2002). However, if the information obtained from $^{3}J_{HH}$, is insufficient, the heteronuclear $^{2}J_{CH}$ and $^{3}J_{CH}$ coupling constants are analyzed to obtain supporting information about the spatial arrangement of substituents around the analyzed bond (Figure 1.9), (Bifulco, et al., 2007; Riccio et al., 2003).

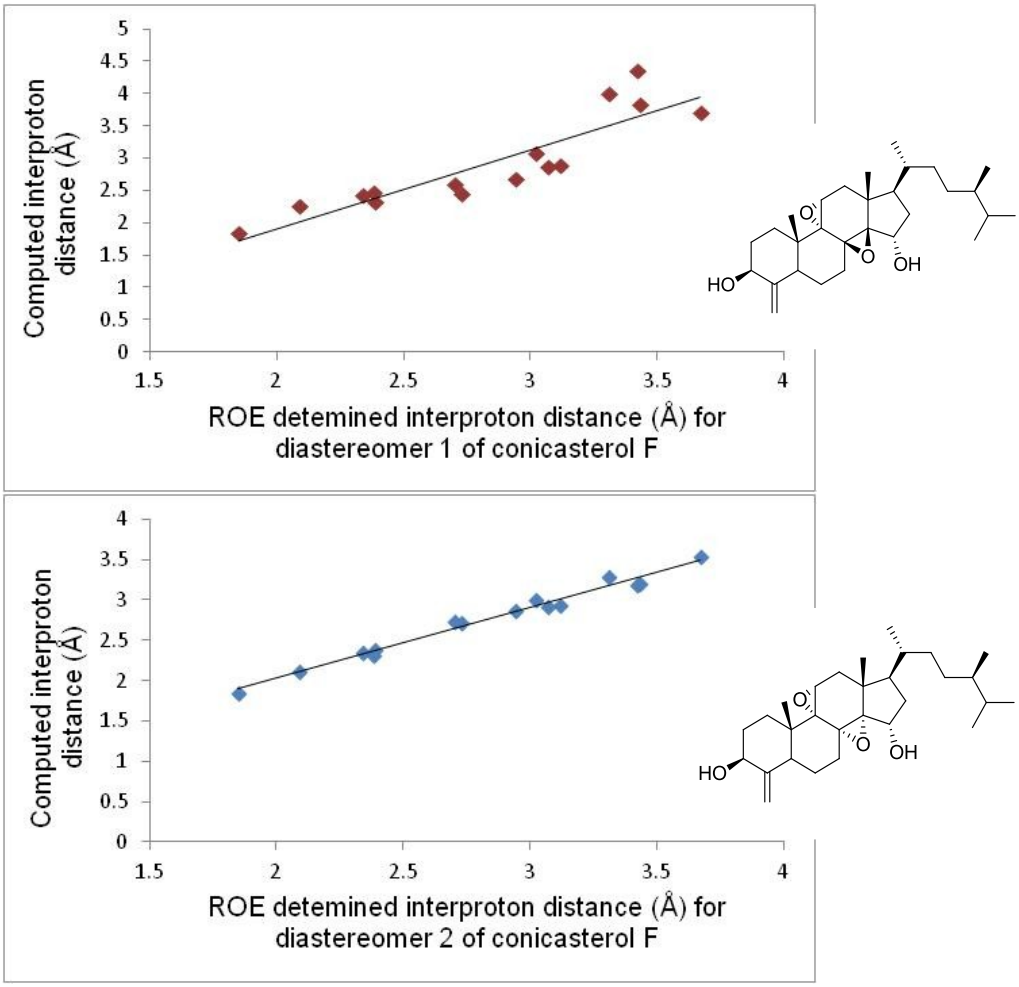

Figure 1.8 Fit of DFT-calculated interproton distances to experimental values from 1D-ROESY experiments for both diastereoisomers of conicaterol F. The fit for the lower graph is clearly better, indicating that the second diastereoisomer is the correct one.

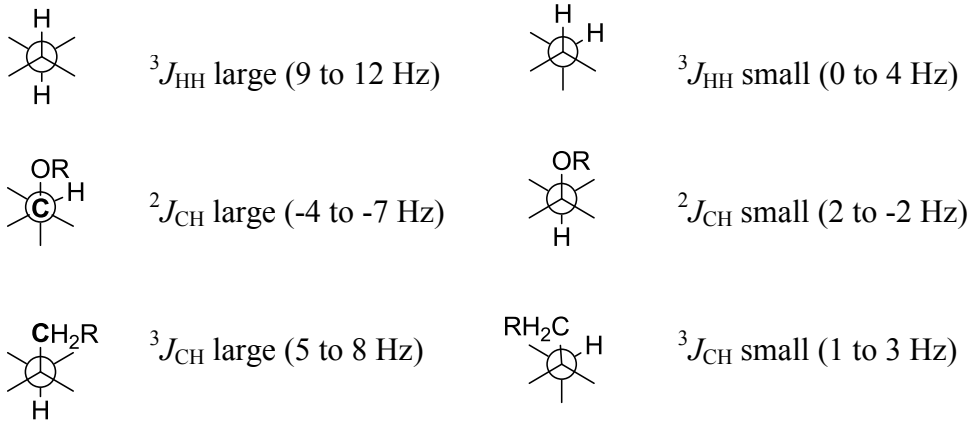

Figure 1.9 Relationships between dihedral angles and coupling constant values for $^3J_{HH}$, $^2J_{CH}$ and $^3J_{CH}$.

The different experiments have been designed to allow measurement of $^2J_{CH}$ and $^3J_{CH}$ values, with the main difference between them being the ability to acquire coupling constants around quaternary centers. Among these experiments are the phase-sensitive HMBC, hetero half-filtered TOCSY (HETLOC), HSQMBC or selHSQMBC-TOCSY (Kurz et al., 1991; Marquez et al., 2001; Saurí, et al., 2012).

The HETLOC is the most commonly used technique for natural products due to its simplicity in data interpretation and ability to identify not only the size but also the magnitude of coupling constants (Fukushi, 2006). The main drawback of this experiment is that each carbon must have at least one proton attached, i.e. heteronuclear coupling constants can only be obtained for atoms within a spin system (comprising TOCSY-correlated protons). The 2D spectrum resulting from the HETLOC experiment has ^{1}H chemical shift information in both *F1* and *F2* dimensions, where for each signal a ^{1}H chemical shift in *F1* represents the carbon correlated to the proton indicated in the *F2* dimension. All of the resulting correlations are split in the *F1* dimension by the $^1J_{CH}$ value, while the displacement of cross peaks

within a correlation in the *F2* dimension is equal to the $^{n}J_{CH}$ value between the analyzed nuclei (Figure 1.10a).

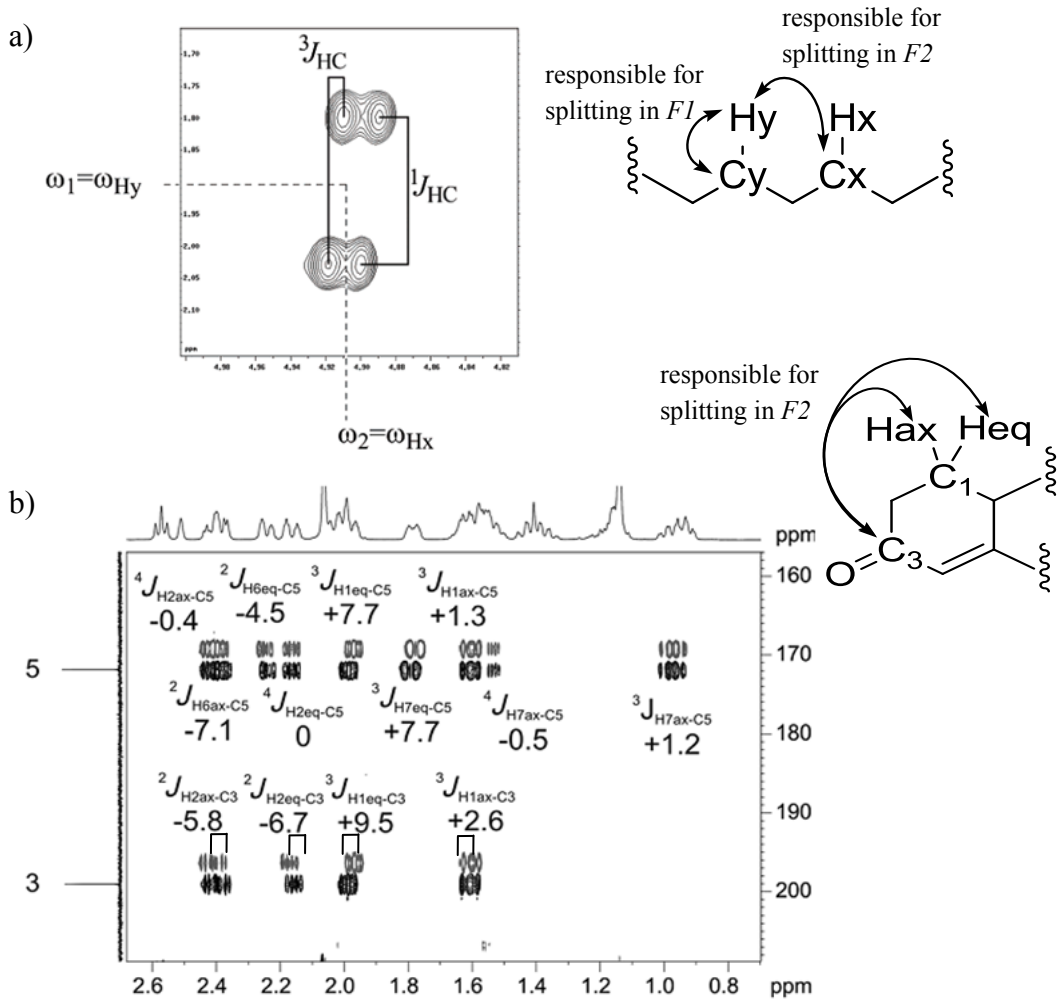

Figure 1.10 a) Partial HETLOC spectrum with correlations responsible for peak splitting in the *F1* and *F2* dimensions indicated on the spectrum together with partial structure. b) The partial α/β-selHSQMBC-TOCSY spectrum for progesterone showing correlations (indicated on the partial structure) that are responsible for peak splitting in the *F2* dimension. Figures modified with permission from John Wiley and Sons and ACS (Bifulco et al., 2007; Saurí et al., 2012).

The selHSQMBC-TOCSY is the most recent method created for the analysis of long range couplings in systems containing quaternary chiral centers (Saurí, et al.,

2012). This experiment enables measurement of the magnitude and sign of coupling constants by analysis of peak displacement in the *F2* dimension (analogous to HETLOC). However, in contrast to HETLOC, ^{13}C values are observed in the *F1* dimension. Determination of the sign for $^{n}J_{CH}$ values requires prior knowledge of any peak in the analyzed row that resulted from a three bond coupling constant (always positive) and assignment of positive $^{n}J_{CH}$ to peaks with the same displacement pattern, while negative $^{n}J_{CH}$ are assigned to peaks with the opposite displacement pattern (Figure 1.10b).

As described previously the determination of relative stereochemistry by NMR spectroscopy is usually accomplished using a combination of scalar *J* couplings and NOE measurements (Tringali, 2001). However, when methods using isotropic solvents are insufficient to solve ambiguities in relative configuration of natural products, measurement of residual dipolar couplings (RDCs) is another source of structural information (Thiele, 2008). RDCs are through space interactions between two nuclei, the size of which depends on the distance as well as direction of the internuclear vector with respect to an external point of reference (Gschwind, 2005). Measurement of RDC values in anisotropic solution is used to determine how these vectors are aligned relative to a magnetic field, and therefore how they are aligned relative to each other. In isotropic solution the values of RDCs average to zero due to isotropic tumbling, therefore it is necessary to orient the compound with respect to the external magnetic field (B_0) by use of alignment media (Marx et al., 2010). Measurement of RDCs is performed by acquisition and comparison of data in isotropic and anisotropic solution, and is based on the fact that the total coupling constant (*T*) is the sum of dipolar (*D*) and scalar (*J*) coupling constants (Luy et al., 2004; Thiele & Berger, 2003). In isotropic solution *D* is averaged to zero and $T = J$. In anisotropic solution, *D* has positive or negative values different from zero. This allows for simple measurement of a *D* value from two data sets by subtraction (Figure 1.11). The experiments commonly used for determination of $^{1}D_{CH}$ are: gated decoupled ^{13}C, *F1*-coupled HSQC and *F2*-coupled HSQC (Thiele, 2004; Thiele & Berger, 2003). To

assign $^{n}D_{CH}$ and $^{n}D_{HH}$ one can use HETLOC and E.COSY pulse sequences (Marquez, et al., 2001; Thiele, 2008; Uhrín et al., 1998).

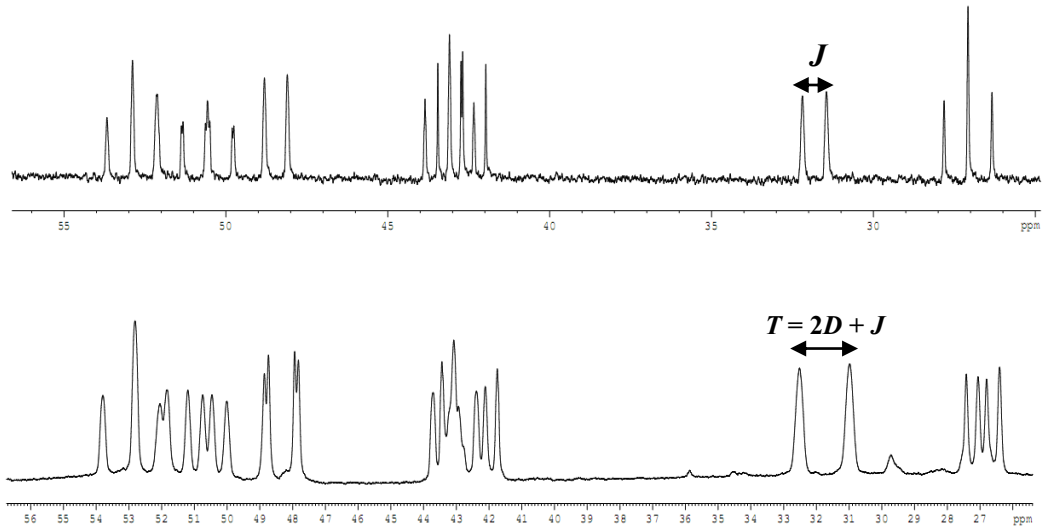

Figure 1.11 Partial (0 to 60 ppm) ^{13}C NMR gated decoupled spectra (175 MHz) for strychnine: isotropic solution of strychnine in $CDCl_3$ (top); anisotropic solution of strychnine in poly benzyl-L-glutamate (PBLG) /$CDCl_3$ (bottom).

The applicability of this method for the assignment of diastereotopic groups as well as relative configuration has been proven for rigid [e.g. menthol (Verdier et al., 2003), ludartin (Gil et al., 2008)] and flexible [e.g. sagittamide A (Schuetz et al., 2007), and archazolide A (Farès et al., 2008)] compounds. Sagittamide A is an example of a natural product for which two different relative configurations have been proposed. The first was based on a combination of *J*-couplings, NOEs and Kishi's database of ^{13}C chemical shifts (Figure 1.12a), (Lievens & Molinski, 2006). The second was based on *J*-couplings, synthesis of two stereoisomers and comparison of ^{1}H chemical shifts in the acetate region (Figure 1.12b), (Seike et al., 2006b). Final confirmation of relative configuration came from a separate study based on *J* couplings and RDC analysis (Schuetz, et al., 2007). The interpretation of $^{3}J_{HH}$, $^{2}J_{CH}$,

and $^{3}J_{CH}$ coupling constants for the bonds C-4 to C-10 led to identification of four potential configurations (Figure 1.12a, c-e). Knowing that RDCs can yield information complementary to that obtained from *J*-couplings and NOEs, the values of $^{1}D_{CH}$ for sagittamide A were measured in two different alignment media. Experimental values were used to predict the alignment tensor and to back-calculate RDCs. Comparison of RDCs calculated for all structural models and experimental values of RDCs indicated that the configuration previously proposed by Lievens and shown in Figure 1.12a gives the best fit and the remaining configurations were rejected.

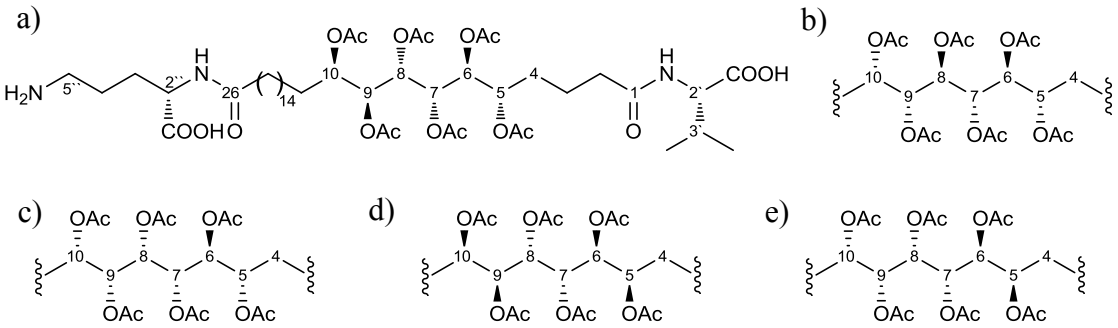

Figure 1.12 a) Chemical structure of sagittamide A as proposed by Lievens and confirmed by analysis of RDCs, b) Configuration of C4/C10 fragment proposed by Seike, c –e) Configurations proposed for sagittamide A by Schuetz.

For polyols, the application of coupling constant values, NOEs and RDCs may not be conclusive. If the analyzed parameters for the polyol of interest are independent of the rest of the molecule, and the nearest steric interactions are at least two methylene bridges away, one can also use differences in chemical shift values for the assignment of relative configuration (Higashibayashi et al., 2003). The first approach to utilize ^{13}C NMR shift variations and create a common ^{13}C NMR shift database has been described by Kishi and used to assign configuration of the C-5/C-10 fragment of oasomycin (Kobayashi et al., 1999). Further research indicated the applicability of ^{1}H NMR, ^{1}H (OH) NMR and especially $^{3}J_{HH}$ coupling constant values as relative configuration profile descriptors (Higashibayashi, et al., 2003). The standard

procedure for ^{13}C NMR shift database utilization involves: a) identification of a representative fragment, b) synthesis of all possible diastereoisomers, c) measurement of ^{13}C NMR shift values for each synthesized fragment, d) assembly of ^{13}C NMR shift profiles by calculating the deviation ($\Delta\delta$) from the average chemical shift for each nucleus in a natural product fragment and all standards to establish the best fit for the natural product. In the case of 1,2,3-triols, 1,3,5-triols, 1,2,3,4-tetraols and 1,2,3,4,5-pentaols one can avoid synthesis of standards by using previously published ^{13}C NMR shift values (Higashibayashi, et al., 2003; Kobayashi et al., 2000). A similar methodology should be applied if one wants to analyze $^{3}J_{HH}$ coupling constants values. However, here the direct comparison of $^{3}J_{HH}$ values (no calculation of $\Delta\delta$ values) is used and, if all of the parameters were previously published, the synthesis step can be excluded (Seike et al., 2006a).

One of the most recent examples of Kishi's chemical shift database application was assignment of the relative configuration of the polyoxy compound prorocentrol (Figure 1.13), (Sugahara et al., 2011). An extensive analysis of *J*-couplings in parallel with NOE correlations was performed for the whole compound. However, assignment of $^{2,3}J_{CH}$ values for the C-52/C-54 and C-18/C-21 fragments proved impossible and prevented assignment of the relative configuration of prorocentrol. Comparisons of $^{3}J_{HH}$ values for prorocentrol with those for 1,2,3-triol and 1,2,3,4-tetraol diastereomers in the database allowed assignment of the relative configuration of challenging motifs as indicated in Figure 1.13.

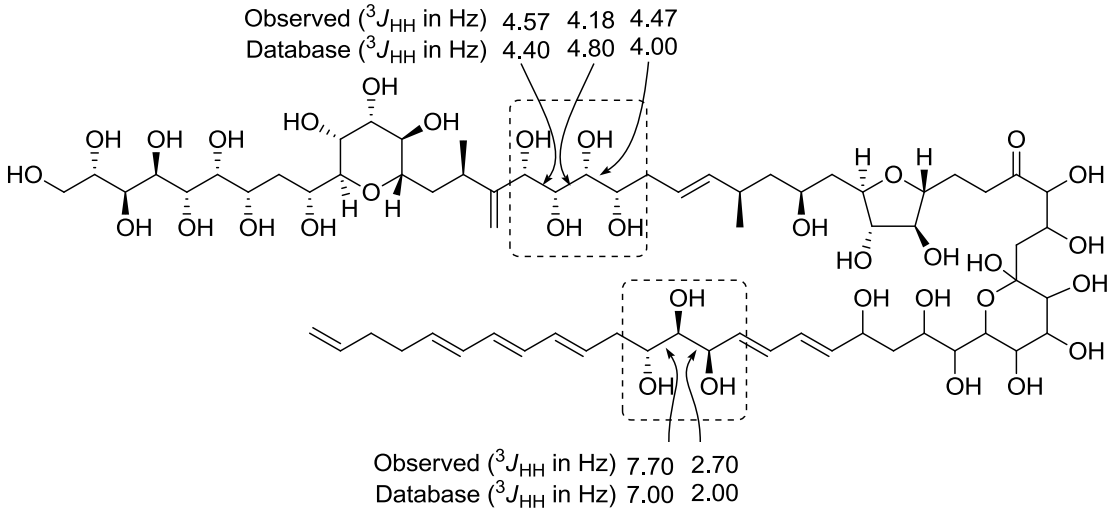

Figure 1.13 Chemical structure of prorocentrol with measured and standard $^3J_{HH}$ values indicated.

Assignment of the relative configuration of 1,3-diols can be accomplished after their conversion to *syn*- and *anti*-1,3-diol acetonides (Rychnovsky et al., 1998). This method is based on a comparison of ^{13}C chemical shifts for acetal methyl groups in *syn*- and *anti*- acetonides, which adopt chair and twist-boat conformations respectively. In the case of the *syn* acetonide, one of the methyl groups is oriented axial and the other is equatorial, resulting in chemical shifts values of ~20 ppm and ~30 ppm, respectively. However, in the *anti* acetonide both methyl groups are in very similar environments and have chemical shifts ~25 ppm (Figure 1.14), (Rychnovsky, et al., 1998). Additionally, comparison of hemiketal C-2 chemical shifts can be used as additional confirmation of relative configuration because ^{13}C chemical shifts are localized more upfield for *syn* acetonides than for *anti* acetonides (Evans et al., 1990).

One of the more challenging structural assignments using the ^{13}C acetonide method was described for marinisporolide A (Figure 1.15), (Kwon et al., 2008). The planar structure was determined by use of a full complement of 1D and 2D experiments, while to assign the relative configuration of the C-25/C-33 fragment, a

comparison of chemical shifts to the Kishi Universal NMR database was utilized in parallel with conversion to the corresponding acetonides.

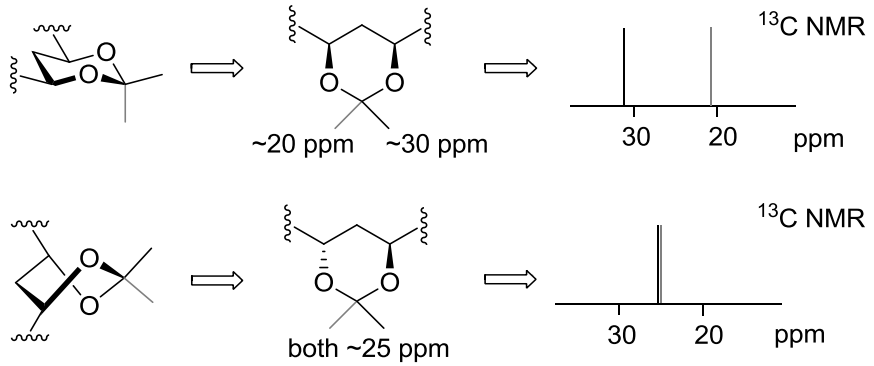

Figure 1.14 Schematic representation of changes in chemical shift values for *syn*- and *anti*- acetonides (top and bottom respectively).

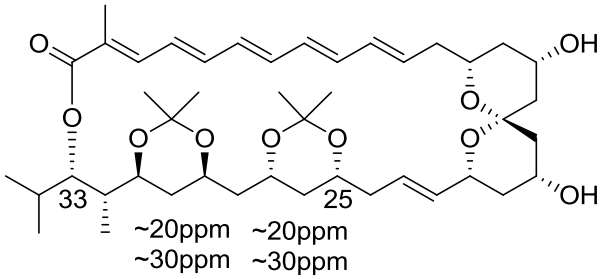

Figure 1.15 Chemical structure of the acetonide derivative of marinisporolide A.

Application of NMR techniques to the assignment of absolute configuration

A majority of natural products are isolated as enantiomerically pure compounds, with at least one chiral center present in the molecule (Kusumi & Ohtani, 1999). Very often only the identified enantiomer is responsible for biological activity. In order to provide larger quantities of compounds by synthetic or semisynthetic means, the correct absolute configuration of the isolated compound has to be established. The main methods applicable to the assignment of absolute configuration are X-ray crystallography, chiral analytical methods, circular dichroism (CD), optical rotation and NMR. Since the nature of natural products very often prevents good quality crystals from being obtained, and CD, optical rotation and chiral separation all require standards for analysis, NMR-based methods are commonly used as an alternative.

The assignment of absolute configuration by NMR can be accomplished with the use of chiral solvating agents (CSA) and chiral derivatizing agents (CDA) (Wenzel, 2007). While CSA are used for enantiomeric discrimination, CDA are utilized for determination of absolute configuration. The Mosher method (or modified Mosher method) is based on derivatization of a compound containing an alcohol, amine, or carboxylic group with each enantiomer of the Mosher reagent (a CDA) separately, and comparison of the NMR data for the resulting diastereomeric natural product derivatives (Kusumi & Ohtani, 1999). The derivatization reagents comprise a functional group to couple to the analyzed molecule, a bulky group to prevent conformational freedom after binding to the analyzed compound, and a substituent (often aromatic) that is able to induce a strong anisotropic effect (Seco et al., 2004). After derivatization, the diastereomer in which specific substituents are shielded by the aromatic group of the CDA will exhibit upfield chemical shifts for those substituents relative to the same substituents in the second diastereoisomer (Figure 1.16a), (Seco, et al., 2004). This change in chemical shift values, due to the shielding effect of the aromatic group, is commonly represented as a $\Delta\delta$ value, calculated for MTPA (methoxytrifluoromethylphenylacetic acid) esters as $\Delta\delta = \delta_S - \delta_R$ or $\Delta\delta = \delta_R -$

δ_S, while for MPA and other esters as $\Delta\delta = \delta_R - \delta_S$, unless stated otherwise (Latypov et al., 1996; Ohtani et al., 1991). To establish the absolute configuration, values of $\Delta\delta$ should be localized on the structure, and based on their arrangement the configuration can be concluded (Figure 1.16b).

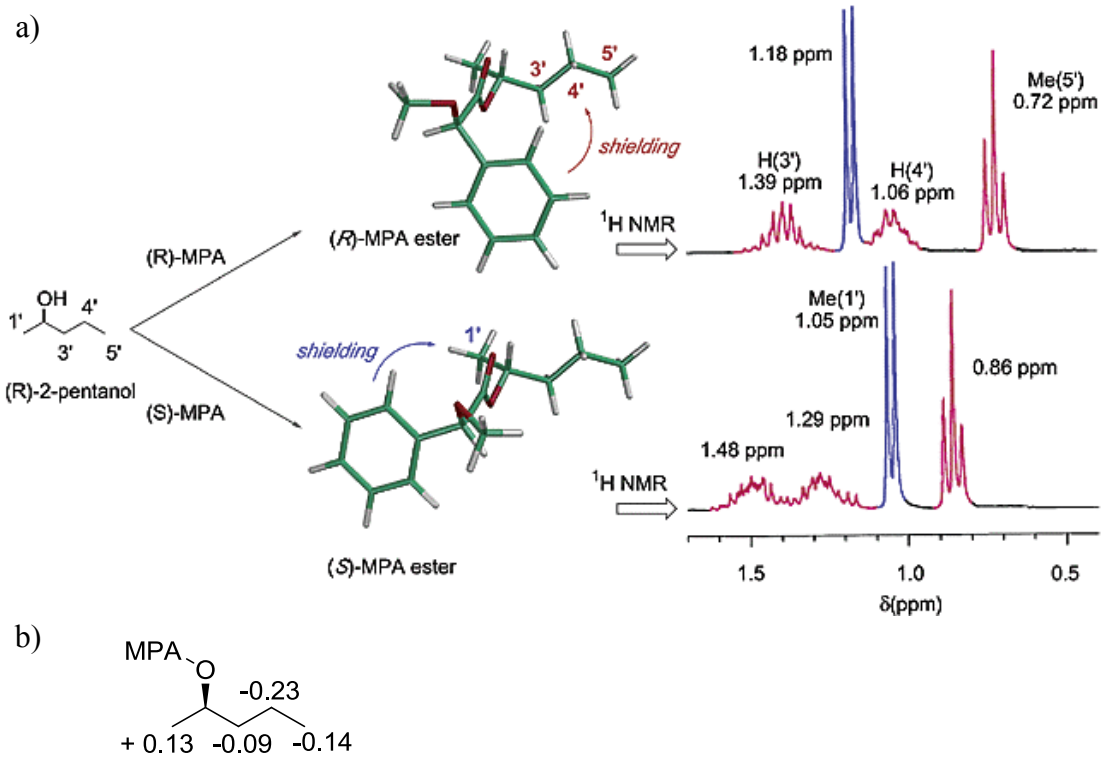

Figure 1.16 a) A schematic representation of the application of the Mosher method for (*R*)-2-pentanol; b) Structure of (*R*)-2-pentanol with $\Delta\delta_{RS}$ values indicated. Modified with permission from Jose M. Seco et al., *Chem. Rev.*, 2004, 104, 17-117. Copyright 2012 American Chemical Society.

The first application of the Mosher method was described in 1973 when Mosher's group observed that the changes in ^{19}F and ^{1}H NMR chemical shifts for alcohols and amines derivatized with MTPA can be correlated to their absolute configuration (Dale & Mosher, 1973; Sullivan et al., 1973). Since then many new derivatizing reagents for natural product and synthetic compounds have been developed, with the most commonly used being:

a) For secondary alcohols: MTPA, MPA, AMAs (arylmethoxyacetic acids), glycosides and chiral silylating reagents (α-[trifluoromethyl]-phenol), see Figure 1.17a (Dale & Mosher, 1973; J. M Seco et al., 1997; Seo et al., 1978; Weibel et al., 2000; Williamson et al., 2003).
b) For primary alcohols: MTPA, 9-AMA (Latypov, Ferreiro, et al., 1998; Tsuda et al., 2003).
c) For polyalcohols: MTPA, MPA, AMMAs (Freire et al., 2005; Freire et al., 2010; Seco et al., 2000).
d) For primary amines: MTPA, MPA, BPG (Boc-phenylglycine), 2-NPP (N-[2-nitrophenyl]proline), CFTA (α-cyano-α-fluoro-phenylacetic acid), chiral carbonate reagent-5, see Figure 1.17b (Ahn & Choi, 2007; Latypov et al., 1995; J. M. Seco et al., 1997; Seco et al., 1999; Takeuchi et al., 2006).
e) For secondary amines: MTPA, MPA (Gao et al., 2008; Hoye & Renner, 1996a, 1996b).
f) For amino alcohols: MPA (Leiro et al., 2005).
g) For carboxylic acids: PGME, arylethylamines (e.g. 1-phenylethylenamine), BINOL-borates, see Figure 1.17c (Freire et al., 2008; Hoye et al., 2000; Hoye & Koltun, 1998; Yabuuchi & Kusumi, 2000).

The most recent applications of the Mosher method involve a significant improvement in efficiency of the methodology. Instead of the previously described double derivatization method with each enantiomer, one can perform derivatization with only one enantiomer of the CDA and compare spectra acquired at different temperatures (MPA esters), or before and after addition of a chelating reagent (MPA esters and amides). The latter approach can conserve limited natural product sample quantities while still enabling an assignment of absolute configuration provided that the changes in chemical shifts are large enough (García et al., 2002; Latypov, Seco, et al., 1998; López et al., 1999).

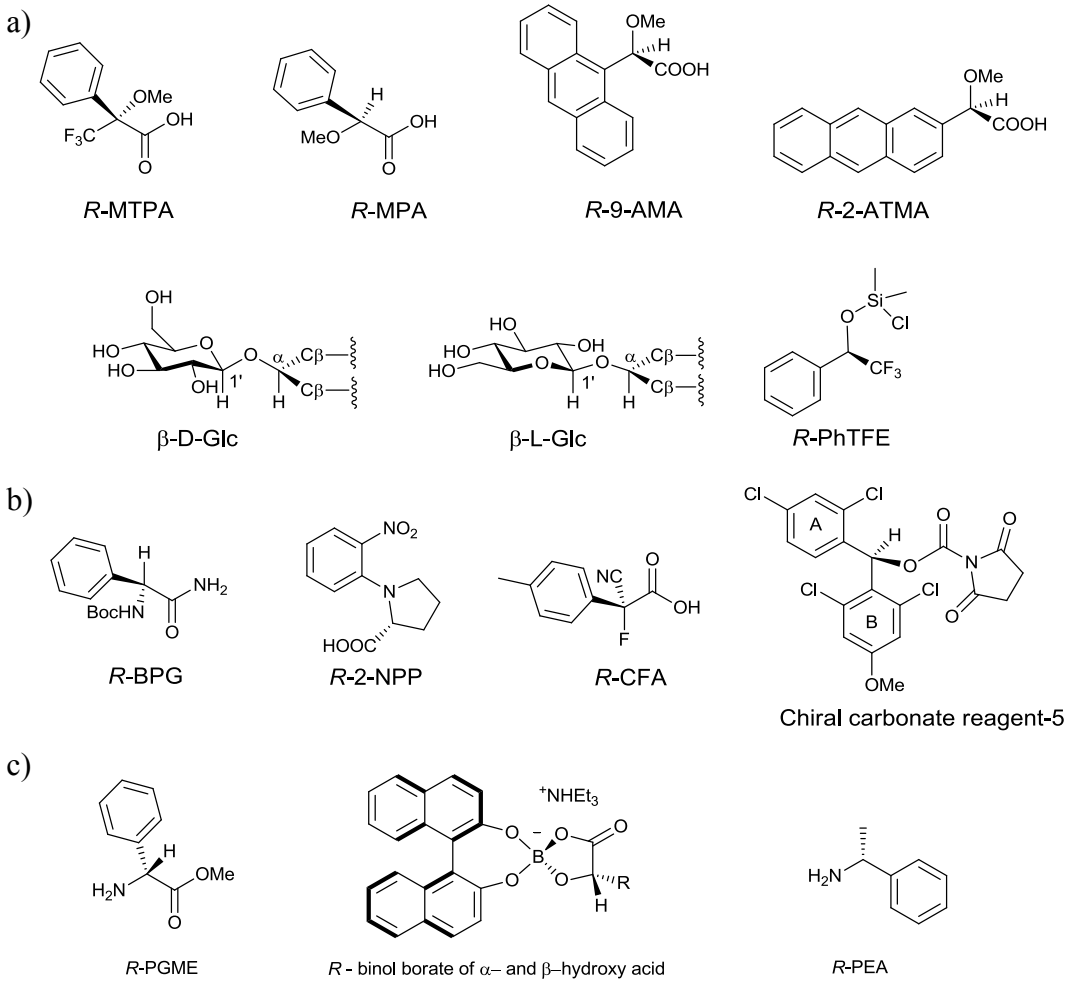

Figure 1.17 The derivatizing reagents used for assignment of absolute configuration of a) alcohols, b) amines, c) acids.

Bibliography

Ahn, H. C., & Choi, K. (2007). N-(2-Nitrophenyl)proline: An Intramolecular Hydrogen Bond Forming Reagent for the Determination of the Absolute Configuration of Primary Amines. *Org. Lett., 9*(19), 3853-3855.

Bax, A., & Summers, M. F. (1986). Proton and carbon-13 assignments from sensitivity-enhanced detection of heteronuclear multiple-bond connectivity by 2D multiple quantum NMR. *J. Am. Chem. Soc., 108*(8), 2093-2094.

Bifulco, G., Dambruoso, P., Gomez-Paloma, L., & Riccio, R. (2007). Determination of Relative Configuration in Organic Compounds by NMR Spectroscopy and Computational Methods. *Chem. Rev., 107*(9), 3744-3779.

Butts, C. P., Jones, C. R., & Harvey, J. N. (2011). High precision NOEs as a probe for low level conformers-a second conformation of strychnine. *Chem. Commun., 47*(4), 1193-1195.

Butts, C. P., Jones, C. R., Towers, E. C., Flynn, J. L., Appleby, L., & Barron, N. J. (2011). Interproton distance determinations by NOE - surprising accuracy and precision in a rigid organic molecule. *Org. Biomol. Chem., 9*(1), 177-184.

Cassani, J., Nilsson, M., & Morris, G. A. (2012). Flavonoid Mixture Analysis by Matrix-Assisted Diffusion-Ordered Spectroscopy. *J. Nat. Prod., 75*(2), 131-134.

Chini, M. G., Jones, C. R., Zampella, A., D'Auria, M. V., Renga, B., Fiorucci, S., Butts, C. P., & Bifulco, G. (2011). Quantitative NMR-Derived Interproton Distances Combined with Quantum Mechanical Calculations of 13C Chemical Shifts in the Stereochemical Determination of Conicasterol F, a Nuclear Receptor Ligand from Theonella swinhoei. *J. Org. Chem., 77*(3), 1489-1496.

Dale, J. A., & Mosher, H. S. (1973). Nuclear magnetic resonance enantiomer regents. Configurational correlations via nuclear magnetic resonance chemical shifts of diastereomeric mandelate, O-methylmandelate, and .alpha.-methoxy-.alpha.-trifluoromethylphenylacetate (MTPA) esters. *J. Am. Chem. Soc., 95*(2), 512-519.

Dalisay, D. S., & Molinski, T. F. (2009). Structure Elucidation at the Nanomole Scale. 2. Hemi-phorboxazole A from Phorbas sp. *Org. Lett., 11*(9), 1967-1970.

Dalisay, D. S., Morinaka, B. I., Skepper, C. K., & Molinski, T. F. (2009). A Tetrachloro Polyketide Hexahydro-1H-isoindolone, Muironolide A, from the Marine Sponge Phorbas sp. Natural Products at the Nanomole Scale. *J. Am. Chem. Soc., 131*(22), 7552-7553.

Evans, D. A., Rieger, D. L., & Gage, J. R. (1990). 13C NMR chemical shift correlations in 1,3-diol acetonides. Implications for the stereochemical assignment of propionate-derived polyols. *Tetrahedron Lett., 31*(49), 7099-7100.

Farès, C., Hassfeld, J., Menche, D., & Carlomagno, T. (2008). Simultaneous Determination of the Conformation and Relative Configuration of Archazolide

A by Using Nuclear Overhauser Effects, J Couplings, and Residual Dipolar Couplings. *Angew. Chem., Int. Ed. Engl., 120*(20), 3782-3786.

Fayette, J., Coquard, I. R., Alberti, L., Boyle, H., Méeus, P., Decouvelaere, A.-V., Thiesse, P., Sunyach, M.-P., Ranchère, D., & Blay, J.-Y. (2006). ET-743: a novel agent with activity in soft-tissue sarcomas. *Current Opinion in Oncology, 18*(4), 347-353

Freire, F., Quinoa, E., & Riguera, R. (2008). In tube determination of the absolute configuration of [small alpha]- and [small beta]-hydroxy acids by NMR via chiral BINOL borates. *Chem. Commun.*(35), 4147-4149.

Freire, F., Seco, J. M., Quiñoá, E., & Riguera, R. (2005). Determining the Absolute Stereochemistry of Secondary/Secondary Diols by 1H NMR: Basis and Applications. *J. Org. Chem., 70*(10), 3778-3790.

Freire, F. l., Seco, J. M., Quiñoá, E., & Riguera, R. (2010). Chiral 1,2-Diols: The Assignment of Their Absolute Configuration by NMR Made Easy. *Org. Lett., 12*(2), 208-211.

Fukushi, E. (2006). Advanced NMR Approaches for a Detailed Structure Analysis of Natural Products. *Biosci. Biotechnol. Biochem., 70*, 1803-1812.

Gao, J., Haas, H., Wang, K. Y., Chen, Z., Breitenstein, W., & Rajan, S. (2008). The use of MPA amide for the assignment of absolute configuration of a sterically hindered cyclic secondary amine by 'mix and shake' NMR method. *Magn. Res. Chem., 46*(1), 17-22.

García, R., Seco, J. M., Vázquez, S. A., Quiñoá, E., & Riguera, R. (2002). Absolute Configuration of Secondary Alcohols by 1H NMR: In Situ Complexation of α-Methoxyphenylacetic Acid Esters with Barium(II). *J. Org. Chem., 67*(13), 4579-4589.

Gil, R. R., Gayathri, C., Tsarevsky, N. V., & Matyjaszewski, K. (2008). Stretched Poly(methyl methacrylate) Gel Aligns Small Organic Molecules in Chloroform. Stereochemical Analysis and Diastereotopic Proton NMR Assignment in Ludartin Using Residual Dipolar Couplings and 3J Coupling Constant Analysis. *J. Org. Chem., 73*(3), 840-848.

Gschwind, R. M. (2005). Residual Dipolar Couplings—A Valuable NMR Parameter for Small Organic Molecules. *Angew. Chem., Int. Ed. Engl. , 44*(30), 4666-4668.

Higashibayashi, S., Czechtizky, W., Kobayashi, Y., & Kishi, Y. (2003). Universal NMR Databases for Contiguous Polyols. *J. Am. Chem. Soc., 125*(47), 14379-14393.

Hoye, T. R., Hamad, A.-S. S., Koltun, D. O., & Tennakoon, M. A. (2000). An NMR method for determination of configuration of [beta]-substituted carboxylic acids. *Tetrahedron Lett., 41*(14), 2289-2293.

Hoye, T. R., Hanson, P. R., & Vyvyan, J. R. (1994). A Practical Guide to First-Order Multiplet Analysis in 1H NMR Spectroscopy. *J. Org. Chem., 59*(15), 4096-4103.

Hoye, T. R., & Koltun, D. O. (1998). An NMR Strategy for Determination of Configuration of Remote Stereogenic Centers: 3-Methylcarboxylic Acids. *J. Am. Chem. Soc., 120*(19), 4638-4643.

Hoye, T. R., & Renner, M. K. (1996a). Applications of MTPA (Mosher) Amides of Secondary Amines: Assignment of Absolute Configuration in Chiral Cyclic Amines. *J. Org. Chem., 61*(24), 8489-8495.

Hoye, T. R., & Renner, M. K. (1996b). MTPA (Mosher) Amides of Cyclic Secondary Amines: Conformational Aspects and a Useful Method for Assignment of Amine Configuration. *J. Org. Chem., 61*(6), 2056-2064.

Hoye, T. R., & Zhao, H. (2002). A Method for Easily Determining Coupling Constant Values: An Addendum to "A Practical Guide to First-Order Multiplet Analysis in 1H NMR Spectroscopy". *J. Org. Chem., 67*(12), 4014-4016.

Huo, R., Wehrens, R., Duynhoven, J. v., & Buydens, L. M. C. (2003). Assessment of techniques for DOSY NMR data processing. *Anal. Chim. Acta, 490*(1–2), 231-251.

Kobayashi, Y., Lee, J., Tezuka, K., & Kishi, Y. (1999). Toward Creation of a Universal NMR Database for the Stereochemical Assignment of Acyclic Compounds: The Case of Two Contiguous Propionate Units. *Org. Lett., 1*(13), 2177-2180.

Kobayashi, Y., Tan, C.-H., & Kishi, Y. (2000). Toward Creation of a Universal NMR Database for Stereochemical Assignment: The Case of 1,3,5-Trisubstituted Acyclic Systems. *Helv.Chim. Acta, 83*(9), 2562-2571.

Kurz, M., Schmieder, P., & Kessler, H. (1991). HETLOC, an Efficient Method for Determining Heteronuclear Long-Range Couplings with Heteronuclei in Natural Abundance. *Angew. Chem., Int. Ed. Engl., 30*(10), 1329-1331.

Kusumi, T., & Ohtani, I. (1999). Determination of the absolute configuration of biologically active compounds by the modified Mosher's method. In J. K. S. Raymond Cooper (Ed.), *The Biology-Chemistry Interface: A Tribute to Koji Nakanishi*

Kwon, H. C., Kauffman, C. A., Jensen, P. R., & Fenical, W. (2008). Marinisporolides, Polyene-Polyol Macrolides from a Marine Actinomycete of the New Genus Marinispora. *J. Org. Chem., 74*(2), 675-684.

Latypov, S. K., Ferreiro, M. J., Quiñoá, E., & Riguera, R. (1998). Assignment of the Absolute Configuration of β-Chiral Primary Alcohols by NMR: Scope and Limitations. *J. Am. Chem. Soc., 120*(19), 4741-4751.

Latypov, S. K., Seco, J. M., Quinoa, E., & Riguera, R. (1995). Determination of the Absolute Stereochemistry of Chiral Amines by 1H NMR of Arylmethoxyacetic Acid Amides: The Conformational Model. *J. Org. Chem., 60*(6), 1538-1545.

Latypov, S. K., Seco, J. M., Quinoa, E., & Riguera, R. (1996). MTPA vs MPA in the Determination of the Absolute Configuration of Chiral Alcohols by 1H NMR. *J. Org. Chem., 61*(24), 8569-8577.

Latypov, S. K., Seco, J. M., Quiñoá, E., & Riguera, R. (1998). Are Both the (R)- and the (S)-MPA Esters Really Needed for the Assignment of the Absolute

Configuration of Secondary Alcohols by NMR? The Use of a Single Derivative. *J. Am.Chem. Soc., 120*(5), 877-882.

Le Tourneau, C., Raymond, E., & Faivre, S. (2007). Aplidine: a paradigm of how to handle the activity and toxicity of a novel marine anticancer poison. . *Curr Pharm Des*(13), 3427-3439.

Leiro, V., Freire, F., Quinoa, E., & Riguera, R. (2005). Absolute configuration of amino alcohols by 1H-NMR. *Chem. Commun.*(44), 5554-5556.

Lievens, S. C., & Molinski, T. F. (2006). Progressive−Convergent Elucidation of Stereochemistry in Complex Polyols. The Absolute Configuration of (−)-Sagittamide A. *J. Am. Chem. Soc., 128*(36), 11764-11765.

López, B., Quiñoá, E., & Riguera, R. (1999). Complexation with Barium(II) Allows the Inference of the Absolute Configuration of Primary Amines by NMR. *J. Am. Chem. Soc., 121*(41), 9724-9725.

Luy, B., Kobzar, K., & Kessler, H. (2004). An Easy and Scalable Method for the Partial Alignment of Organic Molecules for Measuring Residual Dipolar Couplings. *Angew. Chem., Int. Ed. Engl., 43*(9), 1092-1094.

Macías, F. A., Guerra, J. O., Simonet, A. M., Pérez, A. J., & Nogueiras, C. (2010). Characterization of three saponins from a fraction using 1D DOSY as a solvent signal suppression tool. Agabrittonosides E–F. Furostane Saponins from Agave brittoniana Trel. spp. Brachypus. *Magn. Res. Chem., 48*(5), 350-355.

Marquez, B. L., Gerwick, W. H., & Thomas Williamson, R. (2001). Survey of NMR experiments for the determination of nJ(C,H) heteronuclear coupling constants in small molecules. *Magn. Res. Chem., 39*(9), 499-530.

Marx, A., Böttcher, B., & Thiele, C. (2010). Enhancing the Orienting Properties of Poly(γ-benzyl-L-glutamate) by means of Additives. *Chem. Eur. J., 16*(5), 1656-1663.

Masamune, T., Fukuzawa, A., Furusaki, A., Ikura, M., Matsue, H., Kaneko, T., Abiko, A., Sakamoto, N., Tanimoto, N., & Murai, A. (1987). Glycinoeclepins, Natural Hatching Stimuli for the Soybean Cyst Nematode, Heterodera Glycines. II. Structural Elucidation. *Bull. Chem. Soc. Jpn, 60*, 1001-1014.

Matsumori, N., Kaneno, D., Murata, M., Nakamura, H., & Tachibana, K. (1999). Stereochemical Determination of Acyclic Structures Based on Carbon−Proton Spin-Coupling Constants. A Method of Configuration Analysis for Natural Products. *J. Org. Chem., 64*(3), 866-876.

Molinski, T. F. (2010). Microscale Methodology for Structure Elucidation of Natural Products. *Curr. Opin. Biotechnol., 21*, 819-826.

Murata, M., Oishi, T., & Yoshida, M. (2006). State-of-Art Methodology of Marine Natural Products Chemistry: Structure Determination with Extremely Small Sample Amounts In N. Fusetani & A. S. Clare (Eds.), (Vol. 42, pp. 203-220): Springer Berlin Heidelberg.

Neuhaus, D., & Williamson, M. P. (2000). The Nuclear Overhauser Effect in Structural and Conformational Analysis (pp. 494): WILEY.

Novoa-Carballal, R., Fernandez-Megia, E., Jimenez, C., & Riguera, R. (2011). NMR methods for unravelling the spectra of complex mixtures. *Nat. Prod. Rep., 28*(1), 78-98.

Ohtani, I., Kusumi, T., Kashman, Y., & Kakisawa, H. (1991). High-field FT NMR application of Mosher's method. The absolute configurations of marine terpenoids. *J. Am. Chem. Soc., 113*(11), 4092-4096.

Oishi, T., Tsuchikawa, H., Murata, M., Yoshida, M., & Morisawa, M. (2004). Synthesis and Identification of an Endogenous Sperm Activating and Attracting Factor Isolated from Eggs of the Ascidian Ciona intestinalis: An Example of Nanomolar-Level Structure Elucidation of Novel Natural Compound. *Tetrahedron, 60*, 6971-6980.

Politi, M., Zloh, M., Pintado, M. E., Castro, P. M. L., Heinrich, M., & Prieto, J. M. (2009). Direct metabolic fingerprinting of commercial herbal tinctures by nuclear magnetic resonance spectroscopy and mass spectrometry. *Phytochem. Anal., 20*(4), 328-334.

Riccio, R., Bifulco, G., Cimino, P., Bassarello, C., ., & Paloma, L.-G. (2003). Stereochemical Analysis On Natural Products : Approaches Relying On The Combination Of NMR Spectroscopy And Computational Methods. *Pure Appl. Chem., 75*, 295-308.

Rodrigues, E. D., da Silva, D. B., de Oliveira, D. C. R., & da Silva, G. V. J. (2009). DOSY NMR applied to analysis of flavonoid glycosides from Bidens sulphurea. *Magn. Res. Chem., 47*(12), 1095-1100.

Rychnovsky, S. D., Rogers, B. N., & Richardson, T. I. (1998). Configurational Assignment of Polyene Macrolide Antibiotics Using the [13C]Acetonide Analysis. *Acc. Chem. Res., 31*(1), 9-17.

Saurí, J., Espinosa, J. F., & Parella, T. (2012). A Definitive NMR Solution for a Simple and Accurate Measurement of the Magnitude and the Sign of Small Heteronuclear Coupling Constants on Protonated and Non-Protonated Carbon Atoms. *Angew. Chem., Int. Ed. Engl., 51*(16), 3919-3922.

Schneiders, F. L., Scheper, R. J., von Blomberg, B. M. E., Woltman, A. M., Janssen, H. L. A., van den Eertwegh, A. J. M., Verheul, H. M. W., de Gruijl, T. D., & van der Vliet, H. J. (2011). Clinical experience with α-galactosylceramide (KRN7000) in patients with advanced cancer and chronic hepatitis B/C infection. *Clin. Immunol., 140*(2), 130-141.

Schroeder, F., Sinnwell, V., Baumann, H., & Kaib, M. (1996). Myrmicarin 430A: a new heptacyclic alkaloid from Myrmicaria ants. *Chem. Commun.*(18), 2139-2140.

Schroeder, F. C., Taggi, A. E., Gronquist, M., Malik, R. U., Grant, J. B., Eisner, T., & Meinwald, J. (2008). NMR-spectroscopic screening of spider venom reveals sulfated nucleosides as major components for the brown recluse and related species. *Proc. Nat. Acad. Sci., 105*(38), 14283-14287.

Schuetz, A., Junker, J., Leonov, A., Lange, O. F., Molinski, T. F., & Griesinger, C. (2007). Stereochemistry of Sagittamide A from Residual Dipolar Coupling Enhanced NMR. *J. Am. Chem. Soc., 129*(49), 15114-15115.

Seco, J. M., Latypov, S. K., Quinoa, E., & Riguera, R. (1997). Choosing the Right Reagent for the Determination of the Absolute Configuration of Amines by NMR: MTPA or MPA? *J. Org. Chem., 62*(22), 7569-7574.

Seco, J. M., Latypov, S. K., Quiñoá, E., & Riguera, R. (1997). Determining factors in the assignment of the absolute configuration of alcohols by NMR. The use of anisotropic effects on remote positions. *Tetrahedron, 53*(25), 8541-8564.

Seco, J. M., Martino, M., Quiñoá, E., & Riguera, R. (2000). Absolute Configuration of 1,n-Diols by NMR: The Importance of the Combined Anisotropic Effects in Bis-Arylmethoxyacetates. *Org. Lett., 2*(21), 3261-3264.

Seco, J. M., Quinoa, E., & Riguera, R. (1999). Boc-Phenylglycine: The Reagent of Choice for the Assignment of the Absolute Configuration of α-Chiral Primary Amines by 1H NMR Spectroscopy. *J. Org. Chem., 64*(13), 4669-4675.

Seco, J. M., Quiñoá, E., & Riguera, R. (2004). The Assignment of Absolute Configuration by NMR. *Chem. Rev., 104*(1), 17-118.

Seike, H., Ghosh, I., & Kishi, Y. (2006a). Attempts to Assemble a Universal NMR Database without Synthesis of NMR Database Compounds. *Org. Lett., 8*(17), 3861-3864.

Seike, H., Ghosh, I., & Kishi, Y. (2006b). Stereochemistry of Sagittamide A: Prediction and Confirmation. *Org. Lett., 8*(17), 3865-3868.

Seo, S., Tomita, Y., Tori, K., & Yoshimura, Y. (1978). Determination of the absolute configuration of a secondary hydroxy group in a chiral secondary alcohol using glycosidation shifts in carbon-13 nuclear magnetic resonance spectroscopy. *J. Am. Chem. Soc., 100*(11), 3331-3339.

Sugahara, K., Kitamura, Y., Murata, M., Satake, M., & Tachibana, K. (2011). Prorocentrol, a Polyoxy Linear Carbon Chain Compound Isolated from the Toxic Dinoflagellate Prorocentrum hoffmannianum. *J. Org. Chem., 76*(9), 3131-3138.

Sullivan, G. R., Dale, J. A., & Mosher, H. S. (1973). Correlation of configuration and fluorine-19 chemical shifts of .alpha.-methoxy-.alpha.-trifluoromethylphenyl acetate derivatives. *J. Org. Chem., 38*(12), 2143-2147.

Taggi, A. E., Meinwald, J., & Schroeder, F. C. (2004). A New Approach to Natural Products Discovery Exemplified by the Identification of Sulfated Nucleosides in Spider Venom. *J. Am. Chem. Soc., 126*(33), 10364-10369.

Takeuchi, Y., Segawa, M., Fujisawa, H., Omata, K., Lodwig, S. N., & Unkefer, C. J. (2006). The CFTA Method: A Reliable Procedure for the Determination of the Absolute Configuration of Chiral Primary Amines by 1H NMR Spectroscopic Analysis. *Angew. Chem., Int. Ed. Engl., 45*(28), 4617-4619.

Thiele, C. M. (2004). Simultaneous Assignment of All Diastereotopic Protons in Strychnine Using RDCs: PELG as Alignment Medium for Organic Molecules. *J. Org. Chem., 69*(22), 7403-7413.

Thiele, C. M. (2008). Residual Dipolar Couplings (RDCs) in Organic Structure Determination. *Eur. J. Org. Chem., 2008*(34), 5673-5685.

Thiele, C. M., & Berger, S. (2003). Probing the Diastereotopicity of Methylene Protons in Strychnine Using Residual Dipolar Couplings. *Org. Lett., 5*(5), 705-708.

Tringali, C. (2001). *Bioactive compounds from natural sources: isolation, characterisation and biological properties*. New York: Taylor & Francis.

Tsuda, M., Toriyabe, Y., Endo, T., & Kobayashi, J. (2003). Application of Modified Mosher's Method for Primary Alcohols with a Methyl Group at C2 Position. *Chem. Pharm. Bull., 51*, 448-451.

Tsuda, M., Yasuda, T., Fukushi, E., Kawabata, J., Sekiguchi, M., Fromont, J., & Kobayashi, J. i. (2006). Agesamides A and B, Bromopyrrole Alkaloids from Sponge Agelas Species: Application of DOSY for Chemical Screening of New Metabolites. *Org. Lett., 8*(19), 4235-4238.

Uhrín, D., Batta, G., Hruby, V. J., Barlow, P. N., & Kövér, K. E. (1998). Sensitivity- and Gradient-Enhanced Hetero ([omega]1) Half-Filtered TOCSY Experiment for Measuring Long-Range Heteronuclear Coupling Constants. *J. Magn. Res., 130*(2), 155-161.

Verdier, L., Sakhaii, P., Zweckstetter, M., & Griesinger, C. (2003). Measurement of long range H,C couplings in natural products in orienting media: a tool for structure elucidation of natural products. *J. Magn. Res., 163*(2), 353-359.

Ward, J. L., Baker, J. M., & Beale, M. H. (2007). Recent applications of NMR spectroscopy in plant metabolomics. *FEBS Journal, 274*(5), 1126-1131.

Weibel, D. B., Walker, T. R., Schroeder, F. C., & Meinwald, J. (2000). Chiral Silylation Reagents for the Determination of Absolute Configuration by NMR Spectroscopy. *Org. Lett., 2*(15), 2381-2383.

Wenzel, T. J. (2007). *Discrimination of Chiral Compounds Using NMR Spectroscopy*.

Williamson, R. T., Barrios Sosa, A. C., Mitra, A., Seaton, P. J., Weibel, D. B., Schroeder, F. C., Meinwald, J., & Koehn, F. E. (2003). New Silyl Ether Reagents for the Absolute Stereochemical Determination of Secondary Alcohols. *Org. Lett., 5*(10), 1745-1748.

Yabuuchi, T., & Kusumi, T. (2000). Phenylglycine Methyl Ester, a Useful Tool for Absolute Configuration Determination of Various Chiral Carboxylic Acids. *J. Org. Chem., 65*(2), 397-404.

BIOLOGICAL AND CHEMICAL SCREENING OF TUNICATE EXTRACTS

CHAPTER TWO

Justyna Sikorska, Shirley Parker-Nance, Oliver B. Vining, Aleksandra E. Sikora, Michael T. Davies-Coleman, Jane E. Ishmael, and Kerry L. McPhail

Rubrolides subsection accepted, pending minor revision in the Journal of Natural Products

September 12, 2012

Abstract

The diversity and structural complexity of natural products has been central to the development of new pharmaceutical drug leads due to a concomitantly broader spectrum of biological activities than is found for traditional combinatorial libraries. Therefore, the secondary metabolites of a collection of sixty tunicate extracts were explored through *in vitro* biological screening against cancer cell lines and Gram-positive and -negative bacteria, as well as chemical screening using ^{1}H and diffusion ordered NMR spectroscopy together with mass spectrometry. Chemical profiling identified the known homarine (**1**) in several extracts, the moderately antibacterial new rubrolide analogues **2**-**5** and known rubrolides E and F (**6** and **7**) from a *Synoicum* tunicate species, and previously mis-assigned nucleosides (**8**-**11**) from an Antarctic tunicate, which are discussed in this chapter. Biological profiling led to the discovery of the potent cytotoxins mandelalides A-D (Chapter 3) and pseudodistaminols A-C, (2*S*)-amino- (3*S*)-hydroxy-(5*E*)-tetradecene, (2*S*)-amino-(3*S*)-hydroxy-(5*E*),13-tetradecadiene and (1*R*)-aminotridec-(4*E*)-en-2-ol (amino alcohols, Chapter 4).

Introduction

The identification of new pharmaceutical drug leads is a challenging task, often requiring elaborate testing of libraries comprising hundreds of thousands of pure compounds and/or extracts. Although pharmaceutical companies shifted their focus in the 1990's to creation of combinatorial libraries of synthetic compounds, natural product and natural product-derived drugs still constitute approximately 40% of commercially available drugs (Newman & Cragg, 2012). This may be due to the fact that pharmaceutical companies "End up making things they can make, rather than what they should make." C. Decicco (Landers, 2004). Biologically relevant chemical space is much smaller than the total chemical space, and the large synthetic chemical libraries often do not represent the broad diversity of much smaller libraries of natural products, which are complementary with biological structure space (Dobson, 2004). The importance of further exploring the diverse chemical space occupied by marine and terrestrial natural products is suggested by the parallel in reduced focus on natural products discovery and decrease in the number of new molecular entities approved by the FDA over the last 20 years (Johnson et al., 2011). This trend again suggests that the discovery of new drugs should not rely strictly on large synthetic libraries of compounds that generally have less oxygen and more nitrogen atoms, fewer chiral centers and fused rings, and more aromatic rings and rotatable bonds than the more rigid and non-planar natural products (Lachance et al., 2012).

The search for new biologically-relevant chemical entities can be based on two complementary approaches: biological and chemical screening. The advantage of biological evaluation of organic extracts is that it allows for targeted identification of active components by activity-guided fractionation. However, to obtain promising hits one has to subject crude extracts to a broad spectrum of biological assays. A major pitfall of this method is that the active components of extracts are often very minor constituents and assays may not be sensitive enough to detect them at low titers in these complex mixtures. Also, assay detection systems can be impeded by the UV

absorbance of a colorful extract, for example, or otherwise “nuisance compounds”. Finally, in the case of compounds that should be orally bioavailable (e.g. antibiotics), Lipinski’s rule of five parameters is often not taken into account. Chemical screening approaches require the use of LC-MS, LC-UV or NMR methodologies to identify compounds that are in the “druggable” mass range (< 500 for oral bioavailability), have log P < 5 (P = partition coefficient, a measure of solubility), and possess interesting structural features. This methodology often requires prior steps of purification (LC-based techniques) or a substantial amount of the compound of interest present in the mixture (NMR techniques). In addition, one does not directly account for the presence or absence of activity in the fractions or extracts obtained, but instead one uses this method to produce a library of sub-fractions for further testing.

The combination of both approaches (biological and chemical screening) can lead to the identification of compounds that are not only very potent in currently available assays, but are also new chemical skeletons that may finally have unique activities against new drug targets. Therefore, all 60 tunicate extracts obtained from the South African 2004 collection (Algoa Bay, Eastern Cape) were subjected to biological and chemical screening. Chemical screening identified known cytotoxin homarine (**1**), the moderately antibacterial new rubrolide analogues **2-5** and known rubrolides E and F (**6** and **7**) from a *Synoicum* species. In addition nucleosides (**8-11**), of which **8** had been previously mis-assigned twice as different new natural products, were identified from an Antarctic tunicate.

Results and Discussion

A library of sixty organic extracts from tunicates collected in Algoa Bay, South Africa (2004) was subjected to biological screening in a brine shrimp cytotoxicity assay at a concentration of 100 μg/mL, against the mouse Neuro-2A neuroblastoma cell line at 30 μg/mL and against *Vibrio cholerae* (N16961, N0395) and *Staphylococcus aureus* at 120 μg/mL (Table 2.1).

The brine shrimp assay identified twelve extracts (Table 2.1) as containing potent cytotoxins, with extract SAF04-29 additionally active against Neuro-2A cells, and extracts SAF04-40 and -48 also active in antibacterial assays. Bioassay-guided fractionation of extract SAF04-53 from a *Pseudodistoma* species led to isolation of linear and cyclized amino alcohols, the identification of which is described in detail in chapter 4. Taxonomy data indicated that extracts SAF-20, -21, -25, -27, -40, -46, -47, -48 and -53 are from different species of the genus *Pseudodistoma*, suggesting the presence of amino alcohols in these extracts as well.

Extract SAF04-29 from a *Clavelina* species was the only extract that showed potent cytotoxicity to brine shrimp and Neuro-2A cells. However, further fractionation and extensive HPLC separation based on UV absorption resulted in cytotoxicity distributed through all fractions and hindered identification of any single active component. In another case, extract SAF04-45 showed good cytotoxicity to Neuro-2A cells, but a limited amount of extract in parallel with challenging chromatography prevented the isolation of any active compounds. The application of biological activity-guided fractionation to extract SAF04-55 from *Lissoclinum* sp., also active against Neuro-2A cells, led to identification of the potent cytotoxins mandelalides A-D, which are presented in chapter 3.

Table 2.1 Biological activity of organic extracts from South African tunicates.

Extract #	% cell viability				
	Brine shrimp assay	Neuro-2A cell line	*Vibrio cholerae* (N16961)	*Vibrio cholerae* (N0395)	*Staphylococcus aureus*
SAF04-10	-	97.2	124.7	106.7	118.4
SAF04-11	-	84.1	129.3	117.4	118.4
SAF04-12	-	91.9	114.7	90.8	98.2
SAF04-13	-	92.5	105.7	130.1	116.5
SAF04-14	-	85.6	119.1	129.4	114.3
SAF04-15	-	90.3	125.4	156.5	116.0
SAF04-16	-	99.6	119.2	123.9	99.4
SAF04-17	-	91.6	125.9	154.3	128.1
SAF04-18	-	82.5	115.9	125.8	116.1
SAF04-19	-	80.9	125.3	121.6	112.8
SAF04-20	**0**	84.9	120.0	111.2	118.2
SAF04-21	**5**	80.0	103.1	132.2	127.9
SAF04-22	100	85.7	141.9	132.0	115.5
SAF04-24	100	79.2	99.5	131.5	113.3
SAF04-25	**0**	81.1	117.7	132.9	108.1
SAF04-26	100	80.3	125.8	105.7	105.0
SAF04-27	**0**	82.9	126.3	118.7	125.0
SAF04-28	100	90.6	107.8	116.7	121.0
SAF04-29	**0**	**40.6**	105.3	119.1	130.5
SAF04-30	100	90.4	128.5	105.1	108.2
SAF04-31	100	94.1	140.0	121.5	109.6
SAF04-32	100	92.4	136.0	131.6	117.7
SAF04-33	100	93.5	117.9	124.6	116.5
SAF04-34	100	91.6	122.6	100.7	110.2
SAF04-35	100	90.3	118.4	117.9	114.2
SAF04-36	100	80.3	123.9	124.7	120.9
SAF04-37	100	94.7	118.9	97.0	110.2
SAF04-38	100	80.9	96.2	93.9	84.7
SAF04-39	100	87.0	133.8	108.3	118.6
SAF04-40	**0**	80.9	**49.2**	**51.9**	110.4
SAF04-41	100	95.1	127.3	127.1	118.2
SAF04-42	100	98.1	126.3	151.1	132.8
SAF04-44	100	97.7	126.3	112.6	114.4
SAF04-45	100	**62.3**	108.1	139.4	97.4
SAF04-46	**0**	81.7	134.9	135.4	98.2
SAF04-47	**0**	79.5	125.9	134.9	104.6
SAF04-48	**0**	74.2	**49.8**	**26.3**	101.5
SAF04-49	100	98.2	114.6	125.5	116.8
SAF04-50	100	85.9	126.3	96.9	112.6
SAF04-51	100	100.9	133.4	96.1	108.0
SAF04-52	100	81.6	113.1	100.5	114.1
SAF04-53	**0**	75.9	91.6	96.6	105.6
SAF04-54	100	98.2	**61.8**	95.9	**65.8**
SAF04-55	100	**30.9**	133.8	107.9	108.6
SAF04-56	100	81.6	119.8	145.7	111.2
SAF04-57	100	98.1	125.9	101.7	116.8

Table 2.1 (continued) Biological activity of organic extracts from South African tunicates.

Extract #	% cell viability				
	Brine shrimp assay	Neuro-2A cell line	*Vibrio cholerae* (N16961)	*Vibrio cholerae* (N0395)	*Staphylococcus aureus*
SAF04-58	100	76.9	99.5	93.7	125.6
SAF04-59	100	87.5	115.2	131.3	144.4
SAF04-60	**25**	72.6	117.4	128.6	132.0
SAF04-61	100	74.6	121.2	111.7	111.9
SAF04-62	**0**	75.0	118.0	92.6	116.7
SAF04-63	100	75.7	123.9	94.1	116.7
SAF04-64	100	79.0	102.7	121.7	120.2
SAF04-65	100	84.8	107.1	126.6	123.3
SAF04-66	100	77.7	120.2	98.8	111.9
SAF04-67	100	79.9	121.4	102.3	120.3
SAF04-68	100	95.1	117.3	108.9	125.3
SAF04-69	100	78.8	107.4	109.3	99.1
SAF04-70	100	81.5	119.1	117.1	114.3
SAF04-71	100	96.7	128.3	102.6	110.9
SAF04-72	100	79.4	103.2	102.2	109.2

Analysis of the antibacterial properties of the tunicate extract library identified SAF04-40 and SAF04-48 as antibacterial against both strains of *Vibrio cholerae*, while SAF04-54 was active against *V. cholerae* (N16961) and *S. aureus*. Additionally, extract SAF04-54 was also prioritized during chemical screening, as described below.

From the remaining pool of South African tunicate extracts not active against Neuro-2A cells, 17 were randomly selected for chemical screening, together with two Antarctic tunicate extracts: SAF04-16, SAF04-19, SAF04-31, SAF04-38, SAF04-44, SAF04-51, SAF04-54, SAF04-56, SAF04-57, SAF04-59, SAF04-60, SAF04-61, SAF04-62, SAF04-65, SAF04-67, SAF04-68, SAF04-71 and ARC-11-01, ARC-11-02. ^{1}H NMR was used to prioritize fractionation and subsequent biological testing of the first-tier fractions (Figure 2.1). Among these selected extracts, SAF04-59 was fractionated using Sephadex LH-20,followed by C_{18} reversed phase (RP_{18}) solid phase extraction (SPE). ^{1}H NMR of the extract and SPE fractions revealed chemical shifts localized at 7.5 – 9.2 ppm in the 50% MeOH–H_2O SPE fraction (SAF04-59D1). Further separation by RP_{18} HPLC yielded homarine (**1**, Figure 2.2). Interestingly, fractionation of extract SAF04-56 also resulted in the isolation of **1**, and its characteristic d-t-d-t ^{1}H chemical shift pattern was also visible in SAF04-68 (Figure 2.3).

To avoid further isolation of homarine 2D DOSY NMR analysis of extracts SAF04-16, -19, -44, -54, -57, -61 and -65 was performed prior to fractionation (Figure 2.4). Extract SAF04-54 was prioritized for further screening due to the presence of components with downfield chemical shifts correlated to midfield chemical shifts. The fractionation by RP_{18}-SPE followed by LC-MS analysis of the 75% MeOH-H_2O fraction indicated an isotope distribution pattern characteristic of brominated compounds. Successive RP_{18}-HPLC led to the isolation of four new rubrolides **2-5** (Figure 2.5) as well as the known rubrolides E (**6**) and F (**7**).

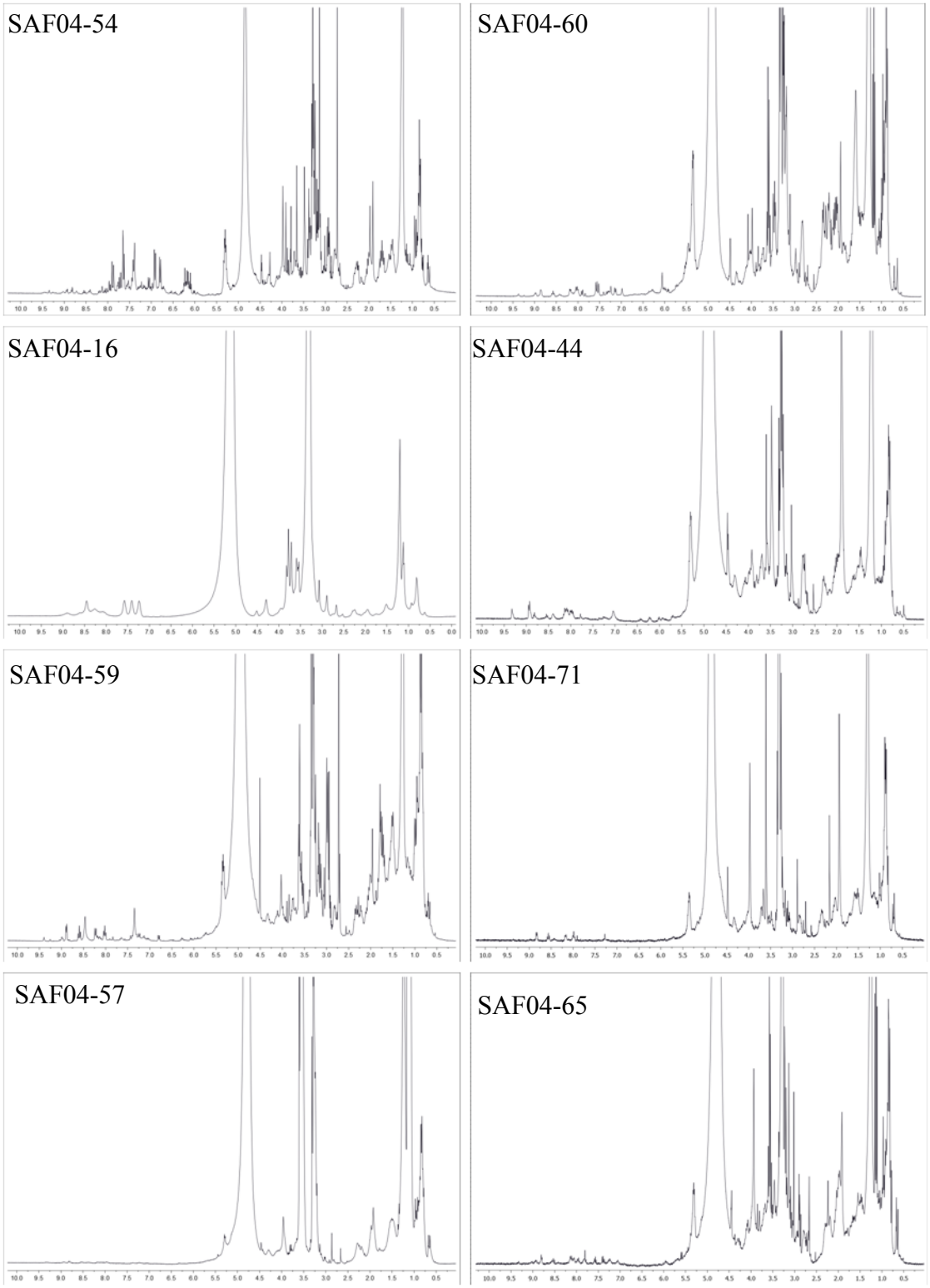

Figure 2.1 ^{1}H NMR spectra at 300 MHz for extracts SAF04-54, -16, -59 and -57 (left from top to bottom), and for SAF04-60, -44, -71 and -65 (right from top to bottom).

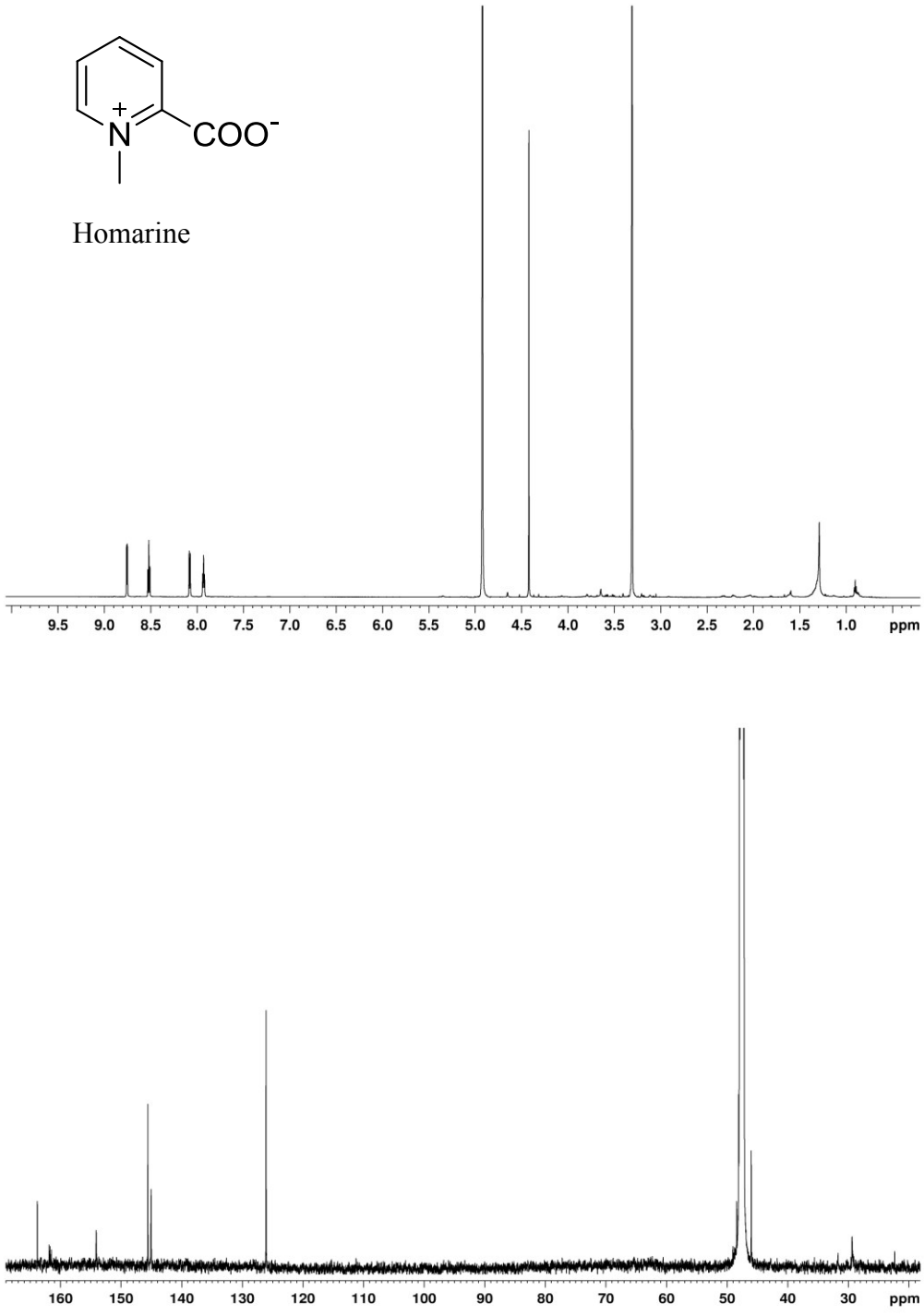

Figure 2.2 ^{1}H (700 MHz) and ^{13}C (175 MHz) NMR spectra for homarine (**1**).

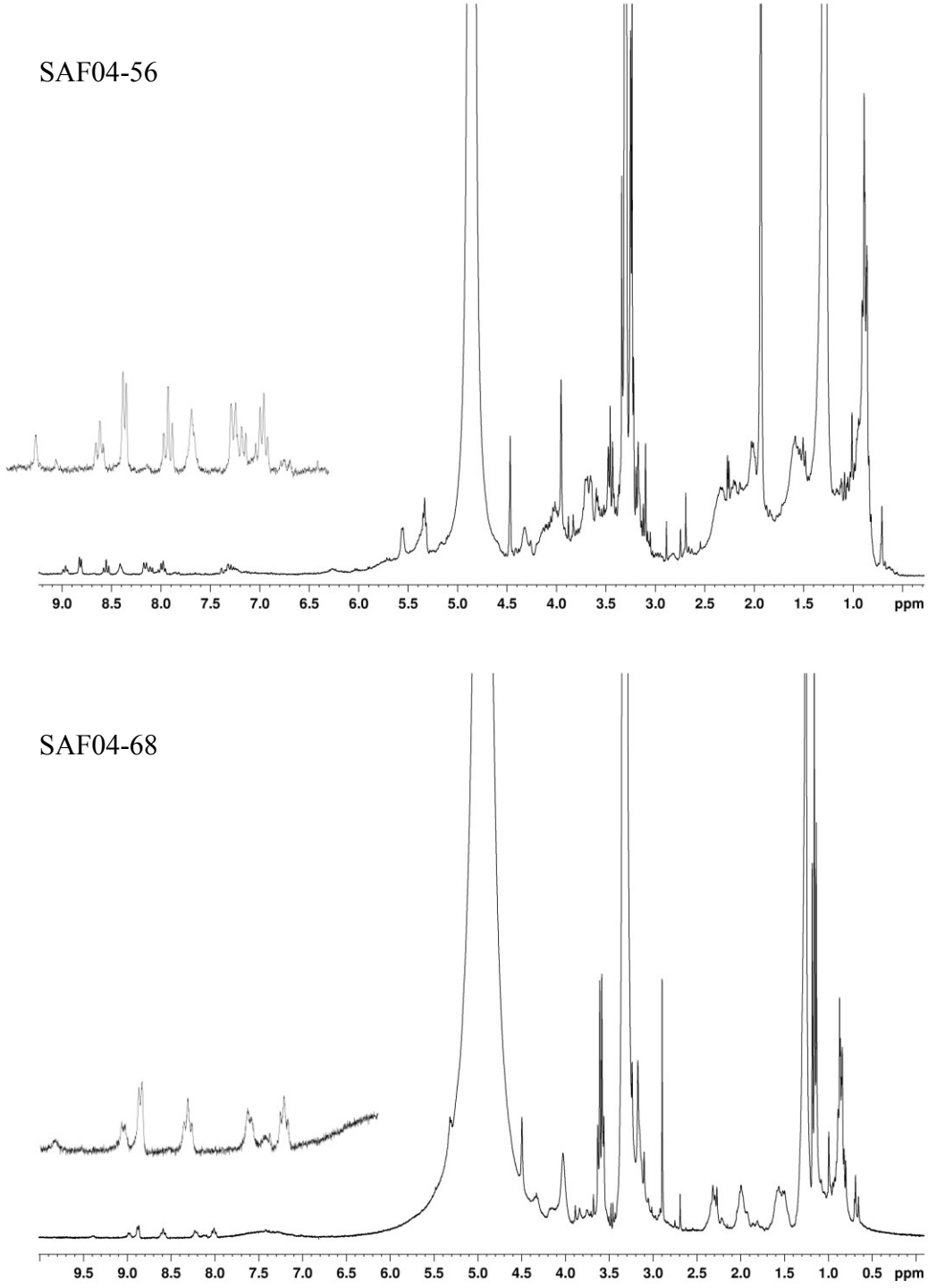

Figure 2.3 ^{1}H NMR spectrum at 300 MHz for SAF04-56 (upper) and SAF04-68 (lower).

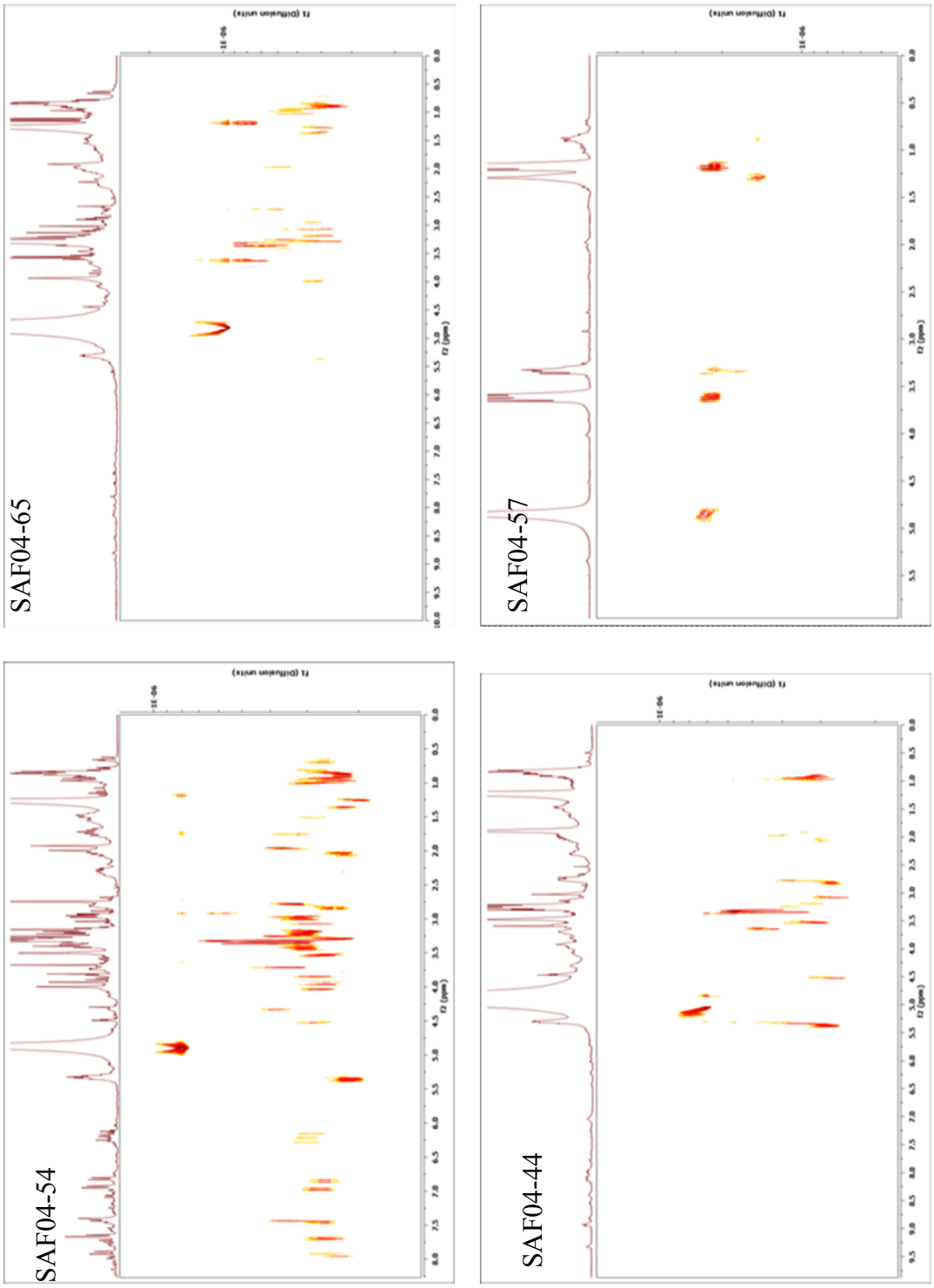

Figure 2.4 2D DOSY spectra at 300 MHz for SAF04-65 and SAF04-54 (left upper and lower, respectively), and SAF04-57 and SAF04-44 (right upper and lower, respectively).

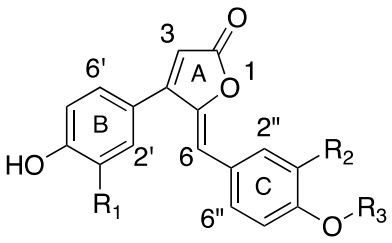

2: R_1 = H, R_2 = Br, R_3 = Me

3: R_1 = Br, R_2 = H, R_3 = H

4: R_1 = Br, R_2 = H, R_3 = Me

5: R_1 = Br, R_2 = Br, R_3 = H

6: R_1 = H, R_2 = H, R_3 = H

7: R_1 = H, R_2 = H, R_3 = Me

Figure 2.5 Chemical structures of new rubrolides **2-5** and known rubrolides E (**6**) and F (**7**).

Rubrolides comprise a central furanone ring substituted at C-4 and C-5 with phenolic moieties. The phenolic moieties are differentially halogenated in the known rubrolides A-O. However, among them only rubrolide F is selectively methylated at C-4″ (Miao & Andersen, 1991; Ortega et al., 2000; A. N. Pearce et al., 2006). Attempts to synthesize new, more potent antimicrobials resulted in a suite of analogues having one or two phenolic moieties with varying halogenation and hydroxy group methylation (Bellina et al., 2003; Bellina et al., 2001). The biological activities of the known rubrolide natural products and their synthetic analogues include antibacterial activity against *Staph. aureus* and *Bacillus subtilis* (rubrolides A, B, C) (Miao & Andersen, 1991), selective inhibition of protein phosphatases 1 and 2A (Miao & Andersen, 1991), weak to moderate activity against various cancer cell lines (rubrolides I, K, L, M) (Ortega, et al., 2000), inhibition of human aldose reductase (rubrolide L) (Manzanaro et al., 2006), and moderate anti-inflammatory properties (rubrolide O) (A. Norrie Pearce et al., 2006). Interestingly, a synthetic series of analogues in which the furanone is substituted with an aryl group comprises potent inhibitors of bacterial cell wall biosynthesis, which have been patented for their potential antimicrobial applications (Caufield et al., 2009).

A molecular formula of $C_{18}H_{14}O_4Br$ for rubrolide **2** was deduced from the HRESIMS 1:1 ion cluster $[M+H]^+$ at *m/z* 373.0081/375.0070. Inspection of the ^1H NMR spectrum revealed nine olefinic or aromatic signals (δ_H 6.23 – 8.10, Table 2.2, Figure 2.6) and a 3H midfield singlet consistent with an aromatic *O*-methyl (δ_H 3.93) group. Multiplicity-edited HSQC and HMBC data indicated the presence of eight quaternary carbons (δ_C 120.5, 126.5, 133.5, 146.7, 156.9, 159.4, 159.9, 169.5), nine methine carbons (δ_C 111.1, 111.6, 111.7, 115.6, 115.6, 129.9, 129.9, 131.2, 134.6) and one *O*-methyl carbon (δ_C 55.3, Figures 2.7-2.8). HMBC correlations from a ^1H doublet at δ 6.23 (H-3) to ^{13}C resonances at δ 169.5 (C-2), 159.4 (C-4) and 146.7 (C-5) defined the furanone (ring A) of the rubrolide skeleton. A *para*-substituted phenolic moiety was indicated by two mutually coupled 2H doublets (δ_H 7.47 and 6.95), and confirmed by apparent HMBC correlations from these doublets to their same HSQC-correlated ^{13}C resonances (Figure 2.8). This ring B could be located at C-4 of ring A based on an HMBC correlation from the H-2′/6′ doublet (δ_H 7.47) to the C-4 resonance. The presence of COSY couplings between H-5″ and H-6″ ^1H signals, in parallel with a long range coupling (2.1 Hz) between H-2″ and H-6″ resonances, led to assignment of ring C as a 1, 3, 4-trisubstitued aromatic moiety. Inspection of the HMBC data for **2** to establish the connectivity between rings A and C identified the olefinic linkage H-6 (δ_H 6.28, s). HMBC correlations were observed from the H-6 singlet to ^{13}C resonances for C-4 and C-5 of ring A, and to C-2″ and C-6″ of ring C. Deshielded methoxy H_3-7″ showed an HMBC correlation to C-4″, thus locating this substituent on ring C. A relatively shielded quaternary carbon resonance at δ_C 126.5, assigned as C-3″ (from HMBC correlations) in the 1, 3, 4-trisubstituted ring C, remained as the site of bromine substitution. Therefore, rubrolide **2** was assigned as 5-(3-bromo-4-methoxybenzylidene)-4-(4-hydroxyphenyl)furan-2(5*H*)-one, and given the trivial name 3″-bromorubrolide F.

HRESIMS of rubrolide **3** gave an $[M+H]^+$ ion cluster at *m/z* 358.9933/360.9916 for a molecular formula of $C_{17}H_{12}O_4Br$. Comparison of the ^1H NMR spectra for **2** and

3 indicated significant changes in the shifts for all downfield ^{1}H signals and the absence of the midfield 3H singlet (δ_H 3.93, (Table 2.2, Figure 2.10). Assignment of COSY and HMBC correlations showed that in the case of **3**, ring B is the 1, 3, 4-trisubstitued aromatic moiety, and ring C is the 1,4-disubstitued aromatic unit. Therefore, it could be concluded that in **3**, the bromine is located at C-3′ of ring B. The lack of an *O*-methyl singlet indicated a free 4″-hydroxy group in **3** compared to **2**. Thus, the structure of **3** was defined as 4-(3-bromo-4-hydroxyphenyl)-5-(4-hydroxybenzylidene)furan-2(5*H*)-one, and given the trivial name 3′-bromorubrolide E.

Table 2.2. ^{1}H (700 MHz) and ^{13}C (175 MHz) NMR Data (CD_3OD) for Rubrolides **2** and **3**.

position	3″-Bromorubrolide F (**2**)		3′-Bromorubrolide E (**3**)	
	δ_C, mult.	δ_H (mult., *J* in Hz)	δ_C, mult.	δ_H (mult., *J* in Hz)
2	169.5 (C)		170.4 (C)	
3	111.1 (CH)	6.23 (d, 0.6)	111.9 (CH)	6.20 (d, 0.5)
4	159.4 (C)		158.3 (C)	
5	146.7 (C)		146.3 (C)	
6	111.6 (CH)	6.28 (s)	114.5 (CH)	6.24 (s)
1′	120.5 (C)		123.2 (C)	
2′	129.9 (CH)	7.47 (d, 8.6)	133.6 (CH)	7.72 (d, 2.0)
3′	115.6 (CH)	6.95 (d, 8.7)	110.9 (C)	
4′	159.9 (C)		157.4 (C)	
5′	115.6 (CH)	6.95 (d, 8.7)	116.8 (CH)	7.03 (d, 8.3)
6′	129.9 (CH)	7.47 (d, 8.6)	129.5 (CH)	7.42 (dd, 8.3, 2.0)
1″	133.5 (C)		125.2 (C)	
2″	134.6 (CH)	8.10 (d, 2.1)	133.2 (CH)	7.70 (d, 8.7)
3″	126.5 (C)		116.0 (CH)	6.83 (d, 8.7)
4″	156.9 (C)		159.6 (C)	
5″	111.7 (CH)	7.10 (d, 8.6)	116.0 (CH)	6.83 (d, 8.7)
6″	131.2 (CH)	7.78 (dd, 8.6, 2.1)	133.2 (CH)	7.70 (d, 8.7)
7″	55.3 (CH_3)	3.93 (s)		

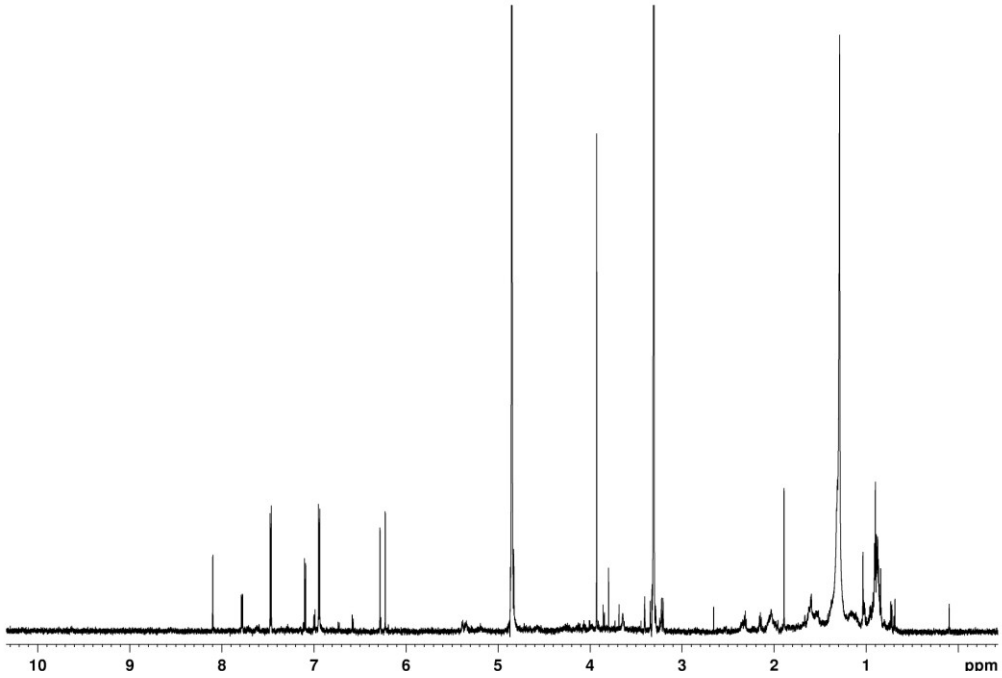

Figure 2.6 ^{1}H NMR spectrum for 3″-bromorubrolide F (**2**; 700 MHz, CD_3OD)

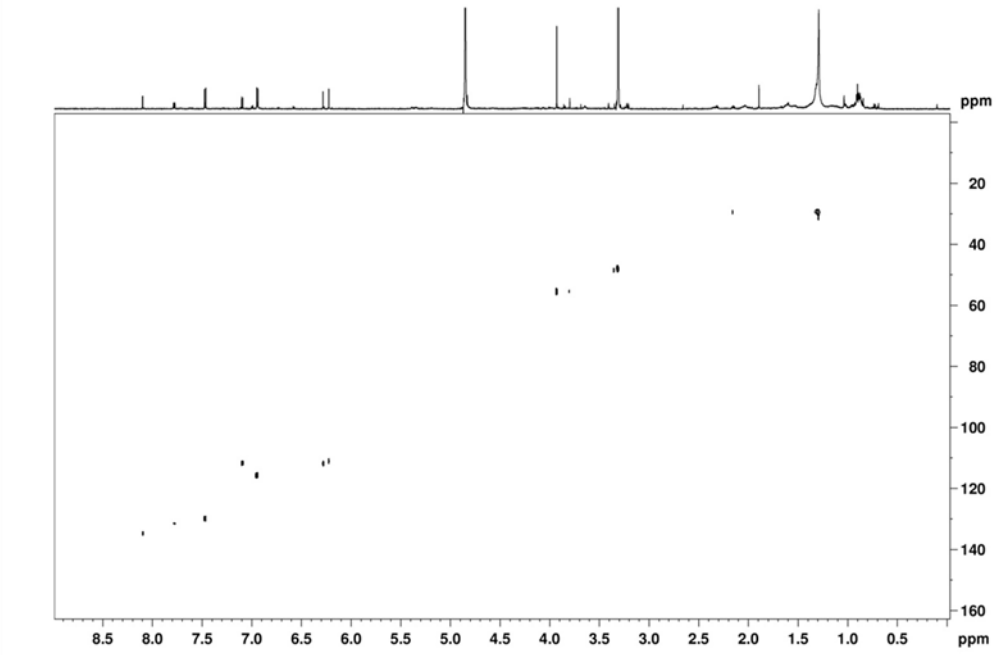

Figure 2.7 HSQC spectrum for 3″-bromorubrolide F (**2**; 700 MHz, CD_3OD)

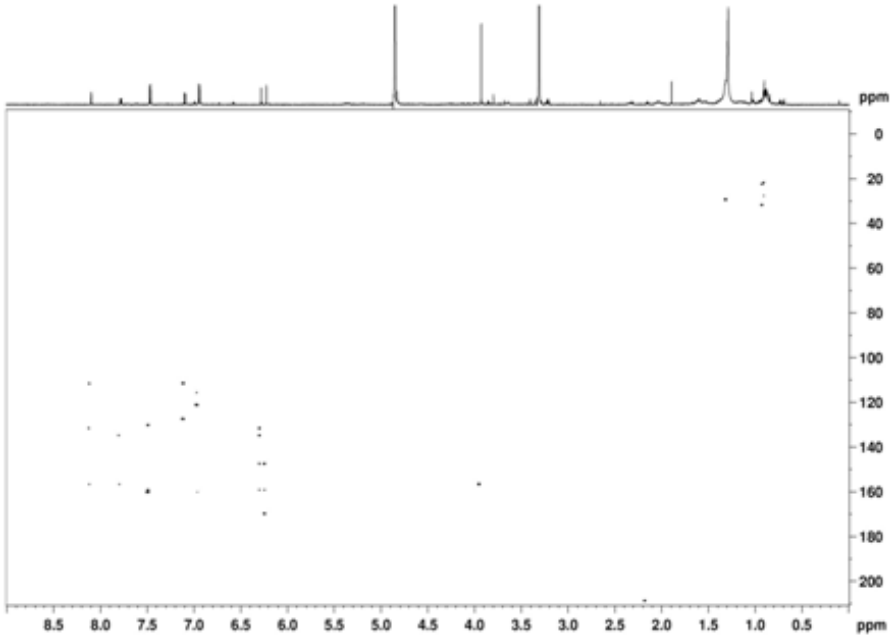

Figure 2.8 HMBC spectrum for 3″-bromorubrolide F (**2**; 700 MHz, CD_3OD)

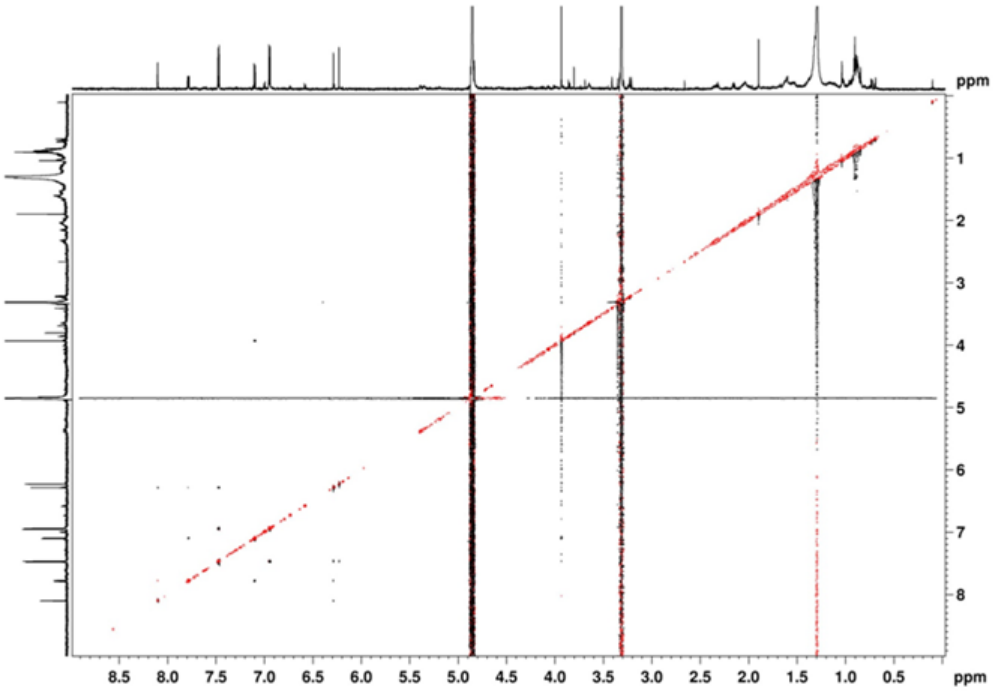

Figure 2.9 NOESY spectrum for 3″-bromorubrolide F (**2**; 700 MHz, CD_3OD)

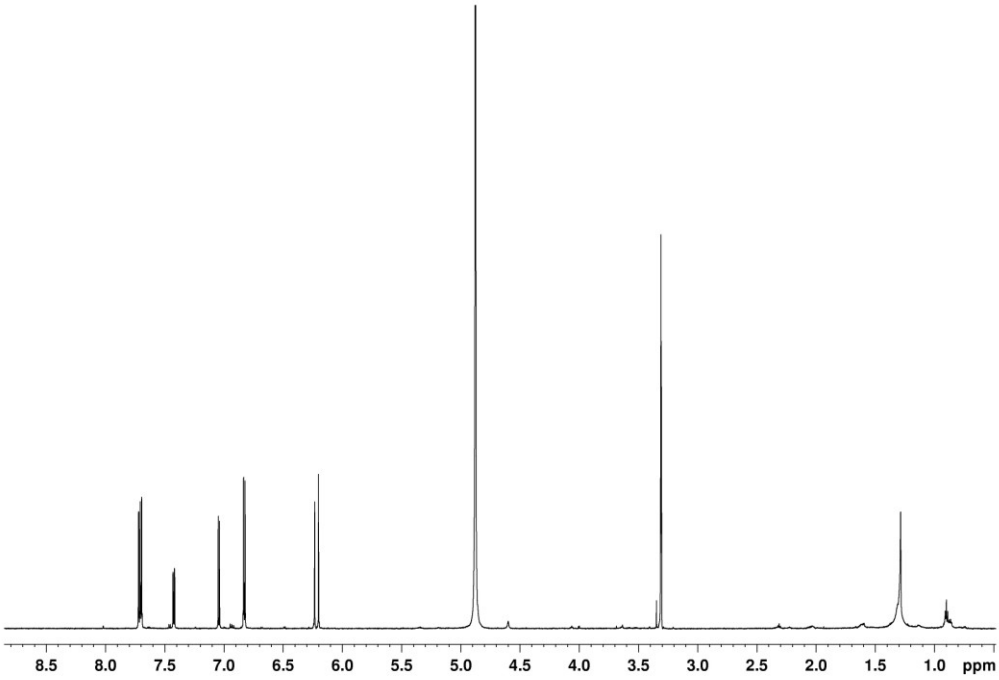

Figure 2.10 ^{1}H NMR spectrum for 3′-bromorubrolide E (**3**; 700 MHz, CD_3OD)

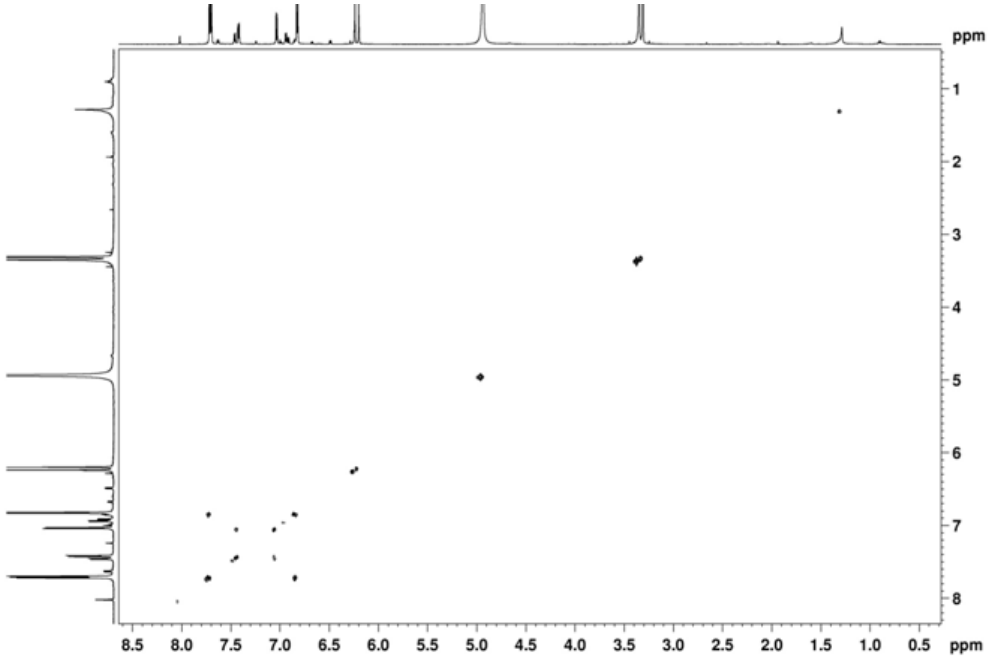

Figure 2.11 COSY spectrum for 3′-bromorubrolide E (**3**; 700 MHz, CD_3OD)

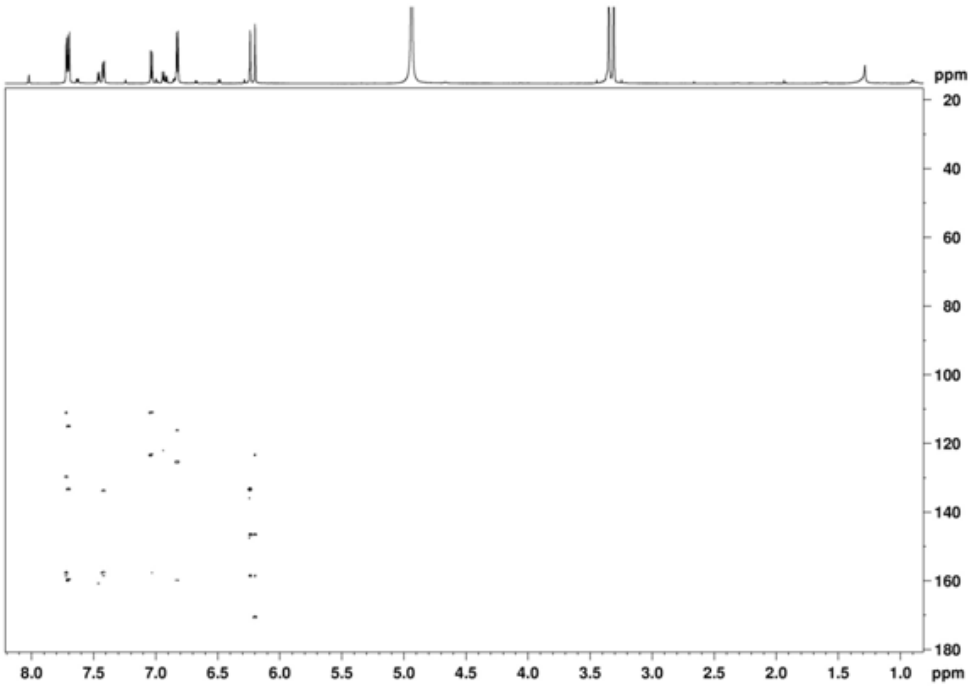

Figure 2.12 HMBC spectrum for 3′-bromorubrolide E (**3**; 700 MHz, CD_3OD)

The HRESIMS data for rubrolide **4** gave an $[M+H]^+$ ion cluster at *m/z* 373.0060/375.0048, for the same molecular formula of $C_{18}H_{14}O_4Br$ as that for **2**. Comparison of the ^1H chemical shifts for **3** and **4** showed a slight upfield shift for ring B ^1H resonances (H-2′, H-5′ and H-6) and a large downfield shift for ring C ^1H resonances (H-2″, H-5″ and H-6″, Table 2.3, Figure 2.13). The larger variations in δ_H values for ring C could be explained by methylation of OH-4″ in **3**, as confirmed by an HMBC correlation from a 3H singlet at δ 3.84 (H_3-7″) to the C-4″ resonance (δ_C 162.1). Therefore, the structure of rubrolide **4** was assigned as 4-(3-bromo-4-hydroxyphenyl)-5-(4-methoxybenzylidene)furan-2(5*H*)-one, and given the trivial name 3′-bromorubrolide F.

Rubrolide **5** has a molecular formula of $C_{17}H_9O_4Br_2$ as assigned from the $[M-H]^-$ 1:2:1 ion cluster at *m/z* 434.8873/436.8929/438.8940. Examination of the ^1H and COSY NMR data indicated that the ^1H shifts for ring B protons (H-2′, H-5′ and H-6′) were similar to those for ring B of 3′-bromorubrolide E (**3**, Table 2.3, Figures 2.14, 2.15). Additionally, COSY-coupled H-2″/H-6″ and H-5″/H-6″ established ring C as a 1, 3, 4-trisubstitued benzene. The assignment of quaternary C-3′ (δ_C 113.1) and C-3″ (δ_C 112.7), as deduced from HMBC (Figure 2.16) and COSY (Figure 2.15), localized bromine substituents at these positions. Thus, rubrolide **5** was assigned as 5-(3-bromo-4-hydroxybenzylidene)-4-(3-bromo-4-hydroxyphenyl)furan-2(5*H*)-one, and given the trivial name 3′,3″-dibromorubrolide E.

For new rubrolides **2**-**5**, determination of the C-5/C-6 double bond geometry relied on NOE data. NOEs between H-6 and both H-2′/H-6′ and H-2″/H-6″ (where one of the pair was always distinguishable) were observed, placing H-6 in close proximity to both phenyl rings and concluding a Z geometry of the exocyclic double bond (Pearce, et al., 2006).

Table 2.3. ^{1}H (700 MHz) and ^{13}C (175 MHz) NMR Data (CD_3OD) for Rubrolides **4** and **5**.

position	3′-Bromo-rubrolide F (**4**)		3′, 3″-Dibromorubrolide E (**5**)	
	δ_C	δ_H (*J* in Hz)	δ_C	δ_H (*J* in Hz)
2	171.5 (C)		171.5 (C)	
3	111.4 (CH)	6.16 (s)	111.7 (CH)	6.16 (s)
4	159.5 (C)		159.5 (C)	
5	147.8 (C)		147.5 (C)	
6	115.0 (CH)	6.31 (s)	114.7 (CH)	6.22 (s)
1′	121.3 (C)		122.3 (C)	
2′	134.1 (CH)	7.70 (d, 2.2)	134.4 (CH)	7.7 (d, 2.2)
3′	113.3 (C)		113.1 (C)	
4′	161.6 (C)		161.2 (C)	
5′	118.9 (CH)	6.94 (d, 8.3)	118.8 (C)	6.97 (d, 8.4)
6′	130.2 (CH)	7.38 (dd, 8.3, 2.2)	130.5 (CH)	7.39 (d, 8.4, 2.2)
1″	127.4 (C)		126.3 (C)	
2″	133.5 (CH)	7.79 (d, 8.6)	136.7 (CH)	8.03 (d, 2.1)
3″	115.2 (CH)	6.98 (d, 8.9)	112.7 (C)	
4″	162.1 (C)		159.6 (C)	
5″	115.2 (CH)	6.98 (d, 8.9)	118.3 (CH)	6.87 (d, 8.5)
6″	133.5 (CH)	7.79 (d, 8.6)	132.9 (CH)	7.59 (dd, 8.6, 2.2)
7″	55.8 (CH_3)	3.84 (s)		

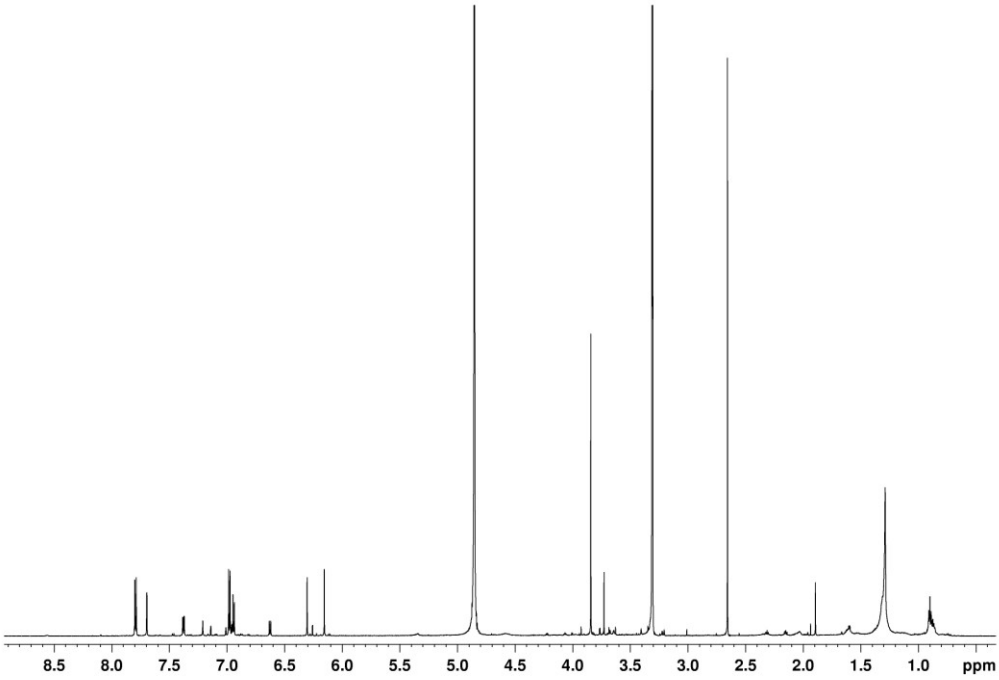

Figure 2.13 ^{1}H NMR spectrum for 3′-bromo-rubrolide F (**4**; 700 MHz, CD_3OD)

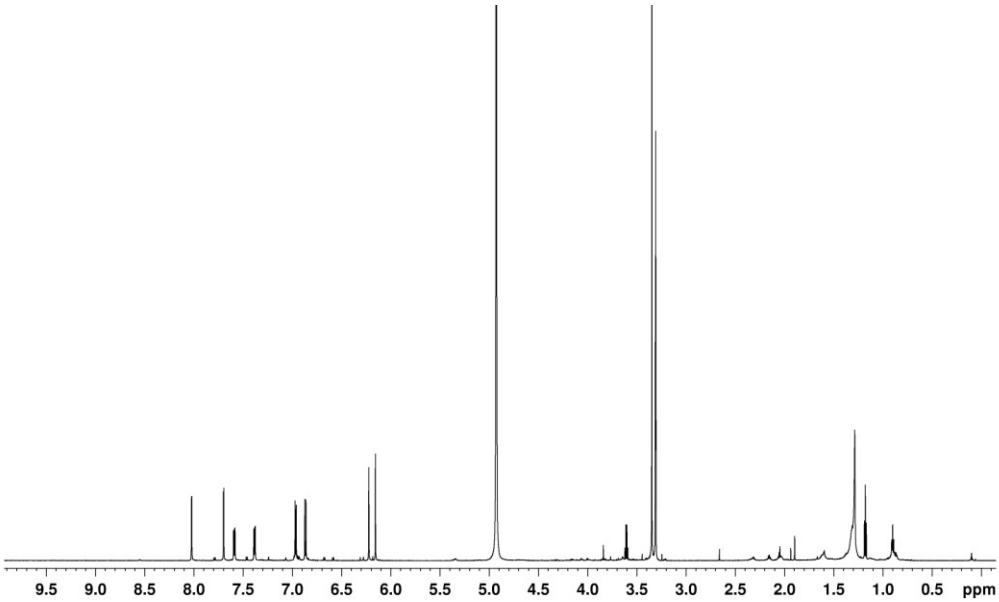

Figure 2.14 ^{1}H NMR spectrum for 3′, 3″-dibromorubrolide E (**5**; 700 MHz,

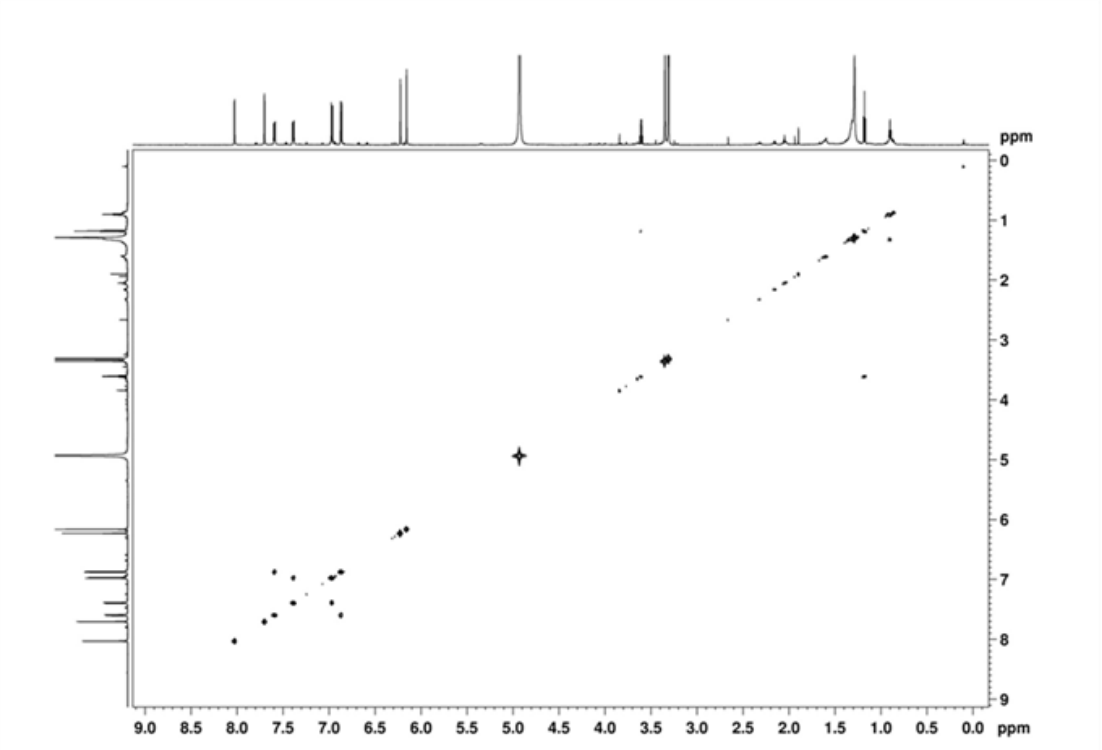

Figure 2.15 COSY spectrum for 3′, 3″-dibromorubrolide E (**5**; 700 MHz, CD_3OD)

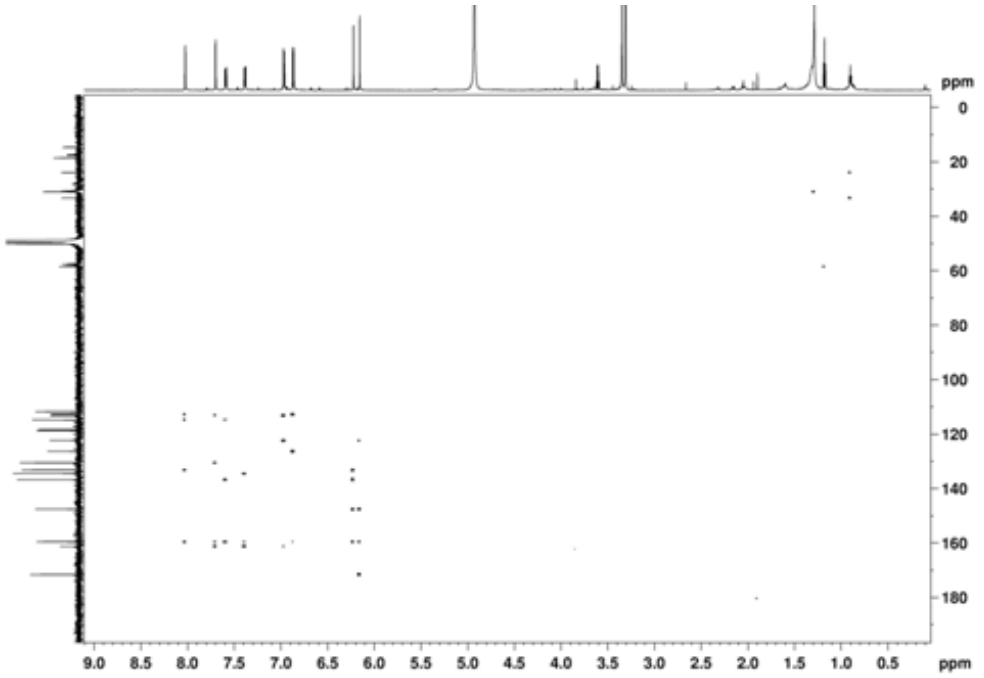

Figure 2.16 HMBC spectrum for 3′, 3″-dibromorubrolide E (**5**; 700 MHz, CD_3OD)

The HRESIMS data for compounds **6** and **7** suggested their identities as rubrolides E and F, respectively. 1D and 2D NMR data were acquired in methanol-d_4 for compound **6**, and readily confirmed its identity as rubrolide E, although previously reported data were acquired in $CDCl_3$ and DMSO-d_6 (Figures 2.17, 2.18), (Miao & Andersen, 1991). Our initially acquired NMR data in methanol-d_4 for compound **7** were consistent with previously published ^{1}H NMR data for rubrolide F (Figure 2.19), (Miao & Andersen, 1991). However, after additional purification of compound **7**, significant changes in ^{1}H shifts for the A and B rings were observed, while 2D NMR data provided the same rubrolide F structure as initially assigned (Figure 2.20). One explanation for this observation was the interconversion of **7** between phenoxy and phenol forms. The addition of NaOH to the NMR tube containing **7** caused a shift in ring A and B ^{1}H resonances, which was reversed after the addition of formic acid (Figures 2.21, 2.22). Although the addition of NaOH did not reproduce the exact chemical shifts previously reported (Miao & Andersen, 1991), or observed for the initially isolated natural product here, it could be concluded that rubrolide F was first isolated as a salt (other than Na^+) of the phenoxy (B-ring) anion in both cases. Our exhaustive separation performed under neutral conditions resulted in protonation to yield the phenol form.

Finally, we tested in vitro activities of rubrolides **2**-**5** as well as **6** and **7** against a panel of pathogenic bacteria including MRSA, *S. epidermidis*, gentamycin and vancomycin resistant *Enterococcus faecalis* and *Escherichia coli*, (Table 2.4, p. 60). Overall, 3′-bromo-rubrolide F (**4**) and rubrolide F (**7**) showed significantly higher IC_{50} values and a lower percentage of growth inhibition than their non-methylated analogues. This trend was previously observed for synthetic rubrolide analogues tested against NCI-H460, MCF-7 and SF-268 cell lines (Bellina, et al., 2003), and may indicate a differential cell permeability.

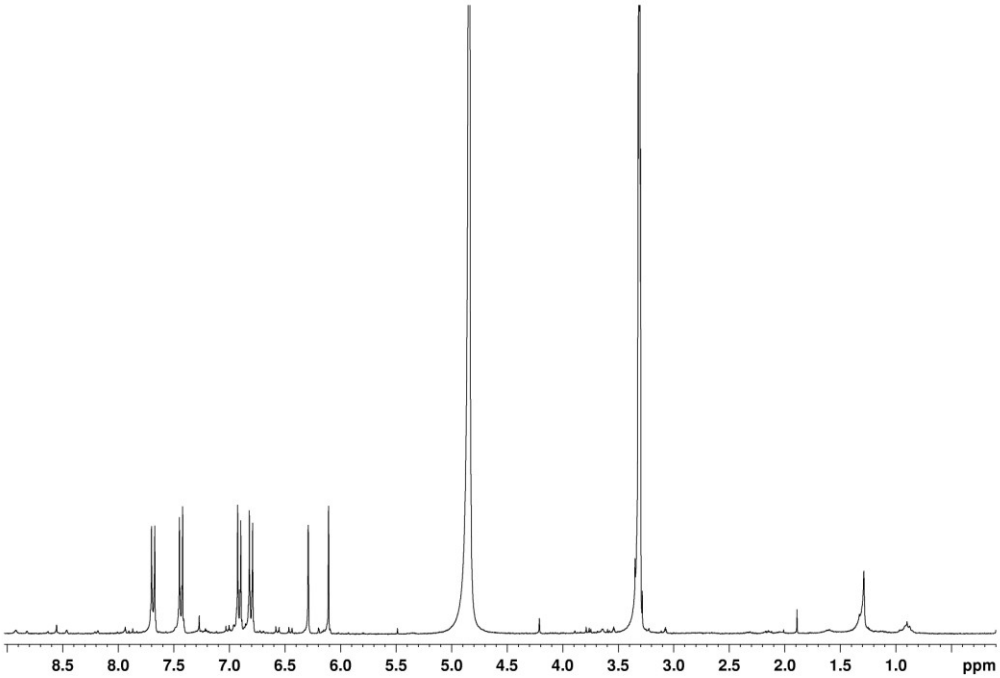

Figure 2.17 ^{1}H NMR spectrum for rubrolide E (**6**; 300 MHz, CD_3OD)

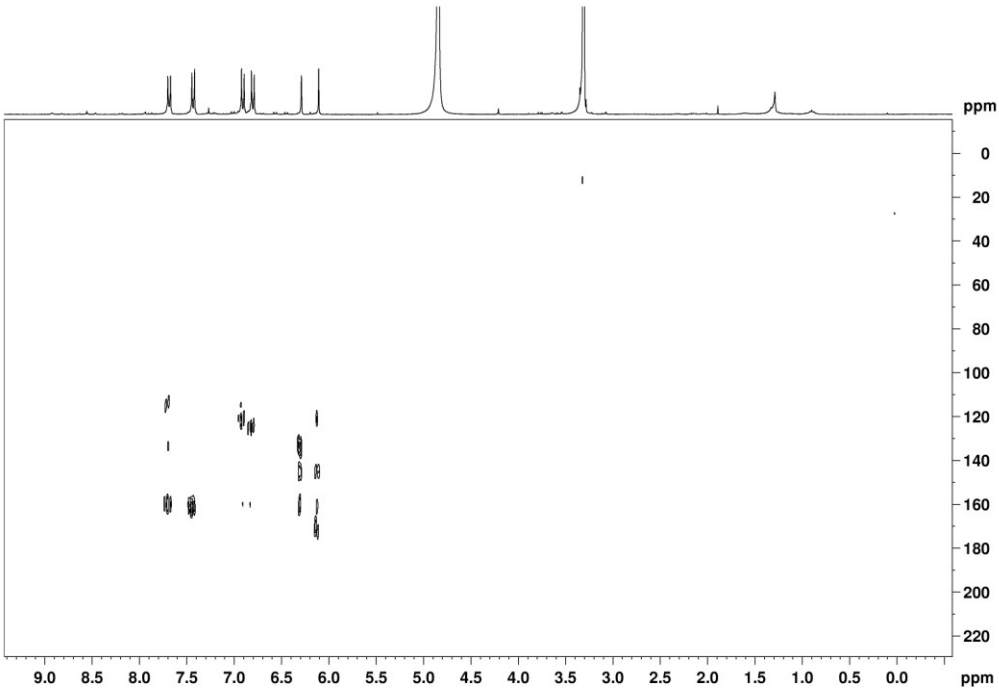

Figure 2.18 HMBC NMR spectrum for rubrolide E (**6**; 300 MHz, CD_3OD)

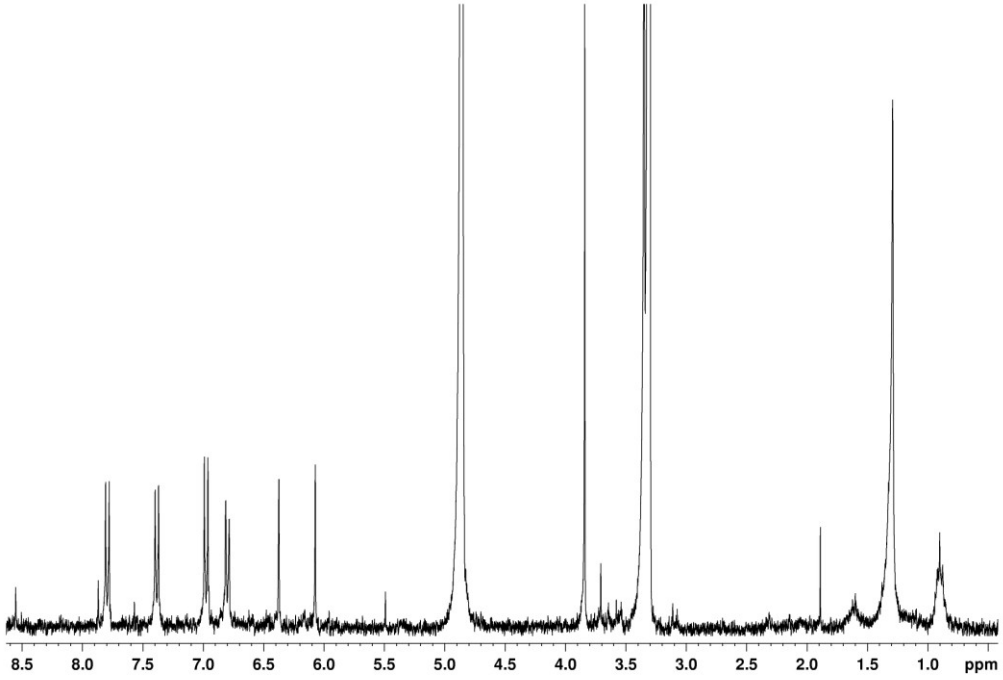

Figure 2.19 ^{1}H NMR spectrum for rubrolide F (**7**; 300 MHz, CD_3OD)

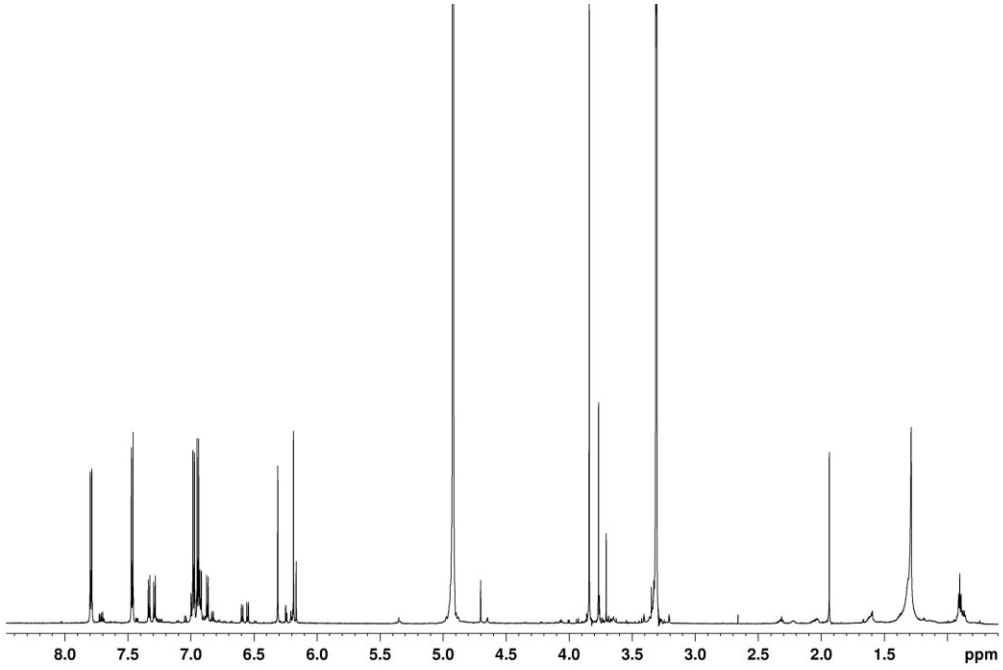

Figure 2.20 ^{1}H NMR spectrum for rubrolide F (**7**; 700 MHz, CD_3OD)

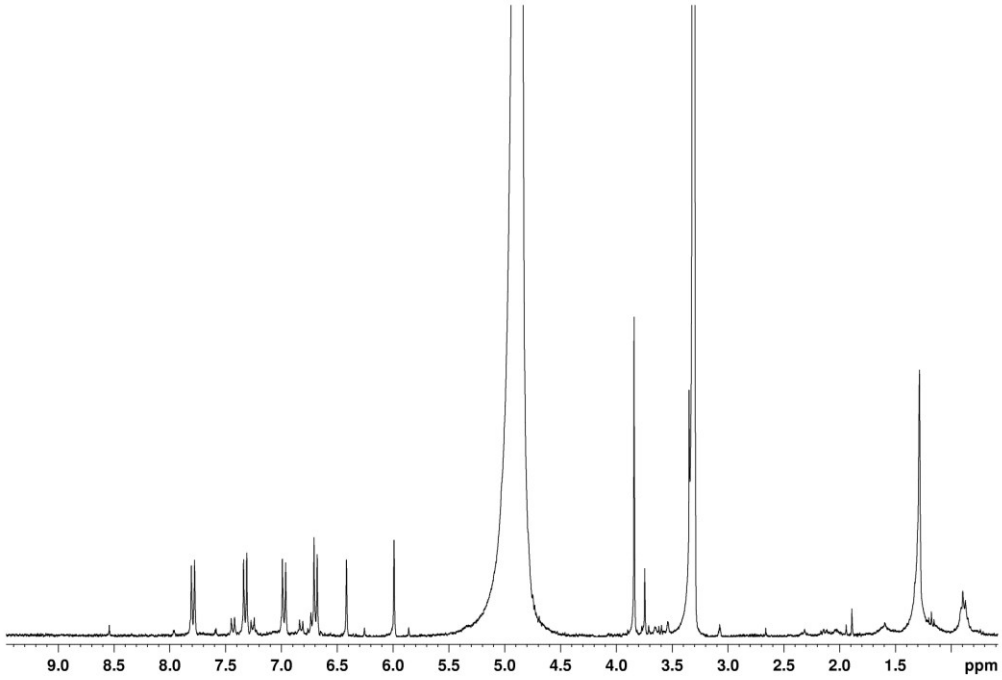

Figure 2.21 ^{1}H NMR spectrum for rubrolide F + NaOH (**7**; 300 MHz, CD_3OD)

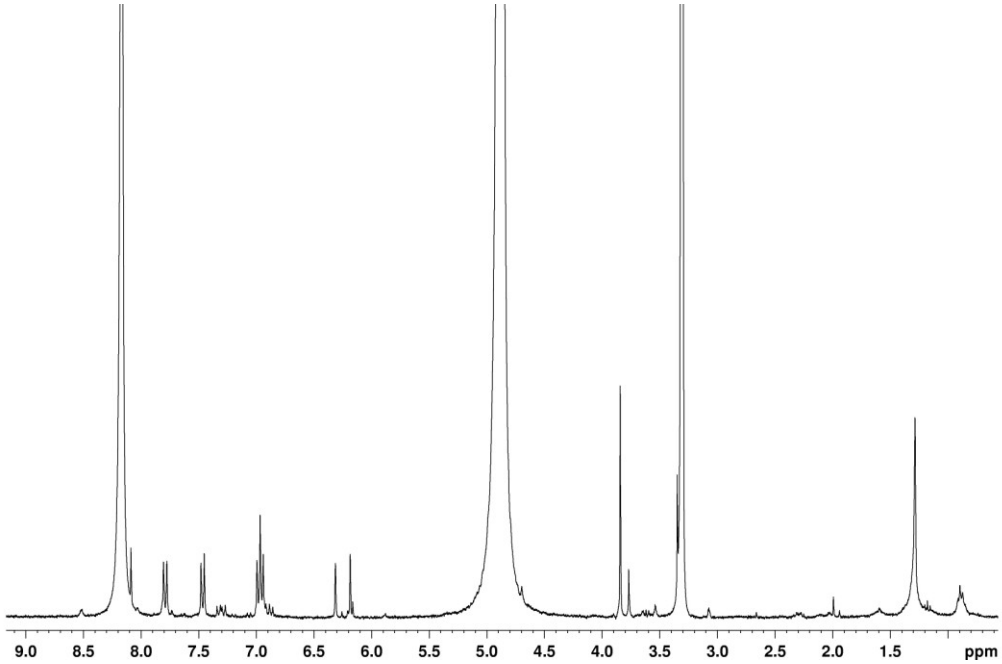

Figure 2.22 ^{1}H NMR spectrum for rubrolide F + NaOH + HCOOH (**7**; 300 MHz, CD_3OD)

Table 2.4 Antibacterial Properties of Rubrolides **2**-**5**, **6** and **7**.
Chloramphenicol was tested at 30 μg/mL as a positive control, and caused 100 % growth inhibition of all analyzed strains.

Compound	*S. aureus* (MRSA)	*S. epidermidis*	*E. faecalis*	*E. coli*
	IC_{50} μM	IC_{50} μM	Percentage of growth inhibition at 100 μg/mL	
3″-Bromorubrolide F (**2**)	256	98	43	22
3′-Bromorubrolide E (**3**)	82	38	16	0
3′-Bromo-rubrolide F (**4**)	360	42	2	14
3′, 3″-Dibromorubrolide E (**5**)	89	28	2	25
Rubrolide E (**6**)	105	21	89	16
Rubrolide F (**7**)	1006	79	47	15

Inspection of the ^{1}H NMR spectra for extract ARC-11-01 from an unidentified Antarctic tunicate suggested the presence of interesting chemical entities. Successive fractionation by RP_{18}-SPE followed by RP_{18}-HPLC led to the isolation of a metabolite having the same chemical shifts as those published for opuntioside III and tetillapyrone (Figure 2.23). However, a discrepancy between the HRESIMS data for our isolated compounds and the molecular formula reported for the previously published structures prompted us to revise the structures of opuntioside III (Qiu Y.K. et al., 2007) and tetillapyrone (Wattanadilok R et al., 2007).

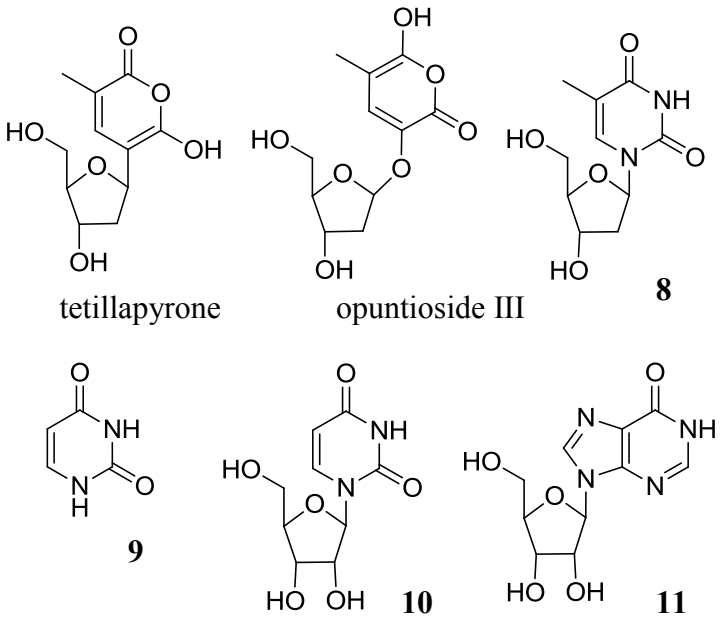

Figure 2.23 Chemical structures of tetillapurone, opuntioside III, thymidine (**8**), uracil (**9**), uridine (**10**), inosine (**11**).

The HRESIMS data for the first of the metabolites we isolated (**8**) indicated a molecular formula of $C_{10}H_{13}N_2O_5$ for an $[M-H]^-$ ion at *m/z* 241.0857, and implied 5 degrees of unsaturation. Analysis of ^{1}H and ^{13}C NMR spectra revealed the presence of four deshielded carbons (δ_C 166.6, 152.5, 138.4, 111.7) and one deshielded proton (δ_H 7.83), suggesting a highly substituted aromatic ring. Five midfield ^{13}C resonances (δ_C

89.0, 86.5, 72.4, 63.0, 41.3) and seven protons coupled in one spin system (δ_H 6.29, 4.40, 3.91, 3.79, 3.73, 2.23, 2.22) were consistent with a carbohydrate. The COSY spectrum showed that the monosaccharide is dehydroxylated at the 2′ position, while HMBC correlations indicated its cyclization between C-1′ and C-4′, with C-1′ additionally connected to the aromatic moiety. Comparison of MS and NMR data for **8** in CD_3OD and DMSO with those of known compounds suggested that isolated compound is the primary metabolite thymidine (Figure 2.24). Since the NMR data for previously published tetillapurone and opuntioside III were also consistent with the structure of thymidine and no low- or high-resolution mass spectrometric data were provided in these publications, we conclude that the compounds reported as tetillapurone and opuntioside III (Qiu Y.K., et al., 2007) are identical to thymidine.

The $[M-H]^-$ ions at *m/z* 111.0200, 243.0652 and 267.0763 for compounds **9-11**, respectively, provided their molecular formulae of $C_4H_3N_2O_2$, $C_9H_{11}N_2O_6$ and $C_{10}H_{11}N_4O_5$, respectively. Comparison of ^1H and ^{13}C NMR chemical shift values with those reported for known nucleotides proved that these isolated metabolites are uracil (**9**), uridine (**10**) and inosine (**11**), Figure 2.23.

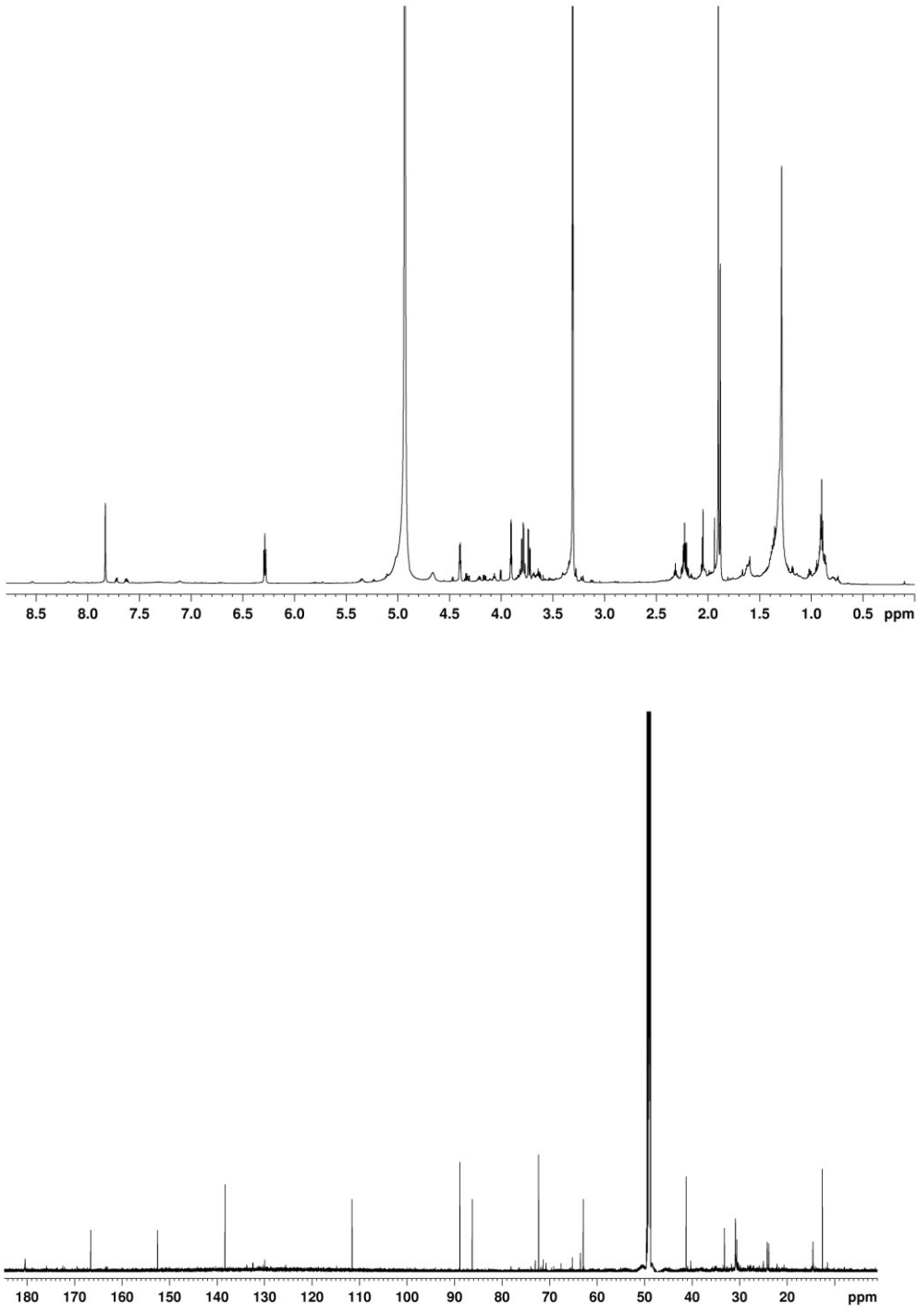

Figure 2.24 ^{1}H and ^{13}C NMR spectra for thymidine (**8**; 700 MHz, CD_3OD)

Experimental

General Experimental Procedures

UV spectra were measured on a JASCO J-815 CD spectrometer. The NMR spectra were referenced to internal residual protonated solvent signals in ppm (^{1}H NMR: CH_3OD, 3.31; ^{13}C NMR: CH_3OD, 49.15). LRESIMS data were acquired on a Thermo Finnigan LCQ Advantage spectrometer, while HRESIMS data were acquired on Water's Micromass LCT Premier and AB SCIEX Triple TOF 5600 spectrometers.

Tunicate Collection and Taxonomy

South African tunicate material was collected in July 2004 by hand using SCUBA at depths of 15-20 m from White Sands Reef in Algoa Bay, Eastern Cape Province, South Africa (33:59.916S, 25:42.573W). Voucher samples are maintained at the South African Institute for Aquatic Biodiversity (SAIAB), South Africa. Antarctic tunicates were collected in Maxwell Bay of King George Island, at a depth of 20 feet.

***Synoicum globosum* Parker-Nance sp. nov taxonomy.** A descriptive synopsis of the new species *Synoicum globosum* Parker-Nance sp. nov. (Ascidiacea, Aplousobranchia) relative to known congeners and a detailed morphological description with figures are provided in the Supporting Information of (Sikorska et al., 2012). In summary, colonies are gelatinous but firm and consist of egg-shaped heads on a short cone-shaped stalk with irregular basal mass. Externally, the surface of the head is free of sand, although a dense accumulation of fine sand particles is visible in the surface layer of the stalk and the wider irregular basal attachment mass is heavily encrusted with larger sand particles and epifauna. Zooids are red and arranged in circular systems clearly distinguishable against the mustard yellow test material of freshly collected material. The internal test is transparent with fine sand, shell pieces, as well as other foreign material that decreases in density towards the central part of the colony. The slender zooids (8-20 mm) are closely packed together in a distinct layer, and comprise a thorax (1.0-2.7 mm), abdomen (0.9-2.0 mm) and posterior abdomen (6.0-14.8 mm). The branchial opening has six small lobes and the atrial

opening is small with a single ribbon-like tongue with small distal teeth. The branchial sac has 11-14 rows of stigmata with 10-11 stigmata in each of the rows. One to two larvae are present in developmental sequence in the atrial cavity. Mature larvae (trunk 0.56-0.66 mm in length and 0.14-0.40 mm in width) have 12 or more lateral ampullae arranged in 2-3 rows with epidermal vesicles present dorsally and ventrally and tail wound about halfway around the trunk.

Extraction and Isolation Procedures

The lyophilized organisms were extracted exhaustively with CH_2Cl_2-MeOH 2:1 and SAF04-29, -38, -44, -48, -51, -53, -55, -56, -59, -61 and -71 were subjected to Sephadex LH-20 with 75 % MeOH-CH_2Cl_2 followed by RP_{18}-SPE using a stepped gradient of 50-100% MeOH-H_2O. In the case of extracts SAF04-31, -45, -54, -65, -68, and ARC-11-01, direct RP_{18}-SPE was performed using a stepped gradient of 50-100% MeOH-H_2O, 100% acetone, 100% ethyl acetate, 100% CH_2Cl_2. The 50% MeOH-H_2O fractions of SAF04-59 and SAF04-56 were further purified by RP_{18}-HPLC (column: Phenomenex Synergi Hydro-RP, 250 mm x 4.6 mm, 100% H_2O) resulting in the isolation of homarine (3.0 mg). The 75% MeOH-H_2O and 100% MeOH fractions from SAF04-54 were subsequently separated by RP_{18}-HPLC (column: Phenomenex Synergi Fusion-RP, 250 mm x 10 mm, 65% MeOH-H_2O) to yield rubrolides E (13.5 mg), F (4.3 mg), P (3.0 mg), Q (7.4 mg), R (2.8 mg) and S (1.4 mg). The 50% MeOH-H_2O fraction from the ARC-11-01 extract was separated by RP-HPLC first on a Phenomenex Synergi Fusion-RP column (250 mm x 10 mm, 10 % MeOH-H_2O), and then on a Phenomenex Luna Hilic column (250 mm x 4.6 mm, 100 % MeCN). This resulted in the isolation of homarine (0.8 mg), uracil (1.8 mg), uridine (0.5 mg), inosine (0.9 mg), thymidine (1.3 mg).

Cell Viability Assays. Cytotoxicity of the organic extract and crude fractions was evaluated in mouse Neuro-2A neuroblastoma cancer cells (ATCC, Manassas, VA) using a previously described protocol subjected to slight modifications (Thornburg et al., 2011). Cells were seeded into 96-well plates (25,000 cells per well)

in 50 μL of medium twelve hours before treatment. Each test sample was added in a 25 μL aliquot generated by serial dilution in serum-free medium on the day of the experiment, after prior removal of 25 μL of media from the treated well. Aliquots were generated from stock solutions of 6 mg/mL compound in 100% DMSO. The cytotoxicity of extracts was evaluated after 24 h treatment. Each extracts was tested at final concentrations of 30 μg/mL. In all cases, cell viability was determined using a standard 3-(4,5-dimethylthiazol-2-yl)-2,5,diphenyl tetrazolium bromide (MTT) assay (Thornburg, et al., 2011). The cytotoxicity of each extract was assessed in at least three independent cultures with the viability of vehicle-treated control cells defined as 100% in all experiments.

Antibacterial Assay. Antibacterial activity was determined using the microtiter dilution method in a 96-well plate format (Smith et al., 2008). Crude extracts were tested at 125, 12.5, and 1.25 μg/mL against a panel of clinically-relevant human pathogens including methicillin-resistant *Staphylococcus aureus* (ATCC® BAA-1720™), *Staphylococcus epidermidis* (ATCC® 35984™), gentamycin and vancomycin resistant *Enterococcus faecalis* (ATCC® 700802™), *Escherichia coli* (O157:H7) (Sikora et al., 2009), *Vibro cholerae* (N16961, wild type El Tor biotype), and *Pseudomonas aeruginosa* (PAO) to determine the appropriate concentration range for testing of pure rubrolides. Bacterial strains were cultured as follows: MRSA and *S. epidermidis* in tryptic soy broth (Becton, Dickinson and Co.), *E. faecalis* in brain heart infusion medium (Becton, Dickinson and Co.), and all Gram-negative bacteria in Luria-Bertani liquid medium (Becton, Dickinson and Co). For all experiments, the cultures were inoculated with 5×10^5 cfu/mL in a final volume of 200 μL in 96-well tissue culture-treated microtiter plates (Greiner Bio-One) and incubated without shaking at 37 °C for 16 h, at which point bacterial growth was determined turbidimetrically (OD_{600}) using a *BioTek Synergy* HT multimode plate reader. Each microtiter plate contained a positive control (chloramphenicol at a final concentration of 30 μg/mL), a negative control (bacteria grown in the presence of DMSO), and a contamination control (medium only). IC_{50} values for rubrolides **2**-**7** were determined

against MRSA and *S. epidermidis* as described above, using a concentration range of 130 - 0.3 μg/mL. Additionally, the susceptibility of *E. faecalis* and *E. coli* to pure compounds was tested at 100 μg/mL. Test samples were inoculated in technical duplicate on each plate and assays were performed in biological triplicate. Percentage growth inhibition was determined using the plate-based microtiter dilution assay, and IC_{50} values were derived using nonlinear regression analysis.

Homarine (**1**) white amorphous solid; ^{1}H NMR (700 MHz, CD_3OD) 8.75 (1H, d, J = 6.6 Hz, H-6), 8.52 (1H, t, J = 7.7 Hz, H-4), 8.08 (1H, d, J = 7.7 Hz, H-3), 7.93 (1H, d, J = 7.1 Hz, H-5), 4.24 (1H, s, H-1′); ^{13}C NMR (175 MHz, CD_3OD) 165.6 (C, C-1), 155.6 (C, C-2), 147.2 (CH, C-4), 146.6 (CH, C-6), 127.6 (CH, C-3), 127.6 (CH, C-5), 47.6 (CH_3, C-1′); LRMS *m/z* 296.9 [2M+Na^+].

3″-Bromorubrolide F (**2**). Yellow amorphous solid; UV (MeOH) λ_{max} (log ε) 248 (3.8), 356 (4.0) nm; HRESIMS $[M+H]^+$ (50%) *m/z* 373.0081, (calcd for $C_{18}H_{14}O_4{}^{79}Br$, 373.0075), $[M+H]^+$ (50%) *m/z* 375.0070, (calcd for $C_{18}H_{14}O_4{}^{81}Br$, 375.0055); ^{1}H and HSQC, HMBC, NOESY (Table 2.2, Figures 2.6-2.9).

3′-Bromorubrolide E (**3**). Yellow amorphous solid; UV (MeOH) λ_{max} (log ε) 250 (4.1), 371 (4.3) nm; HRESIMS $[M+H]^+$ (50%) *m/z* 358.9933, (calcd for $C_{17}H_{12}O_4{}^{79}Br$, 358.9919), $[M+H]^+$ (50%) *m/z* 360.9916, (calcd for $C_{17}H_{12}O_4{}^{81}Br$, 360.9898; ^{1}H and ^{13}C NMR, COSY, HMBC, NOESY (Table 2.2, Figures 2.10-2.12).

3′-Bromo-rubrolide F (**4**). Yellow amorphous solid; UV (MeOH) λ_{max} (log ε) 248 (3.8), 365 (3.9) nm; HRESIMS $[M+H]^+$ (50%) *m/z* 373.0060, (calcd for $C_{18}H_{13}O_4{}^{79}Br$, 373.0051), $[M+H]^+$ (50%) *m/z* 375.0048, (calcd for $C_{18}H_{14}O_4{}^{81}Br$, 375.0055); ^{1}H and COSY, HMBC, NOESY (Table 2.3, Figure 2.13).

3′, 3″-Dibromorubrolide E (**5**). Yellow amorphous solid; UV (MeOH) λ_{max} (log ε) 254 (4.0), 366 (4.1), 444 (3.6) nm; HRESIMS $[M-H]^-$ (25%) *m/z* 434.8872, (calcd for $C_{17}H_9O_4{}^{79}Br_2$, 434.8868), $[M-H]^-$ (50%) *m/z* 436.8853, (calcd for

$C_{17}H_9O_4{}^{79}Br{}^{81}Br$, 436.8847), $[M-H]^-$ (25%) *m/z* 438.8835, (calcd for $C_{17}H_9O_4{}^{81}Br_2$, 438.8827); ^1H and ^{13}C NMR, COSY, HMBC, NOESY (Table 2.3, Figures 2.14-2.16).

Rubrolide E (6). Yellow amorphous solid; UV (MeOH) λ_{max} (log ε) 226 (3.9), 247 (3.9), 368 (4.0) nm; HRESIMS $[M+H]^+$ *m/z* 281.0821 (calcd for $C_{17}H_{13}O_4$, 281.0814); ^1H NMR (400 MHz, CD_3OD) 7.69 (2H, d, *J* = 8.8 Hz, H-2″, H-6″), 7.44 (2H, d, *J* = 8.6 Hz, H-2′, H-6′), 6.91 (2H, d, *J* = 8.5 Hz, H-3′, H-5′) 6.81 (2H, d, *J* = 8.8 Hz, H-2″, H-6″), 6.30 (1H, s, H-5), 6.11 (1H, s, H-2); ^{13}C NMR (100 MHz, CD_3OD) 171.5 (C, C-1), 161.0 (C, C-3), 159.7 (C, C-4′, C-4″), 145.0 (C, C-4), 133.7 (CH, C-2″, C-6″), 131.2 (CH, C-2′, C-6′), 126.5 (CH, C-3″, C-5″), 125.0 (C, C-1″), 120.6 (C, C-1′), 117.2 (CH, C-3′, C-5′), 115.9 (CH, C-5), 110.7 (CH, C-2).

Rubrolide F (**7**). Yellow amorphous solid; UV (MeOH) λ_{max} (log ε) 248 (3.8), 356 (4.0) nm; HRESIMS $[M+H]^+$ *m/z* 295.0985, (calcd for $C_{18}H_{15}O_4$, 295.0970); ^1H NMR (700 MHz, CD_3OD) 7.80 (2H, d, *J* = 9.2 Hz, H-2″, H-6″), 7.47 (2H, d, *J* = 8.5 Hz, H-2′, H-6′), 6.98 (2H, d, *J* = 8.9 Hz, H-3″, H-5″), 6.95 (2H, d, *J* = 8.5 Hz, H-3′, H-5′), 6.31 (1H, s, H-5), 6.19 (1H, d, *J* = 0.6Hz, H-2), 3.85 (1H, s, H-7″), ^{13}C NMR (175 MHz, CD_3OD) 171.4 (C, C-1) 162.1 (C, C-4″), 161.4 (C, C-4′), 160.6 (C, C-3), 147.9 (C, C-4), 133.7 (2C, CH, C-2″, C-6″), 131.3 (2C, CH, C-2′, C-6′), 127.2 (C, C-1″), 122.7 (C, C-1′), 116.8 (2C, CH, C-3′, C-5′), 115.1 (2C, CH, C-3″, C-5″), 114.9 (CH, C-2), 112.0 (CH, C-5), 55.5 (CH_3, C-7″).

Thymidine (**8**). white amorphous solid; HRESIMS $[M-H]^-$ *m/z* 241.0857, (calcd for $C_{10}H_{13}N_2O_5$, 241.0830); ^1H NMR (700 MHz, CD_3OD) 7.83 (1H, d, *J* = 1.0Hz, H-6), 6.29 (1H, dd, *J* = 7.3, 6.4 Hz, H-1′), 4.40 (1H, dt, *J* = 6.3, 3.3 Hz, H-3′), 3.91 (1H, dt, *J* = 3.5, 3.5 Hz, H-4′), 3.79 (1H, dd, *J* = 12.2, 3.2 Hz, H-5b′), 3.73 (1H, dd, *J* = 12.1, 3.6 Hz, H-5a′), 2.22 (2H, m, H-2′), 1.88 (3H, d, *J* = 1.1 Hz, H-7); ^{13}C NMR (175 MHz, CD_3OD) 166.6 (C, C-4), 152.5 (C, C-2), 138.4 (CH, C-6), 111.7 (C, C-5), 89.0 (CH, C-4′), 86.5 (CH, C-1′), 72.4 (CH, C-3′), 63.0 (CH_2, C-5′), 41.3 (CH_2, 2′), 12.7 (CH_3, C-7); ^1H NMR (700 MHz, DMSO) 11.27 (1H, s, NH), 7.71 (1H, d, *J* = 1.3Hz,

H-6), 6.17 (1H, dd, *J* = 7.5, 6.3 Hz, H-1′), 5.25 (1H, d, *J* = 4.1 Hz, OH-3′), 5.04, (1H, t, *J* = 5.2 Hz, OH-5′), 4.24 (1H, dt, *J* = 6.3, 3.5 Hz, H-3′), 3.77 (1H, dt, *J* = 3.7, 3.7 Hz, H-4′), 3.60 (1H, m, H-5b′), 3.55 (1H, m, H-5a′), 2.08 (2H, m, H-2′), 1.78 (3H, d, *J* = 1.1Hz, H-7).

Uracil (**9**). white amorphous solid; HRESIMS $[M-H]^-$ *m/z* 111.0200, (calcd for $C_4H_3N_2O_2$, 111.0200); ^{1}H NMR (700 MHz, DMSO) 10.99 (1H, br s, NH), 10.85 (1H, br s, NH), 7.40 (1H, d, 7.5 Hz, H-6), 5.45 (1H, d, *J* = 7.7 Hz, H-5); ^{13}C NMR (175 MHz, DMSO) 164.8 (C, C-4), 152.0 (C, C-2), 142.7 (CH, C-6), 100.7 (CH, C-5).

Uridine (**10**). white amorphous solid; HRESIMS $[M-H]^-$ *m/z* 243.0652, (calcd for $C_9H_{11}N_2O_6$, 243.0623); ^{1}H NMR (700 MHz, CD_3OD) 8.01 (1H, d, *J* = 8.2 Hz, H-6), 5.90 (1H, d, *J* = 4.9 Hz, H-1′), 5.69 (1H, d, *J* = 8.0 Hz, H-5), 4.18 (1H, t *J* = 5.0 Hz, H-2′), 4.14 (1H, t *J* = 4.9 Hz, H-3′), 4.00 (1H, dt *J* = 4.9, 3.0 Hz, H-4′), 3.84 (1H, dd, *J* = 12.5, 2.7 Hz, H-5′), 3.84 (1H, dd, *J* = 12.3, 3.0 Hz, H-5′); ^{13}C NMR (175 MHz, CD_3OD) 166.8 (C, C-4), 152.6 (C, C-2), 142.9 (CH, C-6), 102.8 (CH, C-5), 90.8 (CH, C-1′), 86.5 (CH, C-4′), 75.9 (CH, C-2′), 71.5 (CH, C-3′), 62.4 (CH_2, C-5′).

Inosine (**11**). white amorphous solid; HRESIMS $[M-H]^-$ *m/z* 267.0763, (calcd for $C_{10}H_{11}N_4O_5$, 267.0735); ^{1}H NMR (700 MHz, CD_3OD); ^{13}C NMR (175 MHz, CD_3OD).

Bibliography

Bellina, F., Anselmi, C., Martina, F., & Rossi, R. (2003). Mucochloric Acid: A Useful Synthon for the Selective Synthesis of 4-Aryl-3-chloro-2(5H)-furanones, (Z)-4-Aryl-5-[1-(aryl)methylidene]-3-chloro-2(5H)-furanones and 3,4-Diaryl-2(5H)-furanones. . *Eur. J. Org. Chem. , 12*, 2290-2302.

Bellina, F., Anselmi, C., Viel, S., Mannina, L., & Rossi, R. (2001). Selective synthesis of (Z)-4-aryl-5-[1-(aryl)methylidene]-3-bromo-2(5H)-furanones. . *Tetrahedron, 57*(50), 9997-10007.

Caufield, C. E., Antane, S. A., Morris, K. M., Naughton, S. M., Quagliato, D. A., Andrae, P. M., Enos, A., & Chiarello, J. F. (2009). USA Patent No. US 7,495,027 B2. U. S. P. Office.

Dobson, C. M. (2004). Chemical space and biology. *Nature, 432*(7019), 824-828.

Johnson, T. A., Sohn, J., Inman, W. D., Estee, S. A., Loveridge, S. T., Vervoort, H. C., Tenney, K., Liu, J., Ang, K. K.-H., Ratnam, J., Bray, W. M., Gassner, N. C., Shen, Y. Y., Lokey, R. S., McKerrow, J. H., Boundy-Mills, K., Nukanto, A., Kanti, A., Julistiono, H., Kardono, L. B. S., Bjeldanes, L. F., & Crews, P. (2011). Natural Product Libraries to Accelerate the High-Throughput Discovery of Therapeutic Leads. *J. Nat. Prod., 74*(12), 2545-2555.

Lachance, H., Wetzel, S., Kumar, K., & Waldmann, H. (2012). Charting, Navigating, and Populating Natural Product Chemical Space for Drug Discovery. *J. Med. Chem.*

Landers, P. (2004). Drug Industry's Big Push Into Technology Falls Short. *Wall St. J.*

Manzanaro, S., Salvá, J., & de la Fuente, J. Á. (2006). Phenolic Marine Natural Products as Aldose Reductase Inhibitors. *J. Nat. Prod., 69*(10), 1485-1487.

Miao, S., & Andersen, R. J. (1991). Rubrolides A-H, metabolites of the colonial tunicate *Ritterella rubra*. *J. Org. Chem., 56*(22), 6275-6280.

Newman, D. J., & Cragg, G. M. (2012). Natural Products As Sources of New Drugs over the 30 Years from 1981 to 2010. *J. Nat. Prod., 75*(3), 311-335.

Ortega, M. a. J., Zubía, E., Ocaña, J. M., Naranjo, S., & Salvá, J. (2000). New Rubrolides from the Ascidian *Synoicum blochmanni*. *Tetrahedron 56*(24), 3963-3967.

Pearce, A. N., Chia, E. W., Berridge, M. V., Maas, E. W., Page, M. J., Webb, V. L., Harper, J. L., & Copp, B. R. (2006). E/Z-Rubrolide O, an Anti-inflammatory Halogenated Furanone from the New Zealand Ascidian Synoicum n. sp. *J. Nat. Prod., 70*(1), 111-113.

Pearce, A. N., Chia, E. W., Berridge, M. V., Maas, E. W., Page, M. J., Webb, V. L., Harper, J. L., & Copp, B. R. (2006). E/Z-Rubrolide O, an Anti-inflammatory Halogenated Furanone from the New Zealand Ascidian *Synoicum* n. sp. . *J. Nat. Prod., 70*(1), 111-113.

Qiu Y.K., Zhao Y.Y., Dou de Q., Xu B.X., & Liu K. (2007). Two new alpha-pyrones and other components from the cladodes of Opuntia dillenii. *Arch. Pharm. Res., 30*(6), 665-669.

Sikora, A. E., Beyhan, S., Bagdasarian, M., Yildiz, F. H., & Sandkvist, M. (2009). Cell Envelope Perturbation Induces Oxidative Stress and Changes in Iron Homeostasis in Vibrio cholerae. *J. Bacteriol., 191*(17), 5398-5408.

Sikorska, J., Parker-Nance, S., Davies-Coleman, M. T., Vining, O. B., Sikora, A. E., & McPhail, K. L. (2012). Antimicrobial Rubrolides P-S from a New South African Species of Synoicum Tunicate. *J. Nat. Prod., Submitted*.

Smith, S. M., Beattie, A. J., Gillings, M. R., Holley, M. P., Stow, A. J., Turnbull, C. L., Wilson, P. D., & Briscoe, D. A. (2008). An enhanced miniaturized assay for antimicrobial prospecting. *J. Microbiol. Methods 72*, 103-106.

Thornburg, C. C., Thimmaiah, M., Shaala, L. A., Hau, A. M., Malmo, J. M., Ishmael, J. E., Youssef, D. T. A., & McPhail, K. L. (2011). Cyclic Depsipeptides, Grassypeptolides D and E and Ibu-epidemethoxylyngbyastatin 3, from a Red Sea Leptolyngbya Cyanobacterium. *J. Nat. Prod., 74*(8), 1677-1685.

Wattanadilok R, Sawangwong P, Rodrigues C, Cidade H , Pinto M , Pinto E , Silva A, & Kijjoa A. (2007). Antifungal Activity Evaluation of the Constituents of Haliclona baeri and Haliclona cymaeformis, Collected from the Gulf of Thailand. *Mar. Drugs, 5*, 40-51.

MANDELALIDES A-D, CYTOTOXIC MACROLIDES FROM A NEW *LISSOCLINUM* SPECIES OF SOUTH AFRICAN TUNICATE.

CHAPTER THREE

Justyna Sikorska, Andrew M. Hau, Clemens Anklin, Shirley Parker-Nance,

Michael T. Davies-Coleman, Jane E. Ishmael, and Kerry L. McPhail

Journal of Organic Chemistry

2012, 77 (14), pp 6066–6075

DOI: 10.1021/jo3008622

Abstract

Mandelalides A-D are variously glycosylated, unusual polyketide macrolides isolated from a new species of *Lissoclinum* ascidian collected from South Africa, Algoa Bay near Port Elizabeth and the surrounding Nelson Mandela Metropole. Their planar structures were elucidated on sub-milligram samples by comprehensive analysis of 1D and 2D NMR data, supported by mass spectrometry. The assignment of relative configuration was accomplished by consideration of homonuclear and heteronuclear coupling constants in tandem with ROESY data. The absolute configuration was assigned for mandelalide A after chiral GC-MS analysis of the hydrolyzed monosaccharide (2-*O*-methyl-α-L-rhamnose) and consideration of ROESY correlations between the monosaccharide and aglycone in the intact natural product. The resultant absolute configuration of the mandelalide A macrolide was extrapolated to propose the absolute configurations of mandelalides B-D. Remarkably, mandelalide B contained the C-4′ epimeric 2-*O*-methyl-6-dehydro-α-L-talose. Mandelalides A and B showed potent cytotoxicity to human NCI-H460 lung cancer cells (IC_{50}, 12 and 44 nM, respectively) and mouse Neuro-2A neuroblastoma cells (IC_{50}, 29 and 84 nM, respectively).

Introduction

Over the last 50 years, ascidians have been shown to be a prolific source of natural products with promising biomedical potential (Blunt et al., 2012). Indeed, ascidian-derived natural products have yielded promising drug leads, among which ecteinascidin 743 (Yondelis®) and dehydrodidemnin B (Aplidin®) are in clinical use for the treatment of specific cancers (Fayette et al., 2006; Le Tourneau et al., 2007). The diverse chemotypes reported from *Lissoclinum* species collected globally have important biological properties that range from cancer cell toxicity to antifungal and antibacterial activities (Blunt, et al., 2012), and include peptides, alkaloids, chlorinated diterpenes, polyether amides, lactones, and macrolides such as haterumalide B (Ueda & Hu, 1999) and patellazoles B and C (Corley et al., 1988; Zabriskie et al., 1988). It has been noted that many secondary metabolites isolated from *Lissoclinum*, as well as other ascidian species, are present in bacteria, sponges and mollusks (Fu et al., 2004; Schupp et al., 2002; Tsukimoto et al., 2011). This diversity of ascidian metabolites can be explained by the fact that tunicates are often hosts to cyanobacterial and heterotrophic bacterial symbionts, as well as being fed upon by predatory mollusks (Fu, et al., 2004; Ogi et al., 2009; Schmidt et al., 2004; Tsukimoto, et al., 2011). Therefore, identification of the biogenetic origin of ascidian natural products is very often challenging (Schmidt et al., 2012). This is highlighted by the recent isolation of didemnin B (an analog of Aplidin®) from the α-proteobacterium *Tistrella mobilis* (Pearce et al., 2006; Tsukimoto, et al., 2011). Didemnin B was originally identified from the ascidian *Aplidium albicans*, and is biosynthetically similar to peptides from the marine cyanobacterium *Lyngbya majuscula* (now *Moorea producta*).

In our search for new potential anticancer compounds, we encountered the highly cytotoxic organic extract (IC_{50} = 0.7 μg/mL against NCI-H460 lung cancer cells) of a new *Lissoclinum* species from Algoa Bay, South Africa. Bioassay-guided fractionation of this extract, yielded a series of new macrolides, named mandelalides A-D (**1-4**), two of which were tested and show good cytotoxicity to mouse Neuro-2A neuroblastoma

and human NCI-H460 lung cancer cells. While the relative configuration of the compounds could be assigned from analysis of ROESY data in tandem with homonuclear ($^{3}J_{HH}$) and heteronuclear ($^{2,3}J_{CH}$) coupling constants, the assignment of absolute configuration relied on hydrolysis of the glycosylated mandelalide A and chiral GC-MS analysis of the released monosaccharide. Remarkably, mandelalide A contains 2-*O*-methyl-α-L-rhamnose, while mandelalide B contains the C-4′ epimer 2-*O*-methyl-6-dehydro-α-L-talose.

Results and Discussion

A new *Lissoclinum* ascidian species was collected from White Sands Reef in Algoa Bay, South Africa, in July 2004. The organic extract (1.45 g) was subjected to bioassay-guided fractionation through consecutive Sephadex LH-20 and RP_{18}-HPLC chromatography to yield mandelalides A-D (**1**-**4**), of which mandelalide D degraded to deacylmandelalide D (**4b**).

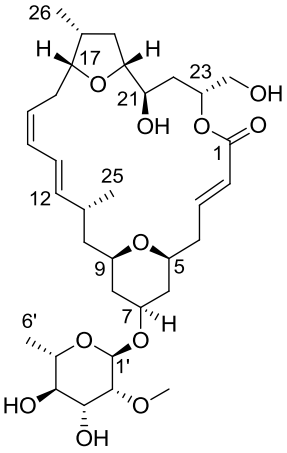

1

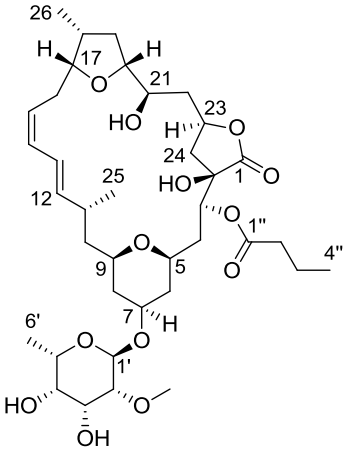

2

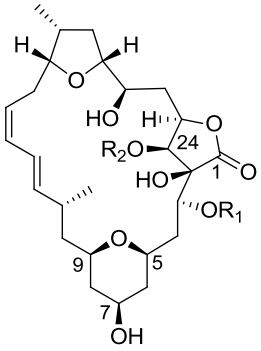

3 R_1 = $COCH_2CH_2CH_3$, R_2 = OH
4 R_1 = $COCH_2CH_2CH_3$, R_2 = $COCH_2CH_2CH_3$
4b R_1 = H, R_2 = H

The HRESIMS data for mandelalide A (**1**) gave an $[M+Na]^+$ ion at *m/z* 647.3394, which is consistent with a molecular formula of $C_{33}H_{52}O_{11}$, and implies 8 degrees of unsaturation. The ^{13}C and multiplicity-edited HSQC NMR spectra for compound **1** (Table 3.1, Figures 3.1-3.3) indicated the presence of an ester carbonyl (δ_C 167.4), fourteen sp^3 methines (δ_C 94.2–68.1, 37.3 and 34.2), twelve of which were oxygen-bearing, six olefinic methines (δ_C 147.1, 141.5, 131.3, 126.9, 123.9 and 123.1), eight methylenes (δ_C 66.1, 43.1, 39.7, 38.8, 37.6, 36.8, 34.1 and 31.1) and four methyl groups (δ_C 59.1, 18.3, 17.7 and 14.5). Interpretation of COSY and TOCSY correlations delineated two spin systems (Figures 3.5-3.6), one comprising 25 carbons

from C-2 to C-26 (Figure 3.4, fragment A), and the other of 6 carbons from C-1′ to C-6′ (Figure 3.4, fragment B). The acquisition of a semi-phase sensitive HMBC (Cicero et al., 2001) optimized for a 4 Hz coupling constant (Figure 3.7), revealed a correlation between δ_H 5.23 (H-23) and δ_C 167.4 (C-1) that indicated cyclization of fragment A into a 23-carbon macrolactone. The C-1 carbonyl also showed HMBC correlations from the olefinic H-2 and H-3 multiplets, for which a $^3J_{HH}$ of 15.5 Hz indicated an *E* double bond geometry. An HMBC correlation between H-9 (δ 3.32) and C-5 (δ 73.9) delineated a tetrahydropyran ring, while a correlation between H-17 (δ 3.98) and C-20 (δ 83.2) was consistent with a tetrahydrofuran ring, both within fragment A (Table 3.1, Figure 3.4). The four contiguous (TOCSY-coupled) olefinic methines CH-12 to CH-15 (δ_H 5.45, 6.28, 6.05 and 5.28 ppm) were consistent with a conjugated diene, situated β to the tetrahydrofuran and γ to the tetrahydropyran on the basis of HMBC correlations from H-15 to C-17 and H-12 to C-10, respectively. From homonuclear coupling constant values ($^3J_{HH}$ = 14.8 and 10.8 Hz, respectively) it was evident that the geometry of H-12 and H-13 is *trans*, while H-14 and H-15 are *cis*. Knowing that $^3J_{HH}$ values are not sufficiently characteristic to assign the orientation between H-13 and H-14, ROESY data were examined (Tanaka & Higa, 1996). ROEs between H-12 and H-10a, as well as between H-13 and H-16b, suggested an *anti* orientation for H-13 and H-14 (Figure 3.8). In the case of fragment B, the downfield shift of C-1′ (δ_C 94.2), the presence of four midfield oxymethine ^{13}C resonances, an upfield methyl doublet (CH_3-6′, δ_C 17.7, δ_H 1.27) and an HMBC correlation between H-1′ (δ 5.02) and C-5′ (δ 68.1) suggested that fragment B is a 6-dehydro monosaccharide. An HMBC correlation between H-2′ (δ 3.40) and deshielded methyl C-7′ (δ 59.1) indicated methylation of the C-2′ hydroxyl group. An HMBC correlation from H-7 (δ 3.82) to C-1′ placed the monosaccharide (fragment B) at C-7 of fragment A.

Table 3.1 NMR data at 700 MHz for mandelalide A (**1**) in $CDCl_3$

No.	δ_C (mult)	δ_H (mult, *J* in Hz)	COSY	HMBC	ROESY
1	167.4 (C)				
2	123.1(CH)	6.01 (dd, 15.5, 1.2)	3, 4a	1, 4	3[b], 4a, 4b, 5
3	147.1(CH)	6.97 (ddd, 15.2, 10.4,	2, 4a, 4b	1, 2, 4, 5	3[b], 4a[b], 4b[b], 5
4a	38.8(CH_2)	2.36 (m)	2, 3	2, 3, 5, 6	2, 3[b], 5[b], 6ax[b], 6eq
4b		2.39 (ddd, 14.1, 10.6,	3, 5	2, 3, 5, 6	2, 3[b], 5[b], 6ax[b], 6eq
5	73.9 (CH)	3.36 (dddd, 11.4, 11.4,	4a, 4b, 6ax, 6eq	3, 4	2, 3, 4a, 4b, 6eq, 7
6ax	37.6(CH_2)	1.20 (m)	5, 6eq, 7	4, 5, 8	4b[b], 7
6eq		2.02 (dddd, 12.6, 4.4,	5, 6ax, 7, 8eq	7, 8	6ax[b], 4a, 4b, 5, 7, 1′
7	73.1(CH)	3.82 (dddd, 11.1, 10.5,	6ax, 6eq, 8ax,	8, 9, 1′	5, 6ax[b], 6eq, 8ax[b], 8eq, 9, 1′
8ax	39.7(CH_2)	1.22 (m)	7, 8eq, 9	6, 7, 9, 10	6eq[b], 7, 8eq[b]
8eq		1.87 (m)	6eq, 7, 8ax, 9	6, 7	7, 8ax[b], 9, 10b, 5′
9	72.5 (CH)	3.32 (dddd, 11.2, 11.2.	8ax, 8eq, 10a,	5, 7	7, 8eq, 10a, 10b[b], 25
10a	43.1(CH_2)	1.21 (ddd, 15.2, 9.6,	9, 10b, 11	11, 12, 25	8eq, 9, 10b[b], 11[b], 12, 25
10b		1.51 (ddd, 15.2, 11.2,	9, 10a, 11	8, 9, 11, 12, 25	8eq, 9[b], 10a[b], 11, 25
11	34.2 (CH)	2.37 (dqd, 9.6, 6.5,	10a, 10b, 12,	10, 12, 25	10a[b], 10b, 12[b], 13, 25[b]
12	141.5(CH)	5.45 (dd, 14.8, 9.7)	11, 13	10, 11, 14, 25	11[b], 10a, 13[b], 14[b], 25
13	123.9(CH)	6.28 (dd, 14.8, 11.0)	12, 14	10, 11, 14, 15	11, 12[b], 14[b], 15[b], 16b, 21
14	131.3(CH)	6.05 (dd, 10.9, 10.9)	13, 15	12, 13,16, 17	12[b], 13[b], 15[b], 16a
15	126.9(CH)	5.28 (ddd, 10.8, 10.8,	14, 16a, 16b	13, 16, 17	13[b], 14[b], 16a, 16b[b], 17[b]
16a	31.1(CH_2)	1.88 (m)	14, 15, 16b, 17	14, 15, 17	14, 15, 16b, 17[b], 26
16b		2.28 (ddd, 13.1, 11.4,	15, 16a, 17	14, 15, 17, 18	13,15[b],16a,17[b],19a,21,26
17	81.0 (CH)	3.98 (ddd, 11.1, 8.1,	16a, 16b, 18	15, 19, 20	15, 16a[b], 16b[b],18, 26
18	37.3 (CH)	2.52 (dddq, 12.0, 7.0,	17, 19a, 19b,	16, 17, 19, 26	17, 19a[b], 19b, 20, 26[b]
19a	36.8(CH_2)	1.17 (ddd, 11.9, 11.9,	18, 19b, 20	18, 20, 21, 26	16b, 18[b], 21, 22b, 26
19b		2.01 (ddd, 12.2, 7.0,	18, 19a, 20	17, 18	18, 19a, 20, 22a, 22b, 26
20	83.2 (CH)	3.63 (m)	19a, 19b, 21	21, 22	18, 19b, 21[b], 22a, 22b
21	73.0 (CH)	3.42 (ddd, 11.1, 8.8,	20, 22a, 22b	20, 22, 23	13, 16b, 19a, 22a[b], 22b, 23
22a	34.1(CH_2)	1.46 (ddd, 14.1, 11.1,	21, 22b, 23	20, 21	19b, 21[b], 22b[b], 23, 24a, 24b
22b		1.76 (ddd, 13.9, 11.7,	21, 22a, 23	23, 24	19a, 19b, 21, 22a[b],23[b], 24a,
23	72.3 (CH)	5.23 (dddd, 11.7, 4.9,	22a, 22b, 24a,	1	21, 22a, 22b[b], 24a, 24b
24a	66.1(CH_2)	3.61 (m)	23, 24b	22, 23	22a, 22b, 23, 24b
24b		3.81 (dd, 12.2, 2.9)[a]	23, 24a	22, 23	22a, 22b, 23, 24a
25	18.3(CH_3)	0.85 (d, 6.6)	11	10, 11, 12	9, 10a, 10b, 11[b], 12
26	14.5(CH_3)	1.03 (d, 6.9)	18	17, 18, 19	16a, 16b, 18[b], 19a, 19b
1′	94.2 (CH)	5.02 (d, 1.1)	2′	7, 2′, 3′, 5′	6eq, 7, 8eq, 2′, 7′
2′	80.8 (CH)	3.40 (dd, 3.8, 1.4)	1′, 3′	3′, 4′, 7′	1′
3′	71.7 (CH)	3.68 (m)	2′, 4′, 8′		2′, 4′[b]
4′	74.3 (CH)	3.34 (dd, 9.4, 9.4)	3′, 5′	3′, 5′, 6′	3′[b], 5′[b], 6′
5′	68.1 (CH)	3.62 (m)	4′, 6′	3′, 4′, 6′	8eq, 4′[b], 6′
6′	17.7(CH_3)	1.27 (d, 6.3)		4′, 5′	4′, 5′[b]
7′	59.1(CH_3)	3.45 (s)		2′	1′
	OH-3′	2.24 (s)	2, 4a, 4b		
	OH-4′	1.54 (s)	2, 3		

HMBC correlations are presented from proton to indicated carbon; [a] $^3J_{HH}$ values obtained from DQFCOSY and/or NMRSim; [b]COSY artifacts observed in ROESY spectrum.

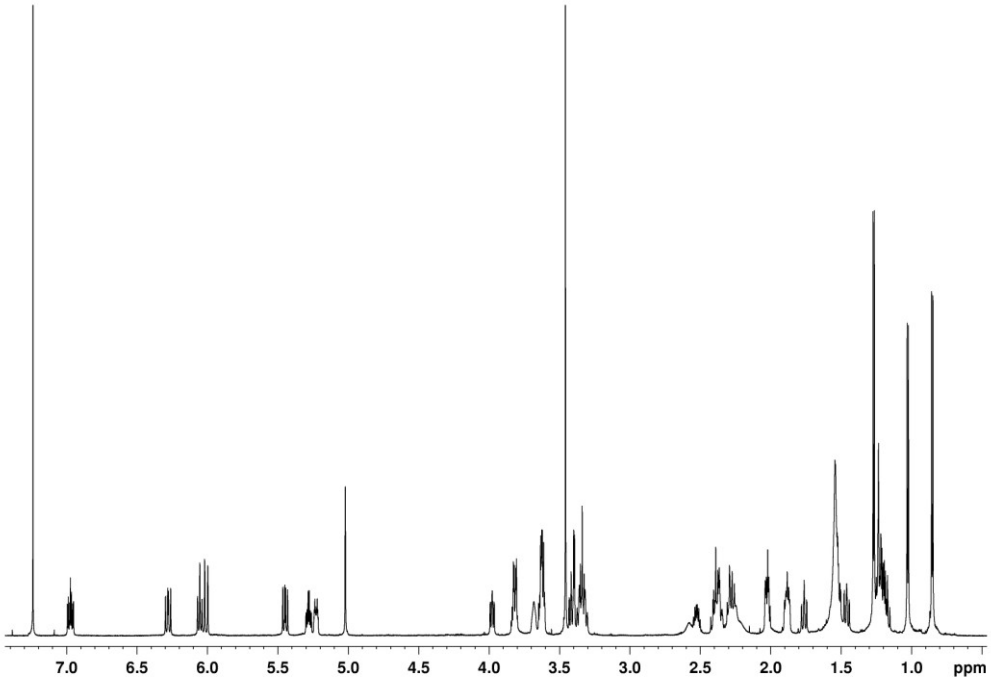

Figure 3.1 ^{1}H NMR spectrum for mandelalide A (**1**; 700 MHz, $CDCl_3$)

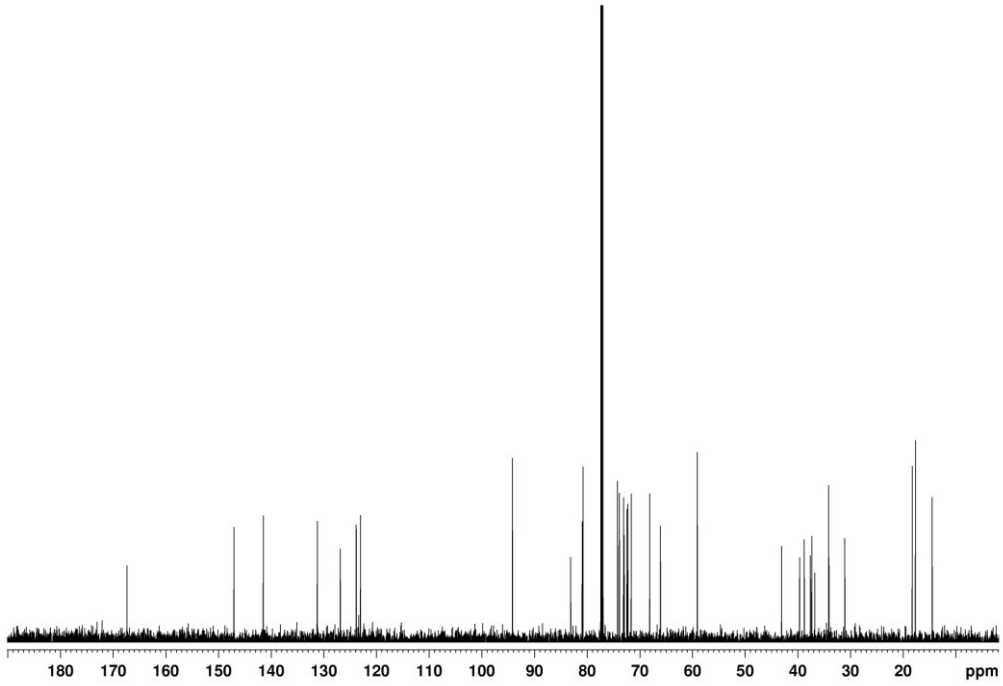

Figure 3.2 ^{13}C NMR spectrum for mandelalide A (**1**; 175 MHz, $CDCl_3$)

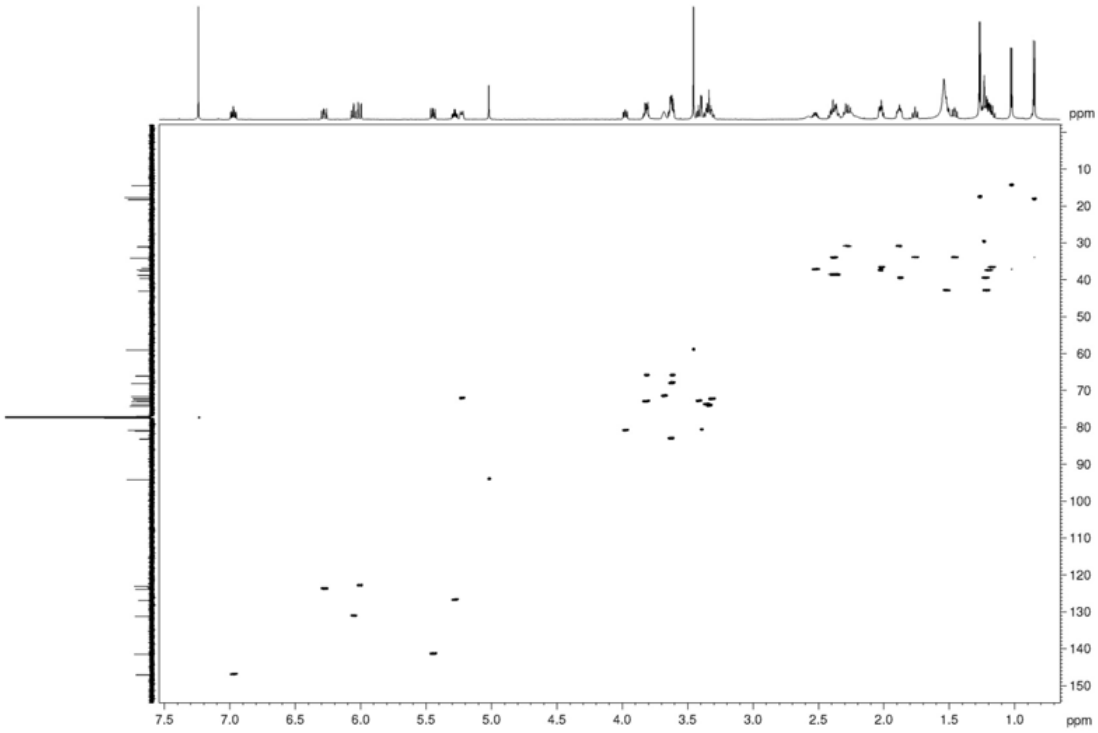

Figure 3.3 HSQC spectrum for mandelalide A (**1**; 700 MHz, $CDCl_3$)

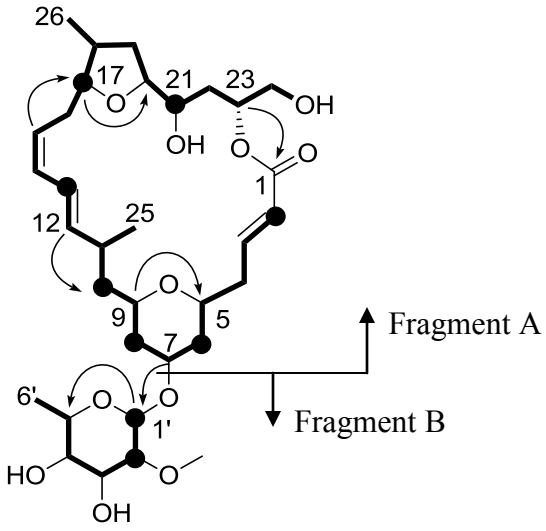

Figure 3.4. Planar structure of 1 showing TOCSY correlations from H-2, H-6, H-8, H-10b, H-13, H-17, H-21, H-1′, H-2′ (black circles) indicated as bolded lines and key HMBC correlations represented by single-headed arrows.

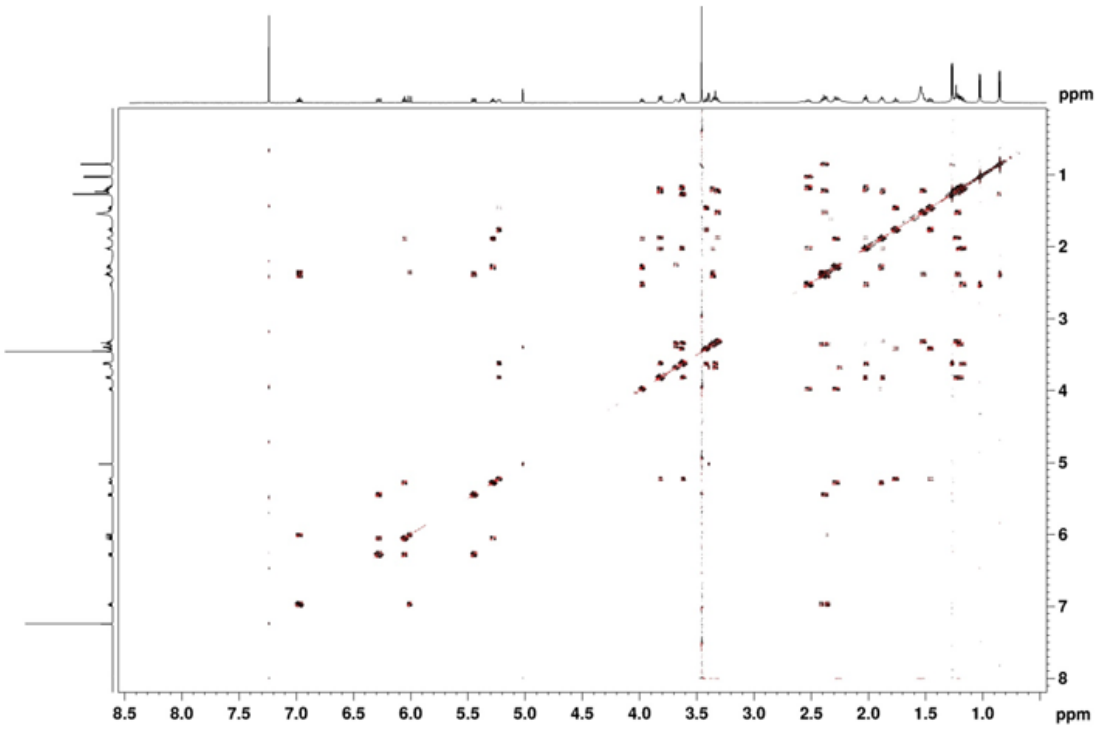

Figure 3.5 COSY spectrum for mandelalide A (**1**; 700 MHz, $CDCl_3$)

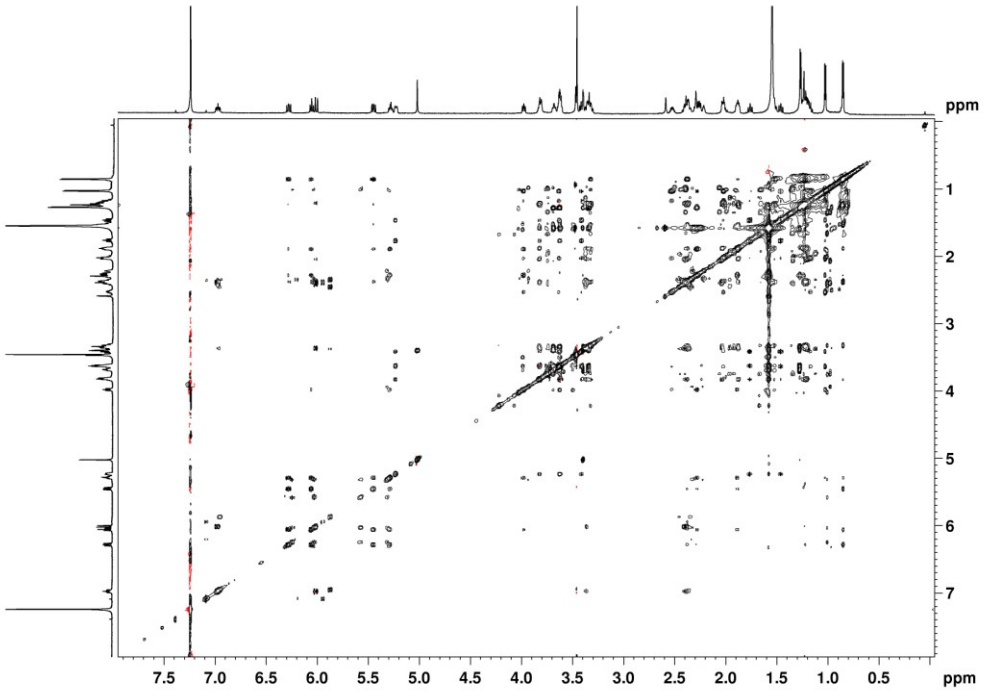

Figure 3.6 TOCSY spectrum for mandelalide A (**1**), TOCSY mixing time = 100 ms (700 MHz, $CDCl_3$)

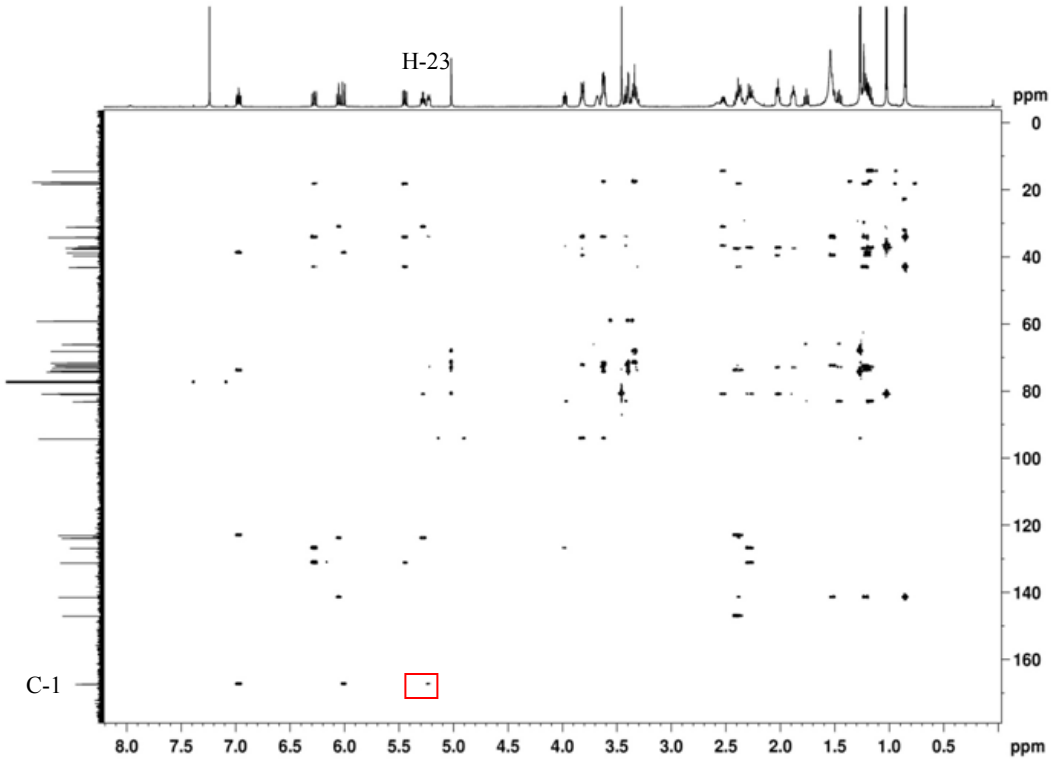

Figure 3.7 HMBC spectrum for mandelalide A (**1**; 700 MHz, $CDCl_3$)

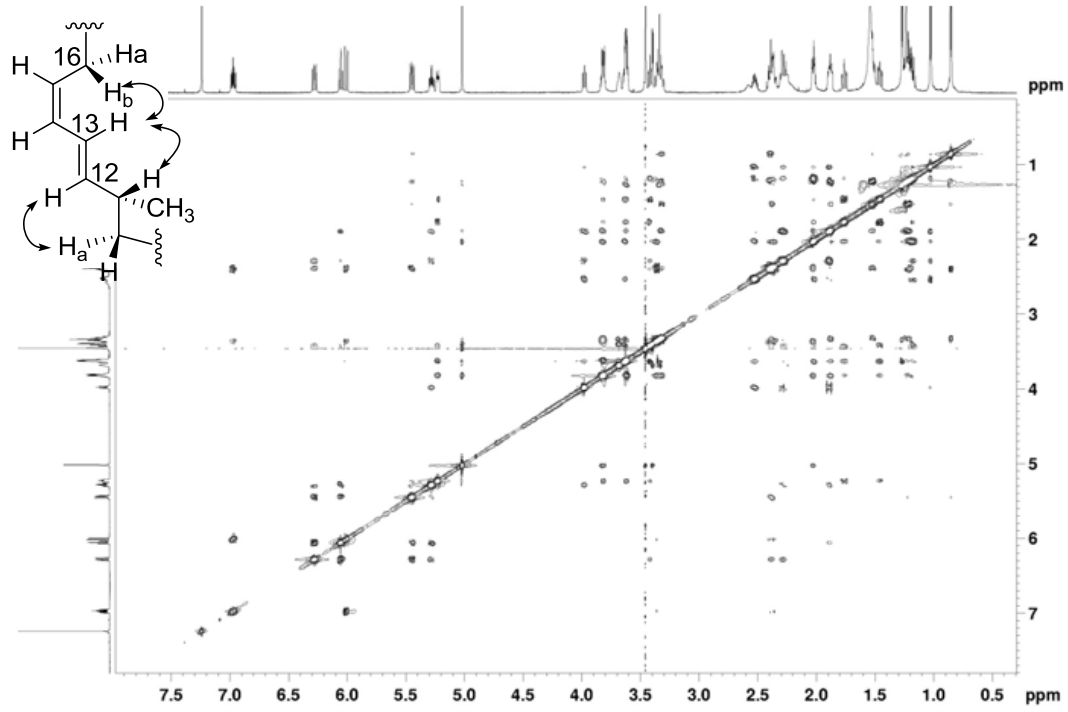

Figure 3.8 ROESY spectrum for mandelalide A (**1**; 700 MHz, $CDCl_3$). The assignment of geometry around the C-13/C-14 bond in **1** using key ROESY correlations indicated by double-headed arrows on partial structure localized in right corner.

The second compound characterized, mandelalide B (**2**), was assigned a molecular formula of $C_{37}H_{58}O_{13}$ based on HRESIMS data for $[M+Na]^+$ *m/z* 733.3773, which is consistent with 9 degrees of unsaturation. Inspection of the ^1H and ^{13}C NMR spectra for mandelalide B (**2,** Figures 3.9, 3.10) suggested that it was structurally related to mandelalide A (**1**). However, the ^1H NMR spectrum for **2** lacked the coupled olefinic signals at δ 6.01 (H-2) and 6.97 (H-3) and the relatively deshielded diastereotopic H_2-24 signals at δ 3.81 and 3.61. Instead an additional oxymethine double doublet at δ 5.48 was evident, as well as a methyl triplet (δ_H 0.95) indicative of an aliphatic chain. Correspondingly, comparison of the ^{13}C NMR spectra for **1** and **2** revealed the absence of olefinic ^{13}C resonances at δ 123.1 (C-2) and 147.1 (C-3) from the spectrum for **2**, and the presence of two additional midfield ^{13}C resonances (δ 79.3 and 69.5), as well as a second carbonyl resonance (δ_C 173.6). These data accounted for 8 of the 9 degrees of unsaturation, implying the presence of an additional cycle in **2**. The analysis of HSQC and HMBC data (Figures 3.11, 3.12) for **2** permitted assignment of an oxygenated quaternary C-2 (δ 79.3) and an oxymethine CH-3 (δ 69.5, δ 5.48). While the same C-1/C-23 macrolactone linkage was apparent in both compounds, two-and three-bond HMBC correlations from H_2-24 (δ 1.93, 2.39) to C-2 and C-3, respectively, indicated a C-2/C-24 bond in **2**. These data described a γ-butyrolactone ring around the ester linkage of the mandelalide B macrocycle. Placement of the second carbonyl carbon (δ_C 173.6) in a butyrate substituent at C-3 was facilitated by HMBC correlations to δ_C 173.6 from δ_H 5.48 (H-3), as well as 2.35 (H_2-2″) and 1.67 (H_2-3″). Further analysis of NMR data confirmed the presence of a 2-*O*-methyl-6-dehydro sugar in **2**. However, differences in both ^1H and ^{13}C shifts for CH-3′ to CH-6′ compared to compound **1** suggested a different relative configuration for the monosaccharide in **2** (Table 3.2).

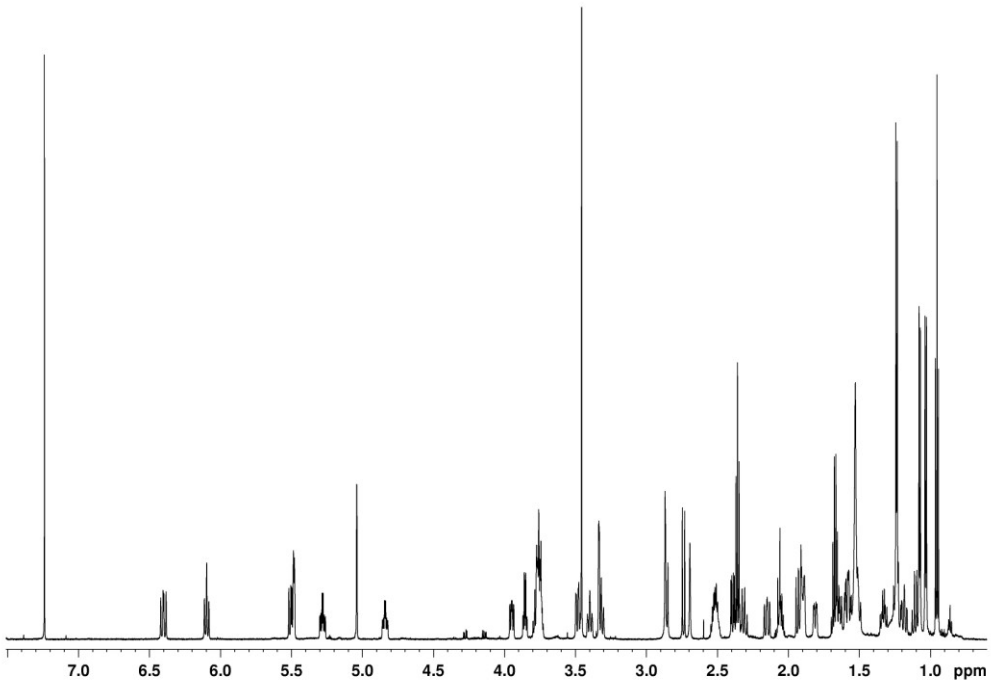

Figure 3.9 ^{1}H NMR spectrum for mandelalide B (**2**; 700 MHz, $CDCl_3$)

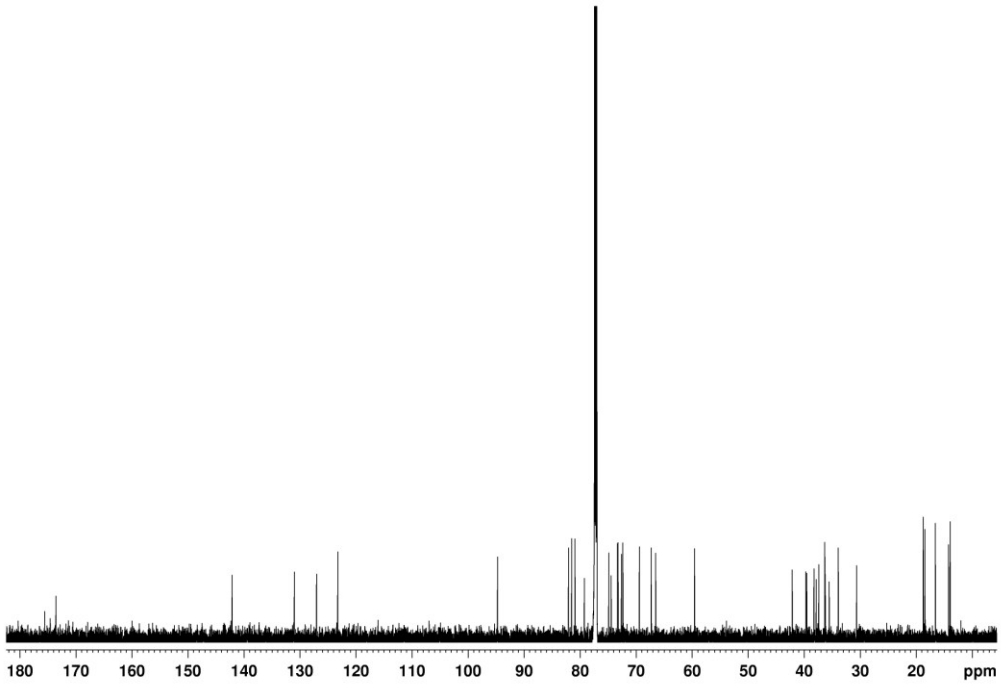

Figure 3.10 ^{13}C NMR spectrum for mandelalide B (**2**; 175 MHz, $CDCl_3$)

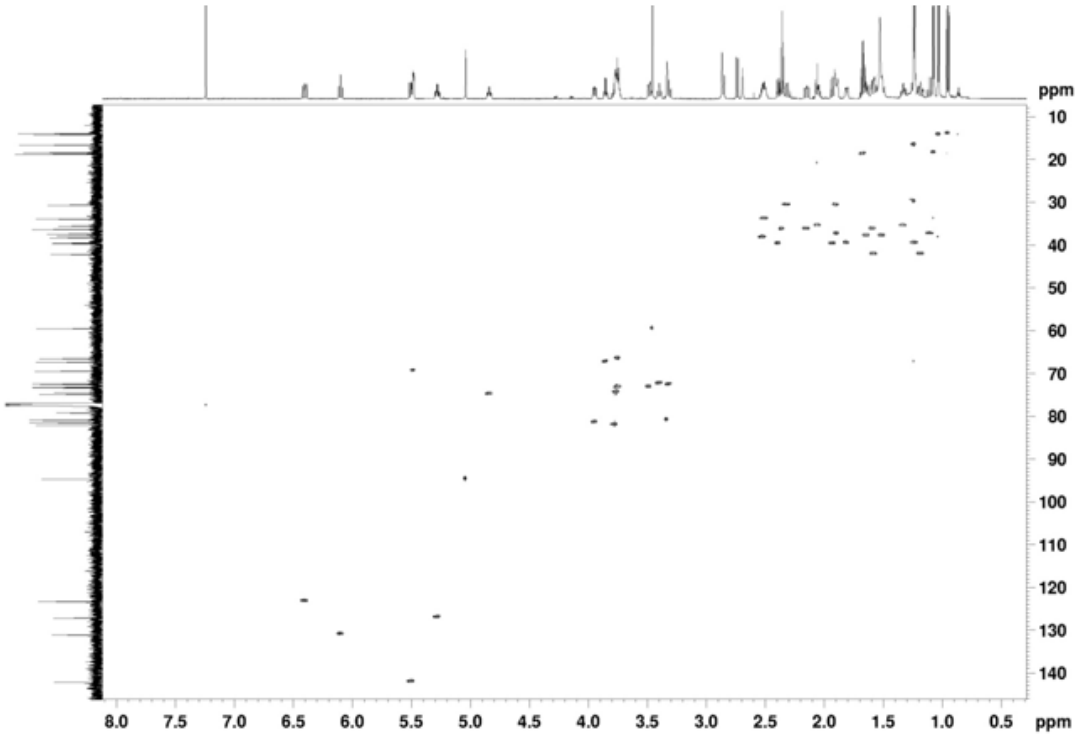

Figure 3.11 . HSQC spectrum for mandelalide B, (**2**; 700 MHz, $CDCl_3$)

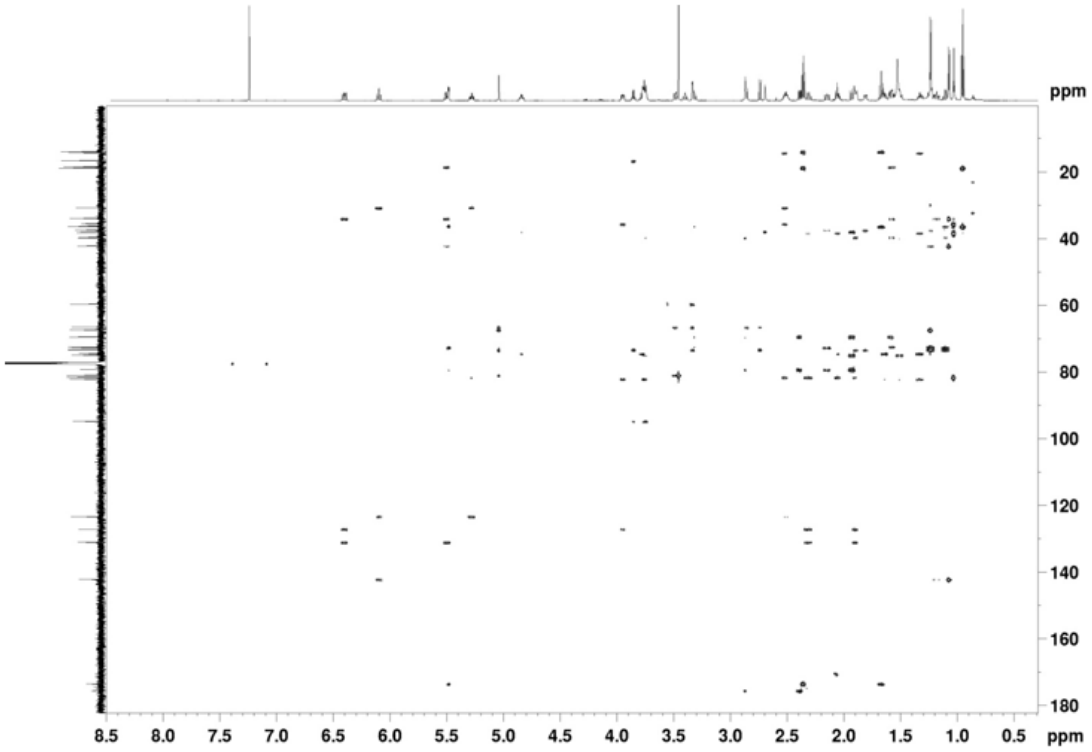

Figure 3.12 HMBC spectrum for mandelalide B, (**2**; 700 MHz, $CDCl_3$)

Table 3.2 ^{1}H and ^{13}C NMR data for mandelalides B-C (**2-3**) in $CDCl_3$

	Mandelalide B (**2**)		Mandelalide C (**3**)	
No.	δ_C (mult)	δ_H (mult, *J* in Hz)	δ_C (mult)	δ_H (mult, *J* in Hz)
1	175.6 (C)	-	174.7 (C)	-
2	79.3 (C)	-	82.0 (C)	-
3	69.5 (CH)	5.48 (dd, 6.0, 1.7)	68.3 (CH)	5.51 (dd, 6.6, 0.9)
4a	36.3 (CH_2)	1.59 (m)	36.4 (CH_2)	1.65 (m)
4b		2.14 (ddd, 15.0, 11.7, 1.5)		2.14 (ddd, 15.6, 11.7, 1.0)
5	72.7 (CH)	3.30 (dddd, 11.4, 11.4, 1.5, 1.5)	72.3 (CH)	3.25 (dddd, 11.4, 11.4, 1.8, 1.8)
6ax	37.4 (CH_2)	1.10 (ddd, 11.7, 11.7, 11.7)	41.2 (CH_2)	1.11 (ddd, 12.5, 11.4, 11.4)
6eq		1.89 (m)		1.86 (m)
7	73.3 (CH)	3.75 (m)	68.3 (CH)	3.76 (dddd, 10.9, 10.9, 4.6, 4.1)
8ax	39.6 (CH_2)	1.23 (m)	41.8 (CH_2)	1.13 (ddd, 12.5, 11.2, 11.2)
8eq		1.81 (dddd, 12.4, 4.8, 1.8, 1.8)		1.83 (m)
9	72.4 (CH)	3.39 (dddd, 11.0, 11.0, 2.2, 2.2)	72.3 (CH)	3.37 (dddd, 10.9, 10.9, 2.1, 2.1)
10a	42.2 (CH_2)	1.18 (ddd, 14.1, 12.3, 2.8)	42.1 (CH_2)	1.19 (ddd, 14.2, 12.1, 2.8)
10b		1.57 (m)		1.57 (m)
11	33.9 (CH)	2.50 (m)	34.0 (CH_2)	2.49 (m)
12	142.1 (CH)	5.50 (dd, 15.1, 9.8)	142.2 (CH)	5.50 (dd, 14.6, 9.6)
13	123.3 (CH)	6.40 (dd, 14.7, 11.3)	123.2 (CH)	6.39 (dd, 14.6, 11.4)
14	131.0 (CH)	6.10 (dd, 11.1, 11.1)	131.1 (CH)	6.10 (dd, 11.0, 11.0)
15	127.1 (CH)	5.28 (ddd, 11.1, 11.1, 5.2)	127.1 (CH)	5.28 (ddd, 11.0, 11.0, 5.4)
16a	30.7 (CH_2)	1.90 (m)	30.7 (CH_2)	1.90 (ddd, 13.6, 5.2, 1.1)
16b		2.31 (ddd, 13.6, 11.6, 11.5,)		2.30 (ddd, 13.8, 11.9, 11.9)
17	81.5 (CH)	3.95 (ddd, 11.6, 7.46, 1.6)	81.6 (CH)	3.95 (ddd, 11.5, 7.5, 1.1)
18	38.3 (CH)	2.52 (m)	38.3 (CH)	2.53 (m)
19a	35.6 (CH_2)	1.33 (ddd, 12.2, 12.2, 8.2)	35.7 (CH_2)	1.33 (ddd, 12.2, 12.2, 9.1)
19b		2.05 (ddd, 12.8, 6.9, 6.9)		2.10 (ddd, 12.5, 7.0, 6.8)
20	82.1 (CH_2)	3.77 (m)	82.4 (CH)	3.82 (ddd, 9.2, 9.2, 7.0)
21	74.5 (CH)	3.76 (m)	74.4 (CH)	3.73 (ddd, 10.8, 9.5, 1.2)
22a	37.9 (CH_2)	1.51 (m)	32.1(CH_2)	1.59 (m)
22b		1.64 (m)		1.82 (ddd, 14.4, 11.0, 1.0)
23	74.9 (CH)	4.84 (dddd, 10.4, 10.4, 4.9, 1.0)	78.9 (CH)	5.01 (ddd, 11.2, 2.0, 2.0)
24a	39.7 (CH_2)	1.93 (dd, 12.7, 10.7)	72.2 (CH)	3.98 (d, 2.8)
24b		2.39 (dd, 12.8, 4.9)	-	-
25	18.5 (CH_3)	1.07 (d, 6.6)	18.4(CH_3)	1.06 (d, 6.2)
26	14.2 (CH_3)	1.03 (d, 6.9)	14.2(CH_3)	1.03 (d, 6.9)
	OH-21	2.70 (br s)	OH	2.80 (br s)
	OH-2	2.87 (s)	-	-
1′	94.8 (CH)	5.04 (s)	173.4 (C)	-
2′a	80.9 (CH)	3.33 (ddd, 3.0, 1.5. 1.3)	36.3(CH_2)	2.34 (td, 7.5, 1.2)
2′b	-	-	-	-
3′	66.6 (CH)	3.74 (m)	18.7(CH_2)	1.65 (m)
4′	73.3 (CH)	3.49 (ddt, 11.8, 3.3, 1.2, 1.2)	13.9(CH_3)	0.94 (t, 7.5)
5′	67.4 (CH)	3.85(br q, 6.6)	-	-
6′	16.6 (CH_3)	1.23 (d, 6.5)	-	-
7′	59.6 (CH_3)	3.45 (s)	-	-

Table 3.2 (continued) ^{1}H and ^{13}C NMR data for mandelalides B-C (**2**-**3**) in $CDCl_3$

	Mandelalide B (**2**)			Mandelalide C (**3**)
No.	δ_C (mult)	δ_H (mult, *J* in Hz)	No.	δ_C (mult)
8′	OH	2.86 (d, 11.6)	-	-
9′	OH	2.74 (d, 11.6)	-	-
1″	173.6 (C)	-	-	-
2″a	36.3 (CH_2)	2.35 (t, 7.5)	-	-
2″b	-	-	-	-
3″	18.8 (CH_2)	1.67 (tq, 7.4, 7.4)	-	-
4″	14.0 (CH_3)	0.95 (t, 7.4)	-	-

a – $^{3}J_{HH}$ values obtained from DQFCOSY and/or NMRSim

The HRESIMS data ($[M+Na]^+$ *m/z* 589.2970) for mandelalide C (**3**) supported a molecular formula of $C_{30}H_{46}O_{10}$, for 8 degrees of unsaturation. The ^1H NMR spectrum for **3** was reminiscent of that for **2**. However, a careful comparison of the two spectra revealed the absence of midfield glycosidic signals in the ^1H spectrum for **3**. Similarly, inspection of the ^{13}C NMR spectrum for **3** showed a lack of midfield resonances for a methoxy methyl (δ 59.6, C-7′ in **2**), anomeric carbon (δ 94.8, C-1′ in **2**), and other glycosidic carbons. Together, the MS and 1D NMR data for compound **3** indicated that the structure of **3** is related to the aglycone of mandelalide B (**2**, Table 3.2, Figures 3.13, 3.14). Indeed, the only difference between the ^{13}C NMR signals for the aglycones of compounds **2** and **3** was a relatively downfield methine resonance at δ 72.2 in the spectrum for **3**, compared to the methylene signal at δ 37.9 (C-24) in the spectrum for **2**. This methine was HSQC-correlated to a 1H doublet at δ_H 3.98, and could be assigned to an oxymethine CH-24 on the basis of HMBC correlations from the latter ^1H doublet to C-1, C-2, C-3 and C-23. Thus, considering its MS and NMR data, mandelalide C (**3**) could be assigned as the C-24 hydroxylated aglycone of mandelalide B (**2**). Unfortunately, an attempt to crystallize mandelalide C (0.5 mg) was unsuccessful and degradation of the compound over several months prevented the acquisition of additional spectroscopic or biological data.

The molecular formula of mandelalide D (**4**) was assigned by HRESIMS ($[M+Na]^+$ *m/z* 659.3424) as $C_{34}H_{52}O_{11}$, implying 9 degrees of unsaturation. Comparison of the similar ^1H NMR spectra (Table 3.3) for mandelalides C (**3**) and D (**4**) indicated a second aglycone structure (Figure 3.15). A key difference between the ^1H spectra for the two compounds was the further deshielded H-24 doublet (δ_H 5.17) for **4** relative to that for **3** (δ_H 3.98). In the HMBC spectrum (Figure 3.16) for **4**, the H-24 doublet was correlated to a carbonyl ^{13}C resonance (δ_C 173.1, C-1"), which also showed correlations from H-2a", H-2b" and H-3", consistent with an additional butyrate substituent at C-24. Thus, mandelalide D (**4**) is 24-butyro mandelalide C (**3**). Over a period of 12 months, we observed changes in the ^1H NMR spectrum for **4** that

were consistent with the loss of both butyrate moieties, resulting in the new compound deacylmandelalide D (**4b**, *m/z* 519.3 $[M+Na]^+$, Table 3.3).

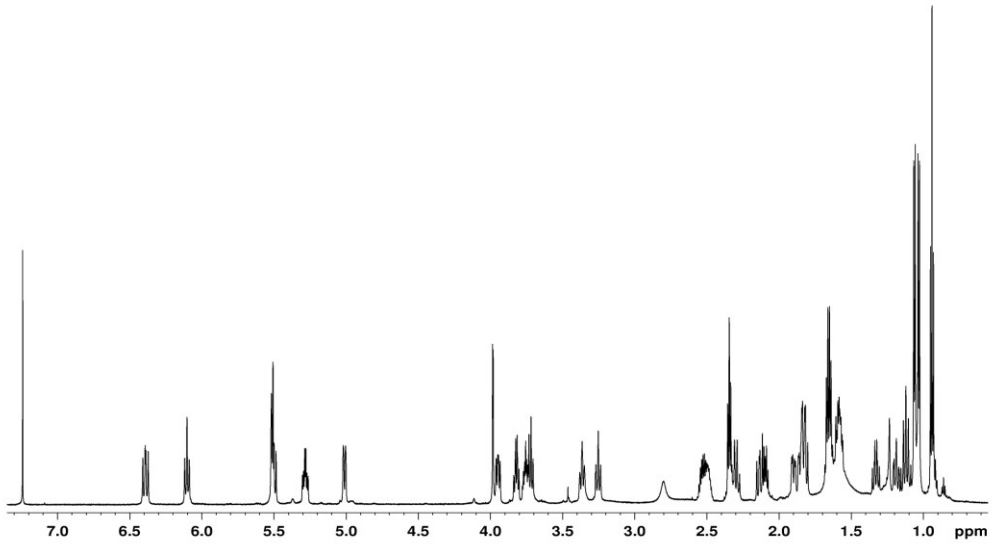

Figure 3.13 ^{1}H NMR spectrum for mandelalide C (**3**; 700 MHz, $CDCl_3$)

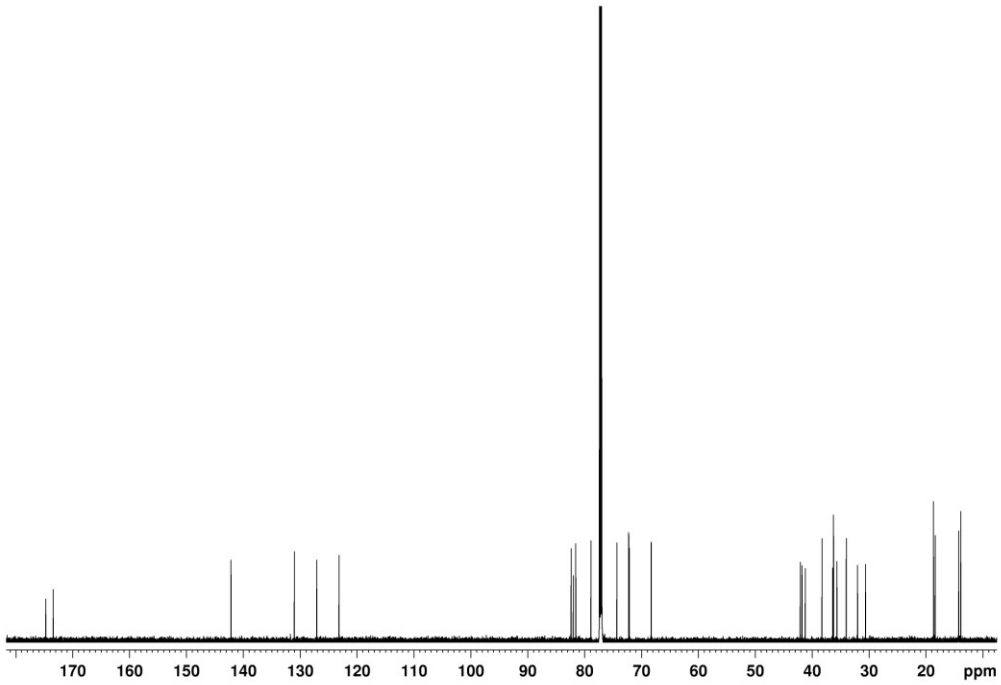

Figure 3.14 ^{13}C NMR spectrum for mandelalide C (**3**; 175 MHz, $CDCl_3$)

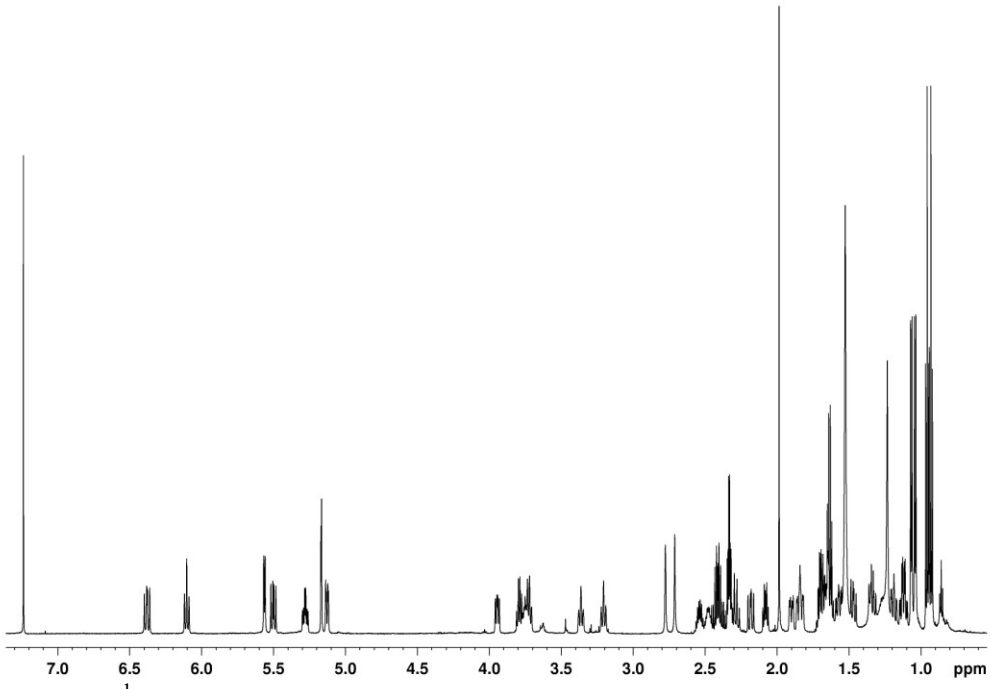

Figure 3.15 ^{1}H NMR spectrum for mandelalide D (**4**; 700 MHz, $CDCl_3$)

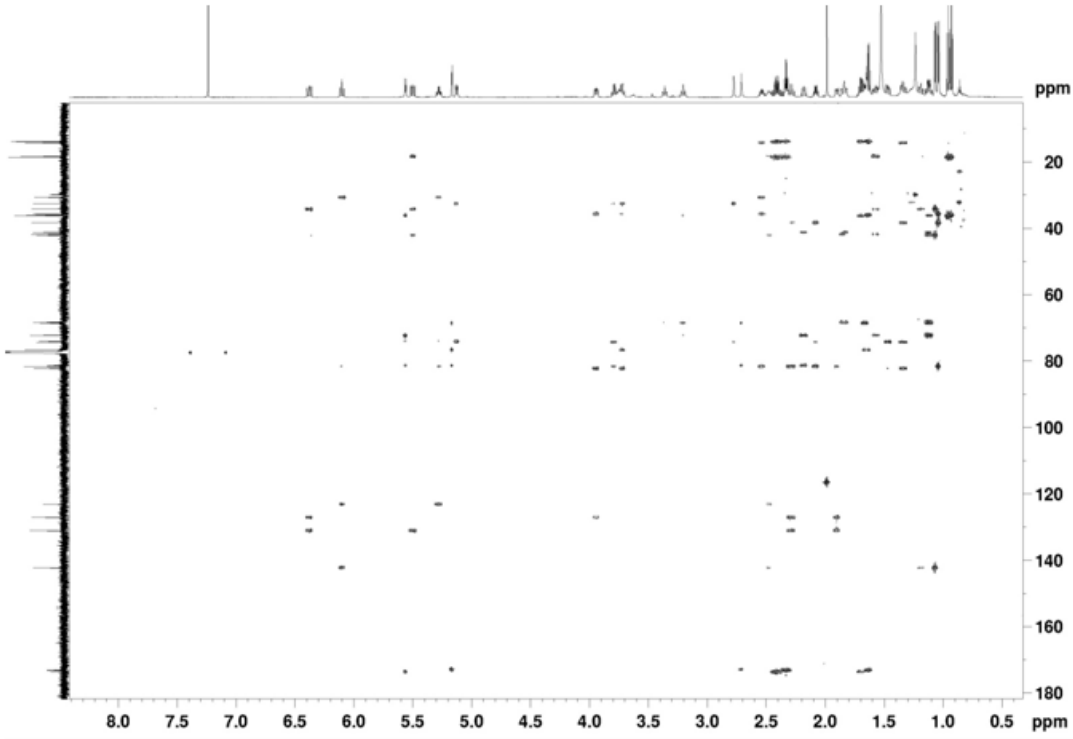

Figure 3.16 HMBC spectrum for mandelalide D (**4**; 700 MHz, $CDCl_3$)

Table 3.3. ^{1}H and ^{13}C NMR data for mandelalides D (**4** in $CDCl_3$ and **4b** in CD_3OD).

	Mandelalide D (**4**)		Deacylmandelalide D (**4b**)	
No.	δ_C (mult)	δ_H (mult, *J* in Hz)	δ_C (mult)	δ_H (mult, *J* in Hz)
1	172.9 (C)	-	176.3 (C)	-
2	81.3 (C)	-	82.4 (C)	-
3	68.6 (CH)	5.56 (dd, 6.6, 0.7)	66.6 (CH)	4.06 (d, 7.5)
4a	36.2 (CH_2)	1.68 (m)	37.4 (CH_2)	1.56 (ddd, 15.1, 7.7, 1.6)
4b		2.18 (ddd, 15.4, 11.5, 0.9)		2.02 (dd, 15.2, 11.1)
5	72.2 (CH)	3.21 (dddd, 11.2, 11.2, 1.3, 1.3)	72.3(CH)	3.39 (m)
6ax	41.2 (CH_2)	1.12 (ddd, 11.3, 11.3, 11.3)	40.3(CH_2)	1.11 (m)
6eq		1.85 (dddd, 12.2, 4.6, 1.5, 1.5)		1.88 (dddd, 12.1, 4.7, 1.6, 1.6)
7	68.4 (CH)	3.75 (m)	67.1(CH)	3.76 (m)
8ax	41.8 (CH_2)	1.12 (ddd, 11.3, 11.3, 11.3)	40.7(CH_2)	1.08 (m)
8eq		1.83 (dddd, 12.2, 4.6, 1.5, 1.5)		1.83 (m)
9	72.2 (CH)	3.36 (dddd, 11.0, 11.0, 2.2, 2.2)	71.1(CH)	3.39 (m)
10a	42.1 (CH_2)	1.19 (ddd, 13.9, 11.5, 2.8)	41.2(CH_2)	1.23 (m)
10b		1.57 (ddd, 14.0, 11.5, 4.0)		1.49 (ddd, 13.8, 11.4, 4.1)
11	34.2 (CH)	2.48 (m)	33.5 (CH)	2.49 (m)
12	142.3 (CH)	5.50 (dd, 14.8, 9.7)	140.7 (CH)	5.51 (dd, 14.6, 9.9)
13	123.1 (CH)	6.38 (dd, 15.0, 11.3)	122.8 (CH)	6.42 (dd, 14.6, 11.2)
14	131.1 (CH)	6.10 (dd, 11.0, 11.0)	130.0 (CH)	6.10 (dd, 10.9, 10.9)
15	127.1 (CH)	5.28 (ddd, 11.3, 11.3, 5.4)	126.3 (CH)	5.30 (ddd, 16.0, 10.9, 5.1)
16a	30.6 (CH_2)	1.90 (ddd, 13.6, 5.3, 1.0)	31.2(CH_2)	1.94 (ddd, 13.5, 5.2, 1.8)
16b		2.29 (ddd, 13.1, 11.3, 11.3)		2.38 (ddd, 13.1, 11.4, 11.4)
17	81.6 (CH)	3.94 (ddd, 12.0, 7.5, 1.1)	81.0 (CH)	3.98 (ddd, 11.6, 7.3, 1.4)
18	38.3 (CH)	2.54 (dddq, 12.3, 7.5, 7.02, 6.8)	37.6 (CH)	2.52 (m)
19a	35.7 (CH_2)	1.34 (ddd, 12.3, 12.3, 9.2)	34.7 (CH_2)	1.37 (m)
19b		2.08 (ddd, 12.2, 7.02, 7.02)		2.14 (m)
20	82.2 (CJ)	3.79 (ddd, 9.3, 9.3, 7.0)	82.2 (CH)	3.84 (ddd, 9.6, 9.6, 6.8)
21	74.3 (CH)	3.73 (ddd, 10.0, 10.0, 1.6)	73.9 (CH)	3.75 (dd, 9.1, 9.1)
22a	32.5 (CH_2)	1.47 (ddd, 14.2, 10.5, 1.0)	32.0 (CH_2)	1.52 (ddd, 13.7, 9.7, 1.0)
22b		1.65 (m)		1.81 (m)
23	76.7 (CH)	5.13 (ddd, 10.8, 3.3, 0.8)	78.3 (CH)	4.81 (dd, 10.8, 2.6)
24	74.0 (CH)	5.17 (d, 3.3)	71.7 (CH)	4.32 (d, 3.0)
25	18.3 (CH_3)	1.07 (d, 6.6)	17.0 (CH_3)	1.01 (d, 6.6)
26	14.3 (CH_3)	1.04 (d, 6.8)	12.3 (CH_3)	1.08 (d, 7.0)
	OH	2.71 (br s)		
	OH	2.78 (br s)		
1′	173.6 (C)	-		
2′a	36.3 (CH_2)	2.40 (dt, 15.5, 7.3)		
2′b		2.43 (dt, 15.5, 7.3)		
3′	18.6 (CH)	1.70 (m)		
4′	13.9 (CH_3)	0.96 (t, 7.4)		
1″	173.1 (CH)	-		
2″a	36.0 (CH_2)	2.31 (dt, 12.8, 7.5)		
2″b		2.33 (dt, 12.8, 7.5)		
3″	18.6 (CH_2)	1.63 (m)		
4″	13.8 (CH_3)	0.93 (t, 7.3)		

Consideration of the differences in the planar macrocyclic structures, and available amounts, of mandelalides A-D (**1**-**4**) led to the conclusion that the assignment of relative configuration should be performed on mandelalide A and one of mandelalides B-D. Similarities in coupling constant ($^3J_{HH}$) values for mandelalides B-D suggested retention of the relative configuration of the macrocycle between these structures (Tables 3.2, 3.3). Therefore besides mandelalide A, mandelalide B (**2**) was selected for further analysis because it also possesses a monosaccharide moiety, although it lacks the C-24 chiral center present in **3** and **4**. For both mandelalides A (**1**) and B (**2**), the relative configuration of the macrocycle could be assigned fully using a combination of ROESY and *J*-based configuration analysis of data acquired in $CDCl_3$ and pyridine-d_5, which were consistent between the two solvents.

Considering the tetrahydropyran ring of **1**, ROESY correlations between H-5, H-7 and H-9 supported their axial orientation, consistent with a chair conformation and equatorial C-7 glycosidic bond (Figures 3.8, 3.17a). The relative configuration for fragment C-9 to C-11 (-$CHCH_2CH$-) was assigned on the basis of coupling constants obtained from the ^{1}H spectrum and a DQFCOSY (Figure 3.5). In $CDCl_3$, $^3J_{HH}$ values of 2.2 and 11.2 Hz for H-9/H-10a and H-9/H-10b, respectively, localized H-10a *gauche* and H-10b *anti* to H-9 in two possible rotamers (Figure 3.17b), the correct one of which should be distinguishable from ROESY data. ^{1}H signal overlap in the $CDCl_3$ ROESY spectrum for mandelalide A (**1**) obscured ROE interactions in the region of interest. However, acquisition of NMR data for **1** in py-d_5 provided sufficient resolution (0.16 ppm, Figure 3.18) between H-8_{ax} and H-10a to reveal ROESY correlations between H-8_{ax} and H-10b, and H-8_{eq} and H-10a. This led to the conclusion that rotamer A is correct, orienting H-10a to the outside of the macrocycle (Figure 3.17). The assignment of relative configuration around the C-10/C-11 bond required direct measurement of $^3J_{HH}$ values from DQFCOSY, again due to significant overlap. In $CDCl_3$, $^3J_{HH}$ values of 9.6 Hz for H-10a/H-11 and 3.7 Hz for H-10b/H-11 indicated *anti* and *gauche* orientations, respectively (Figure 3.17c). Finally, ROESY correlations between H-9 and H_3-25, and H-11 and H-13 were consistent with the

relative configuration shown in Figure 3.17a. This assignment was supported by HETLOC data in $CDCl_3$ (Figure 3.19), which provided very weak, but measurable $^3J_{HC}$ between H-10a and C-25 (0.9 Hz), and between H-10b and C-25 (8.9 Hz).

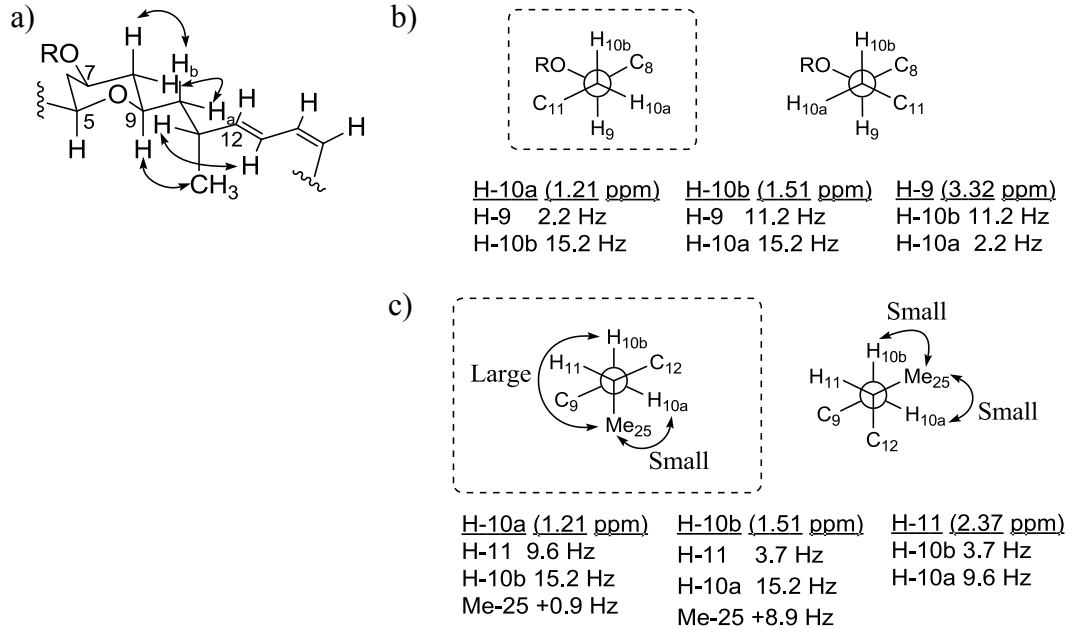

Figure 3.17 a) Key ROESY correlations indicated on the C-5/C-15 fragment of **1**; b) Two possible rotamers around the C-9/C-10 bond; c) Most feasible rotamers around the C-10/C-11 bond of **1**, with anticipated large/small heteronuclear coupling constant indicated on each. For b) and c) the J_{HH} and J_{HC} values ($CDCl_3$) are listed below the Newman projections and the rotamer of best fit is indicated by a dashed outline.

For the tetrahydrofuran ring of **1**, H-17 and H-20 could be in a *cis* or *trans* configuration. There are two close conformational minima (envelope and half-chair) for THF rings (Grindley, 2008). However, in the envelope conformation CH_3-26, H-18, H-19a and H-19b in **1** would be *eclipsed*, while these same moieties would be *gauche* in the half-chair conformation and there would be no eclipsed interaction along the C-18/19 bond (Grindley, 2008). Therefore we decided to analyze ROESY correlations in the context of a half-chair THF ring to assign the relationship of H-17 and H-20.

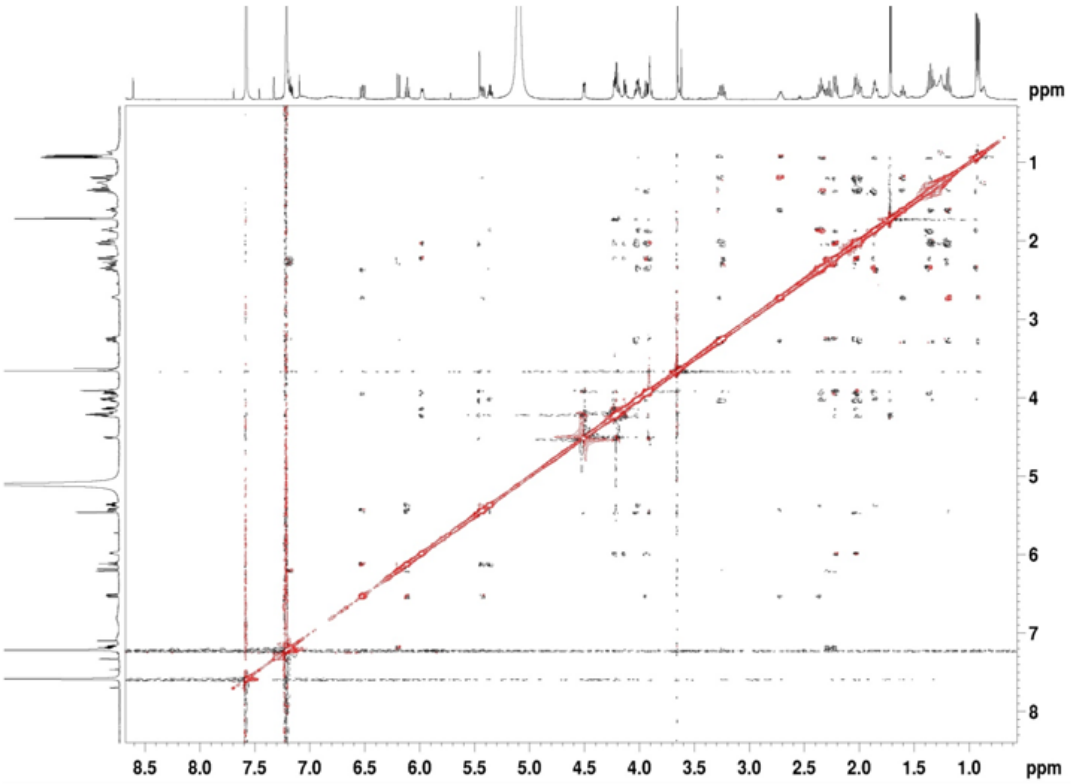

Figure 3.18 ROESY NMR spectrum for mandelalide A (**1**; 700 MHz, py-d_5)

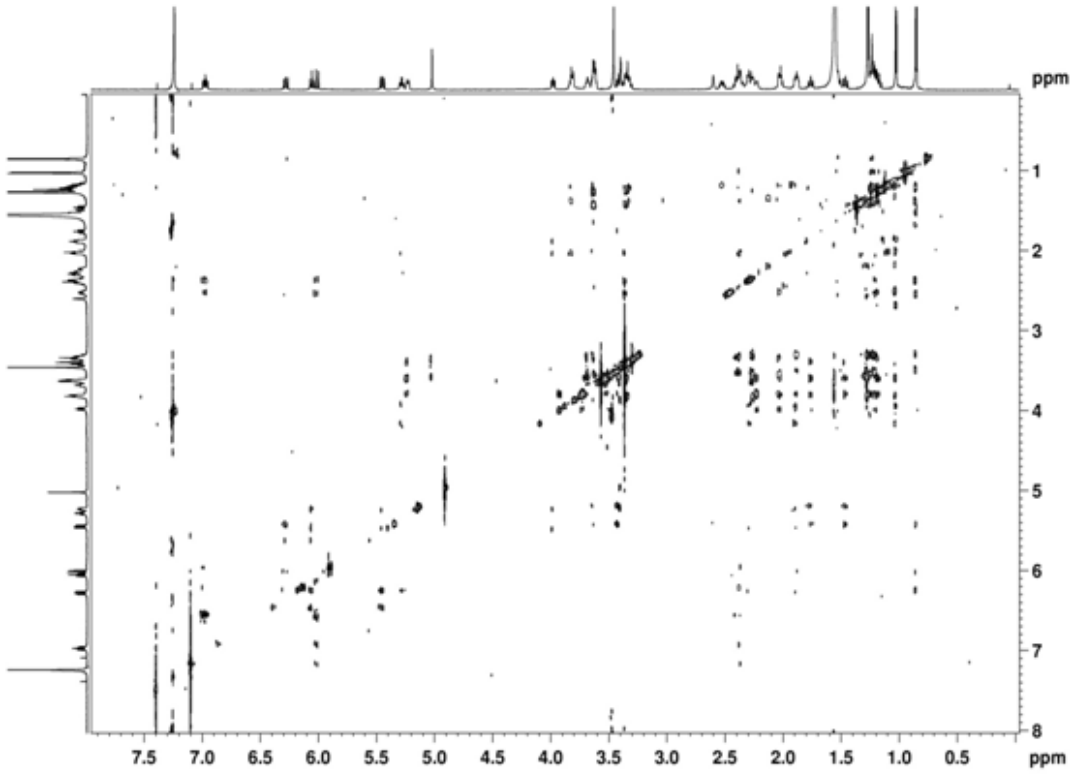

Figure 3.19 HETLOC spectrum for mandelalide A (**1**; 700 MHz, $CDCl_3$)

The relatively large $^{3}J_{HH}$ couplings between vicinal proton pairs H-16b/H-17 (11.4 Hz) and H-20/H-21 (8.8 Hz) supported their *anti* orientation in each case (Figure 3.20a). Moreover, ROESY correlations between H-16b and H-19a, H-16b and H-21, and H-19a and H-21 were consistent with a *cis* localization of H-17 and H-20 (Figure 3.20b), despite that no direct ROESY correlation was observed between H-17 and H-20. Instead, the proposed conformation, consistent with ROESY correlations between H_3-26/H_2-16 and H-16b/H-21, brings ROE-correlated H-18 and H-20 into close proximity (Figure 3.20b). For the C-21 chiral center, the large values of $^{3}J_{HH}$ and $^{2}J_{HC}$ (8.8 and -4.0 Hz, respectively), in parallel with the lack of NOE contact between H-20 and H-21 (resolved in py-d_5), are consistent with their *anti* orientation (Figure 3.20a), as stated above. Analysis of $^{3}J_{HH}$ between H-21/H-22a (11.1 Hz), and H-21/H-22b (1.8 Hz), placed H-22a *anti* and H-22b *gauche* with respect to H-21 (Figure 3.20c). ROESY correlations between H-19a and H-22b, H-19b and H-22a, and H-19b and H-22b suggested that H_2-22 are directed away from the center of macrocycle, with the C-21 hydroxyl pointing towards the center. Analogous reasoning was used to resolve the relative configuration at C-23. The respective large and small $^{3}J_{HH}$ values between H-22b/H-23 (11.7 Hz) and H-22a/H-23 (1.9 Hz) suggested *anti* and *gauche* orientations, respectively (Figure 3.20d).

Configurational assignment of the mandelalide A monosaccharide (C-1' to C-6') relied on $^{3}J_{HH}$ values, obtained from the ^{1}H NMR and assigned by DQFCOSY, given the overlap for H-3' to H-5' signals in both $CDCl_3$ and py-d_5 ROESY spectra. Although the small value of $^{3}J_{H\text{-}1'/H\text{-}2'}$ = 1.1 Hz was inconclusive, H-2' was assigned as equatorial based on $^{3}J_{H\text{-}2'/H\text{-}3'}$ = 3.8 Hz. The H-4' multiplet indicated couplings of 9.4 Hz with both H-3' and H-5', indicative of axial hydrogens, although the direct analysis of H-3' and H-5' multiplets was impeded by their overlap with other ^{1}H shifts. Overall, these data for CH-2' to CH-5' were consistent with the relative configuration of 2-*O*-methylrhamnose. To confirm this and to assign the monosaccharide as α- or β-2-*O*-methylrhamnose, we decided to analyze the magnetization transfer pattern of TOCSY signals originating from the anomeric center (CH-1'), following the method proposed

by Gheysen *et al* (2008). This "TOCSY matching" approach takes advantage of the fact that the size of the $^{3}J_{HH}$ scalar couplings affects the rate of magnetization transfer through a ^{1}H spin system during the TOCSY spin-lock period. The acquisition of a TOCSY with a spin-lock of 100 ms (Figure 3.21) affords a differential presence or absence of the CH_3-6' signal in α- and β-rhamnose, respectively. In the TOCSY acquired for mandelalide A (**1**), the intensity of peaks fit to previously reported data for α-rhamnose (Figure 3.21), (Gheysen, et al., 2008). Additional confirmation that the monosaccharide attached to **1** is 2-*O*-methyl-α-rhamnose was provided by the measurement of $^{1}J_{HC}$ = 167.2 Hz for the anomeric CH-1' from a HETLOC experiment (Figure 3.22). This value is in agreement with that reported previously for 2-*O*-methyl-α-rhamnose, although is smaller than in the case of nonmethylated common sugars [~170 Hz, (Bock & Pedersen, 1974; Motohashi et al., 2010)].

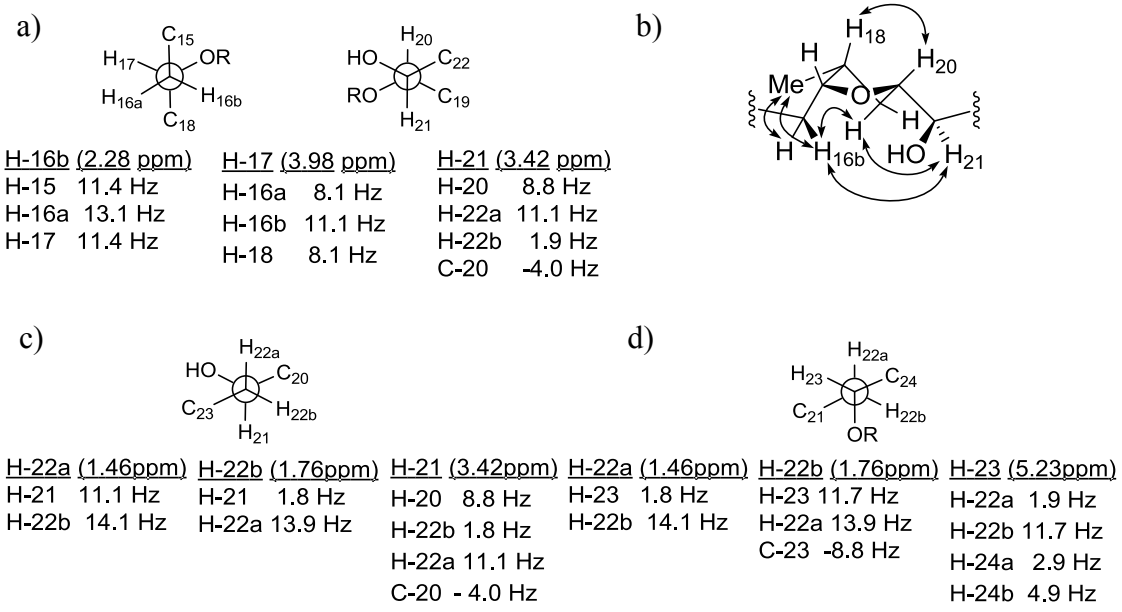

Figure 3.20. a) Newman projections along the C-16/C-17 and C-20/C-21 bonds in **1**; b) The most feasible *cis* orientation of the THF ring with double-headed arrows indicating ROESY correlations; c) Newman projection along the C-21/C-22 bond with applicable J_{HH} and J_{HC} values ($CDCl_3$) indicated on the right. d) Newman projection along the C-22/C-23 bond and relevant coupling constants.

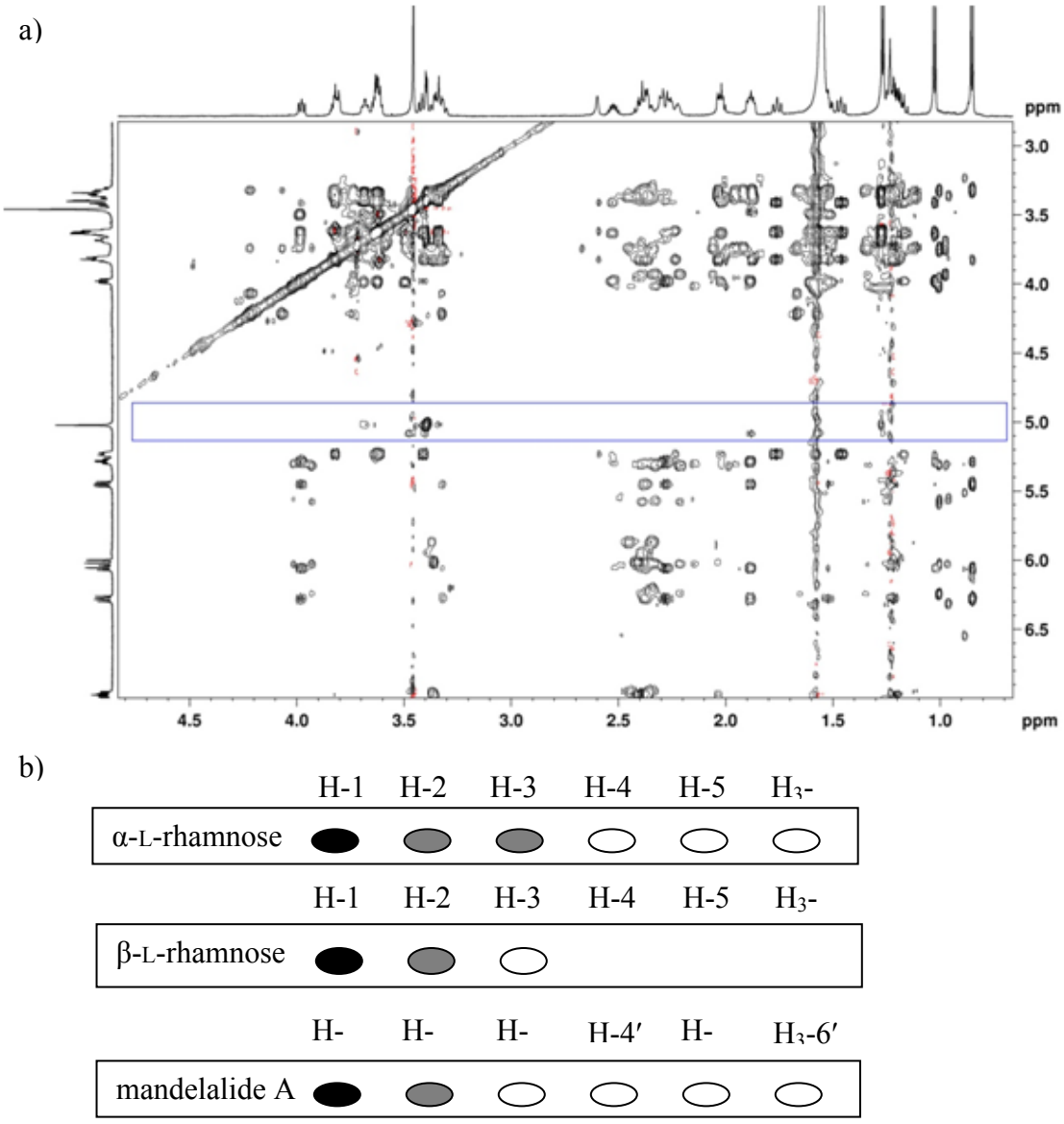

Figure 3.21. a) Partial TOCSY spectrum for mandelalide A (**1**) showing the α-2-O-methylrhamnose region, TOCSY mixing time = 100 ms (700 MHz, $CDCl_3$), b) The magnetization transfer pattern of TOCSY signals for the mandelalide A monosaccharide and α- and β-L-rhamnose. The grey ovals indicate intensity or signal greater than 1.5 % of intensity measured for the anomeric ^1H signal, while white ovals indicate intensity of at least 0.5 % but no more than 1.5% intensity measured for the anomeric ^1H signal.

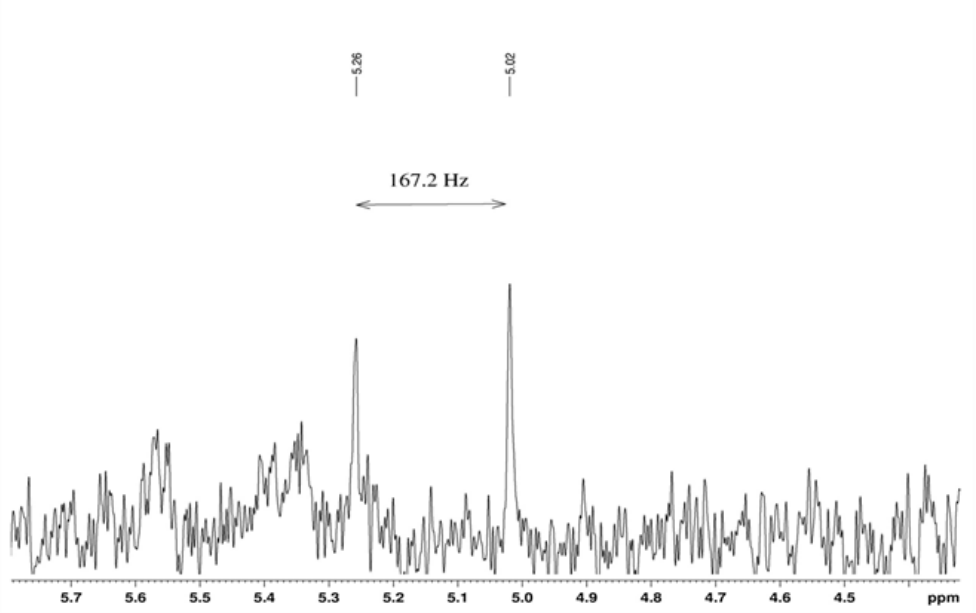

Figure 3.22. *F2* slice of HETLOC spectrum for mandelalide A (**1**) anomeric C-1′ (700 MHz, $CDCl_3$)

As in the case of **1**, the coupling constant values and ROESY correlations measured from both $CDCl_3$ and py-d_5 data for mandelalide B (**2**) were comparable, indicating similar conformations in both solvents. The chair conformation of the THP ring in **2** (C-5 to C-9) was confirmed by the presence of diaxial ROESY correlations between H-5, H-7 and H-9 (Figure 3.23a). For the C-9/C-11 segment, coupling constants of 2.2 and 11 Hz, between H-9/H-10a, and H-9/H-10b confirmed *gauche* and *anti* relationships, respectively. Similarly for H-10a/H-11 and H-10b/H-11, large (12.3 Hz) and small (4.1 Hz in $CDCl_3$, 3.8 Hz in py-d_5) coupling constants assigned from DQFCOSY supported *anti* and *gauche* relationships, respectively, overall leading to the same relative configuration in this region as for **1**. For the C-3/C-5 fragment of **2**, $^3J_{HH}$ values of 1.5 and 11.7 Hz between H-4a/H-5 and H-4b/H-5 supported *gauche* and *anti* orientations, respectively. A small coupling of 1.6 Hz between H-3 and H-4b indicated their *gauche* relationship (Figure 3.23b), and was in

agreement with large H-4a/C-3 (-5.6 Hz) and small H-4b/C-3 (0 Hz) heteronuclear couplings. However, medium couplings for H-3/H-4a (6.0 Hz) and H-5/C-3 (4.3 Hz) suggested that the staggered orientation along C-3/4 may be distorted or that more than one conformation is present along this bond. Clear ROESY correlations between H-3 and each of H-4b, H-5, H-9, H-11, H-23 and H-24b, but not H-4a (apparent COSY artifact only), support a distorted rotamer in which 138° and -102° angles are present between H-3/H-4a and H-3/H-4b, as calculated using MestReJ for $^{3}J_{HH}$ 6.0 and 1.6 Hz, respectively (Figure 3.23b).

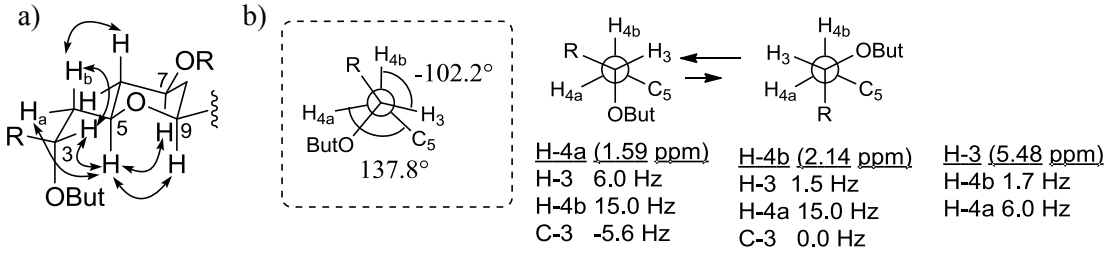

Figure 3.23. a) Key ROESY correlations for the C-3/C-5 fragment of **2** are indicated by double-headed arrows on the partial structure. b) The most probable rotamer along the C-3/C-4 bond highlighted by the dashed outline and alternative equilibrium of two rotamers explaining medium size coupling constants. But = butyrate.

Confirmation of the relative configuration around the C-3 stereogenic center using residual dipolar couplings (RDC) was attempted. In order to assign relative configuration of unknown chiral centers in a compound of interest the acquisition of data in isotropic and anisotropic solution is necessary, and at least five independent experimental values of RDCs should be measured (Gschwind, 2005). These RDCs are used to obtain the alignment tensor (measure of the degree of alignment of compound), which then is used to back-calculate the theoretical RDCs for each structural model of the analyzed compound. The best fit of experimental and theoretical data is assumed to be the correct structure. Given the limited amounts of sample in hand, the detection limits of this method on our available instrumentation

were examined first. The acquisition of gated decoupled ^{13}C NMR spectra for 20 mg and 2 mg of strychnine in poly-γ-benzyl-L-glutamate (PBLG) and $CHCl_3$ indicated insufficient sensitivity for the lower concentration of strychnine, and suggested that the measurement of RDCs is not be feasible on submilligram amounts of mandelalide B (**2**, Figure 3.24).

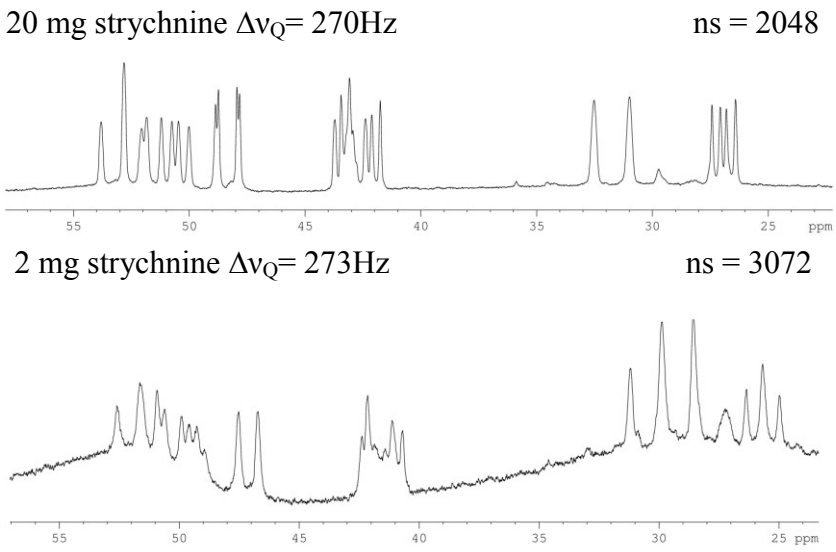

Figure 3.24 Gated decoupled ^{13}C NMR spectra of 20 and 2.9 mg strychnine in PBLG and $CHCl_3$, extended region from 0 - 60 ppm (700 MHz with ^{13}C cryoprobe)

The presence of a ROESY correlation between H-18 and H-20 on the THF ring in mandelalide B (**2**) placed CH_3-26 quasi-equatorial, consistent with ROESY correlations from the latter methyl to H_2-16, (as for **1**, Figure 3.20). ROESY correlations and comparative analysis of coupling constant values (Table 3.2) around the C-16/C-21 fragment confirmed that a *cis* conformation of the THF ring is conserved in mandelalides A (**1**) and B (**2**).

Given extensively overlapped $CDCl_3$ ^1H chemical shifts for the C-20/C-23 fragment in **2**, analysis of ^1H NMR and DQFCOSY in py-d_5 was used to assign the

relative configuration of this region (Figures 3.25, 3.26). The $^3J_{HH}$ values for **2** were similar to those for mandelalide A (**1**), despite the presence of the γ-lactone ring in **2**. However, in contrast to **1**, in which the more shielded H-22a (δ 1.46) is *anti* to H-21 and *gauche* to H-23 (Figure 3.27), for **2** the more shielded H-22a (δ 1.65) is *gauche* to H-21 ($^3J_{HH}$ <1 Hz) and H-22b (δ 1.77) is *anti* to H-21 ($^3J_{HH}$ = 9.4 Hz), while H-20 and H-21 remain *antiperiplanar* ($^3J_{HH}$ = 9.4 Hz) (Figure 3.27a). Coupling constant values obtained directly from the oxymethine H-23 multiplet, and assigned by DQFCOSY, indicate *anti* relationships with H-22a (J_{HH} = 11.2 Hz), and a *gauche* relationship with H-22b (J_{HH} = 1.0 Hz). The orientation of the ester bond in the butyrolactone ring could be assigned knowing the localization of H-23 *anti* to H-22a. The ester oxygen must then be positioned *gauche* or *anti* to H-22b. The ROEs observed between H-24a, H-24b and H-22b in py-d_5, in parallel with the absence of ROEs between H_2-24 and H-21 suggested that the ester bond is *anti* to H-22b (Figure 3.27a). Finally, knowing the relative configuration of the C-3/C-11 and C-20/C-23 fragments, the chirality of the quaternary C-2 in the butyrolactone ring was considered. ROESY correlations between H-24b and both H-3 and H-23 were consistent with an α-oriented H-24b, while H-24a, showing ROESY correlations to H_2-22, is oriented above the butyrolactone ring in a β configuration. Similarly, the C-2 hydroxyl could be oriented to the outside of the macrocycle due to the presence of weak ROESY signals between this OH-2 and H-4b and H-24a, suggesting a 2*R* configuration (Figure 3.27b).

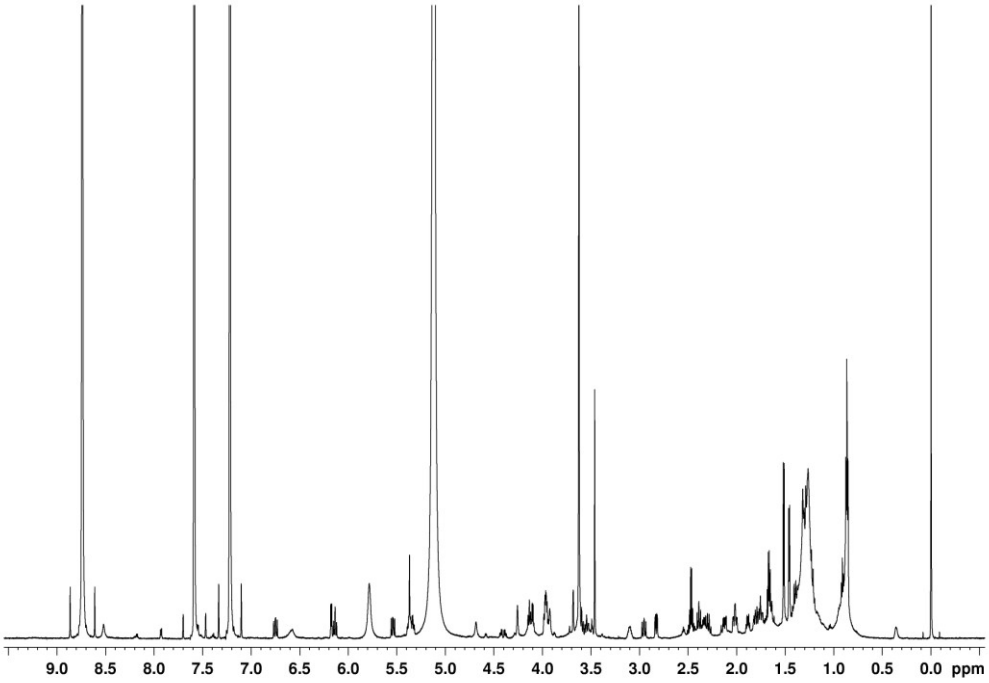

Figure 3.25 ^{1}H NMR spectrum for mandelalide B (**2**; 700 MHz, py-d5)

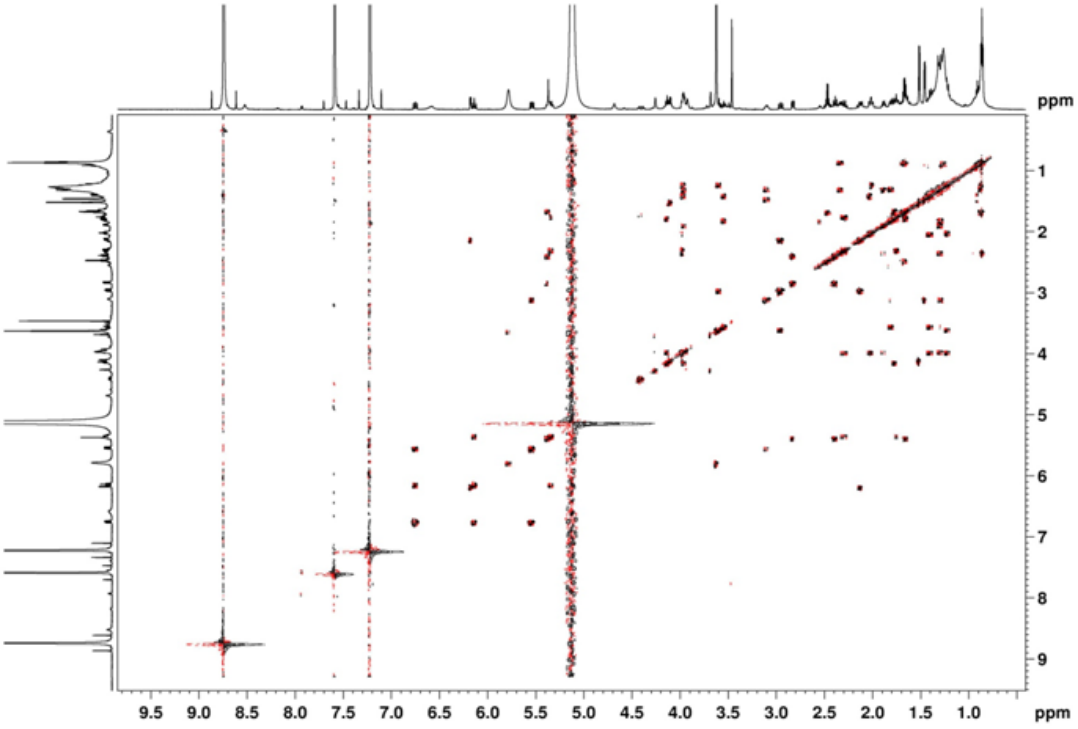

Figure 3.26 COSY NMR spectrum for mandelalide B (**2**; 700 MHz, py-d5)

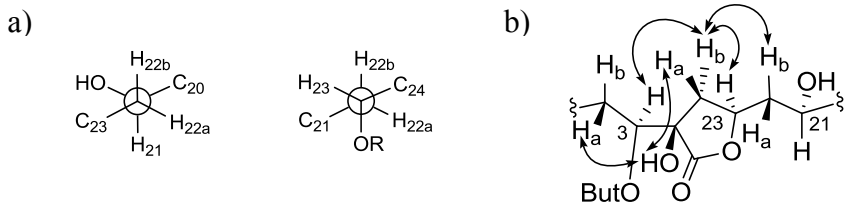

Figure 3.27 a) Assigned rotamers along the C-21/C-22 and C-22/C-23 bonds in **2**. b) ROESY correlations around the γ-butyrolactone of **2**. But = butyrate.

The relative configuration of the 2'-*O*-methyl, 6'-deoxy monosaccharide moiety (C1'-C7') in **2** was established analogously to that in **1**. A very weak ROESY correlation (py-d_5) between H-1' and H-5' together with $^1J_{HC}$ = 167 Hz for anomeric CH-1' suggested the presence of an α-sugar. A ROESY correlation between H-3' and H-5' localized these protons axial, while the small $^3J_{HH}$ between H-2' and H-3', (2.8 Hz) localized H-2' equatorial (Figure 3.28). The presence of a W coupling ($^4J_{HH}$ = 0.98 Hz) between H-2' and H-4', as well as $^3J_{HH'}$ = 3.2 Hz between H-3' and H-4' localized H-4' equatorial, overall leading to the conclusion that mandelalide B (**2**) contains 2-*O*-methyl-6-dehydro-α-L-talose, the C-4' epimer of the monosaccharide in mandelalide A.

Given the assignment of relative configuration of the macrocycle and monosaccharide units of mandelalides A (**1**) and B (**2**), it remained to establish the absolute configuration of these glycosidic macrolides. Despite our desire to conserve the limited sample quantities available for further biological investigations, a chemical degradation/derivatization approach to the absolute configuration would be most rigorous and was facilitated by the contiguous nature of the stereogenic fragments throughout the molecular framework. Importantly, inspection of the $CDCl_3$ and py-d_5 ROESY spectra for **1** and **2** revealed clear correlations between protons of the monosaccharide and THP of the macrocycle (Figure 3.28a, b). Given the well-defined solution structures of monosaccharides and glycosidic bond conformations, (Seo et al.,

1978) assignment of the rhamnose absolute configuration would permit subsequent relay of configurational assignments around the macrocycle, as shown for mandelalide B (Figure 3.28b). Therefore, a portion (100 μg) of mandelalide A (**1**) was sacrificed for hydrolysis of the glycosidic bond and chiral GC-MS comparison of the liberated derivatized monosaccharide with permethylated and silylated D- and L-rhamnose standards. During co-injection of each standard with the derivatized natural product hydrolysate, the natural product sugar coeluted with the L (97.4 min) and not the D (96.4 min) synthetic standard, confirming that the sugar substituent of **1** is 2-*O*-methyl-α-L-rhamnose (Figure 3.29). The absolute configuration of this sugar could then be extrapolated to the aglycone of **1** based on the ROESY correlations between H-1' and H-7, H-1' and H-6_{eq}, and H-5' and H-8_{eq} to provide an assignment of the mandelalide A (**1**) aglycone as 2*E*, 5*S*, 7*S*, 9*R*, 11*R*, 12*E*, 14*Z*, 17*R*, 18*R*, 20*R*, 21*R*, 23*R*. Given retention of the macrocycle configuration (C-5 to C-21) between **1** and **2**, the absolute configuration of **2** could be assigned similarly by considering ROESY correlations between the monosaccharide and THP moiety, and key correlations across this more rigid macrocycle (Figure 3.28b). Thus the aglycone of mandelalide B (**2**) could be assigned as 2*R*, 3*R*, 5*R*, 7*S*, 9*R*, 11*R*, 12*E*, 14*Z*, 17*R*, 18*R*, 20*R*, 21*R*, 23*R*.

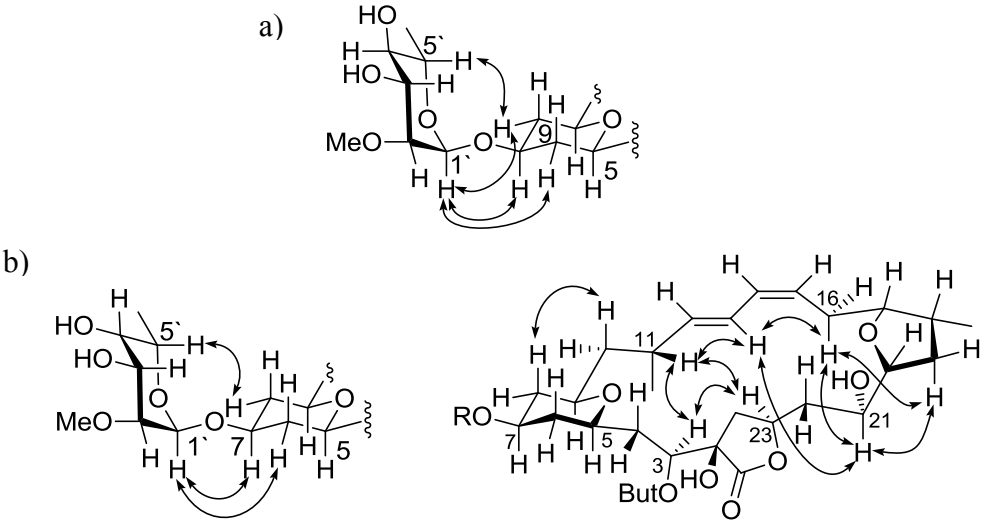

Figure 3.28 a) Key ROE correlations ($CDCl_3$) between the monosaccharide and the macrolide THP moiety in mandelalide A; b) Key ROE correlations between the monosaccharide and the macrolide, as well as through ring correlations for mandelalide B.

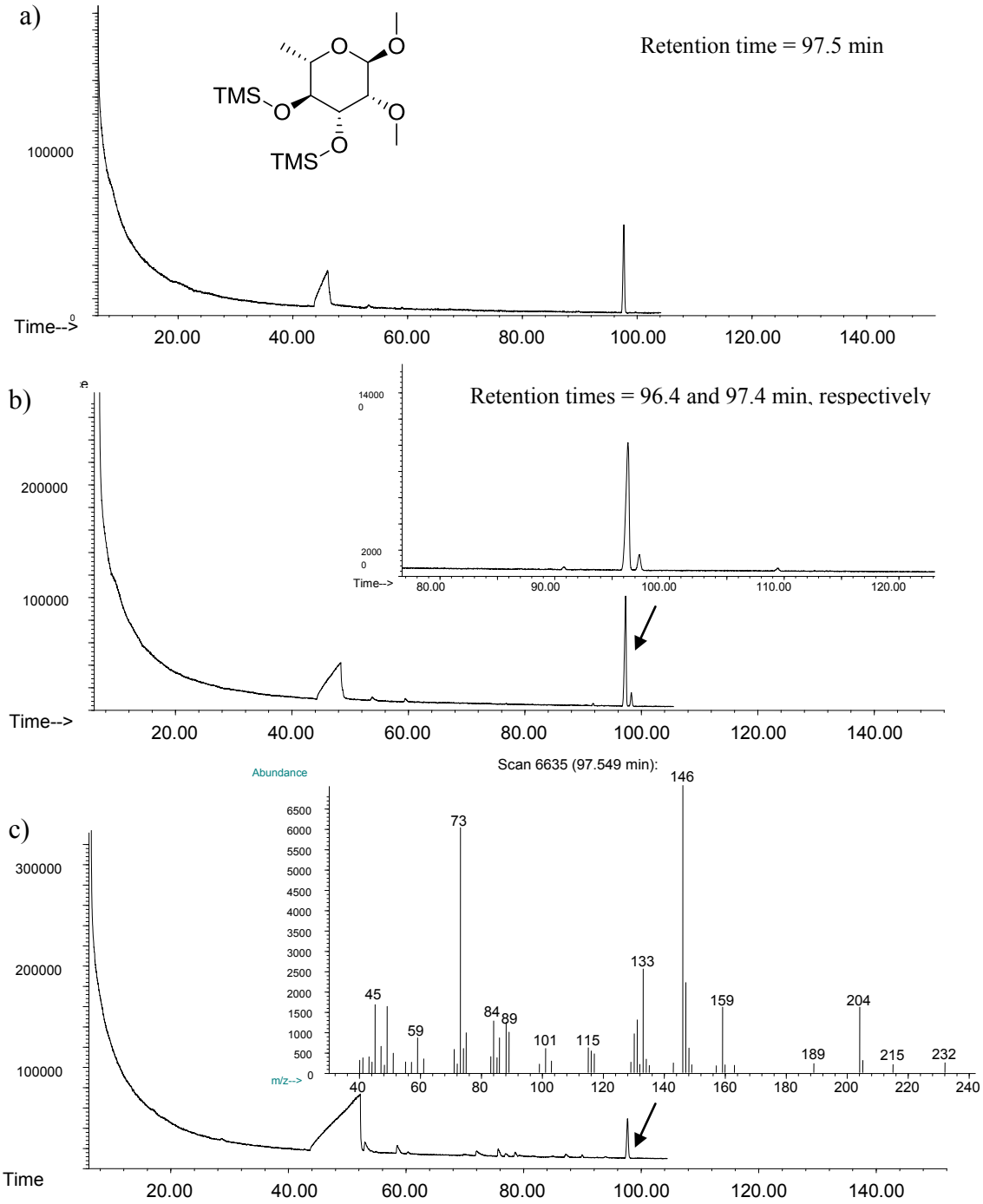

Figure 3.29 GC-MS chromatograms for a) 1,2-di-*O*-methyl-3,4-di-*O*-TMS-α-L-rhamnose ($C_{14}H_{32}O_5Si_2$) co-injected with the permethylated/silylated hydrolysate of mandelalide A (upper), b) 1,2-di-*O*-methyl-3,4-di-*O*-TMS-α-D-rhamnose co-injected with the permethylated/silylated hydrolysate of mandelalide A (middle chromatogram, left and right peaks, respectively), and c) the permethylated and silylated hydrolysate of mandelalide A with EI mass spectrum (bottom).

Computational modeling of mandelalide B was used to examine possible mandelalide B conformations (Figure 3.30). An attempt to investigate the fit of calculated conformations to experimental data was based on measurements of ROE distances across the macrocycle in py-d_5 (Table 3.4), (Zhao et al., 2011). However, as could be expected for a flexible macrolide, for the ten lowest energy conformations of mandelalide B (**2**), the differences between the calculated and experimental average distances between all analyzed protons were significantly different (> 0.2 Å). Nevertheless, the lowest energy computational model assists in visualizing the through ring ROE contacts that facilitated assignment of the absolute configuration (Figure 3.30).

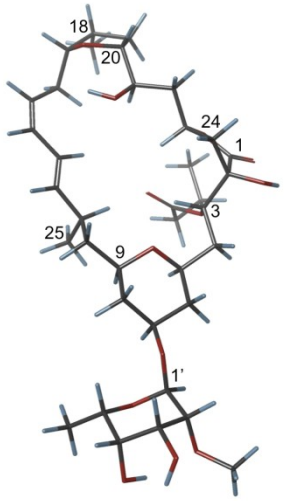

Figure 3.30. Computational model of the lowest energy conformer for mandelalide B (**2**).

The $^3J_{HH}$ values acquired in $CDCl_3$ for mandelalides B-D (**2**-**4**) were all similar, suggesting that the relative configuration of the macrocycle incorporating a γ-butyrolactone is retained. The configuration at the remaining C-24 stereocenter present in mandelalides C (**3**) and D (**4**) was assigned from ROESY data. In each case, the H-24 doublet (δ_H 3.98 and 5.17 in **3** and **4**, respectively) is correlated to the H-3 double

doublet, localizing the C-24 hydroxyl/butyrate moiety *antiperiplanar* to H-3 and H-23, in an *S* configuration.

Table 3.4. The values of interproton distances obtained for mandelalide B (**2**) from ROESY acquired at mixing time = 400ms. ǀ % errorǀ = ǀr_{clcd} - r_{ROE}ǀ / r_{clcd}, MAE = ∑(% error)/n

H_1	H_2	Experimental ROE distance in Å	Calculated ROE distance in Å	ǀ% errorǀ
19a	21	2.54	2.24	13.55
16b	21	2.79	2.11	32.08
13	21	2.26	2.81	19.72
11	21	3.35	4.42	24.18
11	23	2.99	3.21	6.67
11	3	3.10	2.59	19.72
23	3	2.17	2.26	3.96
23	21	2.46	2.43	1.46
MAE				13.92

Cytotoxicity of the organic extract from *Lissoclinum* sp. was examined against mouse Neuro-2A neuroblastoma, and human MDA-MB-231 breast and NCI-H460 lung cancer cell lines following 48 h exposure. In all cases low μg/mL IC_{50} values were obtained (Table 3.5). The Neuro-2A cell line was chosen to perform activity-guided fractionation leading to the purification of mandelalides A–D (**1-4**). The pure compounds mandelalides A and B yielded nanomolar IC_{50} values against Neuro-2A (44.0 and 83.8, respectively) and NCI-H460 (12.0 and 29.4 respectively) cell lines (Table 3.5, Figure 3.31). The potent cytotoxicities of these mandelalides are somewhat surprising given the reported minimal cytotoxicity of the related glycosylated polyketides madeirolides A and B (Figure 3.32), (Winder, 2009). The latter metabolites caused less than 50% inhibition of AsPC-1 and PANC-1 pancreatic cancer cells at 10 μg/mL, but showed potent fungicidal activity against *Candida albicans*. Madeirolides A and B share essentially the same western hemisphere of the mandelalides (C-5 to C-22), including a THP (alternatively substituted), diene, THF and neighboring hydroxymethine. The two series of compounds vary only in the

closure of the macrocycle: the position of the lactone and additional cycle. Given that the madeirolides were isolated from a deep-water lithistid *Leiodermatium* sponge, their structural relatedness is consistent with a microbial biogenetic origin. Side-by-side evaluation of the biological properties of all four mandelalides and the two madeirolides would provide insight into the structure-activity relationships that result in potent cytotoxicity and fungicidal activity, respectively. However, the inaccessible supply of both source organisms means that further investigation of these metabolites will likely await their total syntheses.

Table 3.5 Cytotoxicity of *Lissoclinum* sp. organic extract and mandelalides A (**1**) and B (**2**) to mouse Neuro-2A neuroblastoma and human NCI-H460 lung and MDA-MB-231 breast cancer cells.

	[a]IC_{50} (at 48 h) in Cancer Cell Lines:		
	NCI-H460	**Neuro-2A**	**MDA-MB-231**
organic extract	0.7 μg/mL	5.6 μg/mL	22.1μg/mL
mandelalide A (**1**)	12 nM	44 nM	-
mandelalide B (**2**)	29 nM	84 nM	-

[a]Cell viability was assessed by MTT assay and IC_{50} values were derived using nonlinear regression analysis.

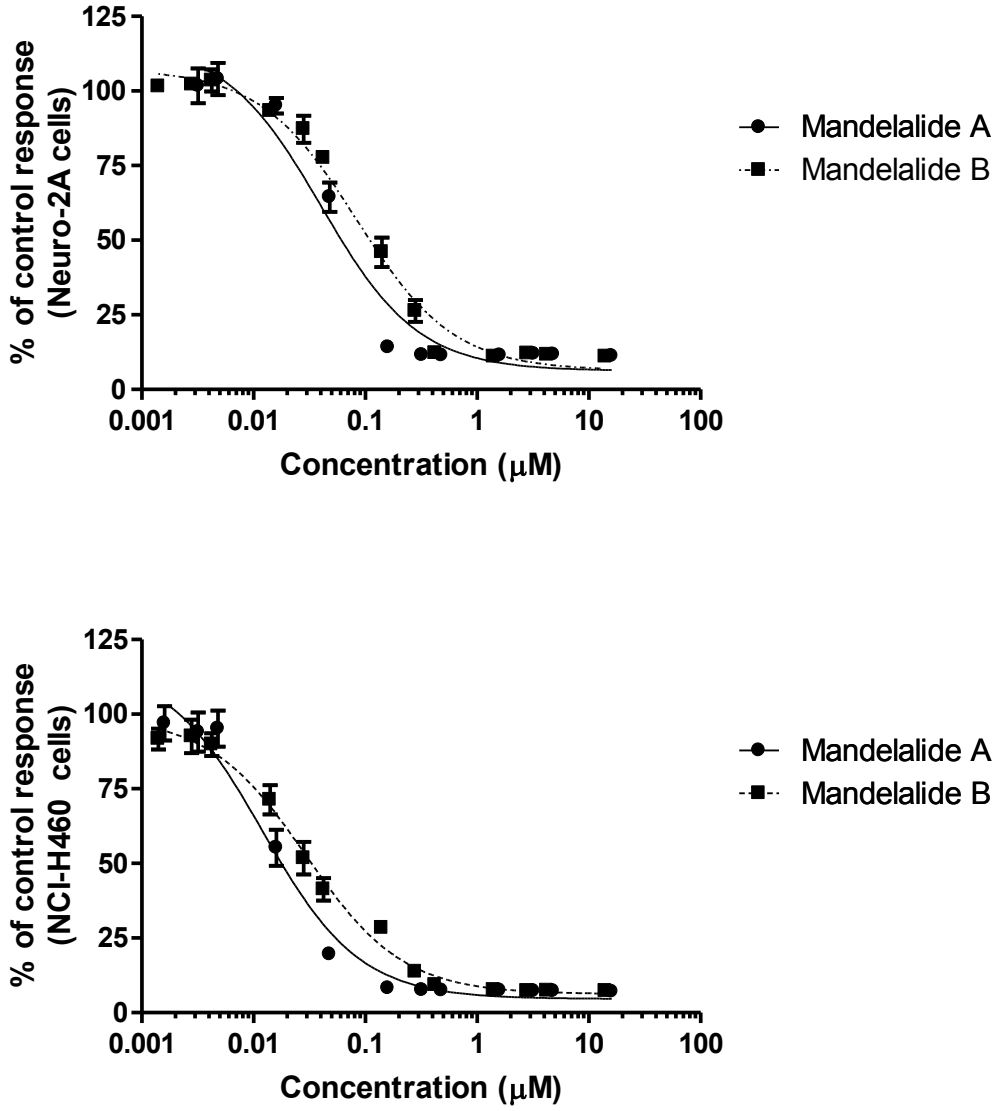

Figure 3.31. The dose response curves for mandelalides A (**1**) and B (**2**) in mouse Neuro2A neuroblastoma and human NCI-H460 cell lines, following 48 h incubation. Cell viability was assessed by MTT assay and is expressed relative to the response of solvent vehicle-treated cells.

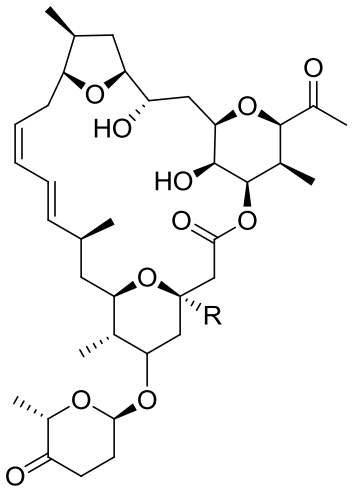

Madeirolide A, R = H
Madeirolide B, R = OH

Figure 3.32 Chemical structures for madeirolides A and B.

Experimental

General Experimental Methods. As described previously (Thornburg et al., 2011). In addition, NMR data in $CDCl_3$ were acquired at 700 (^1H) and 175 (^{13}C) MHz on a 5 mm inverse cryogenic probe. The NMR data in py-d_5, TOCSY (mixing time 100 ms), HETLOCs and gated-decoupled ^{13}C NMR experiments were obtained at 700 (^1H) and 175 (^{13}C) MHz on a 5 mm ^{13}C cryogenic probe. The spectra were referenced to internal residual solvent signals in ppm (^1H NMR: $CDCl_3$, 7.24, py-d_5, 8.74, CD_3OD, 3.31; ^{13}C NMR: $CDCl_3$, 77.23, py-d_5, 150.35, CD_3OD, 49.15). High-resolution MS data were acquired using a Water's Micromass LCT Premier spectrometer.

Extraction and Isolation. The ascidian, *Lissoclinum* sp. (Ascidiacea, Aplousobranchia, Didemnidae) was collected by hand using SCUBA at a depth of 18 m (July 20, 2004) from White Sands Reef in Algoa Bay, Eastern Cape Province, South Africa (33:59.916S, 25:42.573W). The type specimen (SAF2004-55) for this new ascidian species is housed at the South African Institute for Aquatic Biodiversity (SAIAB), Grahamstown, South Africa.

The freeze-dried organism (15.1 g) was extracted with 2:1 CH_2Cl_2-MeOH yielding 1.45 g of organic extract. This organic extract was fractionated on Sephadex LH-20 (CH_2Cl_2-MeOH, 1:3) to give eight fractions, of which fractions six and seven were subjected to reversed phase C_{18} solid phase extraction (RP-SPE) using a stepped gradient of 50-100% MeOH in H_2O. The 75% MeOH-H_2O and 100% MeOH fractions were further separated by RP-HPLC (C_{18} column, 250 mm x 10 mm, 7:3 MeOH-0.1% FA in H_2O) to yield mandelalides A (**1**, 0.8 mg), B (**2**, 0.5 mg), C (**3**, 0.8 mg) and D (**4**, 0.6 mg).

Mandelalide A (**1**). Amorphous solid; $[\alpha]^{23}_D$ –9 (*c* = 0.25, MeOH); UV (MeOH) λ_{max} (log ε) 279 (2.7), 217 (4.1); LRESIMS $[M+Na]^+$ *m/z* 647.4; HRESIMS $[M+Na]^+$

m/z 647.3394, (calcd for $C_{33}H_{52}O_{11}Na$, 647.3407); ^{1}H and ^{13}C NMR, COSY, HMBC, ROESY data (Table 3.1).

Mandelalide B (**2**). Amorphous solid; $[\alpha]^{24}_{D}$ –13 (*c* = 0.5, MeOH); UV (MeOH) λ_{max} (log ε) 279 (3.0), 229 (4.1); LRESIMS $[M+Na]^+$ *m/z* 733.5; HRESIMS $[M+Na]^+$ *m/z* 733.3773, (calcd for $C_{37}H_{58}O_{13}Na$, 733.3775); ^{1}H and ^{13}C NMR data (Tables 3.2).

Mandelalide C (**3**). Amorphous solid; UV (MeOH) λ_{max} (log ε) 280 (2.7), 229 (4.0); LRESIMS $[M+Na]^+$ *m/z* 589.5; HRESIMS $[M+Na]^+$*m/z* 589.2970, (calcd for $C_{30}H_{46}O_{10}Na$, 589.2989); ^{1}H and ^{13}C NMR data (Table 3.2).

Mandelalide D (**4**). Amorphous solid; $[\alpha]^{25}_{D}$ –50 (*c* = 0.2, MeOH); UV (MeOH) λ_{max} (log ε) 280 (2.7), 229 (4.0); LRESIMS $[M+Na]^+$*m/z* 659.5; HRESIMS $[M+Na]^+$ *m/z* 659.3424, (calcd for $C_{34}H_{52}O_{11}Na$, 659.3407); ^{1}H and ^{13}C NMR data (Table 3.3).

Deacylmandelalide D (**4b**). Amorphous solid; $[\alpha]^{27}_{D}$ –10 (*c* = 0.2, MeOH); UV (MeOH) λ_{max} (log ε) 280 (2.8), 227 (3.8); LRESIMS $[M+Na]^+$ *m/z* 519.3; HRESIMS $[M+H]^+$ *m/z* 497.2752, (calcd for $C_{26}H_{41}O_9$, 497.2751); ^{1}H and ^{13}C NMR (Table 3.3).

Measurement of $^{1,2}J_{HC}$ Coupling Constants. The sensitivity and gradient-enhanced HETLOC (ω1-hetero half-filtered TOCSY) experiment was employed to measure J_{HC} coupling constants, with DIPSI-2 spin-lock set to 60 ms (Uhrín et al., 1998). Spectral widths of 6229 Hz and 5597 Hz, with a data matrix of 4K (*F2*) x 128 (*F1*), and 146 or 96 scans were employed in py-d_5 and $CDCl_3$, respectively for mandelalide A. In the case of mandelalide B, a spectral width of 5597 Hz with a data matrix of 4K (*F2*) x 128 (*F1*) and 136 scans were implemented in $CDCl_3$. The 1D spectra that were obtained after extraction of *F2*/*F1* slices were subjected to inverse Fourier transform. The resulting FIDs were multiplied by the exponential window function prior to linear prediction processing (Sugahara et al., 2011).

TOCSY Data Acquisition. To determine the magnetization transfer pattern in 2-*O*-methyl-L-rhamnose a 2D TOCSY was acquired with a DIPSI-2 spin-lock sequence in $CDCl_3$. The spectra were recorded with a spin-lock mixing time of 100 ms, 5597 Hz

spectral width at 2K (*F2*) x 512 (*F1*) data matrix for 40 scans. Data were processed with a sine-bell squared function with 1.5 Hz (*F2*) and 0.3 Hz (*F1*) line broadening before measurement of the absolute volumes of peaks. The following designation was applied to depict intensity of peaks; grey ovals indicate intensity or signal greater than 1.5% of intensity measured for the signal of the anomeric proton, white ovals indicate intensity of at least 0.5% but no more than 1.5% intensity measured for the anomeric ^{1}H signal (Gheysen, et al., 2008).

Sample Preparation and Data Acquisition for RDC Measurement. Poly-γ-ethyl-L-glutamate (100 mg, PELG, Sigma Aldrich) was placed in a 5 mm NMR tube and 20 mg of strychnine dissolved in 1.0 mL $CDCl_3$ was added. The solution was vortexed and frozen/thawed 5 times (-70 °C for 1-2 h, variable time at rt). The degree of alignment was first measured using ^{2}H NMR and then gated decoupled ^{13}C NMR spectra were acquired (Figure 3.24).

Calculation of Dihedral Bond Angles in MestReJ (Navarro-Vázquez et al., 2004). The calculation of angles between H-3/H-4a and H-3/H-4b was performed using the Altona equation with substituents at C-3 defined as CH_2OR and OCOR, and substituents at C-4 as H and CH_2OR. Resulting $^{3}J_{HH}$ values for H-3/H-4a (138.7°) and H-3/H-4b (-102.2°) were 6.0 and 1.6 Hz, respectively.

Computational Modeling of Mandelalide B (**2**). Computational modeling was performed using the 2009 version of a contemporary software package. Minimization using the Amber* force field with PRCG algorithm, in pyridine (ε = 12.9, 10000 steps, maximum derivative less than 0.05 kcal/mol) and constrained torsion angles H-3/H-4a (138°), H-3/H-4b (-102.2°), H-4b/H-5, H-9/H-10b, H-20/H-21, H-21/H-22b, H-22a/H-23 and distance H-4b/H-24b = 5 Å was first performed. All torsions were restrained based on the $^{3}J_{HH}$ coupling constants values. The minimized structure was subjected to conformational searching using the Amber* force field via the low mode sampling method, with an energy cut off of 21 kJ/mol and 1000 steps (100 steps per rotatable bond, (Foloppe & Chen, 2009; Parish et al., 2002). Torsion restraints H-3/H-4a (138°),

H-3/H-4b (-102.2°), H-4b/H-5, H-9/H-10b, H-20/H-21, H-21/H-22b, H-22a/H-23 were applied to obtain ground state conformations. Optimization of the ten lowest energy conformations using DFT with the B3LYP functional and 6-31G** basis set in the gas phase resulted in the structure presented in Figure 3.30.

Measurement of Mandelalide B (2) ROE Distances. ROESY experiments were acquired at 700 (^{1}H) and 175 (^{13}C) MHz on a 5mm ^{13}C cryogenic probe. The sample was dissolved in py-d_5 and placed in a 3 mm low pressure/vacuum NMR tube under air without degassing (Butts et al., 2011). Ten spectra were acquired with a spin-lock that varied from 50 ms to 900 ms, with the ROESY measured at 400 ms being used for final calculations. During acquisition, 2K (*F2*) and 400 (*F1*) data points were collected in 40 scans using a sweep width of 6300 Hz. Data were processed with Bruker TopSpin 3.0 and during integration absolute values of peaks were measured. The calculation of ROE inter-proton distances was performed as described by the equation:

$$r_{ij} = r_{ref} (c_{ref} a_{ref} / c_{ij} a_{ij})^{1/6}$$

where r_{ij} is the interproton distance calculated based on ROE peak volume a_{ij}; r_{ref} is the reference distance between two protons with ROE peak volume a_{ref}; c_{ij} and c_{ref} are coefficients accounting for the offset of cross peaks relative to the transmitter center calculated from the equations:

$$c_{ij} = 1 / \sin^2\theta_i \sin^2\theta_j$$

$$\tan\theta_\alpha = \gamma B_1 / (\omega_\alpha - \omega_\theta)$$

where γB_1 is the spin lock power (2000 Hz here); $\omega_\alpha - \omega_\theta$ is the difference between the chemical shift of the analyzed peak and the center of the spectral window (in Hz, (Caporale et al., 2010; González-Gaitano & González-Benito, 2008).

Methanolysis of Mandelalide A (1). Compound **1** (0.1 mg) was treated with 1 N methanolic HCl (1.0 mL) and heated for 24 h at 70 °C with stirring. The mixture was concentrated *in vacuo*, redissolved in 0.75 mL of 1-(TMS)-imidazole/py (1:4) and the reaction was continued for 40 min at 70 °C with stirring (Lu et al., 2011). The solution

was concentrated, the final residue partitioned between CH_2Cl_2 and H_2O (1:1), and the organic fraction used for GC-MS analysis.

Preparation of 1,2-di-*O*-methyl-3,4-di-*O*-TMS-α-L-Rhamnose and 1,2-di-*O*-methyl-3,4-di-*O*-TMS-α-D-Rhamnose Standards. L-rhamnose (50 mg) was dissolved in 1N methanolic HCl, heated for 24 h at 70 °C with stirring, and concentrated *in vacuo*. The residue was redissolved in dioxane (0.6 mL) and 2 M TMS-diazomethane in diethyl ether (1.5 mL) was added, with H_3BO_3 as catalyst. The solution was maintained at room temperature with stirring for 5 h and then evaporated to dryness *in vacuo* (Evtushenko, 1999). Column chromatography on Si gel GF (15 μm) with 5% MeOH in CH_2Cl_2 as mobile phase afforded a 1:3 mixture of 1,2-di-*O*-methyl-α-L-rhamnose and 1,3-di-*O*-methyl-α-L-rhamnose in ~65% yield from this rate limiting reaction: equivalent to ~16% yield of the desired 1,2-di-*O*-methyl-α-L-rhamnose to be carried forward for silylation. This 1:3 mixture of methylation products was treated with 1-(TMS)-imidazole/py (1:4) for 40 min at 60 °C and concentrated *in vacuo* (Lu, et al., 2011). Finally, the residue was dissolved in CH_2Cl_2, loaded on a Si gel column, washed with 100% hexanes, and eluted with 3% EtOAc in hexanes to obtain pure 1,2-di-*O*-methyl-3,4-di-*O*-TMS-α-L-rhamnose in a final yield of 5.4%. The same procedure was applied to produce 1,2-di-*O*-methyl-3,4-di-*O*-TMS-α-D-rhamnose in 6.4% yield. ^{1}H NMR (700 MHz, $CDCl_3$): δ 0.12 (s, 9H), 0.15 (s, 9 H), 3.31 (s, 3H), 3.32 (dd, J = 1.7, 3.2 Hz, 1H), 3.48 (s, 3H), 3.52 (m, 1H), 3.53 (m, 1H), 3.78 (dd, J = 3.6, 8.4 Hz, 1H), 4.61 (d, J = 1.3, 1H); ^{13}C NMR (175 MHz, $CDCl_3$): δ 0.7, 1.2, 18.5, 54.8, 60.0, 69.1, 73.1, 74.3, 81.6, 98.8, ppm; CI-LR-MS: *m/z* 305 calculated for oxonium ion $C_{13}H_{29}O_4Si_2$.

Absolute Configuration of 2-*O*-methyl-α-Rhamnose from Mandelalide A (1). Analyses of the synthetic standards and permethylated and silylated mandelalide A hydrolysate were performed by GC-MS using a 30 m × 0.25 mm i.d. Cyclosil-B column, and electron impact (EI) ionization. The injector and detector were operated at 250 °C, while the temperature gradient was set to 75 – 175 °C at 0.5 °/min. The

retention times for 1,2-di-*O*-methyl-3,4-di-*O*-TMS-α-D-rhamnose and 1,2-di-*O*-methyl-3,4-di-*O*-TMS-α-L-rhamnose injected separately were 96.5 and 98.3 min, respectively. The retention time for the monosaccharide in the derivatized mandelalide A hydrolysate injected separately was 97.5 min. (Figure 3.29). Therefore co-injection of the natural product hydrolysate with each standard was performed, yielding two peaks with retention times of 96.4 and 97.4 min, which is indicative of the L glycoside in mandelalide A (Figure 3.29).

Cell Viability Assays. Cytotoxicity of the organic extract and crude fractions was evaluated in mouse Neuro-2A neuroblastoma, and human MDA-MB-231 breast and NCI-H460 lung cancer cells (ATCC, Manassas, VA) using a previously described protocol subjected to slight modifications (Thornburg, et al., 2011). Cells were seeded into 96-well plates (20,000 cells per well for MDA-MB-231 and NCI-H460; 25,000 cells per well for Neuro-2A) in 50 µL of medium twelve hours before treatment. Each test sample was added in a 25 µL aliquot generated by serial dilution in serum-free medium on the day of the experiment, after prior removal of 25 µL of media from the treated well. Aliquots were generated from stock solutions of 6 mg/mL compound in 100% DMSO. Pure compounds **1** and **2** were evaluated in Neuro-2A and NCI-H460 cells after 48 h treatment, as described above. Each compound was tested at final concentrations ranging from 0.001 µg/mL to 10 µg/mL. In all cases, cell viability was determined after 48 h treatment using a standard 3-(4,5-dimethylthiazol-2-yl)-2,5,diphenyl tetrazolium bromide (MTT) assay (Thornburg, et al., 2011). The cytotoxicity of each pure compound was assessed in at least three independent cultures with the viability of vehicle-treated control cells defined as 100% in all experiments. Dose response curves were plotted using contemporary biostatistics and curve fitting software.

Bibliography

Blunt, J. W., Copp, B. R., Keyzers, R. A., Munro, M. H. G., & Prinsep, M. R. (2012). Marine natural products. *Nat. Prod. Rep., 29*(2).

Bock, K., & Pedersen, C. (1974). A study of 13CH coupling constants in hexopyranoses. *J. Chem. Soc., Perkin Trans. 2*(3), 293-297.

Butts, C. P., Jones, C. R., Towers, E. C., Flynn, J. L., Appleby, L., & Barron, N. J. (2011). Interproton distance determinations by NOE - surprising accuracy and precision in a rigid organic molecule. *Org. Biomol. Chem., 9*(1), 177-184.

Caporale, A., Sturlese, M., Gesiot, L., Zanta, F., Wittelsberger, A., & Cabrele, C. (2010). Side Chain Cyclization Based on Serine Residues: Synthesis, Structure, and Activity of a Novel Cyclic Analogue of the Parathyroid Hormone Fragment 1−11. *J. Med. Chem., 53*(22), 8072-8079.

Cicero, D. O., Barbato, G., & Bazzo, R. (2001). Sensitivity Enhancement of a Two-Dimensional Experiment for the Measurement of Heteronuclear Long-Range Coupling Constants, by a New Scheme of Coherence Selection by Gradients. *J. Magn. Res., 148*(1), 209-213.

Corley, D. G., Moore, R. E., & Paul, V. J. (1988). Patellazole B: a novel cytotoxic thiazole-containing macrolide from the marine tunicate Lissoclinum patella. *J. Am. Chem. Soc., 110*(23), 7920-7922.

Evtushenko, E. V. (1999). Regioselective methylation of methyl glycopyranosides with diazomethane in the presence of transition-metal chlorides and of boric acid. *Carbohydr. Res., 316*(1), 187-200.

Fayette, J., Coquard, I. R., Alberti, L., Boyle, H., Méeus, P., Decouvelaere, A.-V., Thiesse, P., Sunyach, M.-P., Ranchère, D., & Blay, J.-Y. (2006). ET-743: a novel agent with activity in soft-tissue sarcomas. *Current Opinion in Oncology, 18*(4), 347-353

Foloppe, N., & Chen, I.-J. (2009). Conformational Sampling and Energetics of Drug-Like Molecules *Curr. Med. Chem., 16*, 3381-3413.

Fu, X., Palomar, A. J., Hong, E. P., Schmitz, F. J., & Valeriote, F. A. (2004). Cytotoxic Lissoclimide-Type Diterpenes from the Molluscs Pleurobranchus albiguttatus and Pleurobranchus forskalii. *J. Nat. Prod., 67*(8), 1415-1418.

Gheysen, K., Mihai, C., Conrath, K., & Martins, J. C. (2008). Rapid Identification of Common Hexapyranose Monosaccharide Units by a Simple TOCSY Matching Approach. *Chem. Eur. J., 14*(29), 8869-8878.

González-Gaitano, G., & González-Benito, J. (2008). Pseudorotaxanes of Cyclodextrin and Diglycidyl Ether of Bisphenol A as Precursors of New Intramolecularly Reinforced Epoxy-based Thermosets. *Supramol. Chem., 20*(3), 335-344.

Grindley, T. B. (2008). Structure and Conformation of Carbohydrates. In B. O. Fraser-Reid, K. Tatsuta, J. Thiem, G. L. Coté, S. Flitsch, Y. Ito, H. Kondo, S.-I. Nishimura & B. Yu (Eds.), *Glycoscience: Chemistry and Chemical Biology* (2 ed., pp. 11-13). New York: Springer.

Gschwind, R. M. (2005). Residual Dipolar Couplings—A Valuable NMR Parameter for Small Organic Molecules. *Angew. Chem., Int. Ed. Engl. , 44*(30), 4666-4668.

Le Tourneau, C., Raymond, E., & Faivre, S. (2007). Aplidine: a paradigm of how to handle the activity and toxicity of a novel marine anticancer poison. . *Curr Pharm Des*(13), 3427-3439.

Lu, Z., Van Wagoner, R. M., Harper, M. K., Baker, H. L., Hooper, J. N. A., Bewley, C. A., & Ireland, C. M. (2011). Mirabamides E−H, HIV-Inhibitory Depsipeptides from the Sponge Stelletta clavosa. *J. Nat. Prod., 74*(2), 185-193.

Motohashi, K., Takagi, M., & Shin-ya, K. (2010). Tetracenoquinocin and 5-Iminoaranciamycin from a Sponge-Derived Streptomyces sp. . *J. Nat. Prod., 73*(4), 755-758.

Navarro-Vázquez, A., Cobas, J. C., Sardina, F. J., Casanueva, J., & Díez, E. (2004). A Graphical Tool for the Prediction of Vicinal Proton−Proton 3JHH Coupling Constants. *J. Chem. Inf. Comput. Sci., 44*(5), 1680-1685.

Ogi, T., Margiastuti, P., Teruya, T., Taira, J., Suenaga, K., & Ueda, K. (2009). Isolation of C11 Cyclopentenones from Two Didemnid Species, Lissoclinum sp. and Diplosoma sp. *Mar. Drugs, 7*, 816-832.

Parish, C., Lombardi, R., Sinclair, K., Smith, E., Goldberg, A., Rappleye, M., & Dure, M. (2002). A comparison of the Low Mode and Monte Carlo conformational search methods. *J. Mol. Graphics Modell., 21*(2), 129-150.

Pearce, A. N., Chia, E. W., Berridge, M. V., Maas, E. W., Page, M. J., Webb, V. L., Harper, J. L., & Copp, B. R. (2006). E/Z-Rubrolide O, an Anti-inflammatory Halogenated Furanone from the New Zealand Ascidian Synoicum n. sp. *J. Nat. Prod., 70*(1), 111-113.

Schmidt, E. W., Donia, M. S., McIntosh, J. A., Fricke, W. F., & Ravel, J. (2012). Origin and Variation of Tunicate Secondary Metabolites. *J. Nat. Prod., 75*(2), 295-304.

Schmidt, E. W., Sudek, S., & Haygood, M. G. (2004). Genetic Evidence Supports Secondary Metabolic Diversity in Prochloron spp., the Cyanobacterial Symbiont of a Tropical Ascidian. *J. Nat. Prod., 67*(8), 1341-1345.

Schupp, P., Poehner, T., Edrada, R., Ebel, R., Berg, A., Wray, V., & Proksch, P. (2002). Eudistomins W and X, Two New β-Carbolines from the Micronesian Tunicate Eudistoma sp. *J. Nat. Prod., 66*(2), 272-275.

Seo, S., Tomita, Y., Tori, K., & Yoshimura, Y. (1978). Determination of the absolute configuration of a secondary hydroxy group in a chiral secondary alcohol using glycosidation shifts in carbon-13 nuclear magnetic resonance spectroscopy. *J. Am. Chem. Soc., 100*(11), 3331-3339.

Sugahara, K., Kitamura, Y., Murata, M., Satake, M., & Tachibana, K. (2011). Prorocentrol, a Polyoxy Linear Carbon Chain Compound Isolated from the Toxic Dinoflagellate Prorocentrum hoffmannianum. *J. Org. Chem., 76*(9), 3131-3138.

Tanaka, J.-i., & Higa, T. (1996). Zampanolide, a new cytotoxic marcrolide from a marine sponge. *Tetrahedron Lett., 37*(31), 5535-5538.

Thornburg, C. C., Thimmaiah, M., Shaala, L. A., Hau, A. M., Malmo, J. M., Ishmael, J. E., Youssef, D. T. A., & McPhail, K. L. (2011). Cyclic Depsipeptides, Grassypeptolides D and E and Ibu-epidemethoxylyngbyastatin 3, from a Red Sea Leptolyngbya Cyanobacterium. *J. Nat. Prod., 74*(8), 1677-1685.

Tsukimoto, M., Nagaoka, M., Shishido, Y., Fujimoto, J., Nishisaka, F., Matsumoto, S., Harunari, E., Imada, C., & Matsuzaki, T. (2011). Bacterial Production of the Tunicate-Derived Antitumor Cyclic Depsipeptide Didemnin B. *J. Nat. Prod., 74*(11), 2329-2331.

Ueda, K., & Hu, Y. (1999). Haterumalide B: A new cytotoxic macrolide from an Okinawan ascidian Lissoclinum sp. *Tetrahedron Lett., 40*(34), 6305-6308.

Uhrín, D., Batta, G., Hruby, V. J., Barlow, P. N., & Kövér, K. E. (1998). Sensitivity- and Gradient-Enhanced Hetero ([omega]1) Half-Filtered TOCSY Experiment for Measuring Long-Range Heteronuclear Coupling Constants. *J. Magn. Res., 130*(2), 155-161.

Winder, P. L. (2009). *Therapeutic potential, mechanism of action, and ecology of novel marine natural products.* Ph.D., Florida Atlantic University, Boca Raton.

Zabriskie, T. M., Mayne, C. L., & Ireland, C. M. (1988). Patellazole C: a novel cytotoxic macrolide from Lissoclinum patella. *J. Am. Chem. Soc., 110*(23), 7919-7920.

Zhao, H., Zong, G., Zhang, J., Wang, D., & Liang, X. (2011). Synthesis and Anti-Fungal Activity of Seven Oleanolic Acid Glycosides. *Molecules, 16*(2), 1113-1128.

AMINO ALCOHOLS FROM SOUTH AFRICAN SPECIES OF *PSEUDODISTOMA* TUNICATES.

CHAPTER FOUR

Justyna Sikorska, Shirley Parker-Nance,

Michael T. Davies-Coleman, Jane E. Ishmael, and Kerry L. McPhail

Abstract

New cyclized pseudodistaminols A and B (**1** and **2**) and linear pseudodistaminol C (**3**), as well as three known linear amino alcohols (**4**-**6**), were isolated from South African tunicates *Pseudodistoma* sp. nov. A and *Pseudodistoma digitum.* After initial degradation of these unstable metabolites during purification, their re-isolation as *N*-Boc (**1**-**3**) or *N*-Boc-phenylglycine (**4**-**6**) derivatives of the natural products permitted the assignment of planar structure through application of 1D and 2D NMR techniques. *J* coupling analysis in tandem with interpretation of NOE data led to partial assignment of relative configuration for **1**-**3**. Unfortunately, further determination of relative and absolute configuration was impeded by compound degradation and final conclusion of stereochemistry must await synthesis or re-isolation of the compounds from substantial field recollections. Determination of the relative configuration for **4**-**6** was accomplished similarly to **1**-**3**. The assignment of absolute configuration was possible after comparison of ^{1}H NMR chemical shifts for respective *N*-Boc-*R*- and *N*-Boc-*S*-phenylglycine derivatives of **4**-**6** and led to assignment of these known natural products as 2(*S*)-amino-3(*S*)-hydroxy-5(*E*)-tetradecene, 2(*S*)-amino-3(*S*)-hydroxy-5(*E*),13-tetradecadiene and (*R*)-(*E*)-1-aminotridec-5-en-2-ol, respectively.

Introduction

Widely distributed tunicates of the genus *Pseudodistoma* have been reported from most oceans and seas, and screening for biologically active components present in their extracts has led to the discovery of new purine derivatives (Appleton et al., 2004), β-carbolines [e.g. opacalines A-C, (Chan et al., 2011), and eudistomin V (Davis et al., 1998)], indole alkaloids [e.g. aborescidines A-D, (Chbani et al., 1993)], 6-hydroxyquinoline alkaloids [e.g. distomadines A-B, (Pearce et al., 2003)], and many linear or cyclized amino alcohols [e.g. obscuraminol A, (Garrido et al., 2001), and pseudodistomin D, (Freyer et al., 1997)]. Among these nitrogen-containing compounds, amino alcohols constitute a large group of primarily antibacterial (Clark et al., 2001), but also antifungal (Searle & Molinski, 1993) and moderately cytotoxic natural products (Garrido, et al., 2001). To date the characterized amino alcohols vary in number, localization and stereochemistry of double bonds as well as in the presence or absence of a cyclized (piperidine) terminal moiety. Nevertheless, all compounds have a characteristic amino alcohol fragment and a long aliphatic chain that make them structurally related to spisulosine, a natural product (isolated from a bivalve) that is currently in phase I clinical trials against solid tumors (Vilar et al., 2012).

In the course of our search for bioactive compounds from a collection of South African tunicates, two distinct *Pseudodistoma* extracts were analyzed: SAF04-53 from *Pseudodistoma* sp. and SAF04-48 from *P. digitum*. Organic extracts from both tunicates showed strong cytotoxicity in the brine shrimp assay. However, nitrogenous constituents identified in the active fractions were inseparable under the available chromatographic conditions. Derivatization of the *Pseudodistoma* sp. extract (SAF04-53) with di-*tert*-butyl dicarbonate enabled separation of the cyclized pseudodistaminols A (**1**) and B (**2**) and linear pseudodistaminol C (**3**) as their *tert*-butyloxycarbonyl (Boc) derivatives. To our knowledge this is the first description of amino alcohols that possess a terminal tetrahydropyran moiety. Unfortunately, degradation of these metabolites prevented any assignment of absolute configuration

or biological testing of the pure compounds. In the case of the extract from *P. digitum* (SAF04-48), direct derivatization of each of two extract portions with either *N*-Boc-*R*- or *N*-Boc-*S*-phenylglycine resulted in the purification and assignment of absolute configuration of C_{13} and C_{14} amines previously reported by Hooper et al. from an unidentified species of South African *Pseudodistoma* (Hooper et al., 1995).

Results and Discussion

During biological screening of South African tunicate extracts for cytotoxic compounds using brine shrimp assays, two extracts of *Pseudodistoma* species were identified as active, from the new species *Pseudodistoma* sp., nov. A, Parker-Nance 2008, and from the known *P. digitum* (Parker-Nance, 2003). Cytotoxicity-guided fractionation of the *Pseudodistoma* sp. nov. A extract led to identification of new cyclized pseudodistaminols A and B (**1** and **2**) and linear pseudodistaminol C (**3**), which were separable only after conversion to their *N*-Boc derivatives. Fractionation of the *P. digitum* extract on Sephadex LH-20, and subsequent derivatization of two separate portions of the active fraction with *N*-Boc-*R*- and *N*-Boc-*S*-phenylglycine, enabled isolation of the previously reported linear amino alcohols (2*S*)-amino-(3*S*)-hydroxy-(5*E*)-tetradecene (**4**), (2*S*)-amino-(3*S*)-hydroxy-(5*E*),13-tetradecadiene (**5**) and (1*R*) -aminotridec-(4*E*)-en-2-ol (**6**) (Hooper, et al., 1995; Searle & Molinski, 1993).

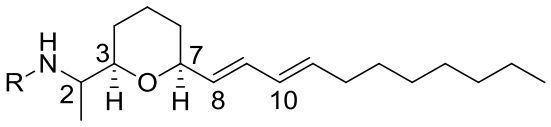

1 R = H
1a R = Boc

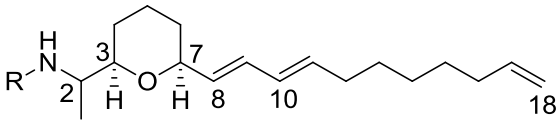

2 R = H
2a R = Boc

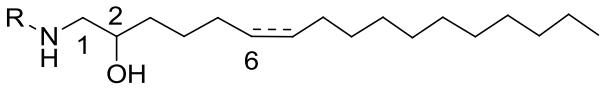

3 R = H
3a R = Boc

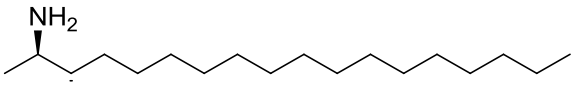

Spisulosine

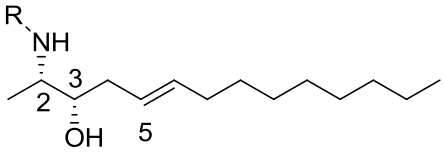

4 R = H
4a R = *N*-Boc-*S*-phenylglycine
4b R = *N*-Boc-*R*-phenylglycine

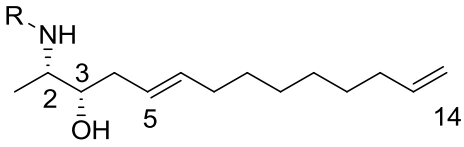

5 R = H
5a R = *N*-Boc-*S*-phenylglycine
5b R = *N*-Boc-*R*-phenylglycine

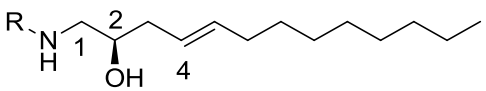

6 R = H
6a R = *N*-Boc-*S*-phenylglycine
6b R = *N*-Boc-*R*-phenylglycine

The HRESIMS of Boc-derivatized pseudodistaminol A (**1a**) gave an $[M+Na]^+$ ion at *m/z* 402.2972, indicating a molecular formula of $C_{23}H_{41}NO_3$ and four degrees of unsaturation. The ^1H NMR spectrum for **1a** showed four deshielded olefinic resonances (δ_H 5.54–6.19), and three midfield resonances (δ_H 3.25, 3.52 and 3.84) indicative of heteroatom bearing groups (Figure 4.1, Table 4.1). The ^{13}C, HSQC and HMBC NMR spectra confirmed the presence of an *N*-Boc group (δ_C 28.7, 80.1, 158.4), four olefinic methine carbons (δ_C 131.5, 131.6, 133.2, 135.9), three heteroatom-bearing methine carbons (δ_C 51.5, 79.6, 82.1), nine aliphatic methylene carbons (δ_C 23.9–33.8) and two methyl groups (δ_C 14.6 and 16.8; Figures 4.2–4.4). COSY correlations readily delineated a diene moiety (H-8 to H-11), of which H-11 (δ_H 5.67) was contiguous with a terminal 7-carbon aliphatic chain (H_2-12 to H_3-18), while H-8 (δ_H 5.54) coupled to midfield multiplet H-7 (δ_H 3.82, Figure 4.5). H-7 was in turn COSY-correlated to diastereotopic H_2-6 and the spin system could be extended through two additional alicyclic methylenes to deshielded methines H-3, H-2 and finally H_3-1 (δ_H 1.10, d). This continuous spin system spanning H_3-1 to H_3-18 was also supported by HMBC data. A ROESY correlation between H-3 (δ_H 3.25) and H-7 (δ_H 3.84) suggested cyclization of the linear spin system into a tetrahydropyran motif α to the diene, despite the absence of any HMBC correlations. Finally, an HMBC correlation from H-2 to carboxyl C-1′ localized the *N*-Boc moiety at the C-2 position. The *trans* stereochemistry of olefins H-8/H-9 and H-10/H-11 were established from the large size of the $^3J_{HH}$ coupling constants, 15.3 Hz and 14.1 Hz, respectively. The ROESY (noted above) and 1D NOE correlation between H-3 and H-7 was indicative of a *cis* oriented tetrahydropyran ring (Figures 4.6, 4.7). Assignment of the relative configuration between H-2 and H-3 was not possible based on the available spectroscopic information, which included a medium size $^3J_{HH}$ value (5.7 Hz) and an absence of any ROE correlation between the two protons. Unfortunately, degradation of compound **1a** made further assignment of the relative and absolute configuration at C-2 impossible.

The molecular formula of Boc-derivatized pseudodistaminol B (**2a**) is proposed as $C_{23}H_{39}NO_3$ based on LRESIMS $[M+Na]^+$ at *m/z* 400.2. Five degrees of unsaturation suggested the presence of an additional double bond in **2a** relative to **1a**, which was confirmed by six downfield ^1H and ^{13}C NMR chemical shifts at δ_H 4.94, 5.55, 5.67, 5.80, 6.01 and 6.19, and δ_C 114.9, 131.5, 131.6, 133.2, 135.6 and 140.2 (Figures 4.8 and 4.9, Table 4.1). A deshielded methylene ^1H resonance at δ_H 4.94 was COSY-coupled to the olefinic methine multiplet at δ_H 5.80, which was in turn coupled to an aliphatic methylene resonance at δ_H 2.04, indicating that the third unsaturation is localized at the terminus of the aliphatic chain (Figures 4.10, 4.11). Comparison of the upfield regions of the ^1H and ^{13}C NMR spectra for **1a** and **2a** revealed strong similarities, confirming the structure of **2a** as the same as that of **1a**, but with an additional (terminal) double bond. $^3J_{HH}$ coupling constants for the conjugated diene and a ROESY correlation between H-3 and H-7 supported retention of relative configuration in the C-3/C11 fragment between **1a** and **2a** (Figure 4.12).

The molecular formula of Boc-derivatized pseudodistaminol C (**3a**) was calculated as $C_{22}H_{43}NO_3$, based on LRESIMS data for $[M+Na]^+$ at *m/z* 392.2. Two degrees of unsaturation, in parallel with a downfield ^{13}C resonance (δ_C 131.0) that was HSQC-correlated to a 2H triplet δ_H 5.34, indicated the presence of only one double bond and the *N*-Boc carbonyl group (Figures 4.13 – 4.15). A pair of mid-field diastereotopic methylene protons (δ_H 2.96, 3.11) were COSY-correlated to an oxymethine (δ_H 3.56) and HMBC-correlated to the amide carbonyl at δ_C 159.2 (Figures 4.16, 4.17). These data, together with the absence of a correlated methyl doublet, suggested that the C-1 terminal methyl in **1a** and **2a** is absent in **3a**. Placement of the double bond proved intractable based on COSY and HMBC interpretation due to strong overlap of the ^1H signals in the aliphatic methylene region (δ_H 1.28–1.38). Unfortunately, degradation of compound **3a** prevented further structure assignment, for example by GC-MS.

Table 4.1. ^{1}H and ^{13}C NMR data for Boc-derivatized pseudodistaminols A and B (**1a** and **2a**) in CD_3OD.

	Pseudodistaminol A (**1a**)		Pseudodistaminol B (**2a**)	
No.	δ_C (mult)	δ_H (mult, *J* in Hz)	δ_C (mult)	δ_H (mult, *J* in Hz)
1	16.8 (CH_3)	1.1 (d, 6.8)	17.8 (CH_3)	1.12 (d, 6.7)
2	51.5 (CH)	3.52 (m)	51.3 (CH)	3.59 (m)
3	82.1 (CH)	3.25 (ddd, 11.6, 5.7, 1.4)	81.4 (CH)	3.30 (m)
4ax	29.0 (CH_2)	1.22 (m)	33.1 (CH_2)	1.26 (m)
4eq		1.61 (m)		1.52 (m)
5ax	24.6 (CH_2)	1.54 (m)	24.5 (CH_2)	1.62 (m)
5eq		1.89 (m)		1.88 (m)
6ax	33.2 (CH_2)	1.27 (m)	28.9 (CH_2)	1.26 (m)
6eq		1.61 (m)		1.62 (m)
7	79.6 (CH)	3.84 (dd, 11.0, 5.5)	79.5 (CH)	3.85 (dd, 11.0, 5.8)
8	133.2 (CH)	5.54 (dd, 15.3, 5.9)	133.2 (CH)	5.55 (dd, 15.0, 5.8)
9	131.6 (CH)	6.19 (dd, 15.3, 10.0)	131.6 (CH)	6.19 (dd, 15.6, 11.0)
10	131.5 (CH)	6.01 (dd, 14.7, 11.2)	131.5 (CH)	6.01 (dd, 15.0, 11.0)
11	135.9 (CH)	5.67 (ddd, 14.1, 6.5, 6.5)	135.8 (CH)	5.67 (dt, 14.5 6.7)
12	33.8 (CH_2)	2.08 (dt, 6.9, 6.9)	33.7 (CH_2)	2.08 (m)
13	30.6 (CH_2)	1.40 (m)	28.9-30.4 (CH_2)	1.39 (m)
14	30.4 (CH_2)	1.30 (m)	28.9-30.4 (CH_2)	1.39 (m)
15	30.4 (CH_2)	1.30 (m)	28.9-30.4 (CH_2)	1.39 (m)
16	33.2 (CH_2)	1.27 (m)	35.0 (CH_2)	2.04 (m)
17	23.9 (CH_2)	1.32 (m)	140.2 (CH_2)	5.80 (m)
18	14.6 (CH_2)	0.90 (t, 6.7)	114.9 (CH_2)	4.94 (m)
1′	158.4 (C)		158.3 (C)	
2′	80.1 (C)		80.1 (C)	
3′	28.7 (CH_3)	1.44 (s)	28.9 (CH_3)	1.44 (s)

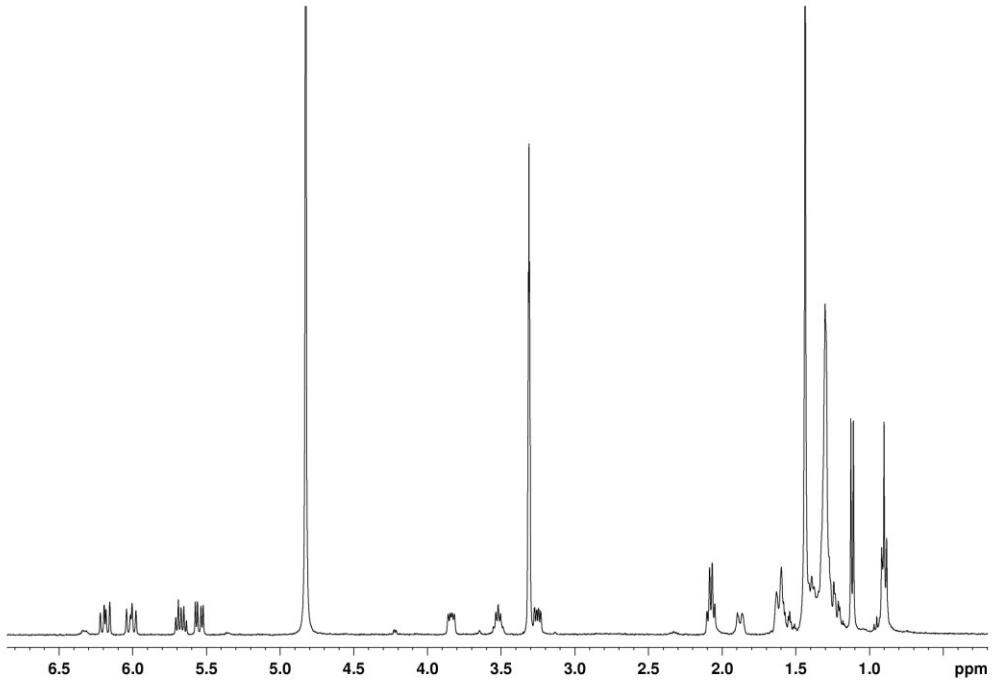

Figure 4.1 ^{1}H NMR spectrum for Boc-pseudodistaminol A (**1a**; 400 MHz, CD_3OD)

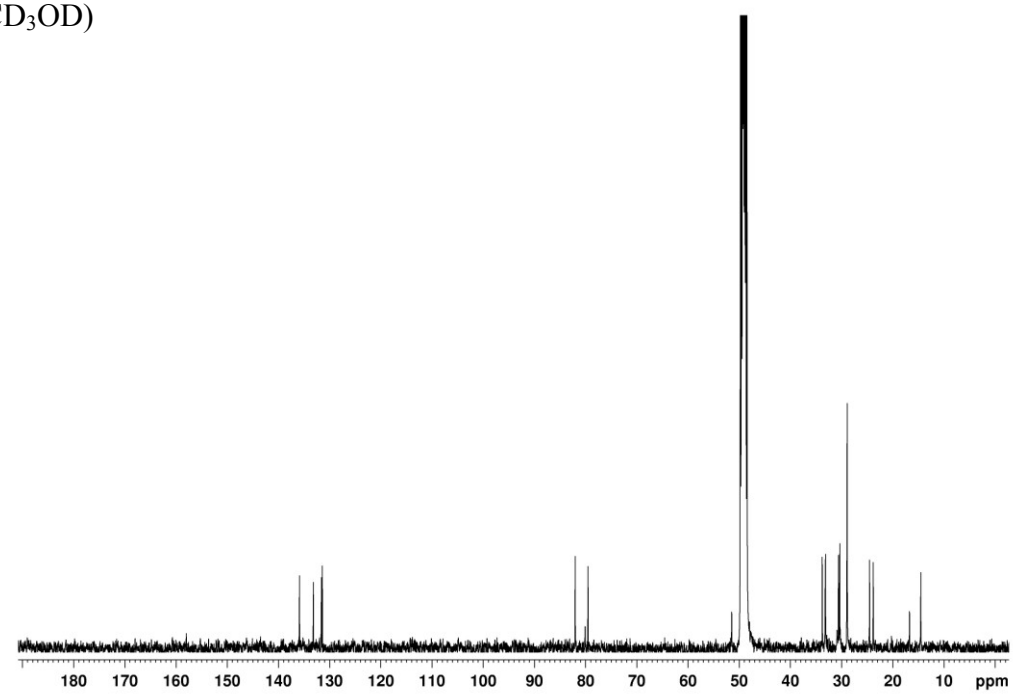

Figure 4.2 ^{13}C NMR spectrum for Boc-pseudodistaminol A (**1a**; 100 MHz, CD_3OD)

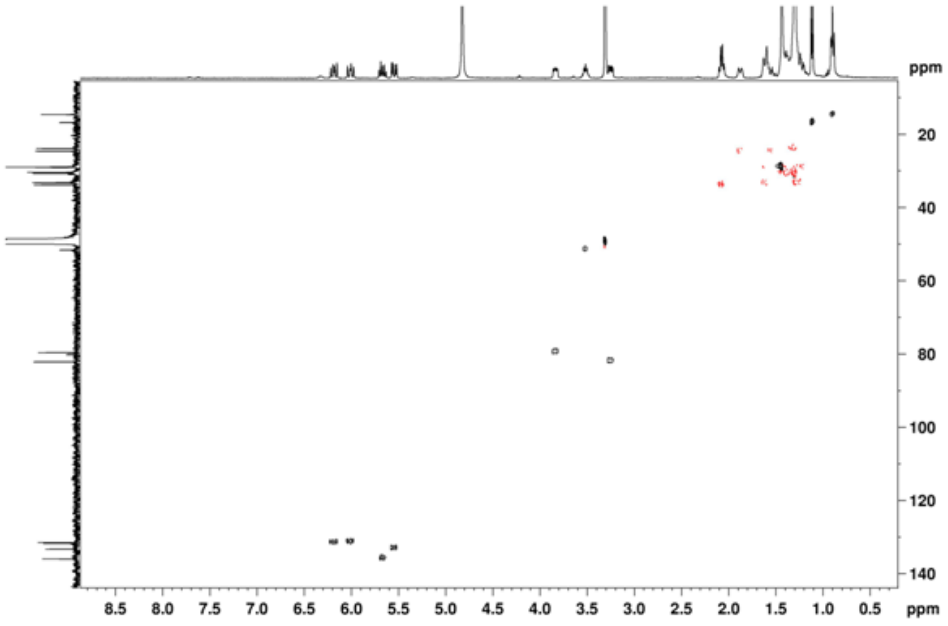

Figure 4.3 HSQC spectrum for Boc-pseudodistaminol A (**1a**; 400 MHz, CD_3OD)

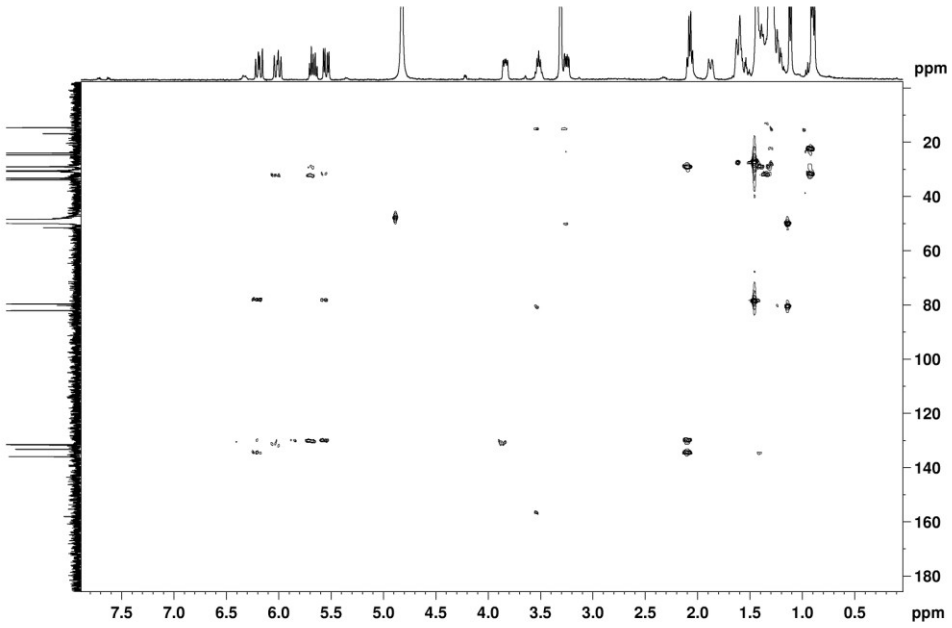

Figure 4.4 HMBC spectrum for Boc-pseudodistaminol A (**1a**; 400 MHz, CD_3OD)

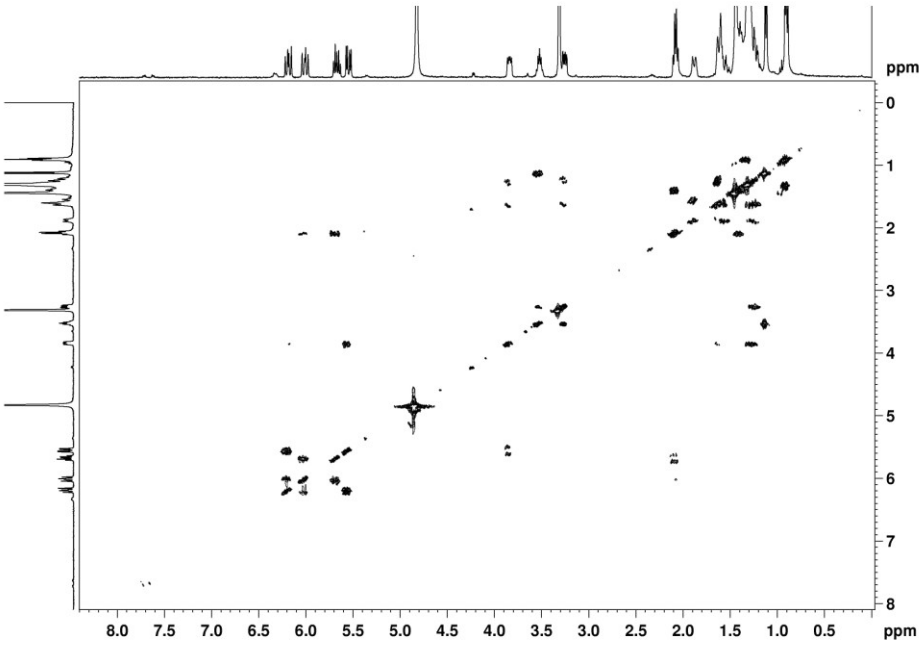

Figure 4.5 COSY spectrum for Boc-pseudodistaminol A (**1a**; 400 MHz, CD_3OD)

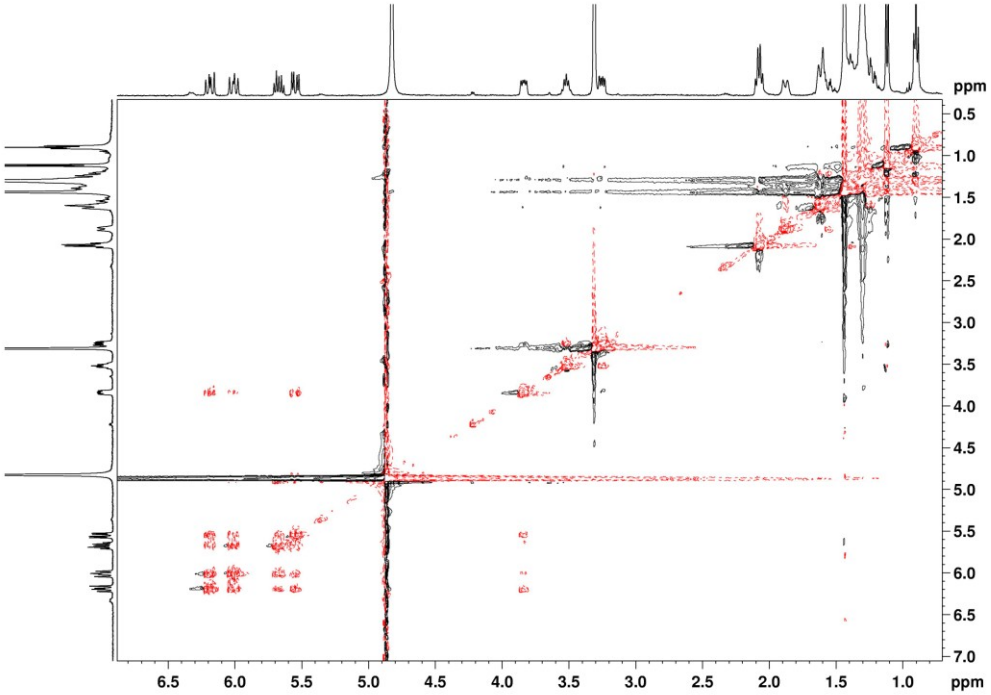

Figure 4.6 ROESY spectrum for Boc-pseudodistaminol A (**1a**; 400 MHz, CD_3OD)

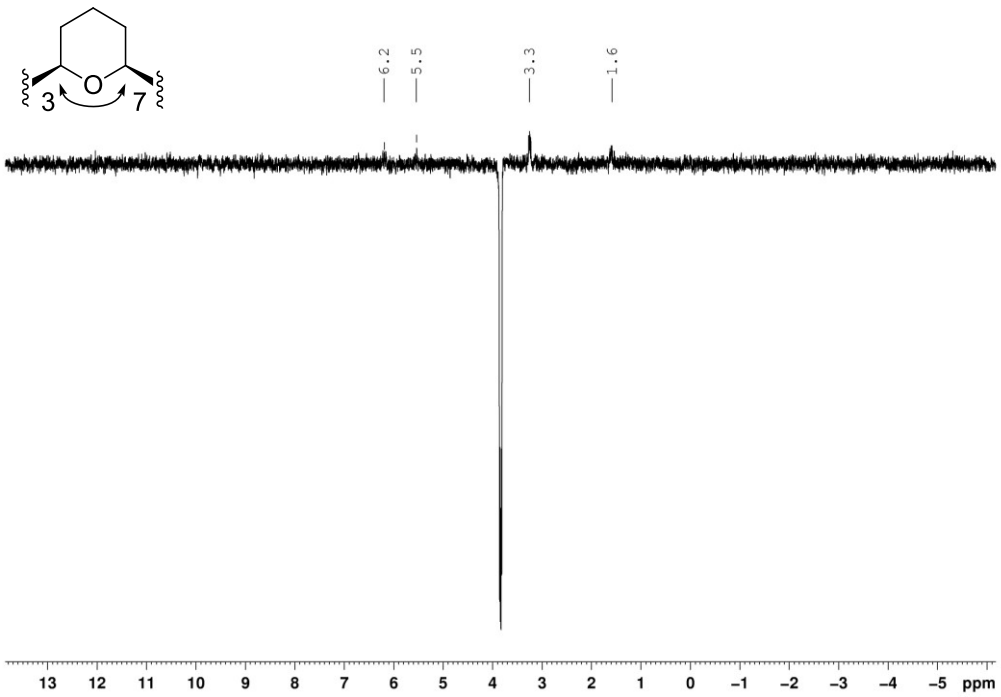

Figure 4.7 1D NOESY spectrum for Boc-pseudodistaminol A confirming a *cis* THP ring, as indicated on partial structure (**1**; 400 MHz, CD_3OD)

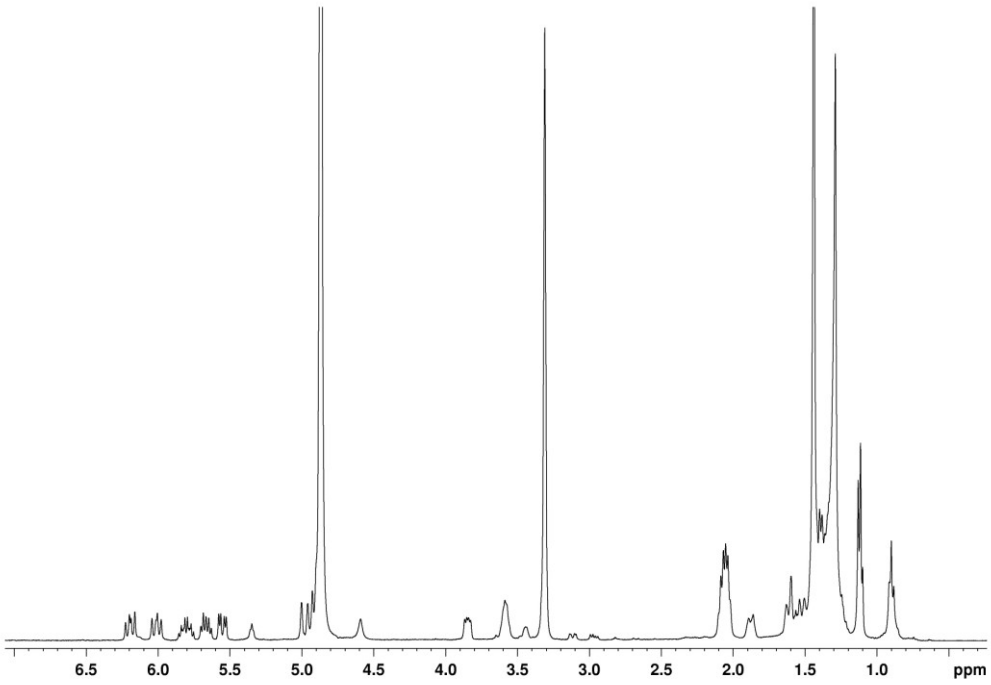

Figure 4.8 ^{1}H NMR spectrum for Boc-pseudodistaminol B (**2a**; 400 MHz, CD_3OD)

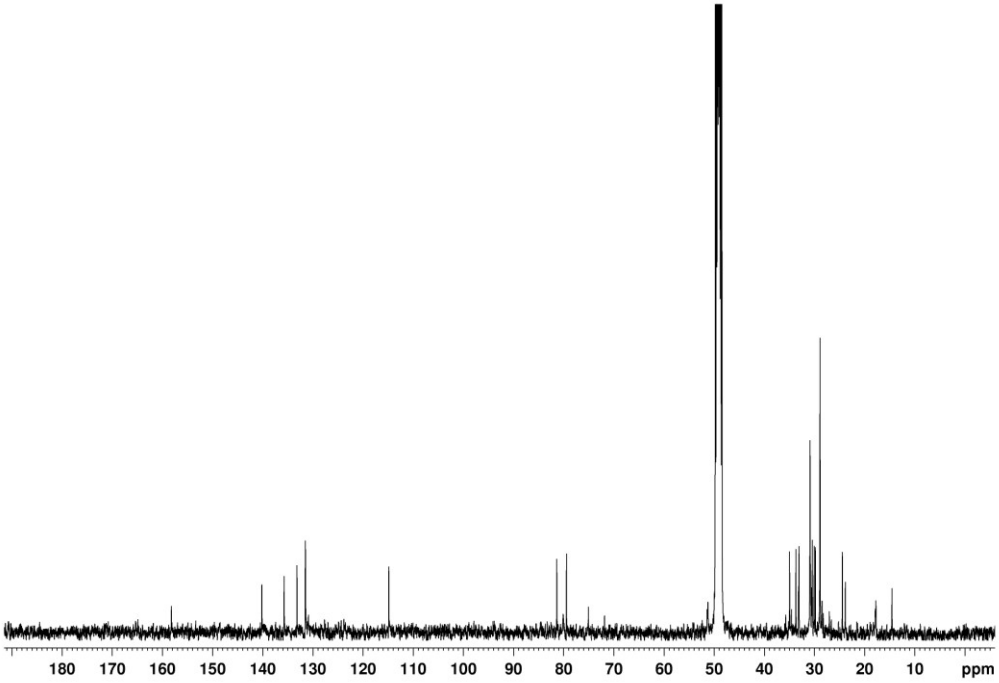

Figure 4.9 ^{13}C NMR spectrum for Boc-pseudodistaminol B (**2a**; 100 MHz, CD_3OD)

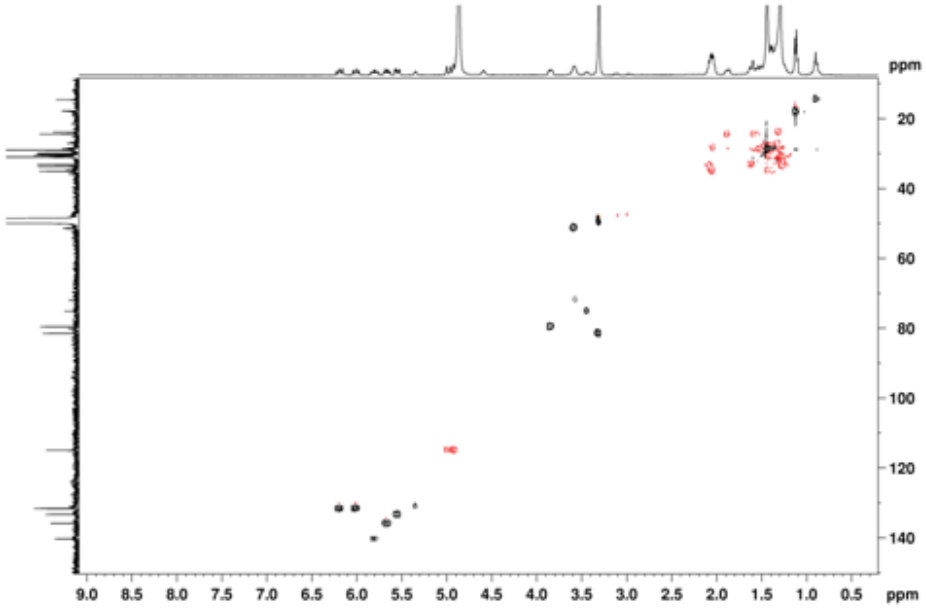

Figure 4.10 HSQC spectrum for Boc-pseudodistaminol B (**2a**; 400 MHz, CD_3OD)

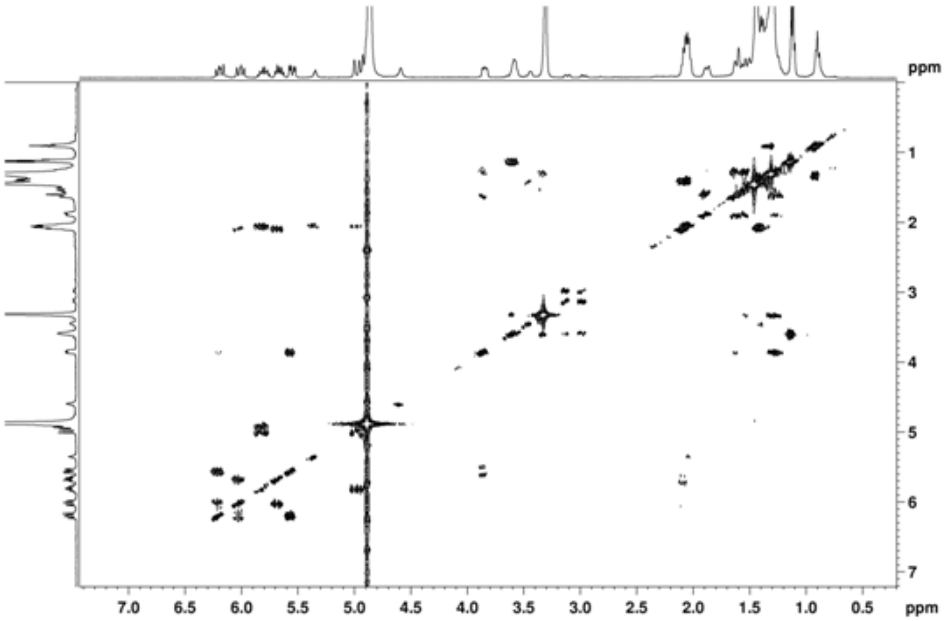

Figure 4.11 COSY spectrum for Boc-pseudodistaminol B (**2a**; 400 MHz, CD_3OD)

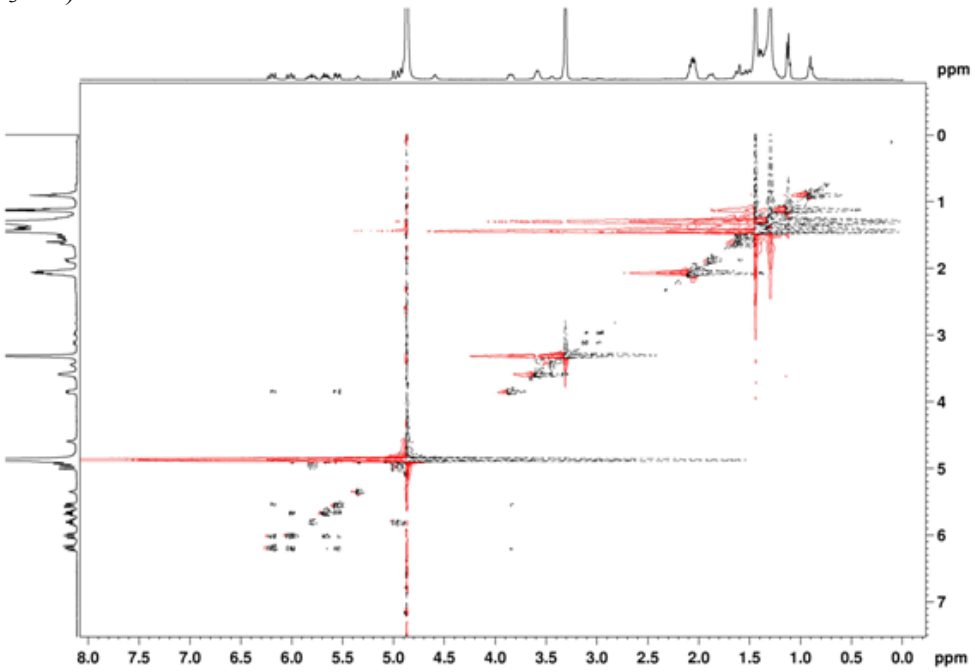

Figure 4.12 ROESY spectrum for Boc-pseudodistaminol B (**2a**; 400 MHz, CD_3OD)

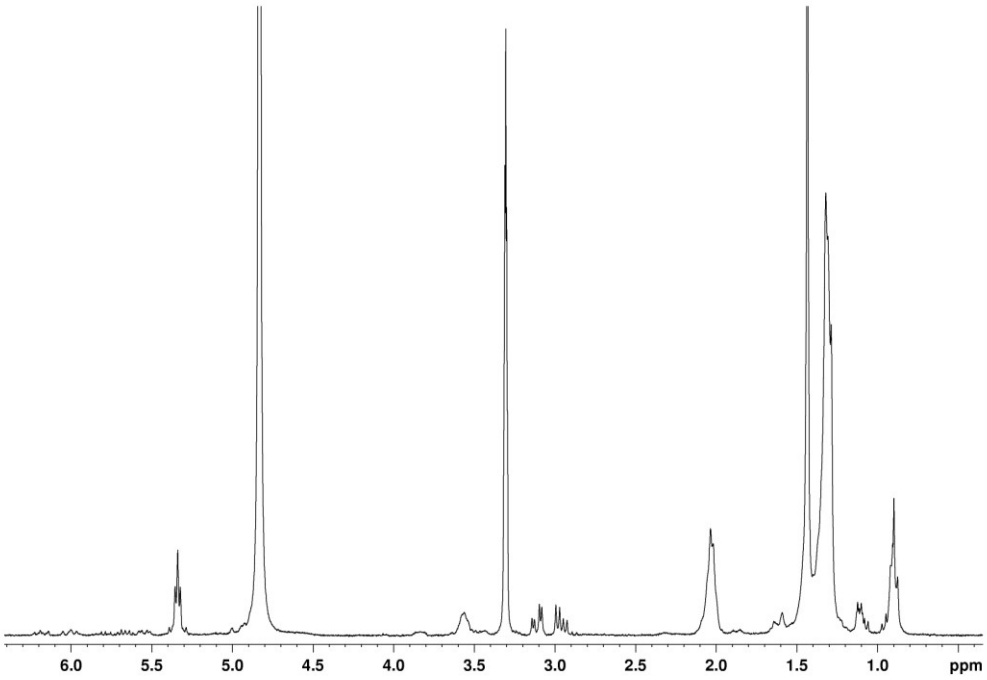

Figure 4.13 ^{1}H NMR spectrum for Boc-pseudodistaminol C (**3a**; 400 MHz, CD_3OD)

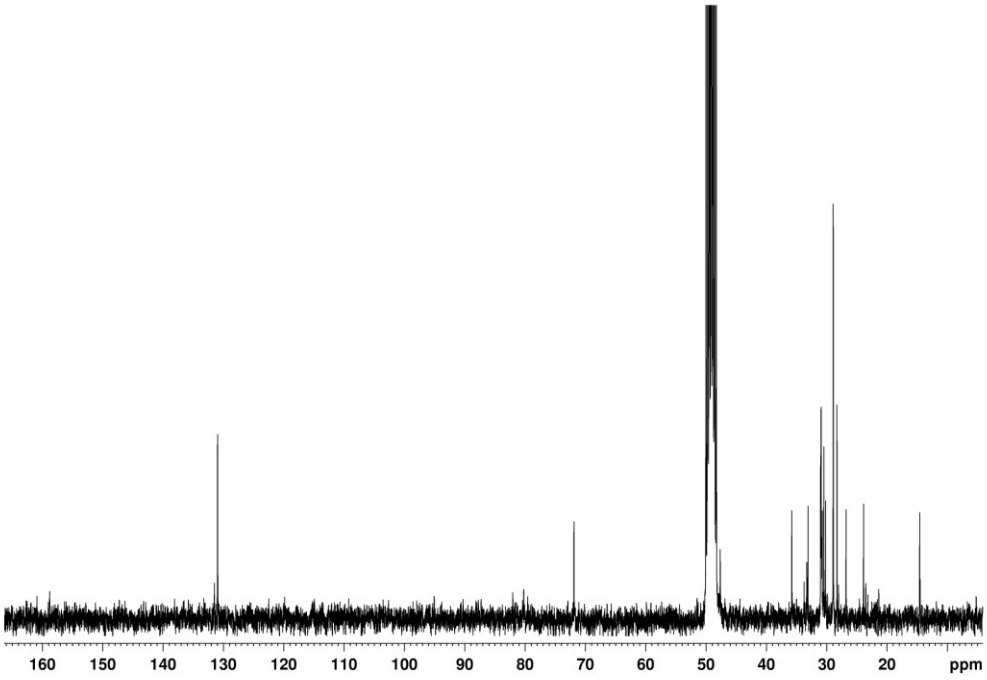

Figure 4.14 ^{13}C NMR spectrum for Boc-pseudodistaminol C (**3a**; 100 MHz, CD_3OD

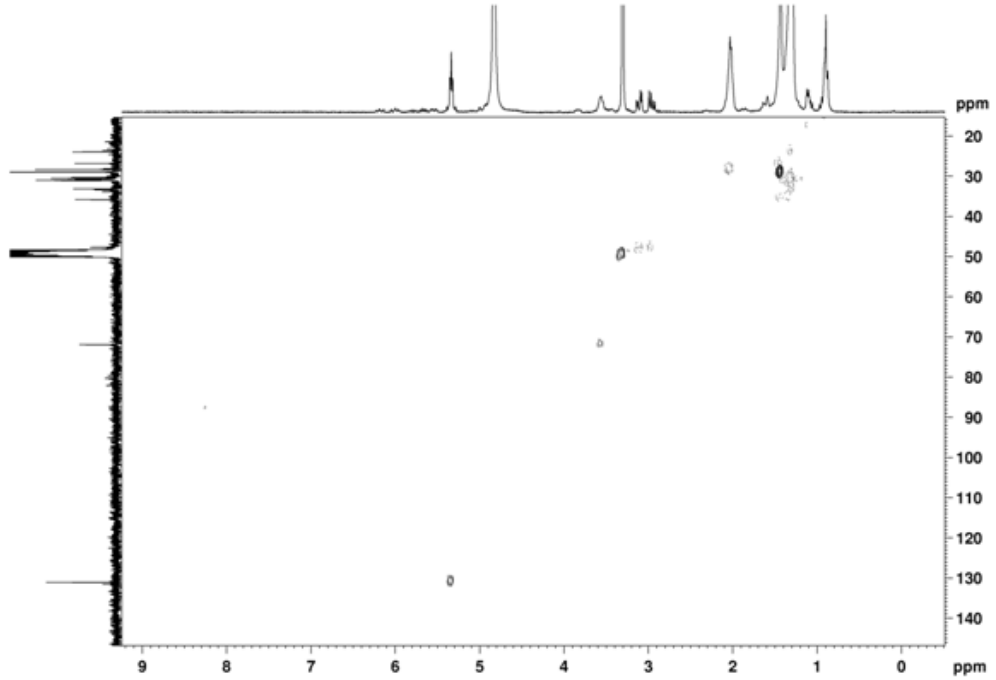

Figure 4.15 HSQC spectrum for Boc-pseudodistaminol C (**3a**; 400 MHz, CD_3OD)

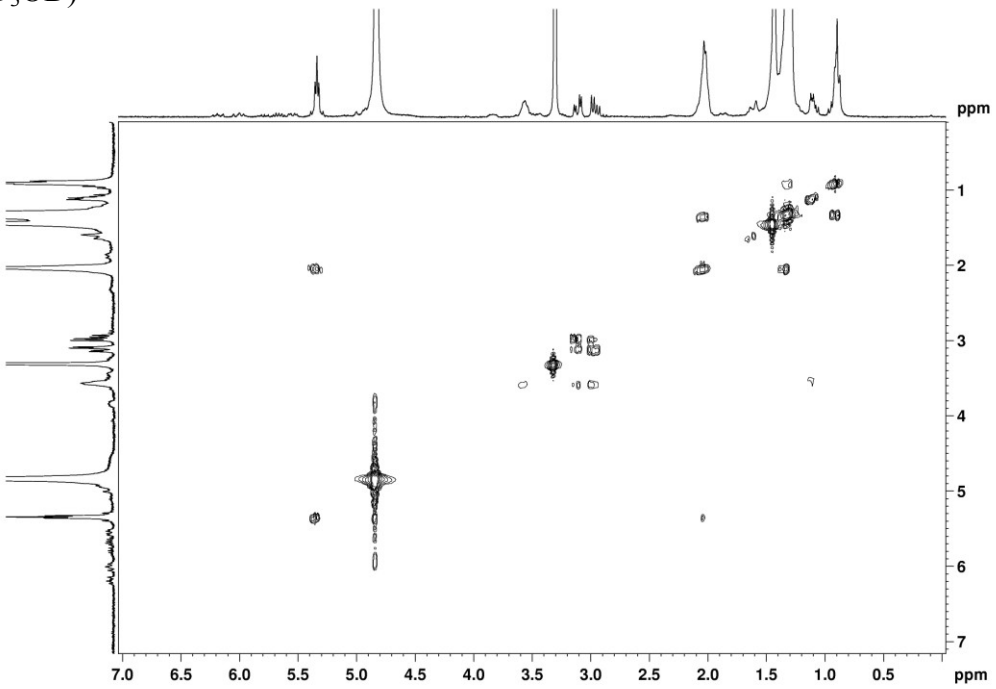

Figure 4.16 COSY spectrum for Boc-pseudodistaminol C (**3a**; 400 MHz, CD_3OD)

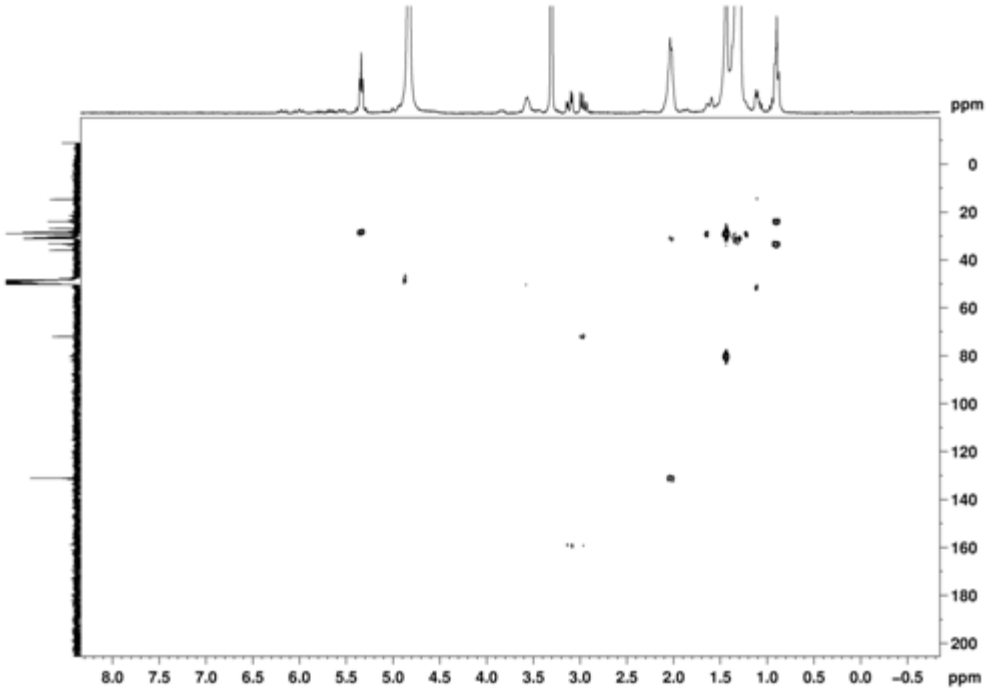

Figure 4.17 HMBC spectrum for Boc-pseudodistaminol C (**3a**; 400 MHz, CD_3OD)

Compound **4a**, the *N*-Boc-*S*-phenylglycine derivative of compound **4**, has a molecular formula of $C_{27}H_{45}N_2O_4$, as calculated for the HRESIMS $[M+H]^+$ ion at *m/z* 461.3398, which indicates seven degrees of unsaturation. Analysis of ^1H and ^{13}C NMR spectra confirmed the presence of Boc-phenylglycine (δ_H 1.39, 5.93, 7.28, 7.33, 7.24 and δ_C 28.5, 127.3, 128.5, 129.2, 155.3, 169.8), one double bond (δ_C 124.9, 136.0) and two carbons (δ_C 48.5 and 73.1) attached to nitrogen and oxygen, respectively (Table 4.2, Figures 4.18 and 4.19). Inspection of the COSY spectrum revealed correlations between the olefinic ^1H signals at δ_H 5.17 and 5.19 (H-5 and H-6) and diastereotopic multiplets at δ_H 1.57 and 1.90 (H-4a,b), with the latter being correlated further to the midfield H-3 signal (δ_H 3.39, Figure 4.20). Thus the double bond was localized β to the hydroxylated C-3 and the planar structure of **4** delineated. The measurement of coupling constants between H-2 and H-3 localized them in a *gauche* orientation, while the presence of NOE correlations (Figure 4.21, 4.23) confirmed that H-2 is localized *anti* to OH-3 and H-3 is localized *anti* to NHR-2. The close ^1H overlap between H-5 and H-6 in the *N*-Boc-*S*-phenylglycine derivative required measurement of the H-5/H-6 coupling constant in the *N*-Boc-*R*-phenylglycine amide **4b** ($^3J_{HH}$ = 14.3 Hz) and indicated a *trans* double bond geometry (Figure 4.22). Comparison of ^1H NMR shifts between *N*-Boc-*R*- and *N*-Boc-*S*-phenylglycine amides of **4** (Figure 4.23) allowed the conclusion that the amino alcohol **4** was previously isolated as a diacetate derivative by the Michael T. Davies-Coleman (Hooper, et al., 1995), and M. L. Ciavatta groups (Ciavatta et al., 2010).

The molecular formula of $C_{27}H_{42}N_2O_4$, calculated for compound **5a** from the HRESIMS $[M+Na]^+$ ion at *m/z* 481.3040, indicated that **5a** lacked two hydrogen atoms as compared to **4a**. A high degree of similarity was observed when ^1H and ^{13}C NMR spectra for **4a** and **5a** (Figures 4.24, 4.25) were compared. The main difference was the presence of three additional downfield ^1H signals (δ_H 5.79, 4.98 and 4.92) that were HSQC-correlated (Figure 4.26) to downfield methylene (C-13) and methine (C-14) carbons (δ_C 114.4 and 139.3, respectively), which supported the presence of a terminal double bond in **5a**. Analysis of homonuclear coupling constants for the C-2

and C-3 chiral centers, as well as the Δ^5 olefin (in the *N*-Boc-*R*-phenylglycine amide, **5b**) confirmed retention of relative configuration between **4a**, **4b** and **5a**, **5b** (Table 4.3, Figure 4.27). Comparison of the chemical structure of **5a** with previously isolated natural products showed that similar to **4a**, the amino alcohol **5** was previously isolated as an acetate derivative (Hooper, et al., 1995).

The HRESIMS $[M+Na]^+$ ion at *m/z* 469.3036 for **6a** suggested a molecular formula of $C_{26}H_{42}N_2O_4$. The ^1H NMR and HSQC spectra showed three midfield ^1H signals (δ_H 3.66, 3.46 and 3.10), the more upfield two of which were correlated to a methylene carbon at δ_C 45.0, suggesting that the terminal methyl group CH_3-1 in **4a** is missing in **6a** (Figures 4.28-4.30). In the COSY spectrum for **6a**, geminally-coupled midfield ^1H resonances at δ_H 3.44 and 3.10 (H_2-1) correlated to the multiplet at δ_H 3.61 (H-2), which was further coupled to upfield ^1H resonances at δ_H 1.95 and 1.20 (H-3a and H-3b) and downfield ^1H resonances at δ_H 5.29 and 5.42 (H-4 and H-5) (Figure 4.31). The large coupling constant between H-4 and H-5 ($^3J_{HH}$ = 14.5 Hz) in **6a** and **6b** supported a *trans* double bond geometry (Figure 4.32). Further literature searching identified the amino alcohol of **6a** and **6b** as (*R*)-(*E*)-1-aminotridec-5-en-2-ol previously isolated from *Didemnum* sp. as an *N*-Boc derivative (Searle & Molinski, 1993).

The cytotoxicity of *R*- and *S*-BPG derivatives of compounds **4**-**6** was examined against mouse Neuro-2A neuroblastoma, and human NCI-H460 lung cancer cell lines following 48 h exposure. The IC_{50} values against Neuro-2A and NCI-H460 cell lines for the pure compounds are reported in Table 4.4. The fractions from organic extracts of both *Pseudodistoma* samples caused 100 % death of Neuro-2A cells at 30 µg/mL after 24 h treatment; however compounds **5b**, **6a** and **6b**, after derivatization with BPG, showed only mild activity against both cell lines after 48 h treatment. Interestingly, the *R*-BPG derivative of **5** showed stronger activity than its *S*-BPG analogue, suggesting that the presence of an aromatic group shielding the aliphatic chain is detrimental to the activity. A literature report comparing the clavaminols,

isolated from *Clavelina phlegraea*, to spisulosine suggested that a 2*S*, 3*R* configuration of the amino alcohol leads to more potent activity than a 2*R*, 3*S* configuration (Menna, 2009). However, no compound containing the 2*S*, 3*S* stereochemistry, as assigned for compounds **4** – **5** here, was isolated for comparison in that report. The presence of an additional *cis* double bond was detrimental for activity of the clavaminols, while in the case of **4b** and **5b** here, an increase in activity is observed and presumed due to the second unsaturation. Finally, for both the clavaminols and amino alcohols **4** – **6**, a marked decrease in activity was observed after derivatization, indicating the necessity of the free amine for cytotoxic effect.

Table 4.2. ^{1}H and ^{13}C NMR data for derivatized amino alcohols **4a** and **4b** in $CDCl_3$

	S-BPG derivatized amino alcohol **4a**		*R*-BPG derivatized amino alcohol **4b**
No.	δ_C (mult)	δ_H (mult, *J* in Hz)	δ_H (mult, *J* in Hz)
1	18.8 (CH_3)	1.18 (d, 6.9)	1.05 (d, 6.9)
2	48.5 (CH)	3.92 (m)	3.94 (m)
3	73.2 (CH)	3.39 (ddd, 8.9, 4.1, 2.2)	3.48 (m)
4a	37.9 (CH_2)	1.57 (m)	2.06 (m)
4b		1.90 (m)	2.17 (m)
5	124.9 (CH)	5.17 (br s)	5.34 (dt, 15.0, 7.5)
6	136.0 (CH)	5.19 (br s)	5.50 (dt, 14.4, 6.2)
7	32.7 (CH_2)	1.90 (m)	1.98 (m)
8	29-30 (CH_2)	1.23-1.27 (m)	1.23-1.32 (m)
9	29-30 (CH_2)	1.23-1.27 (m)	1.23-1.32 (m)
10	29-30 (CH_2)	1.23-1.27 (m)	1.23-1.32 (m)
11	29-30 (CH_2)	1.23-1.27 (m)	1.23-1.32 (m)
12	29-30 (CH_2)	1.23-1.27 (m)	1.23-1.32 (m)
13	29-30 (CH_2)	1.23-1.27 (m)	1.23-1.32 (m)
14	14.3 (CH_3)	0.86 (t, 7.1)	0.85 (t, 6.9)
1′	169.8 (C)		
2′	59.1 (CH)	5.05 (s)	5.07 (s)
3′	139.2 (C)		
4′- 8′	127-130 (CH)	7.20-7.40 (m)	7.20-7.40 (m)
9′	155.3 (C)		
10′	80.2 (C)		
11′-13′	28.5 (CH_3)	1.39 (s)	1.39 (s)

Table 4.3. ^{1}H and ^{13}C NMR data for derivatized amino alcohols **5a** and **5b** in $CDCl_3$

	S-BPG derivatized amino alcohol **5a**		*R*-BPG derivatized amino alcohol **5b**
No.	δ_C (mult)	δ_H (mult, *J* in Hz)	δ_H (mult, *J* in Hz)
1	18.8 (CH_3)	1.19 (d, 7.0)	1.05 (d, 6.9)
2	48.5 (CH)	3.93 (m)	3.95 (m)
3	73.2 (CH)	3.40 (br d, 8.2)	3.48 (ddd, 8.5, 4.2, 3.0)
4a	37.9 (CH_2)	1.55 (m)	2.08 (m)
4b		1.89 (m)	2.18 (m)
5	125.0 (CH)	5.20 (br s)	5.34 (dt, 14.5, 7.0)
6	135.9 (CH)	5.20 (br s)	5.50 (dt, 14.3, 6.9)
7	32.7 (CH_2)	1.92 (m)	1.98 (m)
8	29-30 (CH_2)	1.27 (m)	1.26 (m)
9	29-30 (CH_2)	1.27 (m)	1.26 (m)
10	29-30 (CH_2)	1.27 (m)	1.26 (m)
11	29.3 (CH_2)	1.36 (m)	1.35 (m)
12	34.0 (CH_2)	2.02 (m)	2.02 (m)
13	139.3 (CH)	5.79 (ddt, 17.3,10.4, 6.9)	5.79 (m)
14a	114.4 (CH_2)	4.92 (br d, 10.4)	4.91 (ddd, 10.2, 2.3, 1.2)
14b		4.98 (br d, 17.3)	4.97 (ddd, 17.2, 3.2, 1.5)
1′	169.9 (C)		
2′	59.0 (CH)	5.06 (s)	5.09 (s)
3′	139.3 (C)		
4′- 8′	127-130 (CH)	7.20-7.40 (m)	7.20-7.40 (m)
9′	155.3 (C)		
10′	80.0 (C)		
11′-13′	28.5 (CH_3)	1.40 (s)	1.39 (s)

Table 4.4 Cytotoxicity of derivatized amino alcohols **4-6** to mouse Neuro-2A neuroblastoma and human NCI-H460 lung cancer cell lines.

	[a]IC_{50} (at 48 h) in Cancer Cell Lines:	
	NCI-H460	**Neuro-2A**
(**4a**)	>50 μM	>50 μM
(**4b**)	>50 μM	>50 μM
(**5a**)	>50 μM	>50 μM
(**5b**)	33 μM	34 μM
(**6a**)	27 μM	38 μM
(**6b**)	25 μM	19 μM

[a]Cell viability was assessed by MTT assay and IC_{50} values were derived using nonlinear regression analysis.

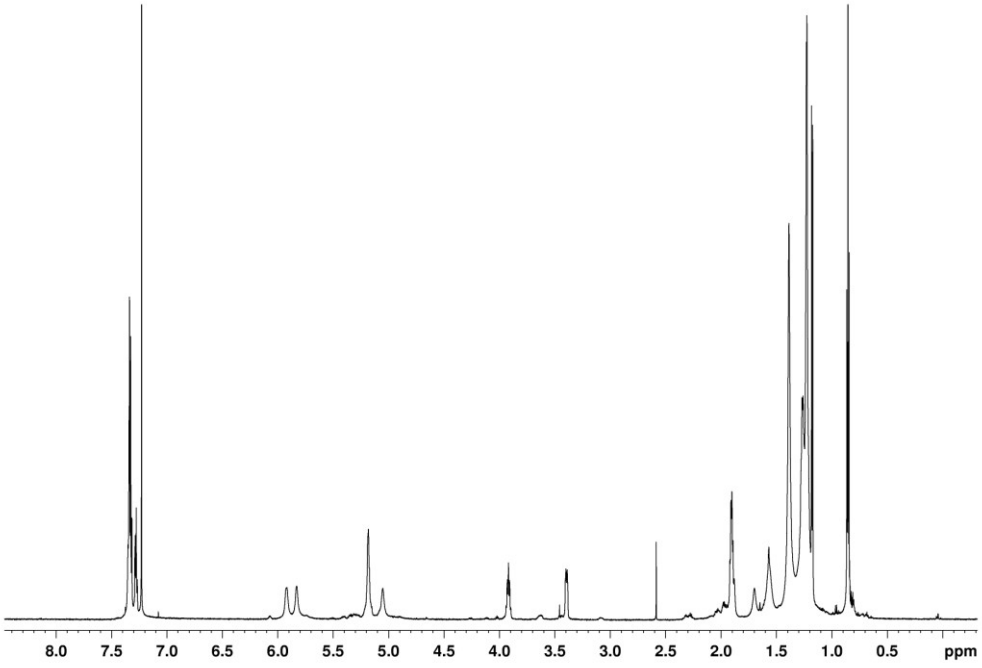

Figure 4.18 ^{1}H NMR spectrum for *S*-BPG amide of **4** (**4a**; 700 MHz, $CDCl_3$)

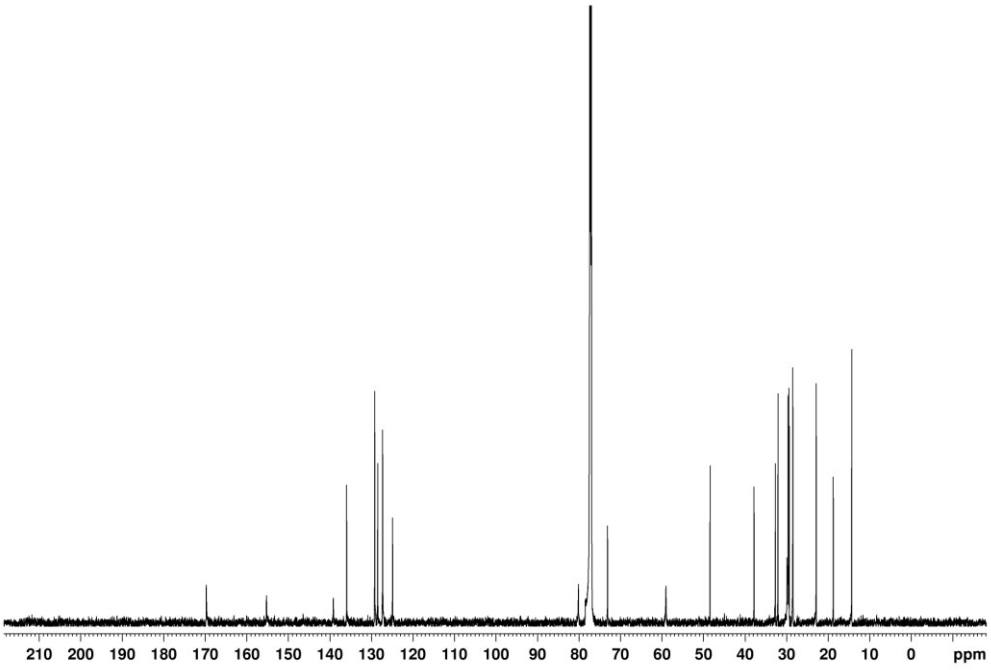

Figure 4.19 ^{13}C NMR spectrum for *S*-BPG amide of **4** (**4a**; 175 MHz, $CDCl_3$)

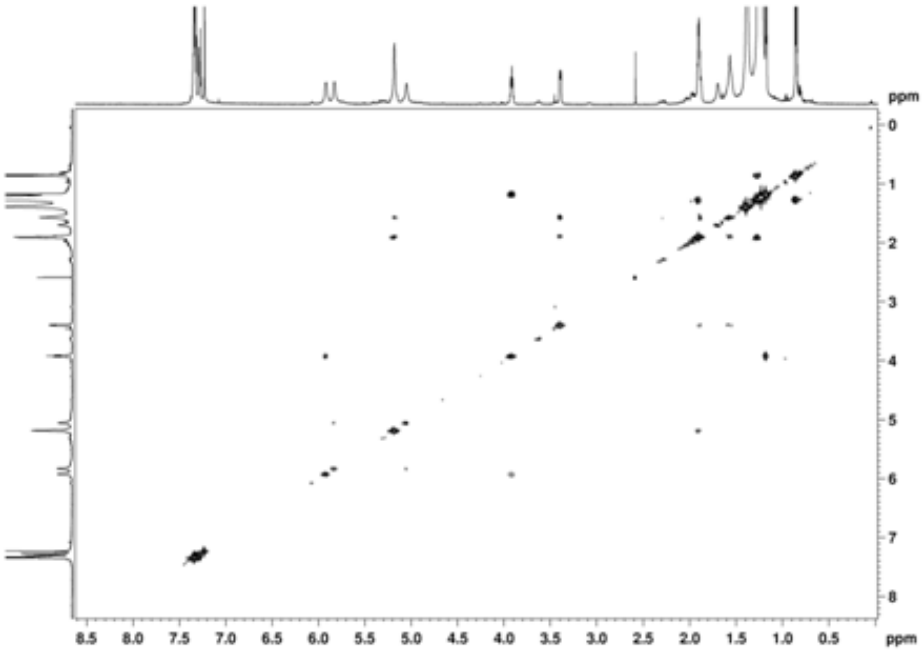

Figure 4.20 COSY spectrum for *S*-BPG amide of **4** (**4a**; 700 MHz, $CDCl_3$)

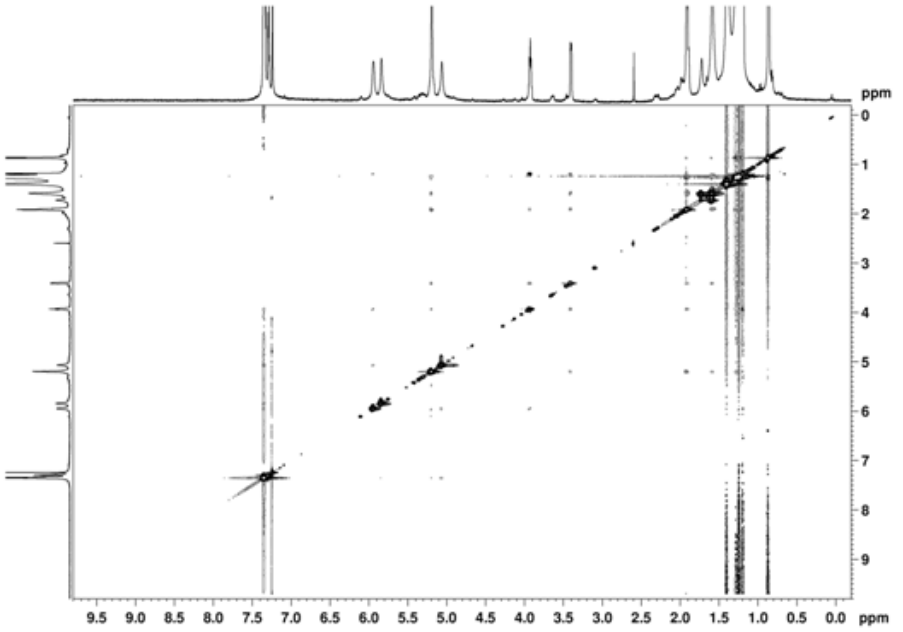

Figure 4.21 NOESY spectrum for *S*-BPG amide of **4** (**4a**; 700 MHz, $CDCl_3$)

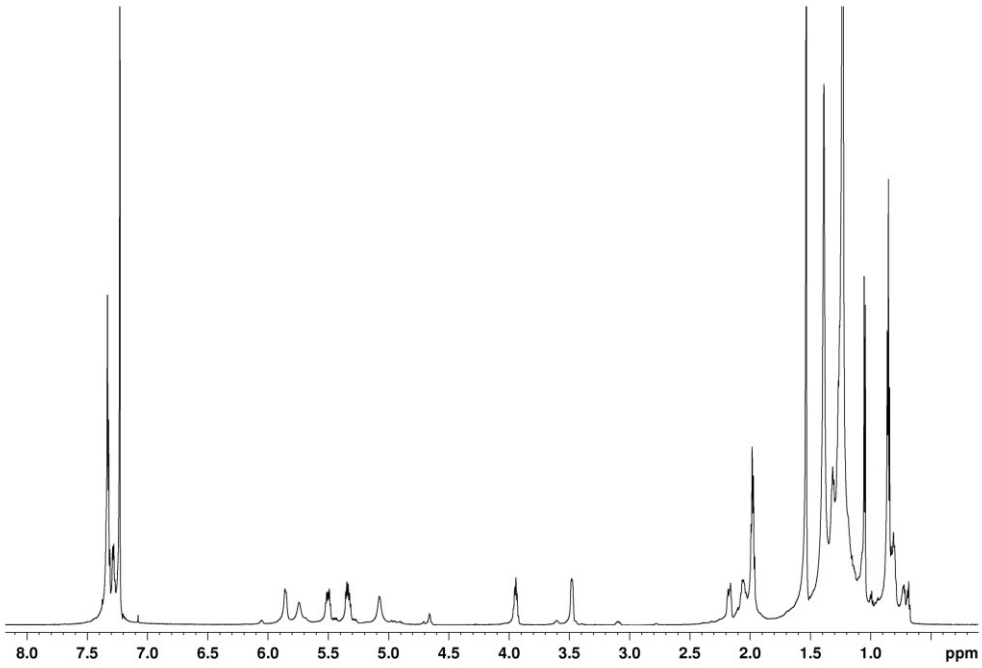

Figure 4.22 ^{1}H NMR spectrum for *R*-BPG amide of **4** (**4b**; 700 MHz, $CDCl_3$)

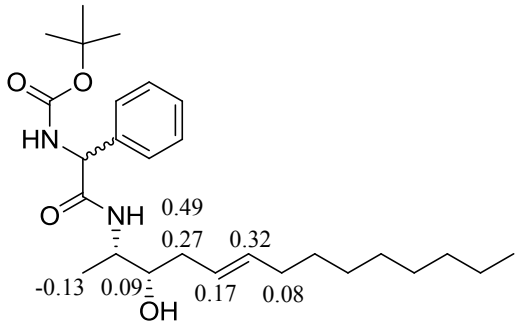

Figure 4.23 The absolute configuration of **4** (2*S*, 3*S*) with $\Delta\delta = \delta_R - \delta_S$ values indicated on the structure.

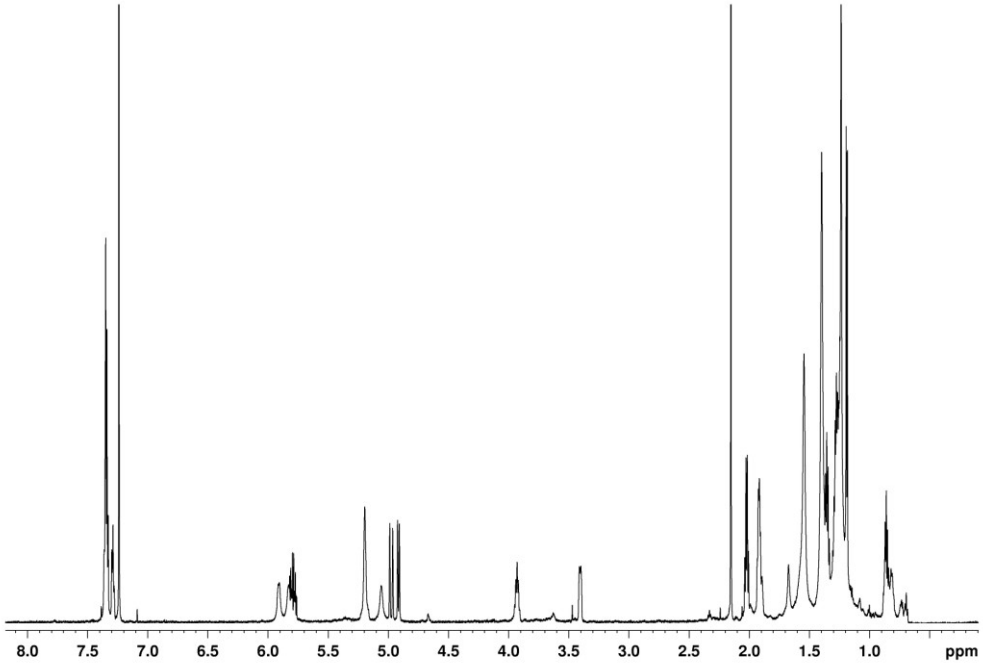

Figure 4.24 ^{1}H NMR spectrum for *S*-BPG amide of **5** (**5a**; 700 MHz, $CDCl_3$)

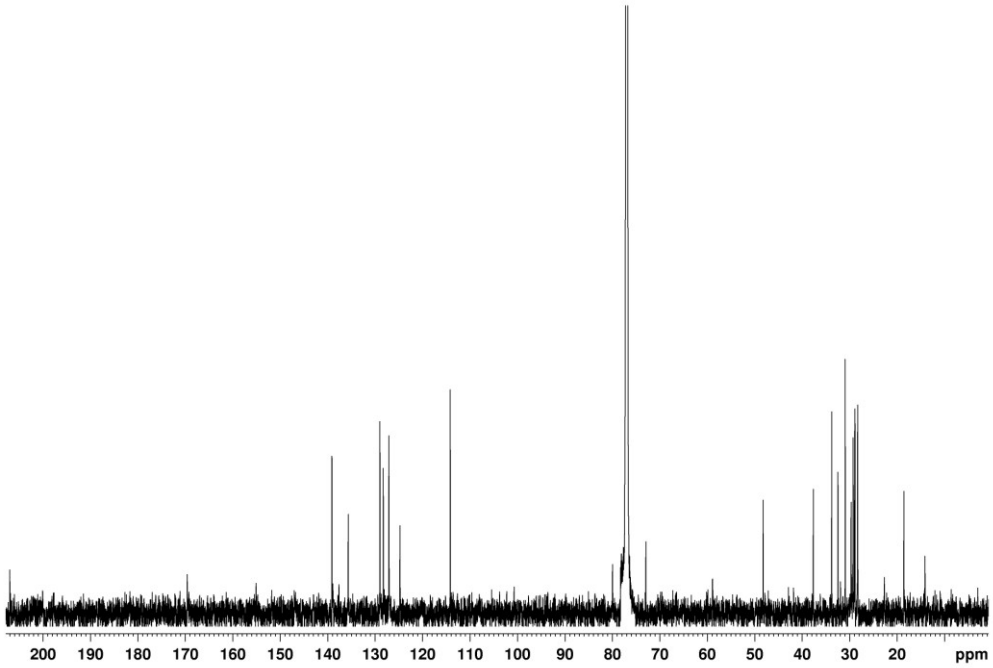

Figure 4.25 ^{13}C NMR spectrum for *S*-BPG amide of **5** (**5a**; 700 MHz, $CDCl_3$)

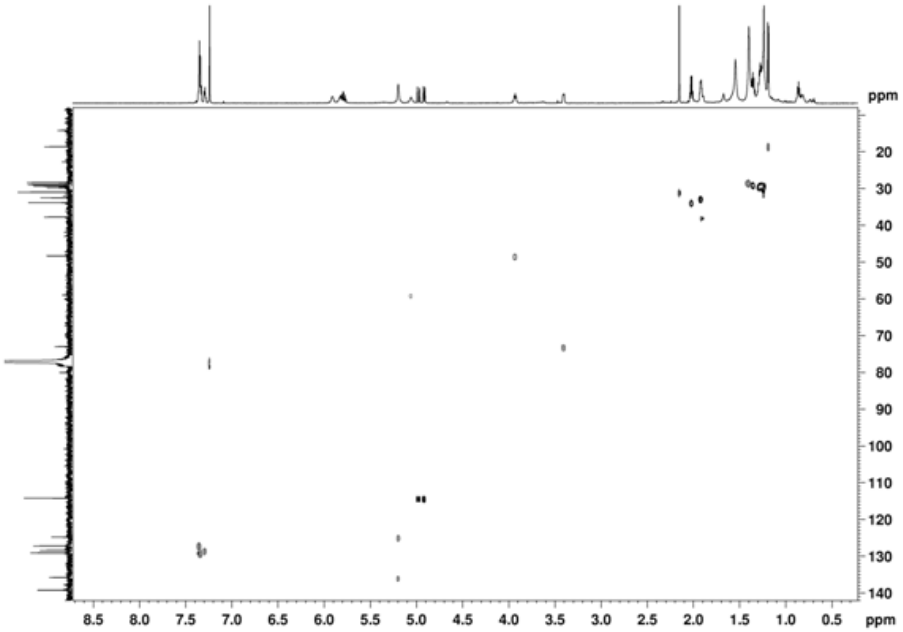

Figure 4.26 HSQC spectrum for *S*-BPG amide of **5** (**5a**; 700 MHz, $CDCl_3$)

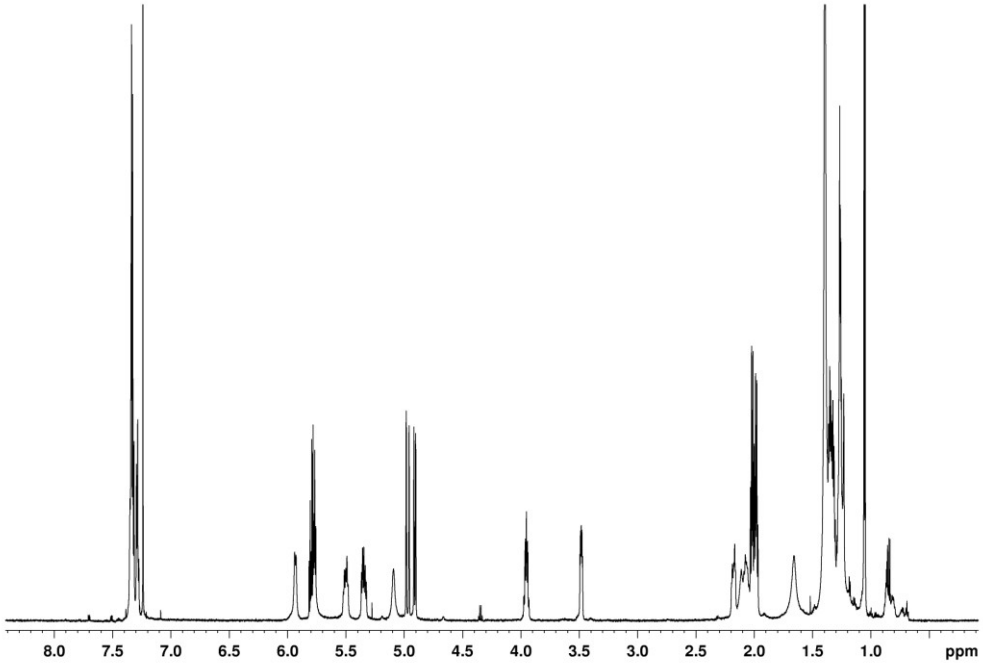

Figure 4.27 ^{1}H NMR spectrum for *R*-BPG amide of **5** (**5b**; 700 MHz, $CDCl_3$)

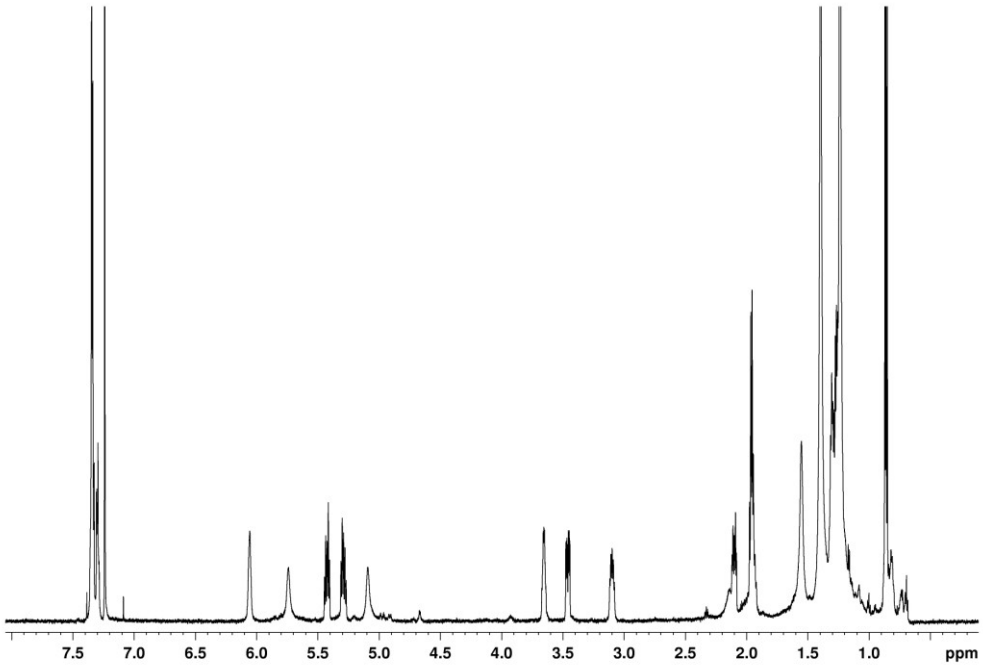

Figure 4.28 ^{1}H NMR spectrum for *S*-BPG amide of **6** (**6a**; 700 MHz, $CDCl_3$)

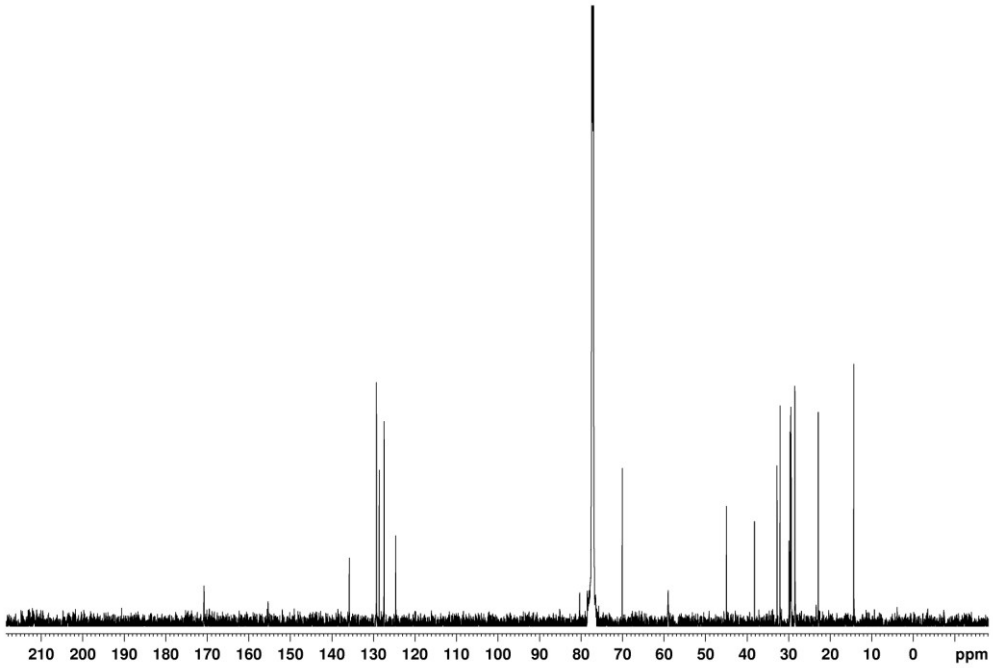

Figure 4.29 ^{13}C NMR spectrum for *S*-BPG amide of **6** (**6a**; 175 MHz, $CDCl_3$)

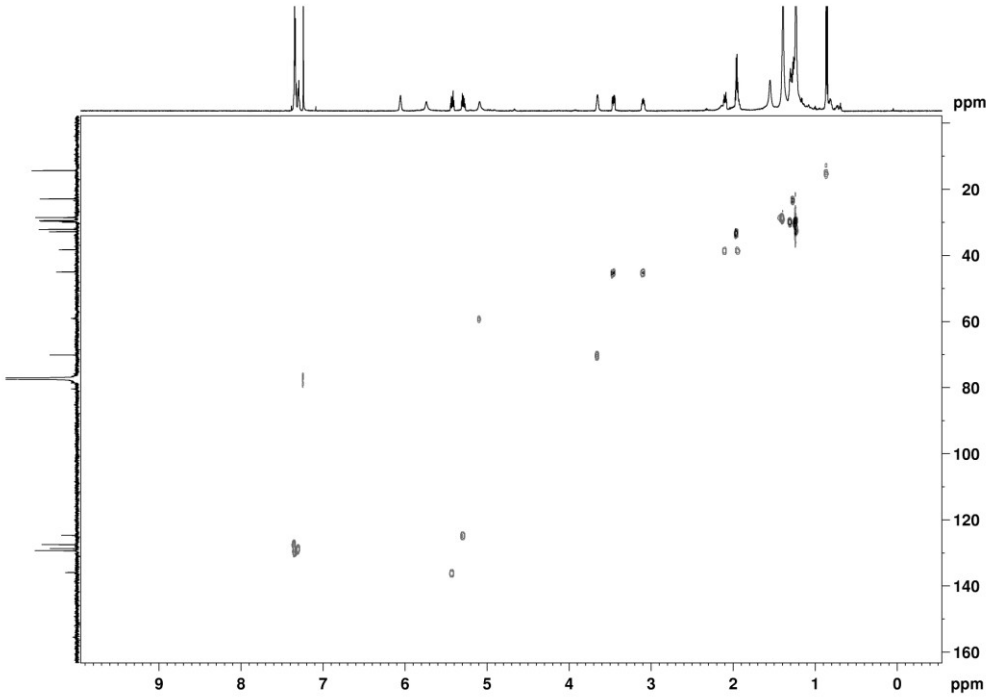

Figure 4.30 HSQC spectrum for *S*-BPG amide of **6** (**6a**; 700 MHz, $CDCl_3$)

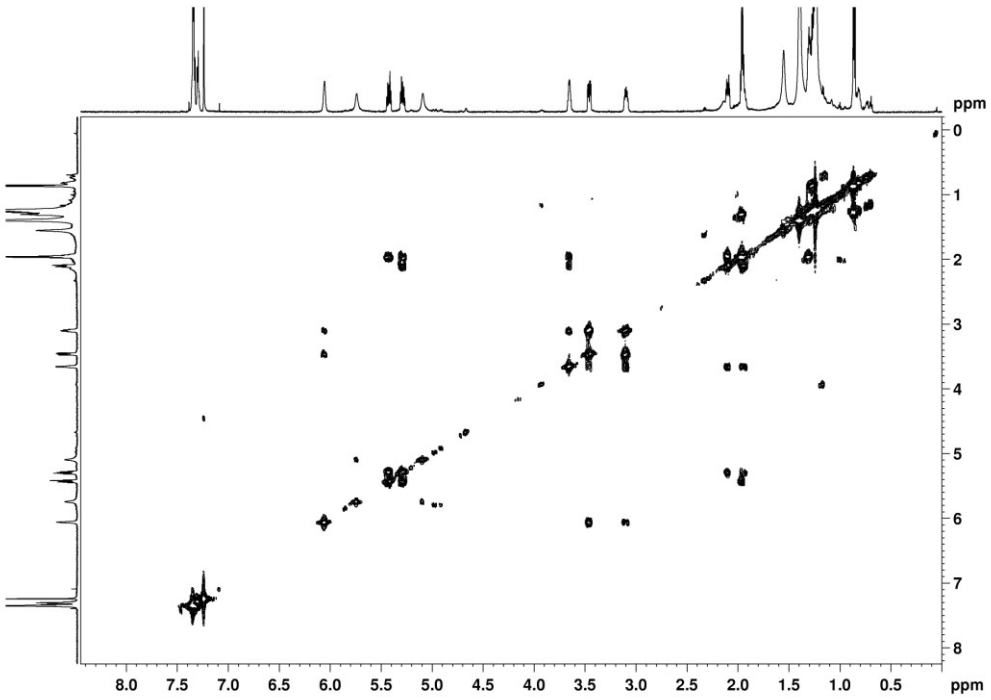

Figure 4.31 COSY spectrum for *S*-BPG amide of **6** (**6a**; 700 MHz, $CDCl_3$)

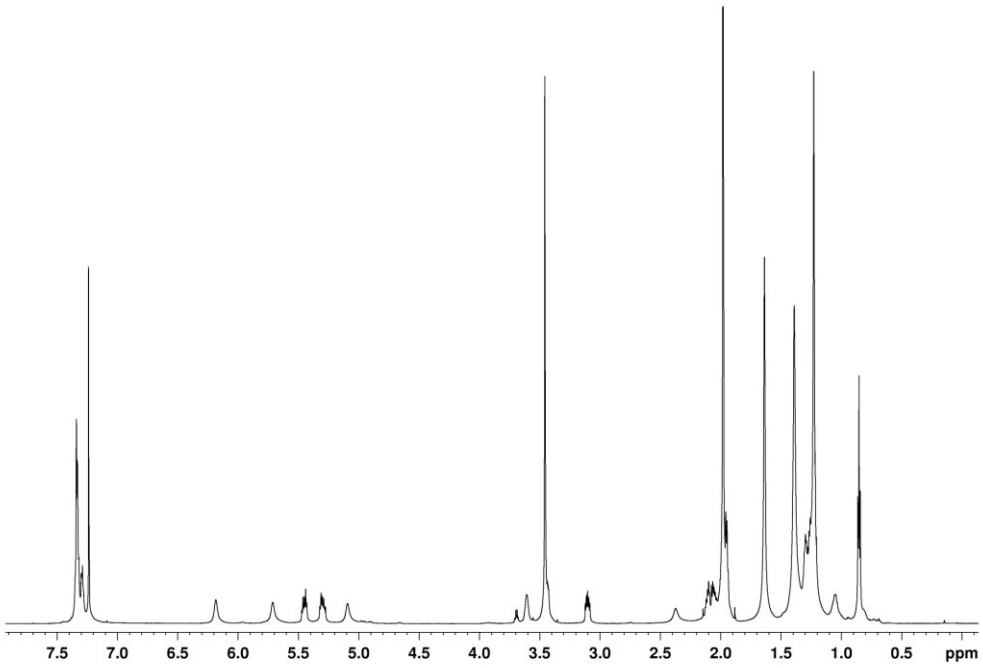

Figure 4.32 ^{1}H NMR spectrum for *R*-BPG amide of **6** (**6b**; 700 MHz, $CDCl_3$)

Experimental

General Experimental Methods. As described previously (Sikorska et al., 2012). In addition, NMR data for **1a**-**3a** were acquired at 400 (^{1}H) and 100 (^{13}C) MHz on a 5 mm inverse probe. The spectra were referenced to internal residual solvent signals in ppm (^{1}H NMR: $CDCl_3$, 7.24, CD_3OD, 3.31; ^{13}C NMR: $CDCl_3$, 77.23, CD_3OD, 49.15). High-resolution MS data were acquired on a Waters Micromass LCT Premier spectrometer.

Tunicate Collection, Extraction and Isolation. The ascidians *Pseudodistoma* sp. nov. A and *P. digitum* (Ascidiacea, Aplousobranchia, Didemnidae) were collected as described in Chapter 3. Both specimens (SAF2004-53 and SAF2004-48) are housed at the South African Institute for Aquatic Biodiversity (SAIAB), Grahamstown, South Africa.

The freeze-dried organisms were extracted with CH_2Cl_2-MeOH 2:1 to yield 3.87 g (*Pseudodistoma* sp.) and 2.71 g (*Pseudodistoma digitum*) of organic extract. The *Pseudodistoma* sp. organic extract was fractionated on Sephadex LH-20 (CH_2Cl_2-MeOH, 1:3) to give eight fractions, of which fractions four to six were subjected to reversed phase C_{18} solid phase extraction (RP-SPE) using a stepped gradient of 50-100% MeOH in H_2O. All 75% MeOH-H_2O fractions were dissolved in THF-H_2O (3:2), and K_2CO_3 was added followed by di-*tert*-butyl dicarbonate in a ratio of 1: 1: 1 before the reaction was stirred for 24 h at room temperature (Searle & Molinski, 1993). The *N*-Boc derivatized amino alcohols were further separated by RP_{18}-HPLC (column: Phenomenex Synergi Hydro, 250 mm x 10 mm, 85% MeOH in 0.1% FA/H_2O) to yield pseudodistaminol A (**1a**, 1.0 mg), pseudodistaminol B (**2a**, 2.5 mg) and pseudodistaminol C (**3a**, 1.0 mg). Despite storage of these compounds under argon at -20 °C, they degraded over a period of two months. The *P. digitum* organic extract was also subjected to consecutive LH-20 and RP-SPE fractionations as described above, but instead of MeOH, EtOH was used at each step. The 50% EtOH-

H_2O fraction was divided into two portions and further derivatized with *N*-Boc-*R*- or *N*-Boc-*S*-phenylglycine (*R*/*S*-BPG). In each case, the fraction was dissolved in dry CH_2Cl_2 and 1-ethyl-3-(3-dimethylaminopropyl)carbodiimide, 1-hydroxy-7-azabenzotriazole and *R*-BPG or *S*-BPG were added in ratio (1: 1.2: 1: 1.2) at 0 °C. The reaction mixture was allowed to warm up to room temperature and left for 24 h (Ito et al., 2004). The isolation of compounds **4-6** was performed by RP_{18}-HPLC (column: Phenomenex Synergy Fusion, 250 mm x 10.0 mm, 65% MeCN) resulting in **4a** (1.4 mg), **4b** (1.8 mg), **5a** (0.6 mg), **5b** (2.5 mg), **6a** (1.5 mg) and **6b** (3.0 mg).

Cell viability assays were performed as described previously in chapter 3.

Boc-pseudodistaminol A (**1a**). Amorphous solid; $[\alpha]^{27}_D$ –82 (*c* = 0.25, MeOH); HRESIMS $[M+Na]^+$ *m/z* 402.2972; (calcd for $C_{23}H_{41}NO_3Na$, 402.2984); ^1H and ^{13}C NMR, COSY, HSQC, HMBC, ROESY, 1D NOESY data (Figures 4.1-4.7, Table 4.1).

Boc-pseudodistaminol B (**2a**). Amorphous solid; LRESIMS $[M+Na]^+$ *m/z* 400.2; ^1H and ^{13}C NMR, COSY, HSQC, HMBC, ROESY data (Figures 4.8-4.12, Table 4.1).

Boc-pseudodistaminol C (**3a**). Amorphous solid; LRESIMS $[M+Na]^+$ *m/z* 392.2; ^1H NMR (400 MHz, CD_3OD) 5.34 (2H, t, *J* = 4.6 Hz, H-5, H-6), 3.56 (1H, d, m, H-2), 3.11 (1H, dd, *J* = 13.9, 4.6 Hz, H-1), 2.96 (1H, dd, *J* = 13.7, 6.7 Hz, H-1), 2.03 (4H, m, H-5, H-8), 1.43 (9H, s, H-3′, H-4′, H-5′), 1.31-1.35 (14H, m, H-3, H-4, H-9/H-13), 1.31 (4H, m, H-15, H-16), 1.29 (2H, m, H-14), 0.90 (3H, t, *J* = 7.0 Hz, H-17); ^{13}C NMR (100 MHz, CD_3OD) 159.2 (C, C-1′, from HMBC), 130.9 (2C, CH, C-6, C-7), 80.4 (C, C-2′, from HMBC), 71.9 (CH, C-2), 47.6 (CH, C-1), 33.1 (CH_2, C-15), 30.0-31.0 (8C, CH, C-3/C-4, C-9/C-15), 28.9 (3C, CH_3, C-3′/ C-5′), 28.3 (2C, CH_2, C-5, C-8), 23.9 (CH_2, C-16), 14.6 (CH_3, C-17).

***S*-BPG-(2*S*)-amino-(3*S*)-hydroxy-(5*E*)-tetradecene** (**4a**). Amorphous solid; $[\alpha]^{26}_D$ +48.8 (*c* = 0.33, MeOH); UV (MeOH) λ_{max} (log ε) 259 (6.2), 211 (8.0); HRESIMS $[M+H]^+$ *m/z* 461.3398; (calcd for $C_{27}H_{45}N_2O_4$, 461.3379); ^1H and ^{13}C NMR, COSY, NOESY data (Figures 4.18-4.21, Table 4.2).

***R*-BPG-(2*S*)-amino-(3*S*)-hydroxy-(5*E*)-tetradecene** (**4b**). Amorphous solid; $[\alpha]^{30}_{D}$ -13.3 (*c* = 0.33, MeOH); UV (MeOH) λ_{max} (log ε) 258 (6.3), 211 (8.0); HRESIMS $[M+Na]^+$ *m/z* 483.3206; (calcd for $C_{27}H_{44}N_2O_4Na$, 483.3199); ^1H NMR (Figure 4.22, Table 4.2).

***S*-BPG-(2*S*)-amino-(3*S*)-hydroxy-(5*E*),13-tetradecadiene** (**5a**). Amorphous solid; $[\alpha]^{25}_{D}$ +38.6 (*c* = 0.22, MeOH); UV (MeOH) λ_{max} (log ε) 259 (6.2), 211 (7.9); HRESIMS $[M+Na]^+$ *m/z* 481.3040; (calcd for $C_{27}H_{42}N_2O_4Na$, 481.3042); ^1H and ^{13}C NMR, HSQC data (Figures 4.24-4.26, Table 4.3).

***R*-BPG-(2*S*)-amino-(3*S*)-hydroxy-(5*E*),13-tetradecadiene** (**5b**). Amorphous solid; $[\alpha]^{31}_{D}$ –19.4 (*c* = 0.33, MeOH); UV (MeOH) λ_{max} (log ε) 258 (6.4), 214 (8.0); HRESIMS $[M+Na]^+$ *m/z* 481.3047; (calcd for $C_{27}H_{42}N_2O_4Na$, 481.3042); ^1H NMR data (Figure 4.27, Table 4.3).

***S*-BPG-(1*R*)-aminotridec-(4*E*)-en-2-ol** (**6a**). Amorphous solid; $[\alpha]^{26}_{D}$ +50.6 (*c* = 0.33, MeOH); UV (MeOH) λ_{max} (log ε) 259 (6.3), 212 (8.0); ^1H and ^{13}C NMR, COSY, HSQC data (Figures 4.28-4.31); ^1H NMR (700 MHz, $CDCl_3$) 7.10-7.35 (5H, m, H-4′/ H-8′), 6.06 (1H, s, NH), 5.42 (1H, dt, *J* = 15.0, 7.2 Hz, H-5), 5.29 (1H, dt, *J* = 14.6, 6.7Hz, H-4), 5.09 (1H, s, H-2′), 3.66 (1H, m, H-2), 3.46 (1H, dt, *J* = 14.0, 6.1, 3.1 Hz, H-1b), 3.10 (1H, dt, *J* = 13.3, 6.0 Hz, H-1a), 2.10 (1H, dt, *J* = 12.7, 6.0 Hz, H-3b), 1.96 (2H, m, H-6), 1.95 (1H, m, H-3a), 1.41 (9H, s, H-11′/H-13′), 1.24-1.30 (8H, m, H-7/H-10), 1.29 (2H, m, H-11), 1.24 (2H, m, H-12), 0.86 (3H, t, *J* = 7.1, H-13); ^{13}C NMR (175 MHz, $CDCl_3$) 170.8 (C, C-1′), 155.6 (C, C-9′), 135.8 (CH, C-5), 127.0-130.0 (5C, CH, C-4′/C-8′), 124.6 (CH, C-4), 70.1 (CH, C-2), 59.0 (C, C-1′), 45.0 (CH_2, C-1), 38.3 (CH_2, C-3), 32.1 (CH_2, C-12), 29.0-30.0 (4C, CH_2, C-7/C-10), 28.5 (9C, CH_3, C-11′/C-13′), 22.9 (CH_2, C-11), 14.3 (CH_3, C-13); HRESIMS $[M+Na]^+$ *m/z* 469.3036; (calcd for $C_{26}H_{42}N_2O_4Na$, 469.3042).

***R*-BPG-(1*R*)-aminotridec-(4*E*)-en-2-ol** (**6b**). Amorphous solid; $[\alpha]^{30}_{D}$ -35.5 (*c* = 0.33, MeOH); UV (MeOH) λ_{max} (log ε) 258 (6.4), 215 (8.0); ^1H NMR (700 MHz,

$CDCl_3$) 7.20-7.35 (5H, m, H-4′/ H-8′), 6.19 (1H, s, NH), 5.45 (1H, dt, *J* = 14.3, 6.1 Hz, H-5), 5.30 (1H, dt, *J* = 14.6, 7.0 Hz, H-4), 5.09 (1H, s, H-2′), 3.61 (1H, m, H-2), 3.44 (1H, m, H-1b), 3.10 (1H, ddd, *J* = 14.0, 7.6, 5.3 Hz, H-1a), 2.10 (1H, m, H-3b), 2.05 (1H, m, H-3a), 1.96 (2H, m, H-3a), 1.39 (9H, s, H-11′/H-13′), 1.23-1.28 (12H, m, H-7/H-12), 0.86 (3H, t, 6.7 Hz, H-13); HRESIMS $[M+Na]^+$ *m/z* 469.3022; (calcd for $C_{26}H_{42}N_2O_4Na$, 469.3042).

Bibliography

Appleton, D. R., Page, M. J., Lambert, G., & Copp, B. R. (2004). 1,3-Dimethyl-8-Oxoisoguanine, A new purine from the New Zealand ascidian Pseudodistoma Cereum. *Nat. Prod. Res., 18*(1), 39-42.

Chan, S. T. S., Pearce, A. N., Page, M. J., Kaiser, M., & Copp, B. R. (2011). Antimalarial β-Carbolines from the New Zealand Ascidian Pseudodistoma opacum. *J. Nat. Prod., 74*(9), 1972-1979.

Chbani, M., Païs, M., Delauneux, J.-M., & Debitus, C. (1993). Brominated Indole Alkaloids from the Marine Tunicate Pseudodistoma arborescens. *J. Nat. Prod., 56*(1), 99-104.

Ciavatta, M. L., Manzo, E., Nuzzo, G., Villani, G., Varcamonti, M., & Gavagnin, M. (2010). Crucigasterins A-E, antimicrobial amino alcohols from the Mediterranean colonial ascidian Pseudodistoma crucigaster. *Tetrahedron, 66*(38), 7533-7538.

Clark, R. J., Garson, M. J., & Hooper, J. N. A. (2001). Antifungal Alkyl Amino Alcohols from the Tropical Marine Sponge Haliclona n. sp. *J. Nat. Prod., 64*(12), 1568-1571.

Davis, R. A., Carroll, A. R., & Quinn, R. J. (1998). Eudistomin V, a New β-Carboline from the Australian Ascidian Pseudodistoma aureum. *J. Nat. Prod., 61*(7), 959-960.

Freyer, A. J., Patil, A. D., Killmer, L., Troupe, N., Mentzer, M., Carte, B., Faucette, L., & Johnson, R. K. (1997). Three New Pseudodistomins, Piperidine Alkaloids from the Ascidian Pseudodistoma megalarva. *J. Nat. Prod., 60*(10), 986-990.

Garrido, L., Zubía, E., Ortega, M. a. J., Naranjo, S., & Salvá, J. (2001). Obscuraminols, new unsaturated amino alcohols from the tunicate Pseudodistoma obscurum: structure and absolute configuration. *Tetrahedron, 57*(21), 4579-4588.

Hooper, G. J., Davies-Coleman, M. T., & Coetzee, P. S. (1995). New antimicrobial C14 and C13 amines from a South African marine ascidian *Nat. Prod. Lett., 6*, 31-35.

Ito, Y., Ishida, K., Okada, S., & Murakami, M. (2004). The absolute stereochemistry of anachelins, siderophores from the cyanobacterium Anabaena cylindrica. *Tetrahedron, 60*(41), 9075-9080.

Menna, M. (2009). Antitumor potential of natural products from Mediterranean ascidians. *Phytochem. Rev., 8*(2), 461-472.

Parker-Nance, S. (2003). *Aplousobranch ascidians (Tunicata: Ascidiacea) from southern Africa.* Ph.D., University of Port Elizabeth.

Pearce, A. N., Appleton, D. R., Babcock, R. C., & Copp, B. R. (2003). Distomadines A and B, novel 6-hydroxyquinoline alkaloids from the New Zealand ascidian, Pseudodistoma aureum. *Tetrahedron Lett., 44*(20), 3897-3899.

Searle, P. A., & Molinski, T. F. (1993). Structure and absolute configuration of (R)-(E)-1-aminotridec-5-en-2-ol, an antifungal amino alcohol from the ascidian Didemnum sp. *J. Org. Chem., 58*(26), 7578-7580.

Sikorska, J., Hau, A. M., Anklin, C., Parker-Nance, S., Davies-Coleman, M. T., Ishmael, J. E., & McPhail, K. L. (2012). Mandelalides A–D, Cytotoxic Macrolides from a New Lissoclinum Species of South African Tunicate. *J. Org. Chem., 77*(17), 6066-6075.

Vilar, E., Grünwald, V., Schöffski, P., Singer, H., Salazar, R., Iglesias, J., Casado, E., Cullell-Young, M., Baselga, J., & Tabernero, J. (2012). A phase I dose-escalating study of ES-285, a marine sphingolipid-derived compound, with repeat dose administration in patients with advanced solid tumors. *Invest. New Drugs, 30*(1), 299-305.

CHAPTER FIVE

GENERAL CONCLUSIONS

Justyna Sikorska

The investigation of marine natural products chemistry has a rich history and has resulted in the discovery of many promising natural products for research and treatment of human diseases, as well as agriculture. The structural assignment of "inspirational molecular structures" on a nanomolar scale became possible only recently, due to spectacular advances in NMR techniques. The focus of this research was to identify biologically active natural products through the application of modern NMR spectroscopy. To perform this task effectively and avoid re-isolation of known compounds, biological and chemical screening was combined with a dereplication approach and led to the isolation of new biologically active compounds.

The application of biological screening in parallel with ^{1}H and diffusion-ordered (DOSY) NMR analysis of tunicate extracts led to the identification of differentially brominated rubrolides, of which four are new and two are known. The analysis of 1D and 2D NMR and HRESIMS data permitted determination of the bromination pattern, while biological evaluation established their moderate activity against MRSA, as well as *Staphylococcus epidermidis*.

Structural assignment of mandelalides A-D, isolated in sub-milligram quantities from a new *Lissoclinum* species of tunicate, was accomplished only after acquisition of NMR data on a 700 MHz spectrometer equipped with a 5 mm cryogenic ^{13}C-observe probe. While a suite of standard modern NMR experiments was implemented to assign the planar structure of mandelalides, DQFCOSY, TOCSY, HETLOC and gated decoupled ^{13}C NMR experiments were performed to establish the relative configuration of the mandelalides. Moreover, the applicability of quantitative ROESY and RDC (residual dipolar coupling) techniques were also explored for the assignment of relative configuration. Determination of absolute configuration was accomplished on mandelalide A, after degradative methanolysis of the natural product and chiral GC-MS analysis. Biological investigation of mandelalides A-D indicated potent cytotoxicity against mouse Neuro-2A neuroblastoma and human NCI-H460 lung cancer cell lines, once again confirming that tunicates are a prolific source of new, chemically interesting and biologically relevant natural products. Nanomolar

cytotoxicity in parallel with the unusual skeleton of the mandelalides motivates for further investigation of their biological activity and biogenetic origin. This will be facilitated in the short term by re-collection of the *Lissoclinum* tunicate species to obtain additional quantities of the mandelalides, and enable the identification (through metagenomic sequencing) and possible cultivation of their microbial producer. Concurrently, these metabolites have been identified as targets for total syntheses that are already in progress.

The extraction and fractionation of two South African *Pseudodistoma* species led to identification of linear and cyclized amino alcohols, analogs of the Phase I anticancer compound spisulosine. Due to their polarity and close structural similarity, parent fractions containing these metabolites were derivatized to produce *N*-Boc and or *N*-Boc phenylglycine analogs and thus enable efficient separation and potential assignment of configuration. The *N*-Boc-phenylglycine derivatized amino alcohols appeared to be known compounds isolated previously from tunicates. However, the *N*-Boc analogues established an unprecedented group of natural products, presumably with the hydroxyl group of precursor linear amino alcohols being the point of cyclization to form a tetrahydropyran moiety. Knowing that *Pseudodistoma* species are abundant on White Sands Reef in Algoa Bay, South Africa, we will attempt to recollect the organism and re-isolate these natural products for configurational assignment and further biological evaluation. In parallel, a synthetic approach may be developed to obtain individual compounds and potentially circumvent the problem of challenging chromatographic separations of multiple close analogs.

This research has confirmed that the application of parallel chemical and biological screening can lead to the identification of new, biologically-relevant chemical entities that would not otherwise be identified. Isolation of these cytotoxic and antibacterial metabolites contributes to recognition of the importance of marine sources in the drug discovery process, and increases the pool of ascidian-derived natural product drug leads. Application of very recent developments in NMR techniques using a 700 MHz spectrometer equipped with a ^{13}C-observe cryoprobe

contributes to the frontier of natural product structural assignment, which has expanded to permit structure elucidation on sub-milligram sample quantities.